Experimental and Computational Studies on Laser Processing of Dissimilar Metals

A Thesis
Submitted for the Degree of
Doctor of Philosophy
in the Faculty of Engineering

By

Gandham Phanikumar

CENTRE FOR ADVANCED STUDY

DEPARTMENT OF METALLURGY

INDIAN INSTITUTE OF SCIENCE

BANGALORE-560 012, INDIA

MARCH 2002

Synopsis

Recent advances in the manufacturing processes using laser have led to increased use of advanced and dissimilar materials. Fusion weldments of dissimilar metallic joints are not well understood. Physical properties of the two metals being very different from each other lead to complexities in weld pool shape, solidification microstructure and segregation patterns. In this work, three binary systems, iron-copper, copper-nickel and aluminium-bismuth have been chosen to study the microstructural evolution during laser processing. Iron-copper system has solid state immiscibility and liquid miscibility. Copper and nickel have different physical properties but have complete miscibility in solid and liquid states and provide an ideal system for a detailed analysis. Aluminium-bismuth has liquid state immiscibilty and is a candidate material for bearing materials that require a uniform dispersion of soft material in the matrix. The studies comprise of both experimental and computational modelling efforts.

After a brief introduction in the first chapter, a review of literature concerning laser processing of dissimilar metals is presented in the second chapter. Issues that require further studies for understanding are highlighted to put the present work in perspective. In the third chapter, brief studies on the welding of iron and copper are presented. Microstructural features that are common to most dissimilar metal welds are described for low and high laser scan speeds. The weld pool shape is found to be asymmetric with more melting of iron, though the heat source is placed symmetrically on the butt joint. The weld interface also shows asymmetry with a smooth interface on the iron side and a rough interface on the copper side. A transition from planar to cellular growth from iron side in to the weld was also observed. Detailed composition analysis shows a gradual increase in the composition of weldment from the iron side in to the weld pool, and an abrupt increase from the copper side. Microstructural banding was characterised by a change of length scale and composition.

The fourth chapter presents a detailed analysis of laser welding of copper and nickel. Welds have been done at different scanning speeds such that the welding mode changes from conduction mode at high scan speed to keyhole mode at low scan speed. A small number of spot welds were also performed for comparison with computational studies. Detailed microstructural analysis using optical microscopy, scanning electron microscopy, transmission electron microscopy and quantitative composition analysis are presented. The weld pool shape was found to be asymmetric and the microstructural features described for the iron-copper system were found to be similar in copper-nickel system as well, at all the welding speeds. Cellular microstructure was observed in the weld pool at all welding speeds. Composition across the weld indicates good mixing on the nickel side in the weld pool. TEM study shows that the weld pool is highly strained.

A computational modelling of the transport phenomena that take place during laser welding of dissimilar metals of was developed using control volume formulation. Since the process is inherently three dimensional in nature, a 3D transient model was developed to calculate conservation of mass, momentum, enthalpy and composition. Nickel was observed to melt first and the heat is transported to the copper side by convection in the molten nickel due to marangoni and buoyancy forces. The final shape of the weld pool was observed to be asymmetric. The composition profile across the weld pool shows good qualitative agreement with the experimentally observed one. An attempt was also made to explain the interface microstructures using thermodynamic arguments.

The fifth chapter deals with the microstructure development in aluminium-bismuth system under laser processing. The aim of the work is to determine the size distribution of bismuth particles experimentally and to develop a computational model the same through computation to gain further insights in to the factors that govern the distribution. The geometry used here is that of laser surface melting. The alloy was made using laser cladding of elemental powders. Solidification at different speeds was simulated using laser remelting at three speeds namely, 5mm/s, 13 mm/s and 20 mm/s. The microstructures in transverse and longitudinal sections were observed in SEM to observe the shape of remelt pool and microstructure. Bismuth particles were uniformly distributed in the matrix of

aluminium. The orientation of the grains with the laser scan direction was used to obtain the growth rate as a function of height from the bottom of the remelt pool. Size distribution of bismuth particles for alloys remelt at the three different scanning speeds, was determined using image analysis. The longitudinal section shows bending of aluminium grains towards the top with alignment of bismuth particles along the growth direction for higher growth rates.

A computational model was developed to calculate the size distribution of bismuth particles during laser remelting. The model, developed for welding to obtain temperature and velocity profiles, was modified to determine the remelt pool shape and cooling rates during laser surface remelting. Phase separation of Al-Bi takes place in the liquid state and could be understood using homogeneous nucleation and growth. The driving force for nucleation was calculated and a map of nucleation rate was constructed as a function of composition and temperature. Size distribution of bismuth was calculated at different cooling rates taking in to consideration, simultaneous nucleation and growth by diffusion in the melt, till the super saturation is exhausted. Cooling rates used were obtained from the laser remelting program. Collision of particles due to convection in the laser melt pool is taken in to account by a particle tracking algorithm. Final size distribution of bismuth particles was calculated to correlate with the actual distribution obtained for the laser remelted alloys. The thesis concludes with a summary of results and suggestions for future work.

Acknowledgement

Contents

List of Figures

Chapter 1

Introduction

Laser processing is a versatile technique used in several manufacturing processes. Of these, welding and cladding form the most important ones, in terms of solidification microstructure that governs the performance of the final product [1]. Welding is a mature field and is routinely used in the industry to join metals/alloys of similar physical properties [2,3]. Microstructure evolution during welding is well understood in terms of grain structure and phase formation. The growth of the base alloy in to the weld is understood to take place in a continuous fashion without a nucleation barrier. The grain structure is usually columnar in the outer region of the weld with a parting line or equiaxed grains at the centre [4]. Several computational studies exist that have successfully shown insights in to the physical processes that occur during the welding. Computational heat transfer and fluid flow calculations were used to predict the weld pool shape and the cooling rates at various locations in the weld which were used to correlate with the microstructures observed in the experiment [5].

However, not many studies exist on welding of dissimilar metals/alloys. Majority of the existing literature is mainly concentrated on the joining of dissimilar steels and analyse the problem in a case-by-case manner. Quality of weld assessed for several metals was usually used to decide if a combination is weldable [6]. Microstructural features in dissimilar metal welding are not well characterised. The asymmetric shape of the weld, mixing patterns and the solidification microstructure are not well understood. During dissimilar welding of pure metals, the solidification has to take place from base metals into an alloy melt of different composition. A thermodynamic analysis is required to determine the conditions under which such a growth is possible. Microstructural features that emerge due to difference in the physical properties of the two metals could be very different from the features observed in welding of similar metals/alloys. Existing computational models of welding cannot be

extended to dissimilar welding in a straightforward manner, since, welding of dissimilar metals is an inherently three dimensional transient problem. Property variation with compositions that can vary sharply within the weld pool, pose additional difficulties. Hence, from a scientific standpoint, analysis of a dissimilar metal joint offers a number of challenges. A systematic study from a scientific view point is therefore desirable in this area. In the present work, a detailed characterisation of dissimilar welds is attempted. Computational studies are performed to gain insight in to the transport phenomena that take place during dissimilar metal welding. An attempt is also made to explain the microstructures observed in the solidified alloys.

In this work, three binary systems *viz.*, iron-copper, copper-nickel and aluminium-bismuth have been chosen to study the microstructural evolution during laser processing. Iron-copper system has solid state immiscibility and liquid miscibility. Copper and nickel have different physical properties but have complete miscibility in solid and liquid states and thus provide an ideal system for a detailed analysis. Aluminium-bismuth has liquid state immiscibilty and is a candidate material for bearing materials that require a uniform dispersion of soft material in the matrix.

The studies comprise of both experimental and computational modelling efforts. Laser welding experiments were done on Fe-Cu and Cu-Ni at different scanning speeds and a detailed microstructure analysis is presented in chapters 3 and 4 respectively. A three dimensional transient computational model is also developed using control volume formulation to simulate the transport phenomena in laser welding of dissimilar metals. Chapter 5 deals with laser remelting of Al-Bi system at different scanning rates to study the microstructural evolution as a function of processing parameters. A computational model to study nucleation and growth of bismuth particles in aluminium matrix is presented to gain an insight in to the parameters that dictate the final size distribution. The work is summarised in chapter 6 and the scope for future work is presented in chapter 7.

Chapter 2

Literature Review

Lasers are being used in several fields such as materials processing, lithography, communications, medicine, biology and physics [7]. Industrial lasers make use of the laser beam intensity and flexibility of beam delivery for various materials processing techniques. A single laser could be used for processes such as surface modification, alloying, cladding, cutting, and welding of a wide range of engineering materials [1]. Several reviews have been published from time to time describing various advantages of laser welding over other conventional welding processes [2,3,6,8]. Laser cutting and surface modification are now accepted by industry and are used routinely in the automobile industry [9]. Novel processes such as rapid prototyping and direct metal deposition are also being developed using lasers [10].

Figure 2.1 shows a map of various manufacturing processes that use lasers at different power densities and interaction times. The physical mechanisms that operate at various regimes are also indicated. It is clear that during a given manufacturing process there are several physical processes that play role. There are also some common physical processes between different manufacturing processes.

In this chapter, a review of the literature concerning the physical phenomena that govern microstructure evolution during laser welding and cladding will be presented. Relevant issues will be highlighted to place the present work in perspective. The review is organised in the chronology of the physical processes that take place in laser-material interaction, *viz.*, melting, mixing and solidification. In the first section, literature concerning the laser heating, melting and vaporisation is reviewed. Mixing in laser surface alloying and welding are discussed in the second section. The aspects of solidification and microstructure evolution are review in the third section. The chapter is concluded with the issues that

require further studies. The term laser melting will be used interchangeably with laser welding and cladding due to the common nature of the processes.

2.1 Physical processes during laser melting

2.1.1 Laser Heating

The phenomenon of heating by laser radiation is well understood. An in-depth study of the physical and chemical mechanisms governing the interaction of laser radiation with solid metallic targets is given in a book by A.M. Prokhorov *et. al.* [11].

Table 2.1 Absorptivity of several metals at laser wavelengths of 1.06 µm and 10.6 µm [6].

Metal/Alloy	η at room temperature Nd:YAG Laser (1.06 µm)	η at room temperature for CO_2 Laser (10.6 µm)
Al	0.06	0.02
Cu	0.05	0.015
Fe	0.1	0.03
Ni	0.15	0.05
Ti	0.26	0.08
Zn	0.16	0.03
Carbon Steel	0.09	0.03
Stainless Steel	0.31	0.09

When a laser beam strikes a metallic target, only a part of the energy is absorbed as heat. Thus, the heat flux on the surface of the metal could be written as $q''(r) = P\eta f(r)$, where P is the incident laser power, η is the absorption coefficient or coupling coefficient and $f(r)$ is the distribution of laser intensity. The laser power is limited only by the size of the laser that can be manufactured. The coupling coefficient η is dependent on several parameters that include material response to the wavelength of laser and the surface condition. Absorption coefficients for Nd:YAG and CO_2 laser radiations for various metals and alloys are shown in the table 2.1 above. Polished clean metal surfaces have low absorption coefficient. The absorption coefficient is also found to increase with surface

roughness, presence of defects, impurities and oxides on the surface and surface adsorbed substances. At higher temperature, the absorption is higher as shown for a few common metals in the figure 2.2. Several studies also exist that attempt to determine experimentally, the absorption coefficient of a metal surface [12,13,14,15]. The absorption coefficient of a metal surface is a variable difficult to determine experimentally for a given process.

The intensity distribution of the laser beam is governed by the lenses used for focusing. A Gaussian distribution described by equation 2.1, also referred to as TEM_{00} mode has the peak intensity at the centre of the laser beam. At focus, this distribution leads to high energy density at the centre of the laser beam and is thus an appropriate distribution for applications such as welding requiring high depth of penetration. A shallower distribution in TEM_{01} mode, approximated by equation 2.2, has an annular nature of the intensity distribution. This leads to a shallow melt pool with low dilution and is normally used for cladding and alloying processes [3].

$$f(r) = \frac{1}{\pi r_q^2} \exp\left(-\left(\frac{r}{r_q}\right)^2\right) \tag{2.1}$$

$$f(r) = \frac{1}{\pi r_q^2} \exp\left(-\left(\frac{r}{r_q} - \alpha\right)^2\right) \tag{2.2}$$

Where, α is a constant, r is radial distance from the centre of the laser and r_q is the radius of laser. Figure 2.3 shows the radial intensity distributions for these two modes of operation that are commonly used in laser processing.

It is a nontrivial problem to obtain the temperature distribution in a solid under a distributed moving heat source. The nature of the solution depends on the distribution of the heat source. If the solid undergoes phase change to liquid, the solution would involve the tracking of a moving interface between the two phases with a condition of heat flux balance due to the release of latent heat at the interface. Solutions to this problem, referred to as 'Stefan Problem', would be numerical in nature for domains in two or three dimensions with distributed surface heat sources.

2.1.2 Modelling of heat transfer

Analytical and numerical solution of the temperature distribution under a distributed heat source, as applied in welding, has been modelled by several researchers. The earliest work to determine temperature distribution during welding was by Rosenthal who gave analytical solutions for temperature distribution in a solid under a moving point heat source [16].

Cline and Anthony [17] used a Gaussian heat source, constant scan speed of heat source, and a semi-infinite solid to analyse the heat treating and melting under laser. They assumed no latent heat release and equal properties in solid and liquid. Temperature distribution, melt penetration depth, and cooling rates were obtained through analytical expressions as a function of input power. At a constant power, melt depth was observed to decrease with scan speed. At a constant scan speed, melt depth was observed to increase with input power. Deep penetration welding was modelled using method of images and the depth of melt was obtained by a force balance between vapour pressure and combination of buoyancy and capillarity forces. Correlations with experiments were presented to show an agreement with the calculated values.

A summary of analytical solutions was given by Mazumder and Steen [18] along with a numerical solution for a moving Gaussian heat source using finite difference technique considering deep penetration welding as well. Details of the numerical technique used were presented along with temperature distribution on the surface and below the surface. Melt width and depth along with experimental correlations were presented.

Sekhar *et. al.*, [19] have extended the heat conduction models of existing literature by including latent heat of fusion and obtained mushy zone location for alloy substrates. These studies had ignored fluid flow in the molten region, which was shown to be important by later works.

2.1.3 Melting and convection

Laser melting is localised and is initiated on the surface where the temperature is highest. Large temperature gradients exist in the laser melt pool due to distributed heating on the top surface and heat extraction by the base metal. These gradients lead to free convection in the melt pool by buoyancy and Marangoni forces that largely determine the shape and size of the melt pool. Buoyancy forces arise from density changes due to temperature and

composition gradients in the melt pool. The driving force for flow on the free surface due to surface tension gradient induced by temperature gradients is given by equation 2.3.

$$\mu \frac{\partial u}{\partial y} = \frac{\partial \sigma}{\partial x} = \frac{\partial \sigma}{\partial T}\frac{\partial T}{\partial x} = \sigma_T \frac{\partial T}{\partial x}$$

(2.3)

where, σ_T is the temperature coefficient of surface tension, u is the velocity component along x axis, y is the direction perpendicular to the x-axis, and μ is the dynamic viscosity. Figure 2.4 shows a schematic of fluid flow direction for the cases of positive and negative σ_T.

An order of magnitude analysis could be done to determine the relative importance of these two driving forces in laser melting. The maximum velocity that can be obtained by buoyancy forces is given by $u_m \sim \sqrt{g\beta\Delta T d}$ and that due to Marangoni forces is given by

$u_m \sim \frac{d}{2\mu}\sigma_T \frac{dT}{dx}$ [20]. Assuming $\Delta T = 600K$, $d = 0.5mm$, $\sigma_T = -10^{-4} Nm^{-1}K^{-1}$, $\beta = 3\times10^{-5} K^{-1}$, $\mu = 10^{-3} Nsm^{-2}$ and $\Delta x = 2mm$, one can estimate that u_m is 7.5 m/s due to Marangoni force and is 0.9 mm/s due to buoyancy forces. It is clear that Marangoni forces play an important role in the convection of a laser melt pool. The actual velocity field could be obtained only by a detailed numerical solution of the conservation equations of mass, momentum and enthalpy in the melt pool.

2.1.4 Modelling of convection

The studies on numerical solution of heat and fluid flow to quantify the effect of convection on pool shape and mixing have grown over the last three decades both in the understanding as well as the complexity of problem tackled.

A numerical solution of transient heat and fluid flow was first given by Oreper and Szekely [21] to show the effect of buoyancy, Lorentz force and Marangoni driven flow on the shape of melt pool. The authors show that surface tension driven flows have a profound effect on the shape of the melt pool. Negative values of the temperature coefficient of surface tension (σ_T) result in a wide and shallow pool whereas a postive σ_T leads to deep and narrow pool. The magnitude of velocities was shown to be a function of the processing parameters.

Chan $et.\ al.$, [22] developed a two-dimensional transient model for convective heat transfer and surface tension driven fluid flow. They described the effect of material properties and

process parameters on the velocity and temperature on the surface, pool shape and cooling rate. The maximum velocity on the free surface was found to be two orders of magnitude greater than the scan speed of the laser.

A detailed analysis of the fluid flow in laser melting under steady state [23] and transient conditions [24,25] was given by Basu and co-workers for axisymmetric geometry. Latent heat evolution was neglected and the interface between solid and liquid was tracked using melting temperature. The shape of the melt pool and the strength of the vortices in the melt pool were analysed at different processing conditions to conclude that Prandtl number has a significant effect.

Chan *et. al.*, [26,27] extended their earlier model to a three dimensional axisymmetric model to determine surface temperature, velocity field, solute distribution and cooling rate during laser melting and resolidification at small scanning speeds. They used superposition of two two-dimensional models to simulate a three dimensional perturbation model as well. Particles introduced in the melt pool were traced to show that they recirculate several times before solidifying into the advancing solid-liquid front, demonstrating good mixing in the pool. Aspect ratio (width/depth) was shown to increase with increase in both Prandtl number and Marangoni number.

A three dimensional non-axisymmetric transient model of weld pool was developed by Zacharia *et. al.*, [28,29,30] who analysed the effect of surface tension coefficient on the convection and melt pool shape with experimental correlations. The presence of sulphur in the melt changes the sign of σ_T from negative to positive at lower temperatures, leading to two counter circulating vortices in the narrow and deep melt pool. Corresponding experiments were performed on 304 type of stainless steel for different contents of sulphur and a good agreement was demonstrated between the experimentally observed pool shape and the computed one.

Other studies by Kou and Wang [31], Natarajan Ramanan and Korpela [32], Russo *et. al.*, [33], Dutta *et. al* [34] and Joshi *et. al.* [35] also analyse fluid flow and its effect on the shape of melt pool and temperature distribution.

The free surface at the top of the melt pool was assumed flat in all the above studies. Paul and Debroy [36] performed a two-dimensional transient simulation to solve the temperature and velocity distribution in laser welding at low powers. After the steady state profiles were obtained, the free surface was allowed to deform to show the effect of surface velocity on

the shape of top surface. An upward bulge was shown at the edge of the pool and under the heat source. From the direction of the velocity, the upward bulge at the edge of the pool is expected but the bulge at the centre of the pool is not completely understood.

Zehr [37] performed extensive simulations of surface tension driven flow during welding using a three dimensional transient formulation for a moving heat source. Free surface deformation was also taken into account by modifying the descretised equations for the partially filled surface cells, and applying a pressure boundary condition and conserving the total volume. Test cases were run for Aluminium and Steel and the computed melt pool shapes were verified by comparison with experimental results.

While most of the studies mentioned above deal with analysing the melt pool shape and thermal history as a function of processing parameters for different materials, few overviews do exist that discuss the shape of the melt pool as a function of non-dimensional quantities. The size and shape of the laser melt pool depends on material properties of the metal via Prandtl Number ($\Pr = \upsilon / \kappa$, where, υ is the kinematic viscosity and κ is the thermal diffusivity) and surface tension number ($S = \dfrac{\sigma_T q'' d}{\mu u_0 k}$, where d is the diameter of the laser beam, μ is the dynamic viscosity, u_0 is the characteristic velocity and k is thermal conductivity). Figure 2.5 shows shapes of a laser melt pool at different Prandtl and surface tension numbers [38]. Similarly, Peclet Number and Marangoni Number were also shown to be important in determining the melt pool shape [39]. It could be said that prediction of melt pool shape by computational techniques, taking into account convection in the melt, has now reached a mature state.

2.1.5 Vaporisation and Keyhole formation

Most of the studies described above are valid for low laser power where little or no vaporisation of melt takes place. Above a certain threshold laser intensity, the energy transfer from the beam to the work piece increases rapidly and deep penetration welding occurs. A cylinder of vapour/plasma exists below the beam, with an appearance of 'keyhole' (see figure 2.6), and leads to enhanced absorption of energy by plasma or by multiple internal reflection of the laser and plays a dominant role in the welding process.

Metzbower [40] described the keyhole formation in terms of a force balance between the surface tension of the liquid surrounding the vapour plume and the vapour pressure. A

temperature distribution across the keyhole was also obtained assuming a Gaussian distribution of the laser intensity. The author points out that the temperatures in the keyhole must be considerably higher than the boiling point of the work piece.

Dowden *et. al.*, [41] described a model for energy interchange and vapour flow in the keyhole to calculate the shape. The model gives approximate depths of keyholes that are closed at the bottom. Kroos *et. al.*, [42,43] give a linear stability analysis of a keyhole in terms of the ablation pressure that tends to open the keyhole versus surface tension forces that tend to collapse the keyhole as shown schematically in the figure 2.7. A threshold power was calculated at which the keyhole is stable for Al, Cu and Fe. Numerous studies have been performed about the dynamic behaviour of the keyhole both computationally [44,45,46,47,48,49] and experimentally [50,51,52].

Most of the models available do not consider the relevant physical processes and the liquid-vapour interactions in a self-consistent manner to obtain keyhole shape without assuming it *a priori*. Physical properties associated with formation of plasma and its interaction with the liquid, are also not easily available. Recently, Ki *et. al.*, [53] have proposed a level set method considering mass and energy balance, evaporation at the liquid-vapour interface, homogeneous boiling beneath the liquid-vapour interface, fluid flow in a thin liquid layer and multiple reflection of laser in the keyhole to calculate the shape of the keyhole. Free surface temperature profile, mass loss and surface recession speed were calculated. Multiple reflection of laser in the keyhole was shown to be an important factor in the enhanced absorption of laser radiation. A comprehensive model to simulate heat and fluid flow in laser welding considering keyhole formation as well is difficult and is in its early stage of development.

2.2 Mixing and joining

2.2.1 Mixing in alloy melt pool

Computational studies on solute transport in laser melt pool during laser surface alloying and cladding are limited. Chande and Mazumder [54] attempted to explain the mixing and the fluctuations in the composition of laser surface alloyed Fe-Ni using the vigour of fluid flow in the melt pool. A decrease in the diameter of the laser is shown to increase the uniformity of the alloy pool. However, no numerical solution of fluid flow and composition

distribution was made. Kar and Mazumder [55] assumed a well mixed alloy melt pool and solved for temperature and solidified alloy composition as a function of powder feed rate and specific laser energy. A non-equilibrium partition coefficient valid at high growth rates was used to obtain the solidified alloy composition, which exceeds the solidus composition given by the phase diagram.

A numerical solution of temperature, fluid flow and concentration profile in the alloyed region was first studied by He *et. al.* [56]. The temperature field obtained from the classical Rosenthal solution was used as an initial guess. The shape of the melt pool was then modified by incorporating latent heat evolution and convection within the liquid region. Solute conservation equation was solved decoupled with the steady state solution of heat and fluid flow. A diffusional flux condition at the top surface and solute partitioning boundary condition at the solidifying interface were used. Finite element method was used for the solution of composition as a function of depth at different powder feed rates and the computed profiles were compared with the experimentally determined ones.

Mohanraj *et. al.*, [57] presented a three dimensional transient macroscopic numerical model for the description of transport phenomena during laser surface alloying. In order to make accurate estimates for the species composition distribution during the process, the addition of alloying elements was formulated by devising a species generation term for the solute transport equation. By employing a particle-tracking algorithm and a simultaneous particle-melting consideration, the species source term was estimated by the amount of fusion of a spherical particle as it passes through a particular control volume. Numerical simulations were performed for two cases. The first case corresponds to aluminium as alloying element on a nickel substrate, while the second case was for alloying nickel on aluminium substrate. It is observed for the latter case that the melting of the alloying element is not instantaneous, and hence it cannot be modelled as a species mass flux boundary condition at the top surface. The predicted results were compared with experiments, and the agreement was found to be good.

2.2.2 Mixing in laser weld pool

Studies on mixing in laser melt pool in welding geometry are also limited. Most of the studies in welding are for joining metals or alloys that are similar in composition and thus the need for solving species conservation in the melt pool does not arise. However, when

welding dissimilar metals, it is imperative to solve species conservation, as the final shape and microstructure of the weld are strong functions of the composition.

Debroy and co workers [5,58] have developed a control volume based computational model to solve the mass, momentum, energy and nitrogen concentration in the weld pool. The concentration distribution of nitrogen in different sections was obtained and compared to the experimentally observed nitrogen content in the weld pool as a function of scan speed of the heat source and inlet nitrogen pressure.

Very few studies on the calculation of transport phenomena exist in the literature for welding of dissimilar metals, where, the difference in the properties induces considerable change in the weld pool shape. Chung and Wei [59] used a control volume approach using the SIMPLE algorithm [60] to solve non-dimensional temperature, velocity and composition distribution in the melt pool of a dissimilar joint in a two-dimensional transient formulation. A flat free surface with Gaussian heat source, constant average physical properties were considered. Parametric study was performed to study the velocity profile and shape of weld pool in terms of surface width and depth at different coefficients of surface tension, viscosity and thermal conductivity. A detailed description of the flow pattern at different magnitudes and signs of the surface tension coefficients (σ_T) of the two metals was presented to show the effect of strength and direction of convection on the shape of the pool after times of the order of 0.01 s. A contour drawn at a concentration of 0.5 was used to indicate the extent of mixing between the two metals. Asymmetry in the flow pattern, and thus, the shape of the weld pool, were highlighted. A qualitative comparison was made with experiments with a transverse macrograph of GTA weld of Fe with Al to show agreement with computational results. Several issues were unclear in this early work on dissimilar welding. The surface tension coefficients were adjusted for minor surfactant elements such as oxygen and sulphur. The interface between the two metals after solidification was shown, however, no solidification model was discussed in the paper. The validity of existing macro solidification models for a binary system such as Fe-Al containing intermetallic compounds is unclear.

Wei and Chung [61] used the same model as described above, to simulate velocity profile, concentration profile and shape of fusion zone for dissimilar metals at different times. The surface temperature, volume fraction of species and shape of fusion zone was shown for both positive and negative σ_T for the two metals. Mixing was shown to be insufficient for

negative σ_T coefficients due to radially outward flow pattern. Positive σ_T led to a narrow and deep weld pool with more width on the side where σ_T is less positive. When a positive σ_T for side A and negative σ_T for the side B was used, the width of side B increased with the value of σ_T for side A. A quantitative comparison was attempted with an experimental micrograph of laser welded Cu-Ni [62]. The pool shape computed was for constant physical properties after adjusting the σ_T for possible presence of surface active elements.

2.2.3 Joining of Dissimilar metals

Several attempts have been done earlier to obtain a successful weld between two dissimilar metals. The studies are preliminary in nature and provide analysis in a case-by-case manner.

Sun and Ion [6] reviewed laser welding of dissimilar metals. Studies on welds between dissimilar grades of (1) steels and aluminium alloys, (2) stainless steel and carbon/low-alloy steel, (3) steel and copper, (4) steel and aluminium, (5) steel and nickel, (6) aluminium and copper and (7) aluminium and lead. Phase formation in each of these systems along with possible applications was described. Weld quality was assessed with respect to hot cracking. The authors provide a summary of the studies using a chart of weldability of binary metal combinations (figure 2.8) and note that solidification mechanisms in laser weld metal are not well understood.

Seretsky and Ryba [63] used laser spot welding technique to join Titanium and Nickel. Cracking and porosity was observed rendering the welding attempt unsuccessful. The microstructure showed swirls that were supposed to be due to convection. The fusion zone was asymmetric about the joint and it was attributed to the differential absorption of the laser radiation.

Metzger and Lison [64] reviewed phase formation and quality of weld for dissimilar combinations for electron beam welding. Combinations of metals with different magnetic properties such as diamagnetic copper and ferromagnetic nickel, resulted in a deflection of electron beam towards Copper and led to undercut on that side. Based on microstructural characterisation and mechanical properties, weld quality was rated as shown in figure 2.9.

Pan *et. al.*, [65] used transmission electron microscopy to study the phase formation in dissimilar (austenitic/carbon) steels welded using arc. Electron Probe Microanalysis was

used to characterise the composition at various locations. Different zones of phase formation in the weld, such as austenitic, martensitic and pearlitic were found to be in accordance with the Schaeffler map.

Majumdar *et. al.*, [66] studied welding of Titanium and Aluminium using laser. Brittle intermetallic compounds such as TiAl and Ti_3Al were observed in the weld. Cracks were observed to form near the Aluminium interface and were found sensitive to the amount of Aluminium in the fusion zone. A foil of Niobium added as a buffer between the two alloys prevented dissolution of Al in the fusion zone resulted in a crack free joint.

Katayama *et. al.*, [67] successfully produced a crack free lap welding of Steel to Aluminium using a cw YAG laser. Laser welds of lower heat input solidified as α (bcc)-Iron containing small amount of Aluminium and a thin region of intermetallic compounds. Deep penetration welds led to the formation of brittle FeAl phase resulting in cracks.

The shapes of fusion zone in electron beam welding of dissimilar metal combinations of Aluminium-Iron and Iron-Copper was reported by Wei *et. al.*, [68]. Microstructures of the fusion zone, concentration profiles across the weld were presented for welds at low and high currents. The measured dimensionless beam power was plotted against calculated Peclet number to show a linear relationship between the two.

2.3 Solidification of laser melt pool

2.3.1 Growth rate and geometric relationship

Solidification behaviour of the weld pool, solid-liquid interface morphologies and phase selection control the size and shape of the grains, extent of segregation, distribution of inclusions and defects such as porosity and hot cracking. Much of the earlier studies on the weld pool solidification are extrapolation of the knowledge of freezing of castings and single crystals that usually take place at low thermal gradients and growth rates.

The solidification rate V at any location on the freezing front is related to the heat source scan rate V_B by the relation $V = V_B \cos\theta$ as illustrated in figure 2.10. Since there is an easy growth direction for metals, a grain selection process will take place in which, grains whose easy growth directions are optimally aligned with the solidification front normal will

selectively outgrow less optimally aligned grains. Since the liquid metal is in contact with a solid of similar composition, epitaxial growth of the solid grains into the melt takes place.

2.3.2 Structure of interface

Failure analysis of dissimilar welds showed that the weld-base metal interface plays an important role. The interface structure of weld interface is classified into two types:

1. Type-I boundaries, where, the grain boundaries are perpendicular to the weld interface.

2. Type-II boundaries, where, the grain boundaries are parallel to the weld interface.

Figure 2.11 shows examples of these two kinds of boundaries. It has been observed that type-II boundaries are susceptible to failure of dissimilar metal welds. Nelson *et. al.*, [69] studied dissimilar welds of Iron with Monel as filler material. The welds exhibited type-II boundaries, which were characterised using Electron Backscatter Diffraction Analysis. A high angle of misorientation between the base metal grains and the weld region grains was noted. The authors extended their work in a later study and proposed a mechanism for type-II boundary evolution [70]. The transformation of δ to γ and the high mobility of γ/γ boundary at high temperature below the fusion zone were suggested as the reasons for appearance of type-II boundaries which were absent in the welds with a base metal dilution that does not allow such a transformation to take place.

2.3.3 Grain structure of solidified alloy

Savage and Aronson [71] performed a microbeam X-ray diffraction analysis of grains in Silicon-Iron welds to establish the epitaxial growth of base metal grains into the weld region. The tendency for grains with easy growth direction along the maximum thermal gradient to outgrow the other grains was also shown. The shape of weld pool was concluded to have a strong influence on the type of preferred orientation produced during solidification of weld metal.

Clarke *et. al.*, [72] studied change of grain structure from columnar to equiaxed at the centre of the weld during GTA welding of Al-Cu alloys. Thermal gradient and growth were calculated as a function of distance across the weld. Hunt's model was used to estimate the extent of equiaxed region at the centre of the weld. Predicted and experimental widths of equiaxed regions were shown to have good agreement.

Rappaz *et. al.*, [73] used a combination of Finite Element and Cellular Automaton models (CAFE) to obtain the grain structure of the solidified alloy during laser welding. Nucleation and growth of grains were taken into account.

Ichikawa *et. al.*, [74] used a Monte Carlo technique to simulate microstructural evolution for steels welds. The technique takes the simulated temperature distribution as an input to the probability function for jumps of cells into solid grains. The calculated grain width was compared with the experimentally observed one favourably.

2.3.4 Microstructure evolution during solidification

During growth, however, depending on the presence of constitutional undercooling (figure 2.12 a-c [4]), the solidification front could develop instabilities that lead to cellular / dendritic microstructure [75, 76]. The growth rate is low at the edge of the weld pool and high towards the centreline. The thermal gradient is low at the centreline and increases towards the edges. The schematic in figure 2.12(d) shows the variation of these quantities in a laser melt pool [76]. Thus, it is possible to observe microstructural variations in growth mode across the weld (figure 2.13 a, b [77]). Phase selection is also a function of the parameters such as growth rate, thermal gradient and cooling rate.

Much of the studies on microstructural evolution and phase selection during welding are material specific. David and Vitek [4] reviewed relevant literature in weld solidification and microstructure formation. Grong and Matlock [78] reviewed microstructural development in weld metals of mild and low-alloy steels. Effect of alloying elements and processing parameters on the microstructure, hardenability and inclusions were studied in detail. Cam and Kocak [79] reviewed a similar study on several advanced materials such as intermetallics, Ni-base super alloys, Al-Li alloys and metal matrix composites.

The parameters required to predict the microstructure formation in laser melting/welding are difficult to obtain experimentally. Several studies exist that report thermal gradients, and cooling rates by direct measurement [4]. However, it is now accepted that computational modelling provides a reasonable alternative to direct measurements by allowing calculations that yield temperature distributions for use in microstructure prediction.

Zacharia *et. al.*, [80] studied pulsed laser welding of austenitic stainless steels. At high scan speed of the laser, the cooling rate was high, leading to a completely austenitic

microstructure of the weld pool. At low scan speeds, duplex structure was observed. Calculated cooling rates were used to obtain secondary dendrite arm spacing, which was in good agreement with the experimentally observed one.

Hoadley *et. al.*, [81] studied laser surface melting of Al-33Cu alloy using both computations and experiments. Temperature and velocity field were solved to obtain a melt pool shape that matches closely with the experimentally observed one. Using Jackson-Hunt theory, the lamellae spacing was calculated from the growth rate and a comparison with the spacing measured by TEM showed good matching.

Kurz and Trivedi [82] used the non-equilibrium solidification theory in the context of welding. For the case of Fe-Ni alloys, high growth rate was shown to avoid formation of δ phase and thus hot cracking.

Norman *et. al.*, [83] used a three dimensional steady state conduction equation to obtain cooling rate and the ratio of thermal gradient to growth rate as a function of welding speed for Aluminium alloys. Semi empirical relations were used to correlate calculated parameters to dendrite secondary arm spacing, which was compared with the experimentally observed one.

Guo and Kar [84] used a one dimensional semi-infinite heat transfer model to relate solidification time to the laser power and irradiation time. Instability analysis for directional solidification of dilute binary alloys was used to determine transitions from planar to cellular and dendritic morphologies using decay, oscillation and growth of perturbations on the solid-liquid front, respectively. The growth regimes predicted from the experimental solidification rates were compared with the microstructures for the corresponding laser parameters.

2.3.5 Microstructure evolution during polyphase solidification of laser melt pool

Since there is a geometric relation connecting the growth rate and the scanning speed of the heat source at steady state, laser remelting could be used as a technique to simulate directional solidification at high growth rates [85]. By measuring the orientation of the grain boundaries or that of the inter-dendritic phase with respect to the known scanning direction, it is possible to determine the local solidification rate. This possibility opens up a way to understand the microstructural evolution under rapid solidification conditions as a

function of growth rate, a key variable in the microstructure selection [86]. Kurz and co-workers [87] used laser surface remelting to simulate high growth conditions and provided a map of composition of Iron and growth rate for microstructural selection in the Al-Fe system. The velocity dependence of interface temperature, also referred to as interface response function, was theoretically predicted for cells/dendrites of Aluminium, Al_3Fe and eutectic growth of $Al-Al_6Fe$. Maximum growth temperature was used as a selection criterion to determine which phase forms at a given composition and growth rate. Experimentally observed microstructure modes were superposed with the calculated map to show good agreement. This study also brings out the fact that a systematic analysis of polyphase solidification during solidification of a laser melt pool should consider competition of the phases that could nucleate and grow under the given processing conditions. The subjectivity of such an analysis to the alloy system under consideration limits a general study on the solidification microstructure formation.

2.4 Issues and scope of present work

In this section, based on the survey of literature in laser processing of dissimilar metals, the issues that require further work for a better understanding can be summarised as follows:

1. Most of the studies in the literature on dissimilar welding are by a case-by-case manner and concentrate on steels. An attempt to identify differences between welds of similar and dissimilar metals, in terms of weld pool shape and microstructural features that are common to different kinds of binary systems will be important.

2. The evolution of weld pool during laser melting, starting from a solid base metal, is not discussed in the literature, for the case of dissimilar welding. A transient computational model, that takes the differences in melting point and thermal transport properties into account, will provide an insight into the process where laser heating and convection play an important role in determining which side of the dissimilar pair melts first and thus plays dominant role in weld pool development.

3. During solidification of laser melt pool, the growth of base metal into the melt pool is assumed to be spontaneous and an extrapolation of studies on morphological evolution during single phase directional solidification was assumed to be applicable. In their review on solidification and weld microstructures, David and Vitek [4] note that the arguments regarding epitaxial growth and nucleation should apply in dissimilar welds as well. A closer

look at this issue using thermodynamic aspects of growth of solid into an inhomogeneous melt could lead to interesting results.

4. Much of the work on solidification of a laser melt pool deals with the grain structure. The model assumed for solidification is usually that of a pure metal to obtain the temperature distribution from simulation that could be used as an input for microstructure calculations. Melt pool convection plays an important role during microstructure development and was ignored in much of the earlier studies. A study to show the relative importance of the thermal profile and convection during polyphase solidification is needed.

(a)

(b)
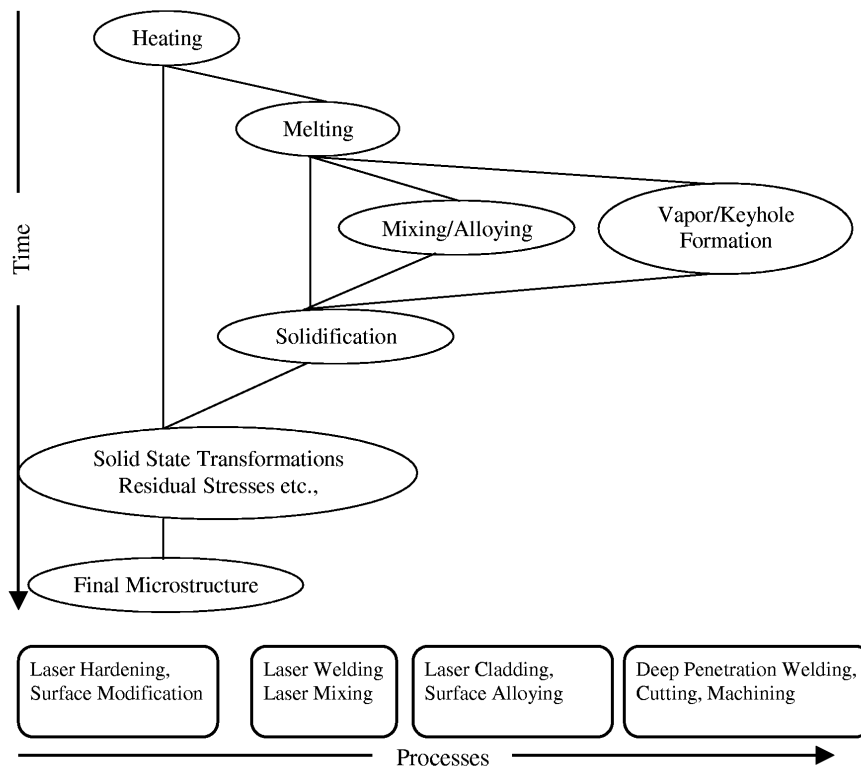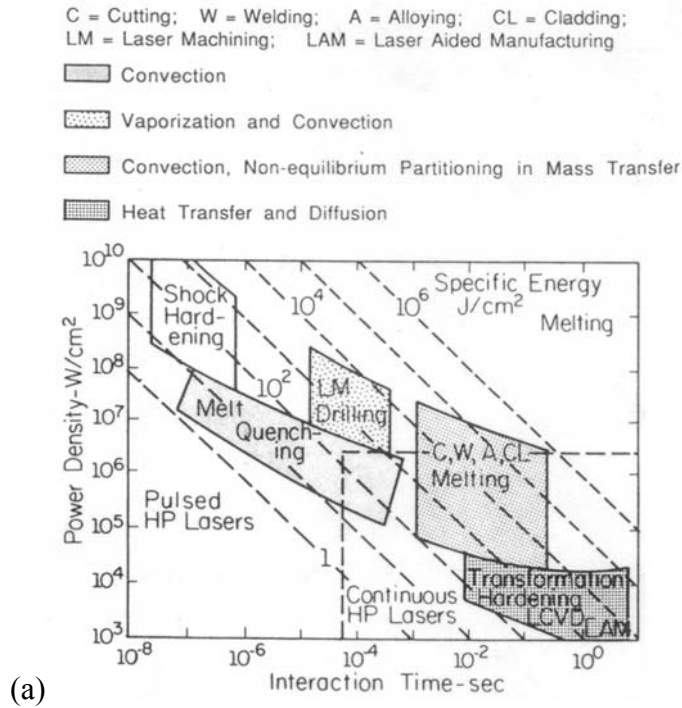
Figure 2.1 (a) Operational regimes for various processing techniques [8] (b) Physical processes that operate during laser-material interaction.
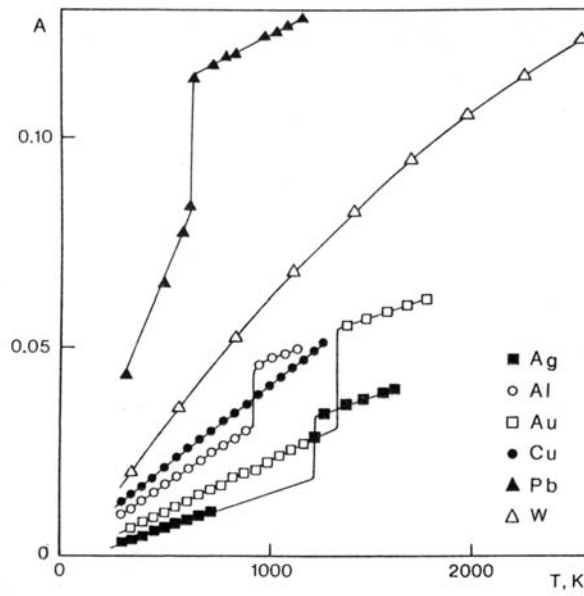
Figure 2.2 Computed intrinsic absorptivity of some common metals, as a function of temperature, for CO_2 laser [11].
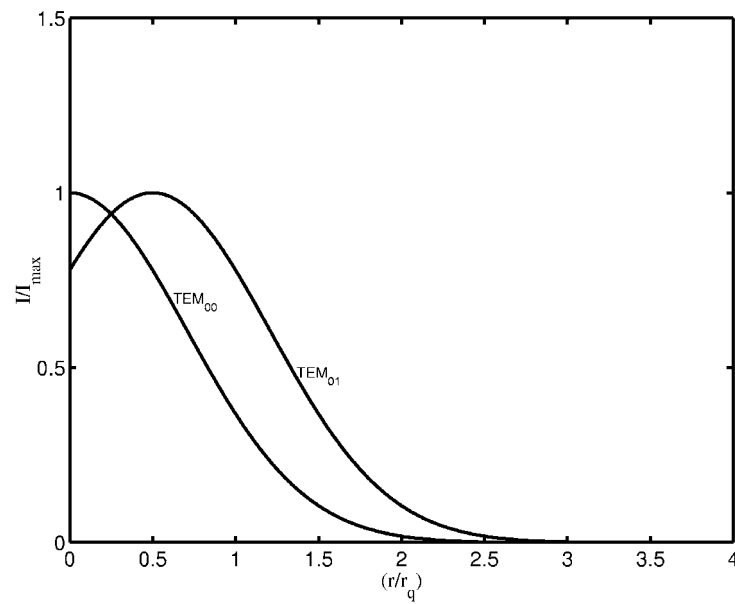
Figure 2.3 Radial Intensity distributions that are commonly used in laser processing.
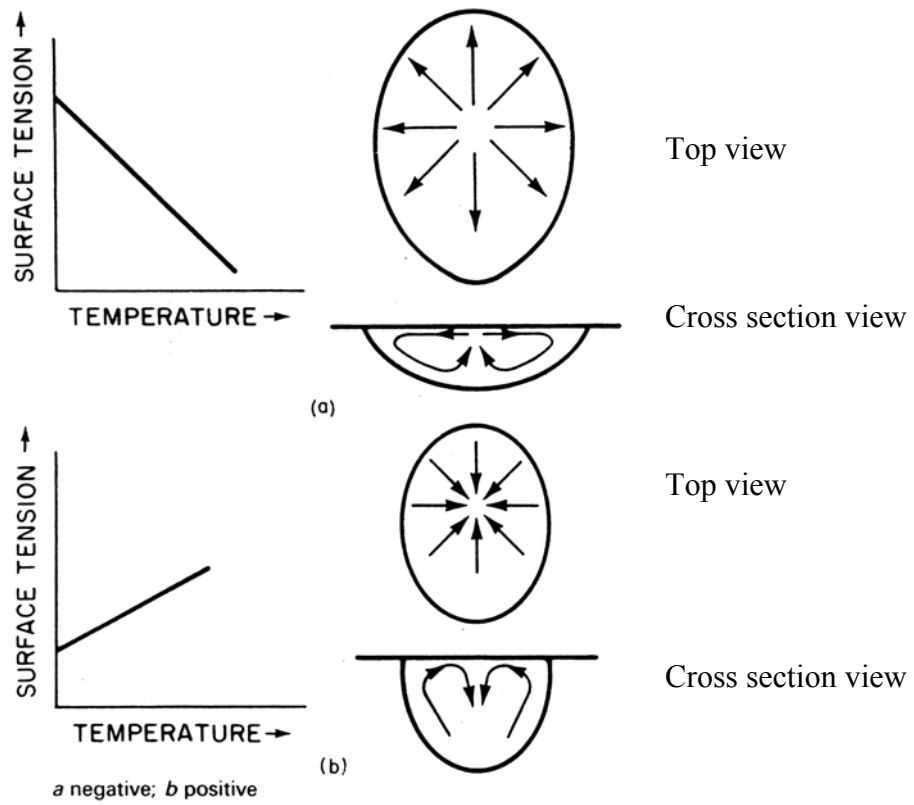
Figure 2.4 Surface tension gradient induced flow on the free surface of laser melt pool [4].
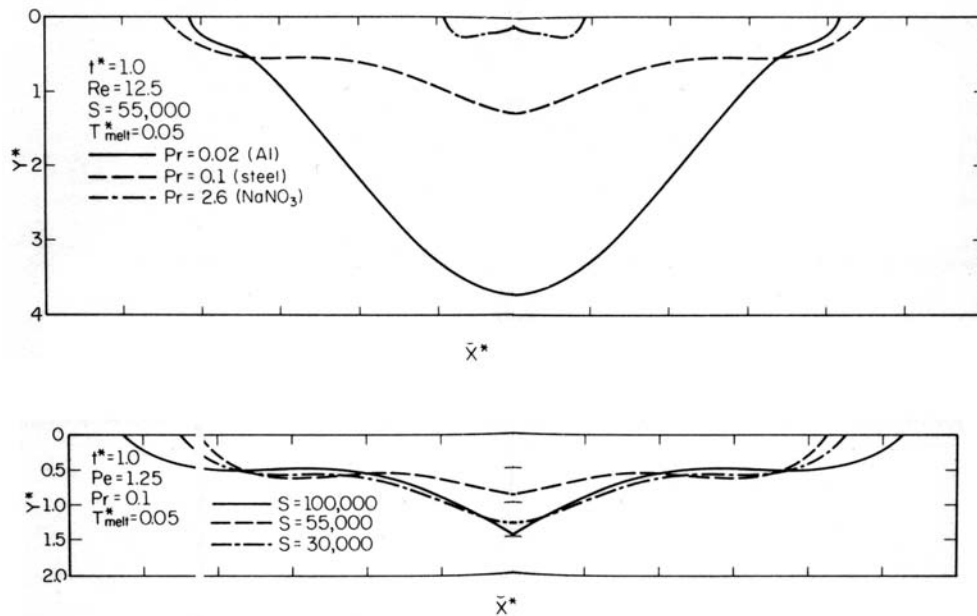
Figure 2.5 Transverse melt pool shapes for different Prandtl and Surface tension numbers. The figure is flipped about the Y* axis to reveal the complete pool shape in cross sectional view [38].
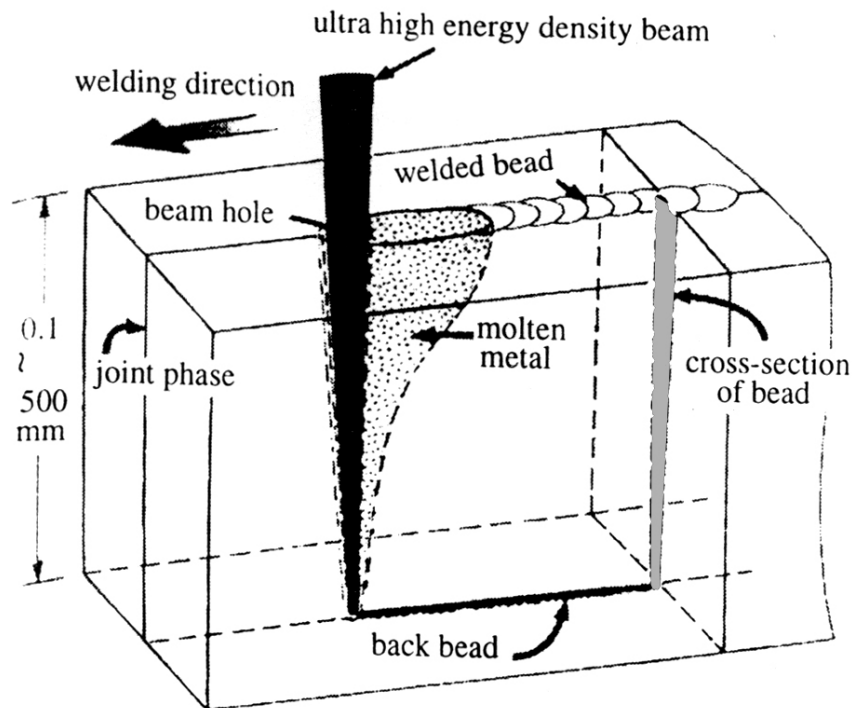
Figure 2.6 Schematic of keyhole formation during deep penetration welding [79].
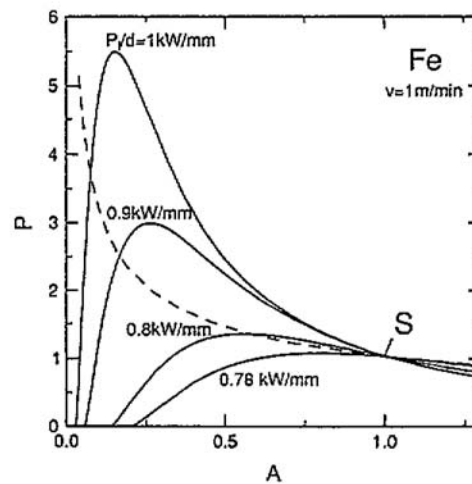
Figure 2.7 Non-dimensional radius of keyhole (A) plotted against non-dimensional ablation pressure (P). The broken curve represents the normalised surface tension pressure. Point S is a stable solution [43].

Laser weldability of binary metal combinations [13]. (E = excellent, G = good, F = fair, P = poor, * = no data available)

	W	Ta	Mo	Cr	Co	Ti	Be	Fe	Pt	Ni	Pd	Cu	Au	Ag	Mg	Al	Zn	Cd	Pb
Ta	E																		
Mo	E	E																	
Cr	E	P	E																
Co	F	P	F	G															
Ti	F	E	E	G	F														
Be	P	P	P	P	F	P													
Fe	F	F	G	E	E	F	F												
Pt	G	F	G	G	E	F	P	G											
Ni	F	G	F	G	E	F	F	G	E										
Pd	F	G	G	G	E	F	F	G	E	E									
Cu	P	P	P	P	F	F	F	F	E	E	E								
Au	*	*	P	F	P	F	F	F	E	E	E	E							
Ag	P	P	P	P	P	F	P	P	F	P	E	F	E						
Mg	P	*	P	P	P	P	P	P	P	P	P	F	F	F					
Al	P	P	P	P	F	F	P	F	P	F	P	F	F	F	F				
Zn	P	*	P	P	F	P	P	F	P	F	F	G	F	G	P	F			
Cd	*	*	*	P	P	P	*	P	F	F	F	P	F	G	E	P	P		
Pb	P	*	P	P	P	P	*	P	P	P	P	P	P	P	P	P	P	P	
Sn	P	P	P	P	P	P	P	P	F	P	F	P	F	F	P	P	P	P	F

Figure 2.8 Table showing weldability of dissimilar couples by laser [6].

	Zr2Sn	V10Ti	V	Ti	Ni15Cr7Fe	Ni	Cb	Fe18Cr8Ni	Cu20Ni	Cu	Al	Ag
Ag	N	N	G	G	G	N	N	G	G	N	G	N
Al	N	N	N	N	P	G	N	P	P	P	N	
Cu	N	F	G	N	G	F	N	G	N	N		
Cu20Ni	N	P	P	N	G	N	N	G	N			
Fe18Cr8Ni	N	N	F	N	G	G	N	N				
Cb	P	G	G	G	N	N	N					
Ni	N	N	N	P	G	N						
Ni15Cr7Fe	N	P	P	N	N							
Ti	G	N	P	N								
V	N	N	N									
V10Ti	N	N										
Zr2Sn	N											

N=Not Investigated; P=Poor; F=Fair; G=Good

Figure 2.9 Weld quality ratings for dissimilar couples during electron beam welding [64].
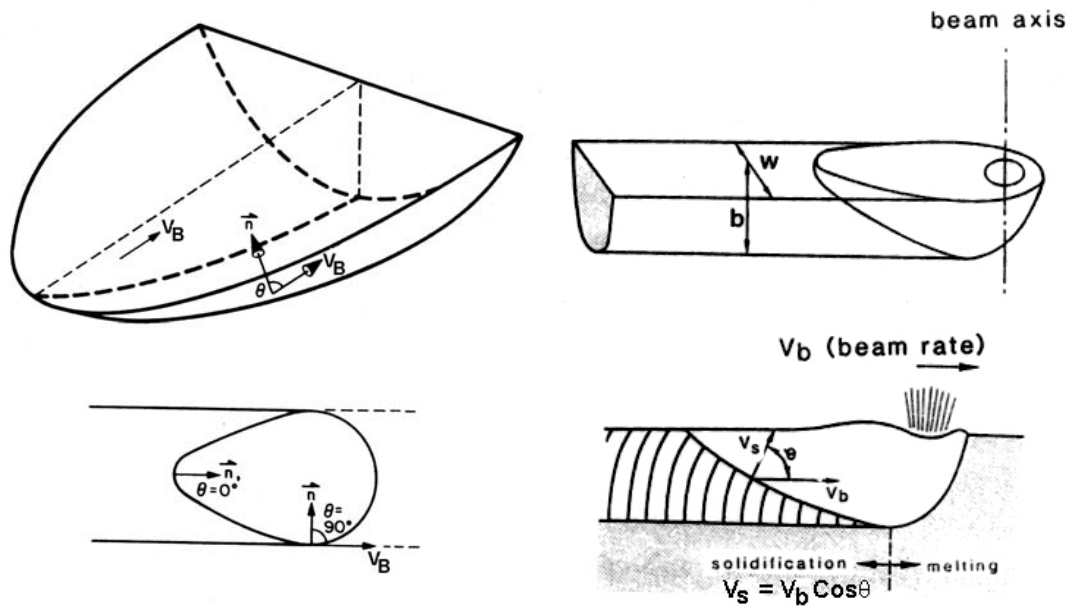
Figure 2.10 Geometrical relations in the weld pool geometry. The top figures show the shape of solid-liquid interface of a weld pool and the bottom figure shows the top view of the same [4,85].
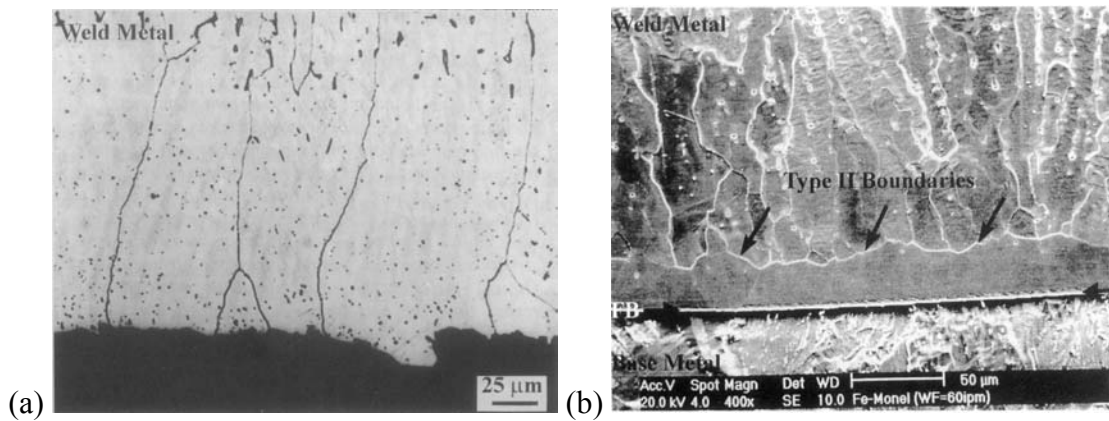
Figure 2.11 Examples of boundaries at the weld interface. (a)Type-I and (b)Type-II [69].
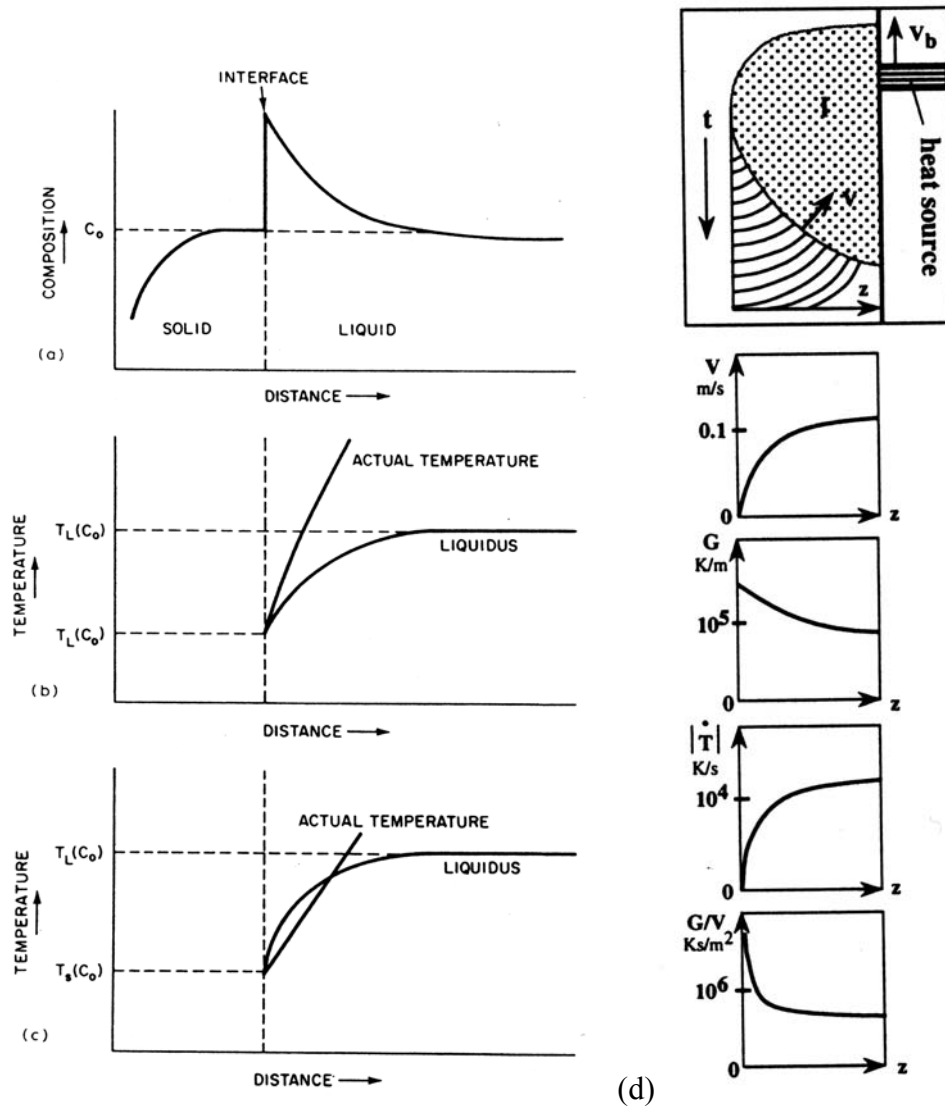
Figure 2.12 (a) Solute concentration ahead of the solid-liquid interface (b) High thermal gradient leading to stable plane front (c) Low thermal gradient leading to constitutional undercooling [4]. (d) Schematic variation of growth rate (V), thermal gradient (G), cooling rate ($|\dot{T}|$) and the constant (G/V) from bottom to top of the laser melt pool [81].

(a)

(b)
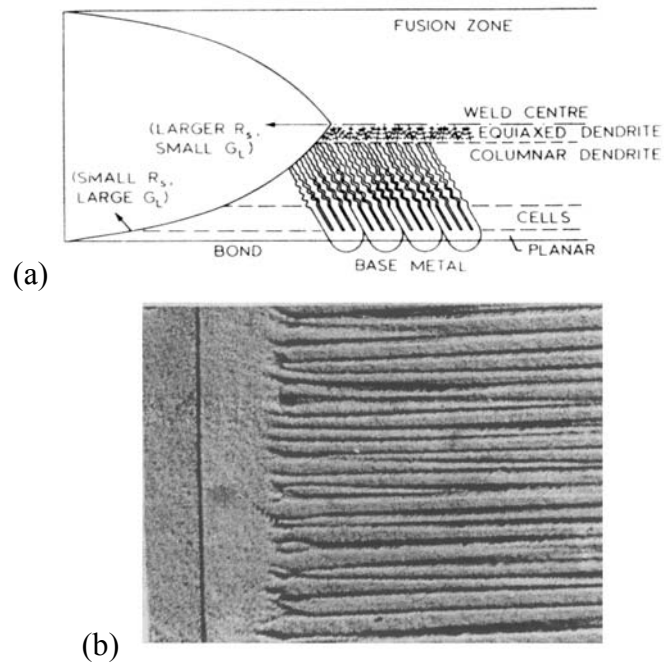
Figure 2.13 (a) Schematic of possible microstructural transitions across a weld [4]. (b) Transition from planar to cellular growth in GTA weld of 49%Ni-Fe alloy [77].

Chapter 3

Laser welding of Fe-Cu Binary Couple

3.1 Introduction

The binary system of iron and copper presents a dissimilar metallic system with differences in physical properties as well as alloying ability. As shown in the table 3.1, there is a large difference in the physical properties of iron and copper. The binary system of iron-copper shows complete mixing in liquid state and a miscibility gap in solid state (figure 3.1). Thus, iron-copper couple could be considered as a representative system to characterise microstructural features in dissimilar welding. In this chapter, microstructural characterisation of iron-copper welds is described. Only selective processing conditions are analysed to highlight the features that are common at different laser scan speeds.

Table 3.1 Physical properties of copper and iron [88]

Property	Copper	Iron
Melting Point (^{o}C)	1083	1536
Thermal Conductivity (Wm^{-1}K^{-1})	399	78.2
Specific Heat (Jkg^{-1}K^{-1})	386	456
Density (kgm^{-3})	8900	7820
Latent Heat (kJmol^{-1})	13.02	15.2

3.2 Experiments

Several experiments on the laser welding of iron with copper were performed in butt welding geometry. Only the representative conditions of conduction mode weld and

keyhole mode weld are analysed in this work. Deep penetration welding is carried out using a Trumpf laser operating at 5.5 kW and at a scan rate of 84 mm/s. Various scan rates are used, ranging from 21 mm/s to 169 mm/s. The laser is used in a focussed condition. A lower power of 4.5 kW is used on a Rofin Sinar R10000 laser to make welds with lower penetration. In this case, the laser is defocussed to ensure that plasma formation does not take place. The weld in conduction mode is done at a laser power of 4.5 kW and a scan speed of 25 mm/s. Transverse sections are taken and analysed using scanning electron microscopy (SEM), transmission electron microscopy (TEM) and energy-dispersive x-ray analysis (EDAX) attached to the SEM. Detailed transmission electron microscopy (TEM) studies are conducted on a sample welded at a laser power of 5.5 kW and a scan speed of 21 mm/s.

3.3 Microstructure Analysis

The complete weld pool shapes for the keyhole mode and conduction mode welding are shown in figure 3.2. The weld pool was asymmetric in shape though the laser beam was placed symmetrically on the butt joint. More iron was found to melt than copper. The keyhole mode weld has a depth of penetration almost equal to the thickness of the samples, however, the conduction mode weld leads to a shallow and wide weld pool.

Interface microstructures for the keyhole weld on the copper and iron sides are shown in figure 3.3. The interface between the fusion zone and base metal is not clearly distinguishable on the copper side. The microstructure is banded ahead of a rough interface. On the other hand, the iron side shows a sharp interface with the weld. The growth of iron grains into the weld in cellular mode is clearly observed.

The interface microstructure features are similar in the conduction mode weld as well. Figure 3.4 shows the microstructure at the copper side. A composition analysis done along the direction of growth of copper base metal into the weld shows a sharp decrease in the copper content of the alloy followed by large fluctuations. The microstructure also shows bands across which the cellular morphology is not continuous. Figure 3.5 shows interface microstructure on the iron side of the conduction weld. The growth of iron in to the weld is characterised by a cellular morphology. The copper content in the alloy changes in the alloy from the interface into the weld at locations where microstructural banding is also observed. However, the composition fluctuations are not as large as on the copper side. A

higher magnification microstructure of the interface on the iron side shows that iron initially grows in a planar front for a small extent before changing over to a cellular morphology (figure 3.6). The composition of copper in the alloy also increases gradually as it grows in the alloy.

The microstructure within the weld region is mostly cellular in nature as is evident from figure 3.7. Microstructural banding was observed through out the weld pool. As shown in figure 3.8, the bands are characterised by fluctuations in the composition of copper and a change in the length scale of microstructure. The morphological patterns are usually similar inside the bands while there exist discontinuities at the boundaries (figure 3.8c). The composition analysis done near the top of the weld pool for the conduction weld shows that the most of the weld region on the iron side is well mixed with an average composition of 80 at% Fe (figure 3.9). However, the composition of iron increases sharply on the copper side.

TEM studies were done at the top, middle and bottom of the weld regions for a weld performed at a laser power of 5.5 kW and a scan speed of 21 mm/s. The overall features are similar through out the weld pool, however, certain interesting differences could be noted. The cellular microstructure that is observed throughout weld (figure 3.8), consists of grains of iron with copper occupying the intergranular regions, as shown in figure 3.10. The SADP taken from the intergranular regions and the grains could be indexed to copper and iron, respectively. A low magnification microstructure shown in figure 3.11(a) is comprised of grains mainly of iron. The dark field image (figure 3.11c) taken from the (101) reflection shows bright contrast of several grains that are in the [111] zone. Globules of copper were also observed at several locations in the middle of the weld pool (figure 3.12). As shown in figure 3.13, the microstructure near the top of the weld shows droplets of iron formed in a matrix, presumably of copper. The selected area diffraction pattern (SADP) taken around the iron globule shows no clear orientation dependence between the matrix and the particle. This is not surprising as there is a possibility of formation of such droplets in the liquid state itself. The microstructural features described in this chapter are similar to those in other dissimilar welding combinations such as copper-nickel described in chapter 4. Computational modelling is not attempted for the iron-copper system due to the complexity arising out of immiscibility of the two metals, which precludes simplistic assumptions for any meaningful study.

3.4 Discussion

The results presented above indicate development of unique microstructural features during dissimilar welding of iron with copper in both conduction mode and keyhole welding. The weld pool microstructure contains several unique features which are not reported in the literature. We now discuss the possible mechanisms responsible for the origin of these features. Though the heat source was applied symmetrically on the two metals in butt weld geometry, the weld pool shape is asymmetric with bulk of the weld pool displaced towards the iron side. This indicates that the high thermal conductivity of copper leads to less amount of heat available as sensible heat for melting and thus, the extent of melting on copper side is less. The composition is nearly uniform across the weld, indicating a good mixing by convection in the weld pool. However, the uniformity of composition is only at the macroscopic level. The pronounced differences in the interface microstructure and the composition on the iron side and the copper side show different modes of growth of copper and iron grains from the two sides into the weld pool.

In order to understand the origin of the microstructure we shall first discuss our observations with respect to the phase diagram (figure 3.1). This will be followed by a detailed discussion of the special features of the microstructures in the context of the substrate and the prevalent convection.

Composition analysis indicates that although there exists considerable local variation, the average composition in the middle of the weld pool is about 80 at% Fe. This is nearly same as that observed when copper powder was alloyed on iron substrate using a laser. Clearly, the coupling efficiency of laser with the two materials is responsible for the average composition observed in both the cases. The composition increases gradually towards the iron rich end. While there is a rapid increase in the composition towards the copper side. The composition in the most of the regions in the weld pool suggests that the solidification product must be fcc(γ)–Fe and copper. In case of cellular solidification, one therefore expects the primary phase during solidification to be γ–iron with copper decorating the intercellular region. The TEM results (figure 3.10) indicate that primary phase is α–Fe with intercellular region being copper. This is consistent with the expectation since the γ–Fe will transform to α Fe below 750 ^{o}C. TEM results suggest a significant refinement of the α–Fe grains near the middle of the pool. The ring patterns in the electron diffraction suggest

random orientation within themselves as well as with copper grains indicating a random nucleation of α–Fe during γ to α transformation.

Transmission electron microscopy reveals the presence of globules near the centre and top of the weld pool. The analysis of the diffraction pattern clearly identifies establishes the globules to be of copper. The morphology suggests that the globule originated in the liquid state. There exists a submerged miscibility gap below the liquidus region, where the liquid can separate into two melts [89,90,91]. Several investigators have calculated the miscibility gap. A typical calculation from the work of Majumder *et. al.* [90] is given in figure 3.14. It requires 180K undercooling for the Fe 20 at%Cu alloy to access this immiscible region. Achievement of such an undercooling with the associated spheroidal microstructure was shown for electron beam surface remelting of Fe-Cu at speeds of ~10 cm/s by Munitz [91]. Similar globular microstructure was also reported in the MIG welding of iron with copper wire [92]. The appearance of the globules near the top of the sample indicates that they appear only at higher growth rates. However, the growth rates employed in our work are much less than that employed by Munitz and is of the order of few cm/sec. Thus, the results suggest significant undercooling of the melt in the weld pool prior to solidification.

We shall now discuss the solidification process occurring near the two substrates. On the iron side, the solidification progresses normal to the substrate in a cellular fashion. However, careful observation of the substrate-weld interface indicates the presence of a planar zone with no segregation. The composition of copper in this region increases linearly up to the point where the interface breaks down to yield a cellular microstructure. The iron rich solid solution grains grow continuously in the weld pool, initially in a planar morphology. The composition of copper in this planar region rises from ~5 at% to a maximum of ~13 at% before the breakdown of the interface. The morphology at this point changes to cellular mode.

The grains in the iron substrate also show significant refinement near the interface compared to that existing in the interior (figure 3.15 [93]). However, these grains do not grow into the weld pool. One always observes a sharp contrast at the interface indicating an enhanced etching effect. The grains in the weld pool are much coarser. One can rationalise the observation with respect to the phase diagram. Since iron had melted to yield the melt

pool, the composition in front of the interface can be assumed to be pure iron initially. The convective mixing at a later stage enriches the melt with copper. However, the process will lead to a stationary boundary layer, which will remain essentially in an unmixed state at the interface. Only the thermal diffusion of copper can enrich this layer. The phase diagram suggests that iron at the interface during melting should have δ Fe structure. The γ Fe forms by a peritectic reaction. The sharp band at the interface has a composition of around 5-6at% Cu. This suggests that a peritectic reaction may have taken place at a very early stage of solidification at the iron interface, producing a layer of γ Fe. The morphology suggests that this phase may have wetted the interface and spread across the interface. Subsequent solidification of the melt ahead is due to a planar growth of this phase across the iron rich boundary layer. It can be noted that the maximum composition of this layer in our experiment corresponds to the maximum solid solubility of copper of the γ Fe phase. Due to retrograde nature, temperature below this maximum solid solubility will lead to very large partitioning of copper, thus enhancing the tendency of the cellular breakdown of the interface.

The solidification of the weld pool near the copper interface is more complex. A thermodynamic description of the scenario of growth of a pure metal into an alloy melt is shown in figure 3.16. Since the liquidus has a downward slope for the iron end of the phase diagram, a liquid alloy of Fe-Cu can solidify to an alloy of lower Cu content. Thus, with a small increase in composition of copper by diffusion, the chemical potential barrier indicated by $\Delta\mu$ in figure 3.16(a) could be overcome, and iron can grow in to the alloy melt. On the other hand, the liquidus is upward sloping at the copper end and a liquid alloy of Fe-Cu solidifies into an alloy melt of higher copper content. Thus, the pure copper substrate cannot grow into a Fe-Cu melt unless significant solid state diffusion changes the composition of the substrate in solid state. Except for a very dilute solution, copper forms from the Fe-Cu melt by a peritectic reaction. Iron first solidifies from the melt, which further reacts with the melt to yield copper solid solution. We always observe close bands of iron and copper at the jagged interface near the copper end. The jagged region is due to the convective mixing of pure copper melt with iron rich melt. This region solidifies before the molten copper solidifies. The reaction with this region is peritectic with solidification of iron rich solid solution followed by the formation of copper by peritectic reaction. The resulting iron rich regions solidify before the molten copper solidifies. Since diffusion of Fe through copper is very sluggish, the reaction stops due to the formation of a copper layer on

the previously formed iron. For solidification to continue, the iron again re-precipitates from the melt followed by peritectic copper. The repetition of this process results in the banding observed in the microstructure near the copper substrate.

One observes a second kind of banding following the closely spaced banding mentioned above. These are bands of cells separated by a boundary region. They occur near the substrates as well as in the interior of the weld pool. The microstructural banding are characterised by compositional fluctuations in the weld. The orientation of these bands is observed to be parallel to the solidifying interface. While solidification of the weld proceeds, the liquid at the centre of the weld is still at higher temperatures and convection of the melt due to surface tension and buoyancy forces takes place. This could lead to a fluctuation in the growth due to remelting by hot liquid brought near the solidifying interface. Direct visualisation studies on laser welding by Mohanty and Mazumder [94] show evidence of fluctuations in the growth leading to band formation. Thus, the weld region at a micro level is inhomogeneous.

3.5 Summary

Laser welding of iron and copper at low and high scan speeds showed similar microstructural features. The weld pool shape is found to be asymmetric with more melting of iron, though the heat source is placed symmetrically on the butt joint. This phenomenon was attributed to differences in thermal diffusivity between the two metals. The overall composition is uniform at a macro scale. The weld interface also shows asymmetry. The iron side has a smooth interface with a transition from planar to cellular growth into the weld and a gradual increase in composition. The copper side showed a rough interface with extensive banding, indicating a peritectic reaction. Microstructural bands due to fluctuations in growth are present throughout the weld pool characterised by a change of length scale and composition. The difference in the growth mode from the copper side to iron side was explained using thermodynamic arguments. Droplet formation in the weld region, as shown by TEM studies, indicates access to submerged liquid miscibility gap during solidification of the weld.

Figure 3.1 Phase diagram of the iron-copper system [88].

(a)   (b)
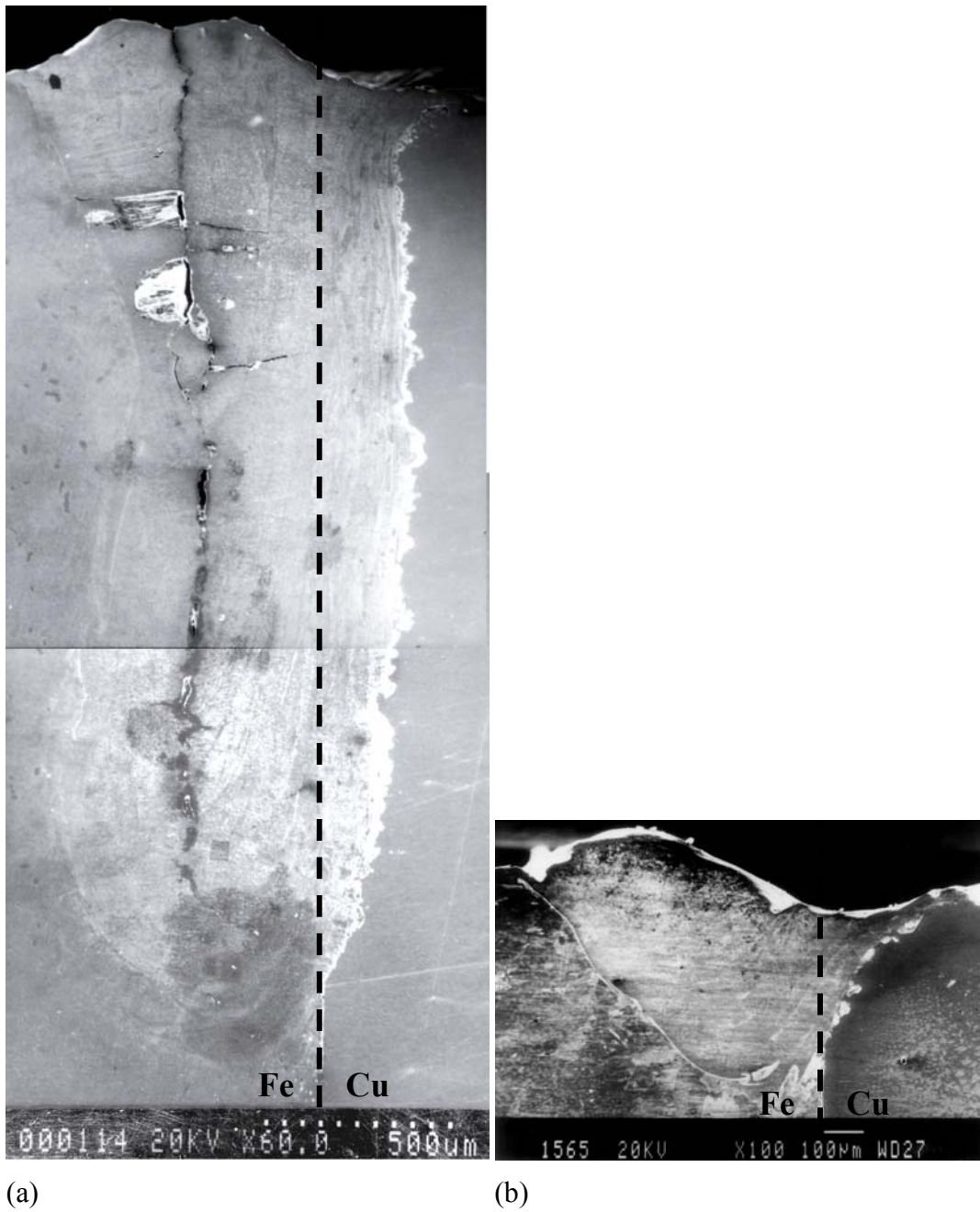
Figure 3.2 Fe-Cu Weld pool shapes at (a) laser power of 5.5 kW, and a scan speed of 84 mm/s and (b) laser power of 4.5 kW and a scan speed of 25 mm/s. The dotted line shows the original interface between the two metals.
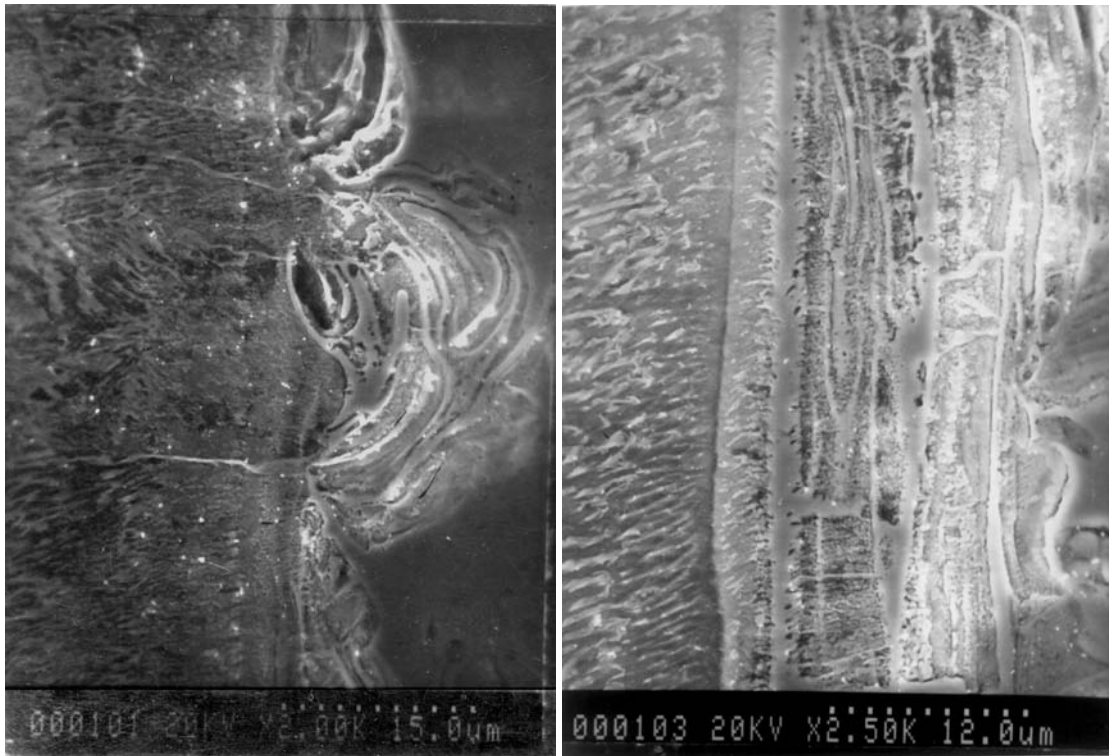
(a)   (b)
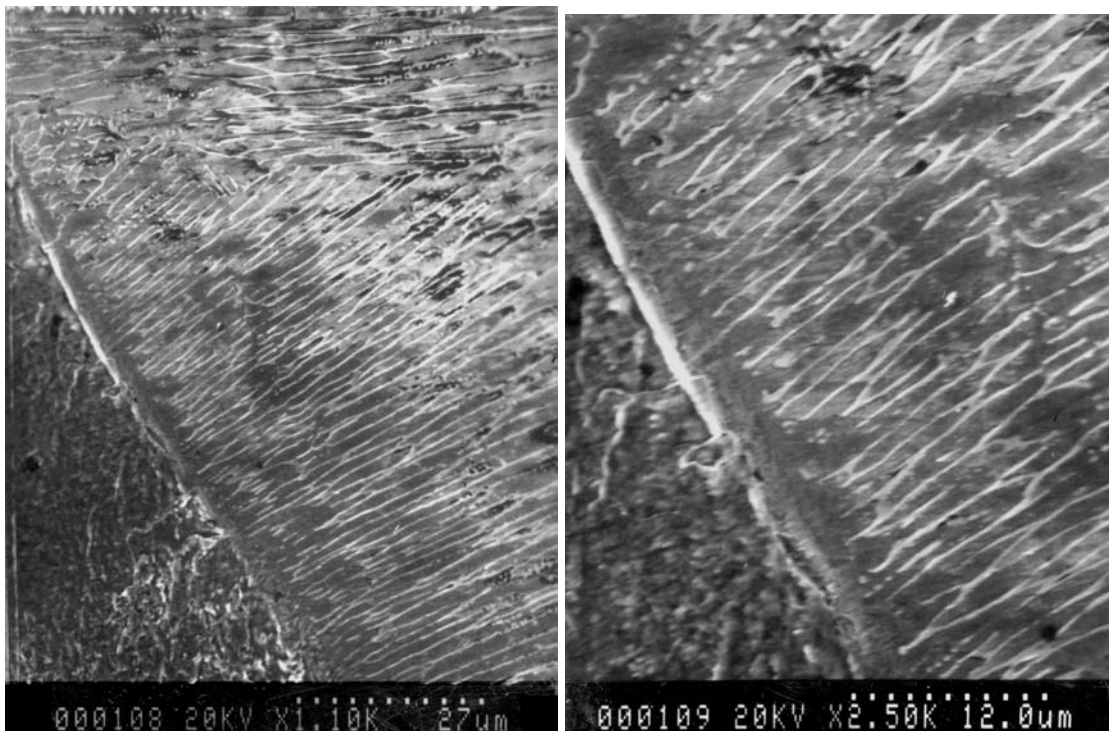
(c)   (d)

Figure 3.3 Interface microstructures on the (a&b) copper side and (c&d) iron side of the Fe-Cu weld at 5.5 kW and 84 mm/s.

(a)

(b)

(c)
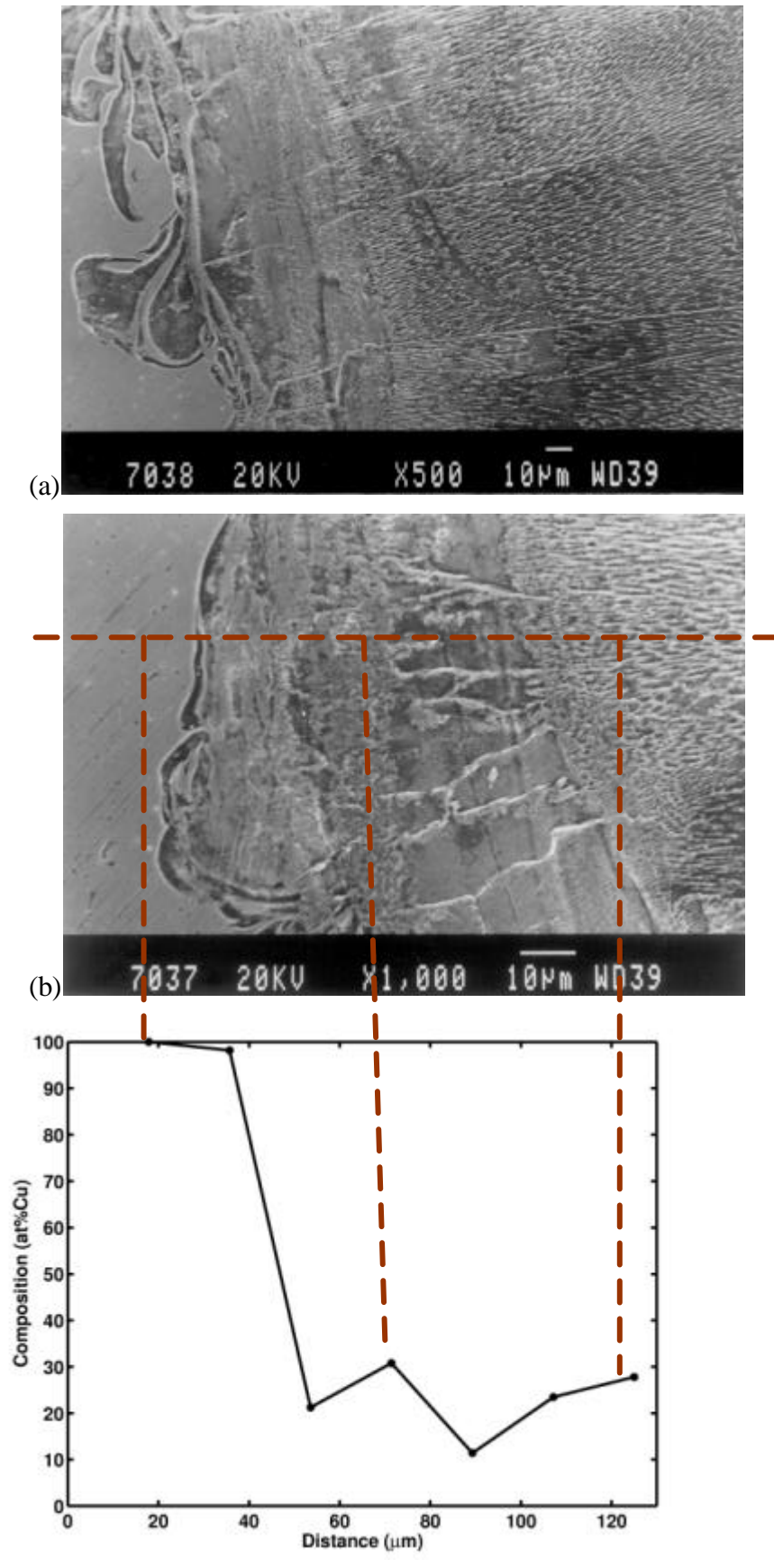
Figure 3.4 Interface microstructures on the copper side the Fe-Cu weld at 4.5 kW, 25 mm/s.
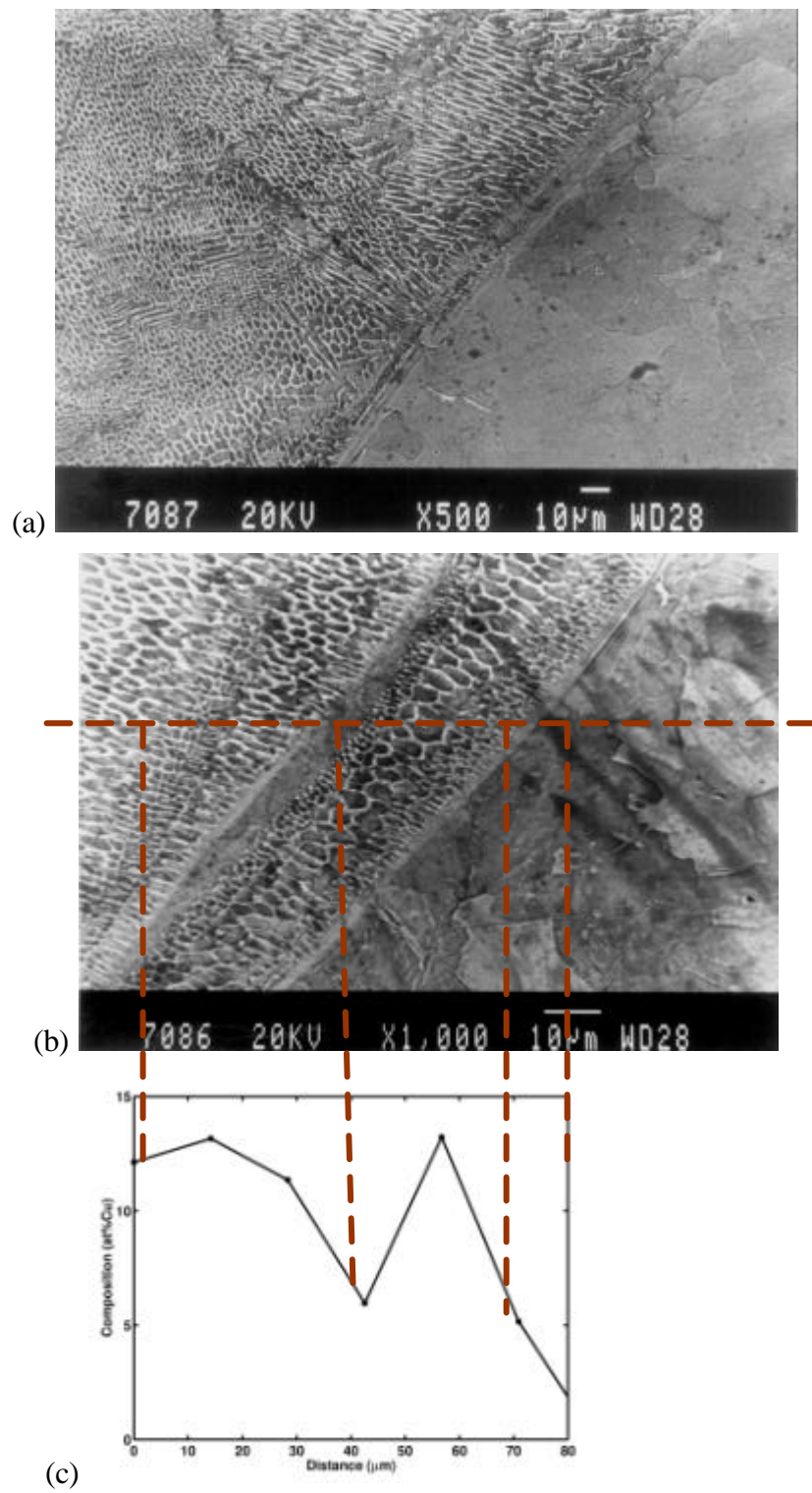
Figure 3.5 Interface microstructures on the iron side the Fe-Cu weld at 4.5 kW, 25 mm/s.
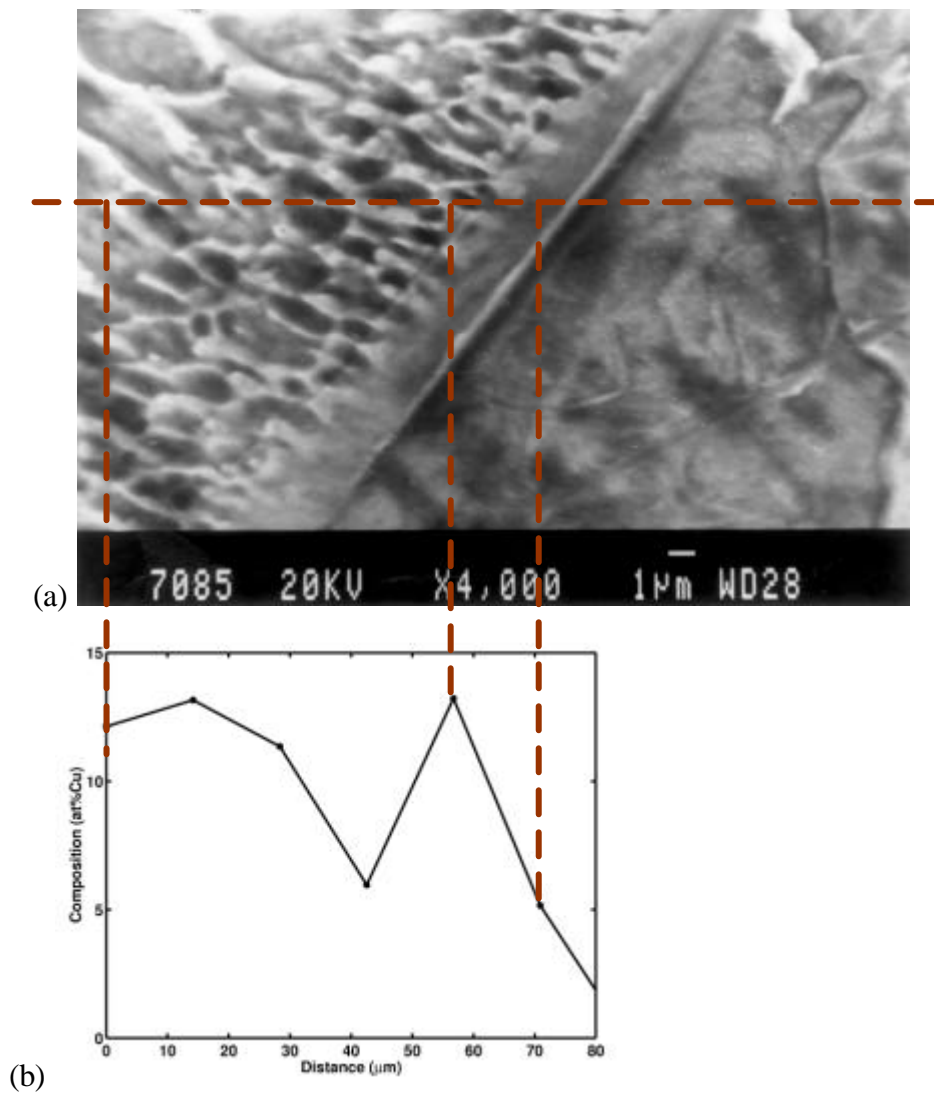
Figure 3.6 (a) Planar to cellular transition on the interface of Iron side (b) Gradual increase in the copper content in the alloy. Laser power used for welding is 4.5 kW and scan speed is 25 mm/s.
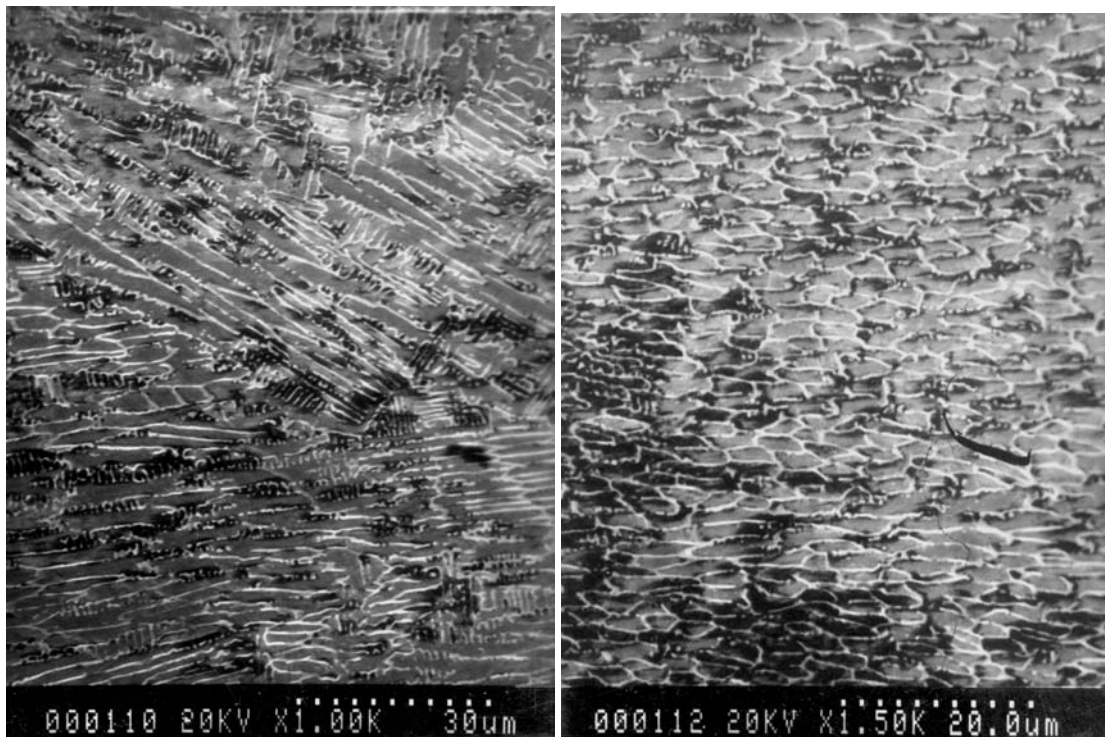
(a)   (b)
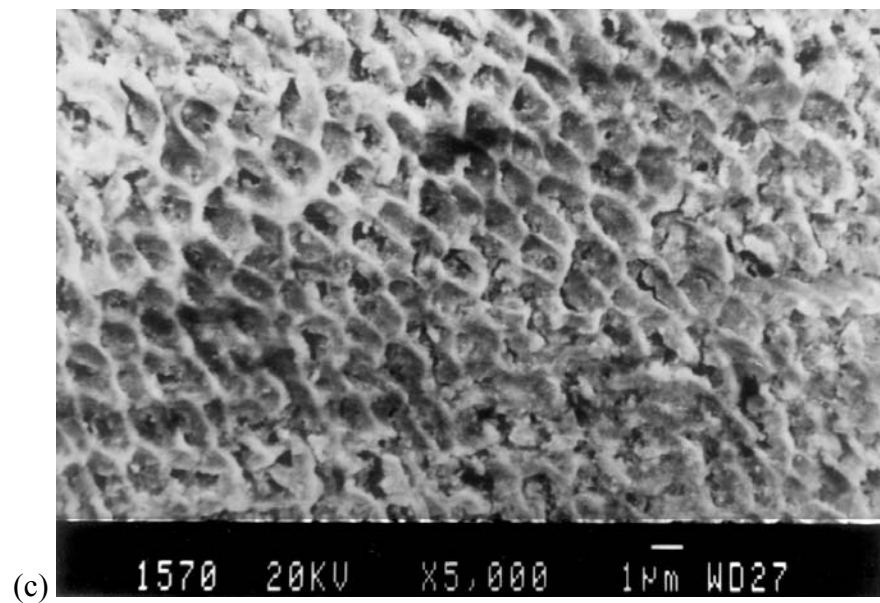
(c)

Figure 3.7 Microstructure within the weld region. (a&b) 5.5 kW, 84 mm/s (c) 4.5 kW, 25 mm/s.
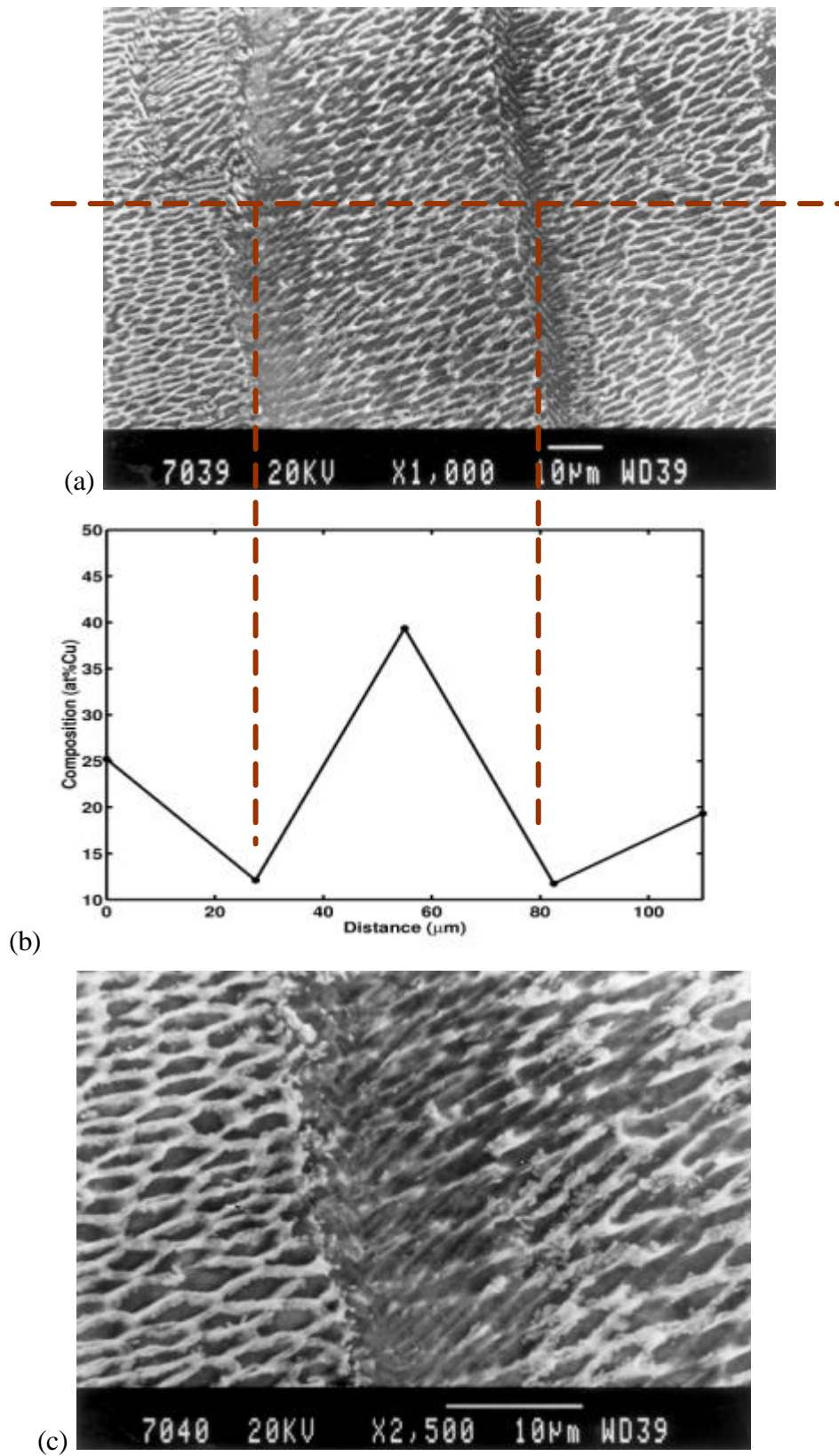
Figure 3.8 Microstructural banding in the Fe-Cu weld pool (4.5 kW, 25 mm/s).
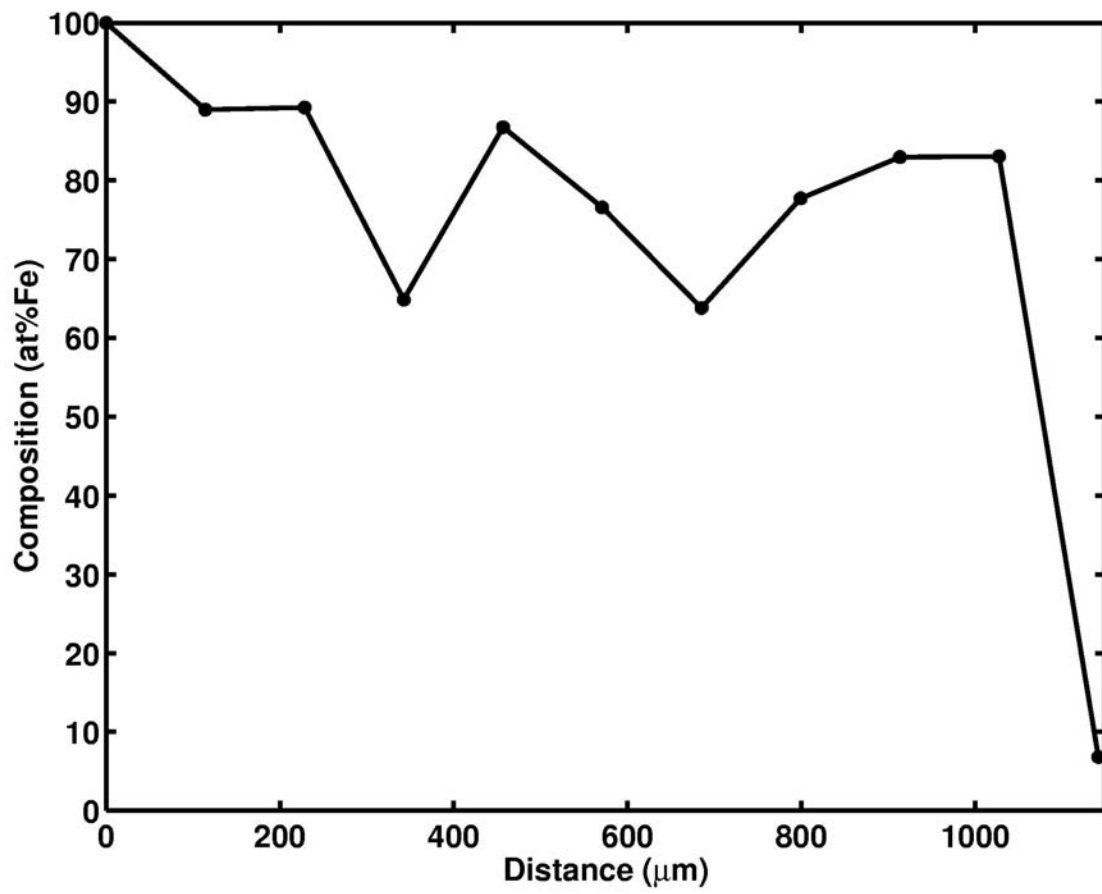
Figure 3.9 Composition across the weld near the top (4.5 kW, 25 mm/s).

(a)   (b)

(c)   (d)
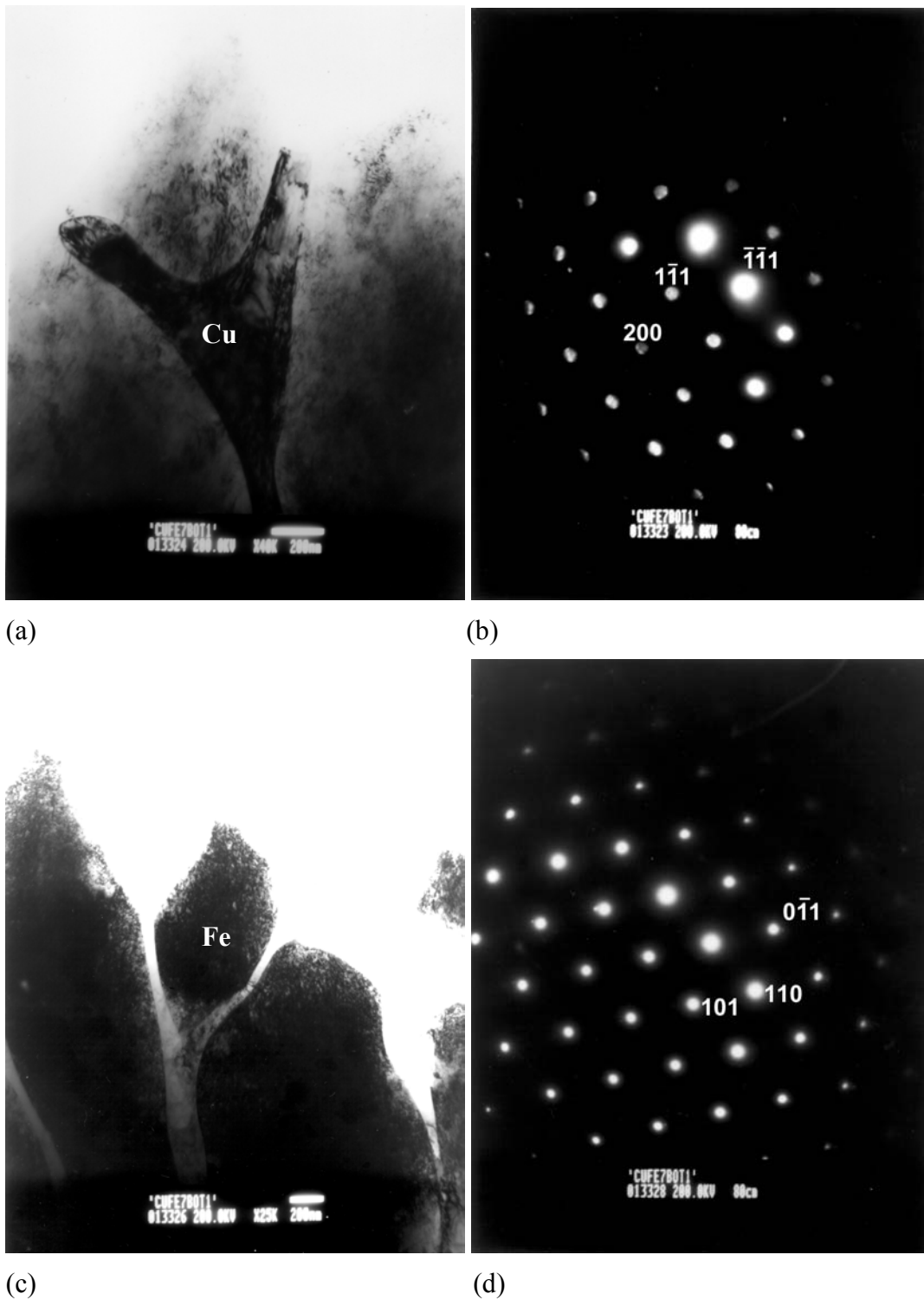
Figure 3.10 Microstructure from the bottom of the weld pool: (a) Bright field image showing iron grains and intergranular copper. SADP from the copper region is shown in (b) in [011] zone. (c) shows iron grains in [11$\bar{1}$] zone and the corresponding SADP is shown in (d).

(a)

(b)

(c)

(d)
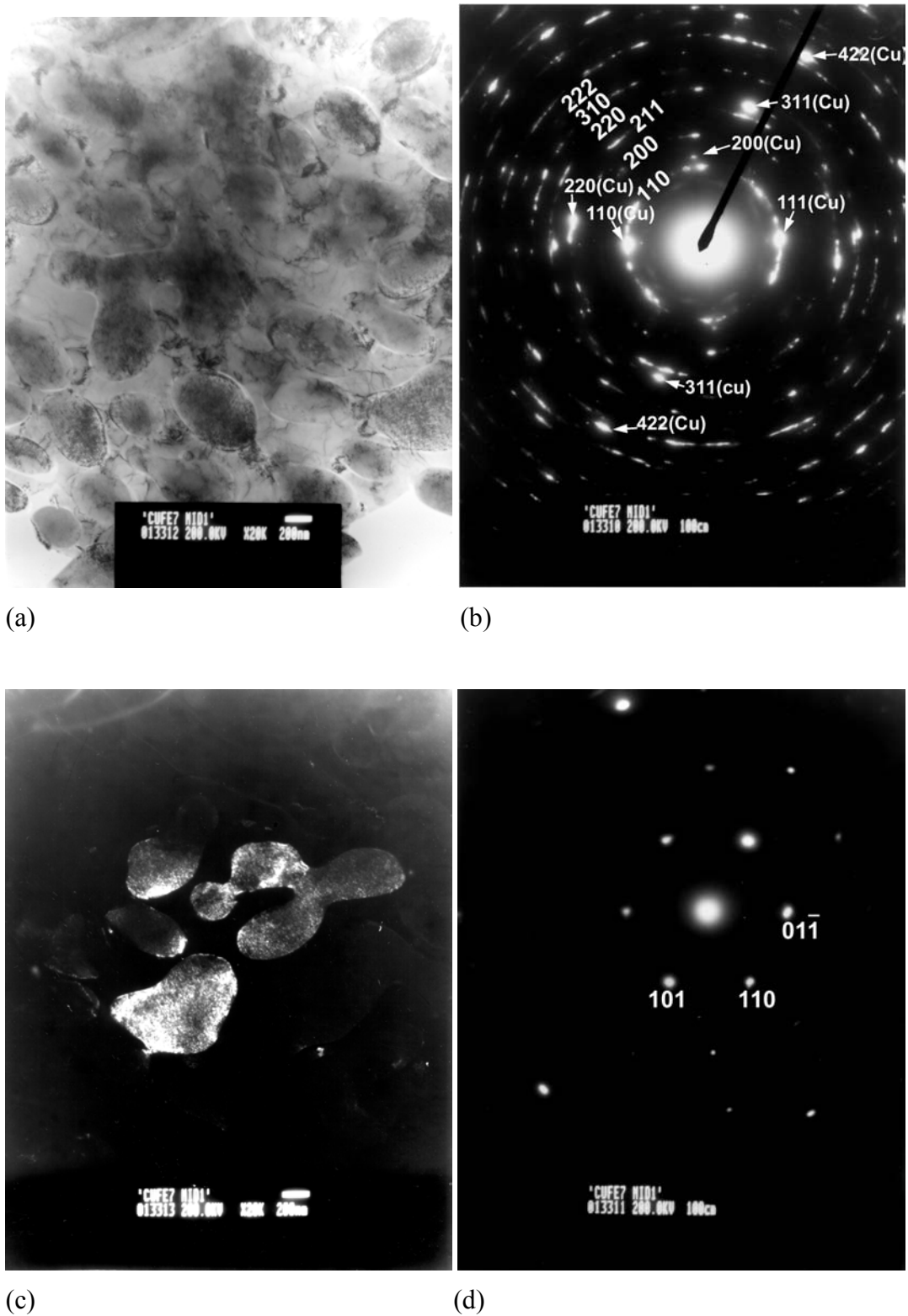
Figure 3.11 Microstructures in the middle of the Fe-Cu weld. (a) Low magnification micrograph showing several Fe-grains percolated with Cu grains. (b) Corresponding diffraction pattern. Note that finer rings belong to iron while brighter spots belong to copper. (c) Dark field from the (101) reflection of the iron grains. (d) The diffraction pattern of iron grains in $[\bar{1}11]$ zone.
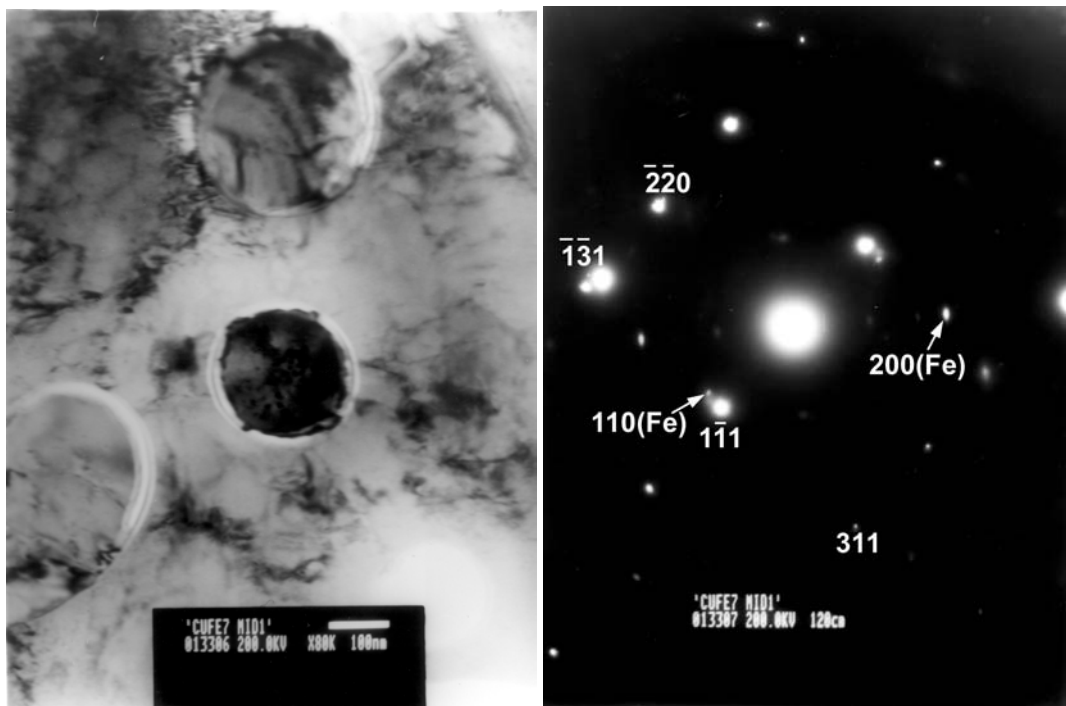
(a)   (b)
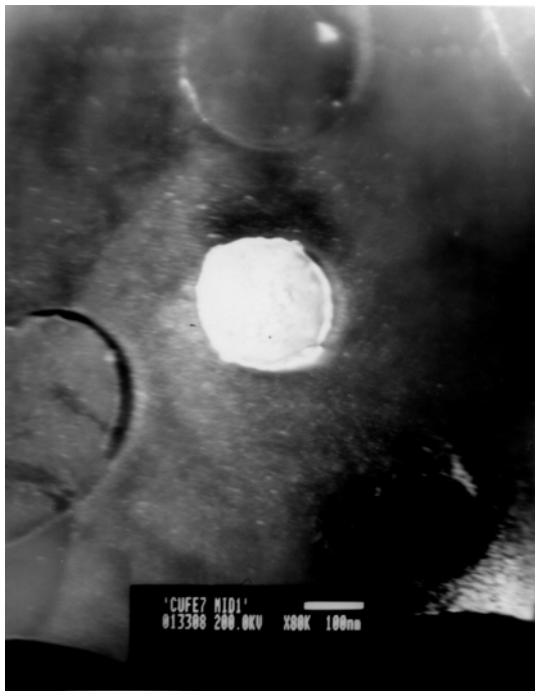
(c)

Figure 3.12 Microstructure in the middle of the Fe-Cu weld: (a) bright field image in $[\bar{1}12]$ zone showing a copper globule in the iron matrix. Corresponding SADP is shown in (b). (c) Dark field from the $(1\bar{1}1)$ reflection of the copper. The weak (110) reflection of α-iron spot shown also contributes giving illumination to the matrix.

(a)   (b)

(c)
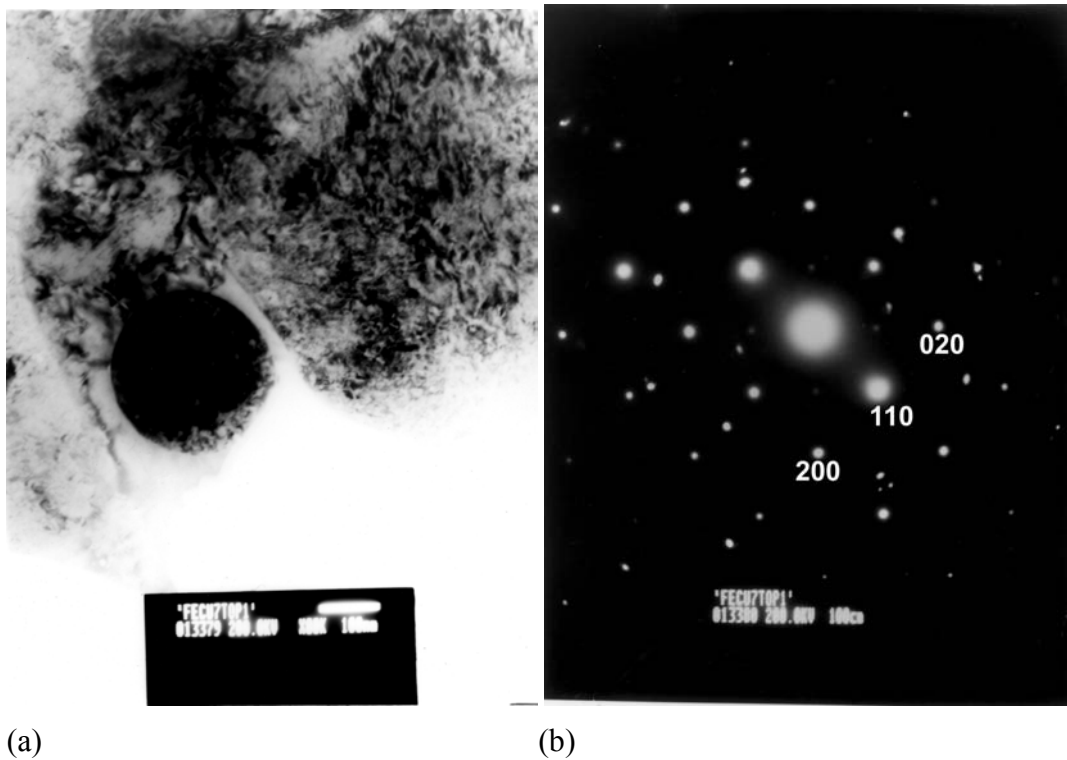
Figure 3.13 Microstructures near the top of the Cu-Fe weld at 5.5 kW, 21 mm/s. (a) bright field image of the bcc-Fe globule (b) Selected Area Diffraction pattern from the globule showing [001] zone of bcc-Fe and (c) dark field image from the $(\bar{1}\,\bar{1}0)$ reflection.
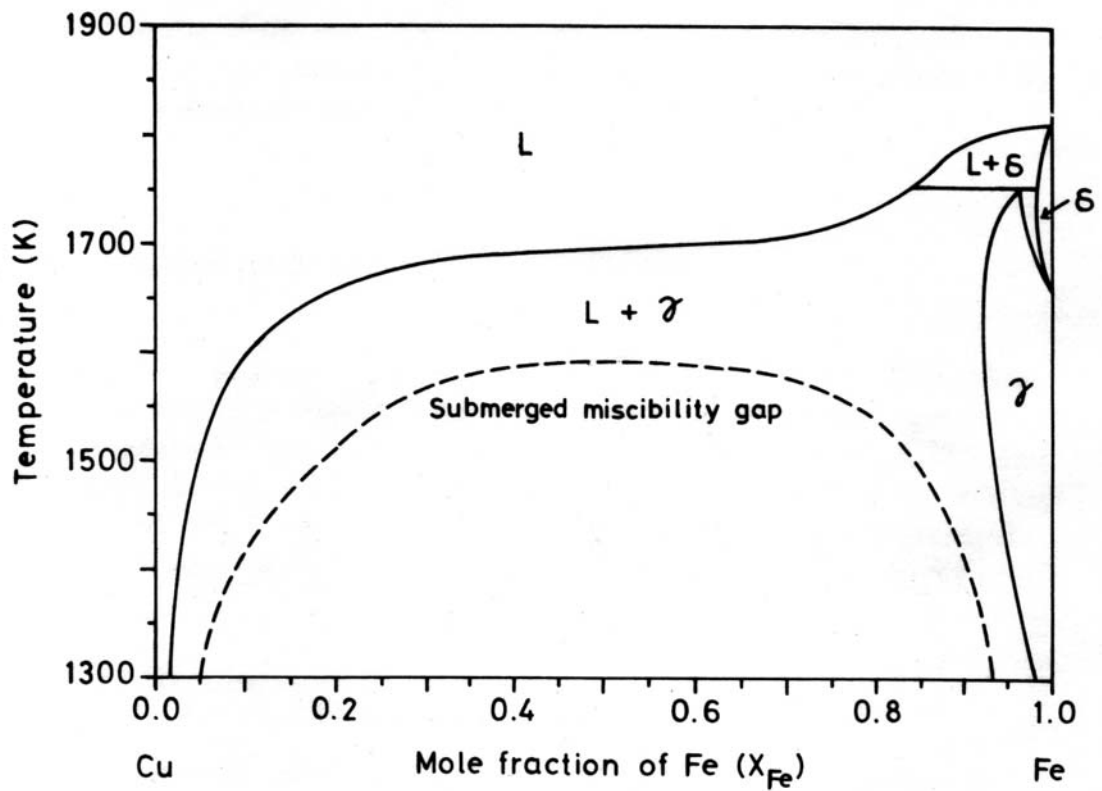
Figure 3.14 Equilibrium and calculated metastable phase diagrams of the iron-copper system [90].
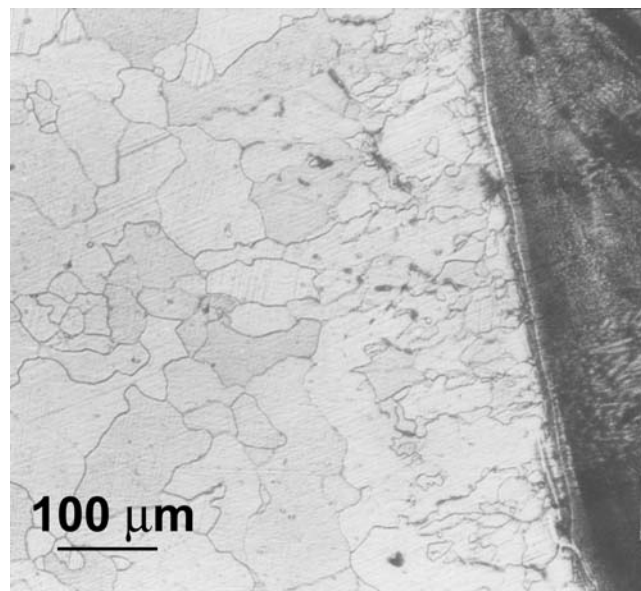
Figure 3.15 Grain refinement on the iron side near the interface of Cu-Fe weld at 5.5 kW, 2 mm defocus, 21 mm/s [93].
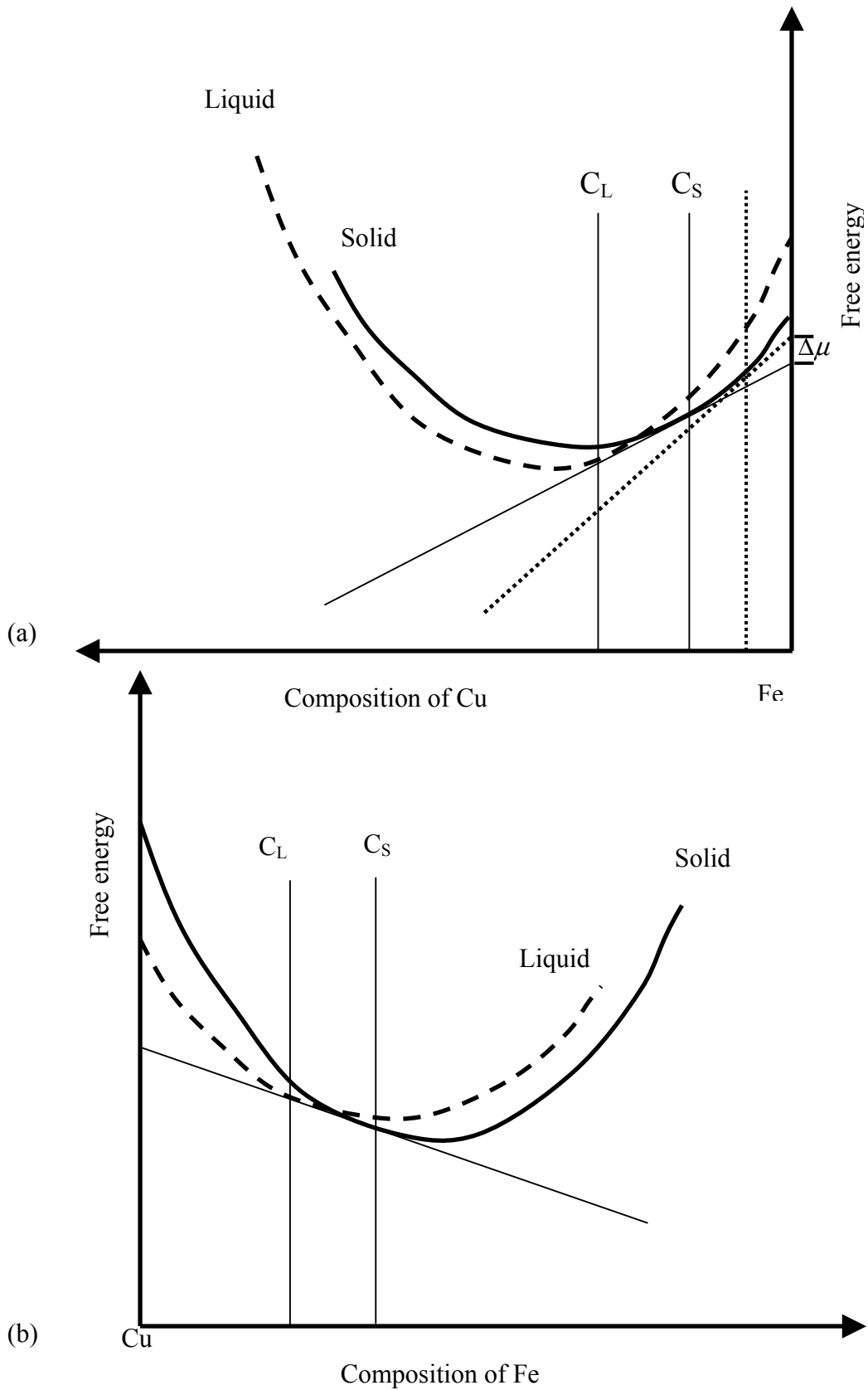
Figure 3.16 Schematic of the free energy of iron-copper near (a) iron rich end (b) copper rich end.

Chapter 4

Laser welding of Cu-Ni binary couple

4.1 Introduction

A binary couple of pure metals is simpler to start with in order to understand the basic issues in dissimilar joints. In a model dissimilar couple, the two metals should have a significant difference in their physical properties so that the main issues are highlighted. Also, for a preliminary study, it is not desirable to choose a binary system with a phase diagram containing any miscibility gap or intermetallic compounds in it, which would make the system additionally complex and difficult for a systematic analysis.

Table 4.1 Physical properties of copper and nickel [88]

Property	Copper	Nickel
Melting Point (^{o}C)	1083	1453
Thermal Conductivity (Wm^{-1}K^{-1})	399	88.5
Specific Heat (Jkg^{-1}K^{-1})	386	452
Density (kgm^{-3})	8900	7905
Latent Heat (kJmol^{-1})	13.02	17.16

As shown in table 4.1, copper and nickel have a large difference in thermophysical properties. The binary system of copper and nickel has a simple isomorphous phase diagram without any miscibility gap or intermetallic compounds (figure 4.1). Thus, copper and nickel form an ideal binary system satisfying the above mentioned desired criteria. the present chapter reports a detailed study of dissimilar metal welding using a copper-nickel couple. After a brief description of the spot weld experiments in section 4.2, weld microstructures are analysed in detail in section 4.3. A three dimensional model of the

transport phenomena during spot welding is presented in the next section. Section 4.5 presents an extension of the model to continuous welding. An attempt to explain the interface microstructures using thermodynamic arguments is made in the section 4.6. The chapter is summarised with conclusions in the last section.

4.2 Spot welding experiments

A schematic of the laser welding setup is shown in figure 4.2(a). The physical properties of the base metal vary across the butt weld i.e., along the *x*-axis, gravity is along *y*-axis and the heat distribution is Gaussian on the top surface along *x*- and *z*-axes. Thus, the process is inherently three dimensional and non-axisymmetric in nature. The physical processes that take place during welding are as given below:

1. Laser Heating

2. Melting

3. Mixing by buoyancy and Marangoni convection

4. Solidification

During continuous welding, melting and solidification take place simultaneously at the two ends of the laser melt pool as illustrated in figure 4.2 (b). The symmetry about the *z*-axis is also lost, rendering the system completely three dimensional and transient in nature. During spot welding, the laser is switched off after a controlled time period called as lasing time. Heat is extracted by the base metal and solidification takes place. Thus, spot welding enables the various stages of process to be understood in a step-by-step manner. A small set of spot welding experiments were performed on the binary couple of copper-nickel in butt joint geometry and the microstructural features observed are described below.

Figure 4.3(a) shows the top view of a Nd:YAG pulse laser spot weld performed with an energy of 20 J and pulse width of 0.1 ms. The weld is laterally asymmetric and is of small width. Composition analysis was done at locations across the weld using an EDAX attached to the SEM. A plot of composition of nickel across the spot weld is shown in figure 4.3(b). As can be noted, the weld is well mixed for most of the pool on the nickel side. The composition gradient is sharp near the copper interface and shallow near the nickel interface. Figure 4.4 (a) shows the top view of a cw-CO_2 laser spot weld with a laser power of 4.5 kW and a lasing time of 0.4 s. A plot of the composition across the weld is

shown in figure 4.4(b). The features are similar to those described for the Nd:YAG weld. A spot weld for a long time scale of 0.8 s at a power of 3.5 kW is made and the top view of the same is shown in the figure 4.5 (a). The weld pool shape is not as asymmetric as in the case of spot welds of smaller lasing times. The concentration across the weld shows essentially the same feature. There is a sharp gradient on the copper side and a shallow gradient on the nickel side with some fluctuation. Figure 4.6(a) shows frozen ripples on the surface of the spot weld. The microstructure on the top surface was found to be dendritic as shown by the figure 4.6(b).

A cross section of the spot weld at a laser power of 3.5 kW and lasing time of 0.5 s is shown in the figure 4.7(a). The deep pool shows that there could have been plasma formation during the spot welding. The microstructure is cellular in most of the regions of the cross section. A typical cellular microstructure is shown in the figure 4.7(b). The cell spacing measured by a random line intercept method is 1.3 µm at the top and 1.0 µm at the centre of the weld. The weld also exhibits a small amount of porosity. Figure 4.7(c) shows dendritic microstructure in a pore due to exhaustion of liquid ahead of solidification interface. The spot welds in the butt weld geometry are very small in dimension and often led to breakage of welds while taking sections. A detailed analysis of the spot welds was found to be difficult. The continuous welding experiments performed on the copper-nickel system are detailed in the following section.

4.4 Continuous welding

4.4.1 Experiments

Two sets of continuous welds are done with varying laser scan speed. In the first set, commercial high purity metals are taken in the form of bars of square cross section of 7mm × 7mm each and are fixed on a CNC table in butt-weld geometry. A continuous wave CO_2 laser of Trumpf make is used as the heat source with a co-axial inert gas shroud. Laser scan speed is varied from 126 mm/s to 10.6 mm/s at a power of 5.5 kW. In the second set, bars of cross section 10mm × 5mm are joined in butt weld geometry using a Rofin Sinar R10000 cw CO_2 laser. The laser is slightly defocussed to avoid formation of keyhole. Laser scan speed is varied from 16 mm/s to 4 mm/s at a power of 4.5 kW. The welding conditions are summarised in the table 4.2. Weld samples are cut to make transverse sections for

characterization. Optical microscopy using Olympus and Scanning Electron Microscopy using JEOL JSM 840-FX for microstructure and composition analysis by EDAX form the characterization studies. Limited transmission electron microscopy is also done using a JEOL 2000-FX II.

Table 4.2 Processing conditions used in the continuous laser welding of Cu-Ni.

Laser	Laser Power (kW)	Scan speed (mm/s)
Trumpf cw-CO_2 Laser	5.5	10.6
	5.5	21
	5.5	42
	5.5	84
	5.5	126
Rofin Sinar R10000 cw-CO_2 laser	4.5	4
	4.5	8
	4.5	12
	4.5	16

4.4.2 Microstructure analysis

The weld pool shapes, at low and high laser scan speeds, are shown in figure 4.8. At low scan speeds, the weld is deep and narrow indicating keyhole formation during welding (figure 4.8(a-b)). As the laser scan speed is increased, the depth of penetration decreases. At high scan speeds, the melt pool is a shallow one with an aspect ratio of 2 (figure 4.8(c)). The depth and width of the weld pool for various laser scan speeds are presented in the table 4.3. At lower power and low scan speed, the weld pool shape has a small dip at the bottom (figure 4.8(d-e)) indicating that there could have been some plasma formation during welding. The weld pool shape at lower laser power and high scan speed is shallow (low depth of penetration). An asymmetry in the pool shape with more melting of nickel is observed at all scan speeds and is more pronounced at higher scan speeds. At lower speeds, more amount of copper melts, leading to a decrease in the asymmetry of weld pool shape. Some amount of porosity is also noticed.

The microstructure reveals segregation patterns and banding that are asymmetric in nature. At high scan speeds, the 'eye' of the pattern lies on the nickel side and at low scan speed,

there is one 'eye' towards the top and one towards the bottom. Microstructural banding is less prominent at higher scan speeds.

Table 4.3 Dimensions of the weld at a laser power of 4.5 kW and different scan speeds.

Laser scan speed (mm/s)	Depth (mm)	Width (mm)
4	2.0	3.2
8	1.3	2.5
12	0.59	1.58
16	0.133	0.587

The grain structure of the base metals showed no heat affected zone except at low scan speeds (10.6 and 21 mm/s) for the welds at a laser power of 5.5 kW. A top view of the weld shown in figure 4.9 shows significant coarsening of copper grains but no such effect is noticeable on the nickel side. The starting grain size of copper is of the order of 100 μm which can be seen in the parent metal away from the weld pool. The grains are considerably coarsened near the weld pool. The dark line revealing a slightly different etching effect at the weld interface, indicated by the arrow, shows the actual extent of fusion.

The asymmetry of the microstructure of the weld interface can be clearly seen at higher magnification. On the copper side, the interface is rough with swirls of copper-rich and nickel-rich regions in an irregular pattern (figure 4.10(a-e)). No clear interface showing growth of copper grains into the weld is distinguishable. Bands of different microstructural scale could be noticed in the weld near the interface. The optical micrograph shown in figure 4.10(e) shows that the fusion zone extends in to the copper base metal and the irregular interface suggests different level of mixing than in the fusion zone. The microstructural patterns suggest insufficient mixing near the copper interface.

Nickel-weld interface is sharp and shows growth of the base metal into the weld (figure 4.11(a-d). A clear interface between the weld and the nickel region is distinguishable. The different grains of nickel growing into the weld with different orientation of cellular/dendritic pattern could be observed easily. A closer observation of the growth of nickel into the weld is made by measuring composition variation from nickel to the weld region at the interface. As shown in figure 4.12(a-b), the grains of nickel initially grow in a planar fashion and as the copper content in the solidified region increases gradually, the

microstructure changes to a cellular/dendritic mode. This observation is confirmed by the microstructures at higher magnification shown in figure 4.13. The nickel grains seem to grow initially in a planar fashion and, after an extent, change over to a cellular mode of growth. The scale of microstructure also increases as growth proceeds into the weld, as noticeable in figure 4.12(a).

Microstructural banding is observed throughout the weld and in particular, near the interface. Figure 4.14 (a&b) shows features resembling a swirl observed at the centre of the weld. The bands are characterised by a change in composition as well as microstructure length scale. As could be noted from figure 4.15(a), cellular patterns extend across the bands. The shape of the bands closely follows the solidification front, as could be noted from figure 4.8(c), 4.9(b) and 4.15(b). The bands are normal to the solidification direction suggesting an oscillatory growth of solid into the weld. The presence of such a kind of growth mode is confirmed recently by direct visualization [94]. The growth of the solid is not steady and is found to oscillate from a fine scale to a coarse scale with coinciding compositional fluctuations as the growth progresses. In the extreme case, the composition fluctuation near the nickel interface was found to vary from ~4 at% Cu to ~20 at%Cu in two adjacent bands with cell free and cellular microstructure respectively. These bands are termed as low velocity bands by Gremaud *et. al.* [95].

The microstructure throughout the weld exhibits a cellular/dendritic structure (figure 4.16). The cell spacing is generally found to be smaller near the top of the weld region (figure 4.16(c)) compared to the interior (figure 4.16(b)), indicating differences in cooling rate from the top to the bottom of the weld pool.

The composition variation in the weld region was studied in detail for the processing conditions discussed in this section. Composition of the weld region was measured across the weld near the top surface to indicate the extent of macrosegregation in the weld pool. Figure 4.17 shows composition profiles across welds performed using defocussed beam at a (a) high scan speed and (b) a low scan speed using a focussed beam. It could be noted that the composition profile shows the same features as that for a spot weld at higher speeds. In the weld performed at low scan speed and using focussed beam, the extent of mixing on the copper side is significant, leading to a change in the average composition of the weld. In order to know the composition distribution across the weld, several spot EDAX measurements were taken to cover the entire weld pool for the conditions of laser power of 5.5 kW, 84 mm/s and 4.5 kW, 8 mm/s. The measured compositions are plotted using

contours to reveal the distribution. As could be noted from the figure 4.18, much of the weld region on the nickel side is well mixed with shallow composition gradients. On the copper side, the close spacing between the iso-composition contours indicate high gradients.

A small set of transmission electron microscopy studies were done on the Cu-Ni welds. The weld processed at 4.5 kW, 16 mm/s shows high strain contrast as shown in the figure 4.19. As shown in figure 4.20, the weld processed at and 5.5 kW, 21 mm/s shows similar features. The lattice spacing calculated from the electron diffraction patterns correspond to a Cu-50 at% Ni alloy. In addition, a selected area diffraction taken from the region shown (figure 4.20 (a)) shows extra spots near the cubic reflections (shown by an arrow) indicating that Cu-Ni alloys of two different compositions could be present in the area. However, there is no sufficient evidence to confirm phase separation of the Cu-Ni alloy in the weld region.

4.4.3 Discussion of experimental observations

Dissimilar welds of copper and nickel were made at two different laser powers and scan speeds. The weld shows certain common features at all the welding speeds. The weld is asymmetric with more melting of nickel. The higher thermal conductivity of copper leads to less sensible heat and thus less extent of melting. The overall composition in the weld pool is nearly uniform on the nickel side and has a sharp increase on the copper side. As will be shown in the computational results, the copper side melts after nickel and solidifies before nickel thus, spends less time in the liquid state. As a result, mixing is not complete. However, nickel melts first and undergoes vigorous convection leading to uniform mixing.

The interface microstructures are also asymmetric with a continuous growth of nickel in to the weld and lack of mixing on the copper side. An analysis of the driving force required for the growth of a pure metal in to an alloy pool is made using the free energy vs. composition curves. Free energy data for the liquid and solid phases are obtained for copper nickel from literature [96]. The free energy was plotted at the liquidus temperature of Ni-20 at%Cu in figure 4.21 (a). A liquid of composition Ni-20 at%Cu ('C') is in equilibrium with a solid of about 10at%Cu at 1350 $^{\circ}$C. All compositions of solid up to 'F' can form since the free energy curve for solid lies below that of liquid. If the base metal, which is pure nickel, were to grow continuously in to the alloy liquid, the composition of the solid should increase to that given by 'B' before the growth can begin. For an intermediate composition

of solid given by 'E', the chemical potential for nickel ('D') is higher than that for the parent liquid ('A'). Thus, certain amount of undercooling is necessary to overcome this barrier. As shown schematically in figure 4.21 (c), an undercooling at the interface also leads to a region of constitutionally undercooled region ahead of the nickel interface. One could clearly see that this leads to the breakdown of the planar front growth mode of nickel yielding cellular morphology in the weld pool. In the absence of such an undercooling, the high and positive temperature gradient ahead of the solid-liquid interface in to the weld pool should lead to a planar growth in to the weld pool.

Consider the situation on the copper side. Figure 4.21(b) shows the free energy vs. composition plot at the liquidus temperature of a Cu-7 at%Ni alloy (1140 $^\circ$C). An alloy liquid of composition Cu-7 at%Ni ('B') is in equilibrium with a solid of higher copper content ('C', Cu-13 at%Ni). All compositions of solid below 'F' have higher free energy compared to the liquids of same composition at this temperature. Only solids of composition higher than that given by 'F' are possible to form. If the copper grains were to grow continuously from the substrate in to the weld, the composition has to increase beyond the value indicated by 'F' by diffusion. Any intermediate composition (such as 'E') would melt back due the free energy being higher than that of the liquid of same composition. Thus, we can conclude that growth from copper side is not continuous and solidification on copper rich side takes place directly from the melt. As in the case of iron-copper, a peritectic reaction is not present. Bands that were present in the iron-copper weld very close to the copper interface (figure 3.3(a&b), 3.4 (a)) are not present in the case of copper-nickel weld. The bands near the copper side in copper-nickel weld are similar in nature to those near nickel side indicative of their origin in the fluctuations during growth. Cellular microstructure in the weld pool is expected due to the large temperature range between the liquidus and solidus in the phase diagram and possibility of undercooling to overcome the chemical potential barrier. Higher cooling rates experienced at the top of the pool lead to finer cellular patterns as also observed in figure 4.16(c).

In the next section, a model to understand the transport processes that take place during laser welding of dissimilar metals is presented. Attempts are made to understand the experimentally observed microstructural features with the help of the computational results.

4.4.4 Summary of experimental results

Detailed analysis of laser welding of copper and nickel was presented. Welding have been performed at different scanning speeds such that the welding mode changes from conduction mode at high scan speed to keyhole mode at low scan speeds. The weld pool shape was found to be asymmetric and the microstructural features observed for the case of iron-copper system were found to be similar to those of copper-nickel system. Cellular microstructure was observed in the weld pool at all welding speeds. Composition across the weld indicates good mixing on the nickel side in the weld pool. The growth of nickel was continuous into the weld pool with a gradual increase in composition. On the copper side, such a continuous growth was not observed. The bands near the copper side were similar in nature to those at the nickel side. They originate due to growth rate fluctuations. Microstructural banding with fluctuations in length scale and composition were observed. TEM study shows that the weld pool is highly strained.

4.5 Computational Modelling of spot welding

A full scale model of a moving dissimilar weld pool (i.e. produced by a continuous laser welding) requires modelling of the melting, mixing, and solidification at both micro and macro scales. Solidification modelling in such a situation is a very difficult task, since the composition can vary sharply at any location. In addition, the solidification process would depend on the scale of mixing of the two metals at the interface, which may be very difficult to determine using present modelling tools. In the case of a stationary spot weld, however, the process of melting is a distinct stage during the application of the laser, followed by a solidification process after the laser is switched off (assuming there is no remelting). Since the melting process involves only pure metals (initially separated in a butt welding arrangement), one has the option to model it without having to consider the solidification process. It may be noted that any mixing of metals due to convection occurs only after the material is molten. In this section, melting and mixing processes at a macroscopic level are modelled by considering a stationary-welding situation of a copper-nickel couple. The objective is to study the asymmetry of a weld pool caused by a symmetric heat source on a dissimilar metal joint, along with the associated temperature, velocity and mass fraction distributions. At this point, one may note that dissimilar metal

welding is inherently a three-dimensional process even in a stationary spot-welding mode because of the asymmetry created by the difference in properties of the two metals.

4.5.1 Choice of Model

In the welding of dissimilar metals, the two metals melt and mix in the weld pool. In order to model such a phenomenon, there are generally two classes of mathematical models that can be used for the flow of a multi-component fluid:

(1) Locally homogeneous mixture model, and

(2) Multi-fluid model.

In the flow of a multi-component mixture, if we assume that the various species are mixed at the atomic level and share the same velocity, pressure, and temperature fields, and that mass transfer takes place by convection and diffusion, then we can use a locally homogeneous model. The more complex situation where different species are mixed on larger scales, and may have separate flow fields, is called a 'multi-phase' flow [97,98]. The distinct flow fields of different fluids can interact via empirically specified 'inter-phase transfer' terms. Simulation of such a flow would require a multi-fluid model, in which there is a separate solution field for each phase. Multi-fluid models rely on constitutive relations that are often difficult to determine empirically.

A locally homogeneous model is considered for the present study, where flow is characterized by the properties assigned according to the relative proportion of each phase in the mixture. Although some information regarding the interface related quantities will be lost, the locally homogeneous model study would still give some insight into this complex problem with regard to flow field, asymmetry of pool shape, temperature field, and mixing.

4.5.2 Mathematical Formulation

A schematic diagram of the computational domain used for numerical simulation is shown in the figure 4.1. Two pieces of copper and nickel with equal dimensions are kept in a butt joint. A laser heat input with a Gaussian distribution is applied from the top at the centre line of the butt joint such that the heat is distributed equally on both pieces. The following are the assumptions made in the model:

1. The weld pool surface is flat.

2. The fluid motion in the melt pool is assumed to be laminar and incompressible.

3. Thermophysical properties are taken to be different for solid and liquid metals, and variation with temperature taken into consideration using a smooth fit over the data available in the literature [88]. The expressions used are given in the table 4.4. The physical properties also vary according to the concentration of the mixture, and are evaluated according to mixture theory.

4. Laser power is distributed in a Gaussian manner at the top surface. The coupling coefficient (laser power efficiency) remains uniform and constant.

Table 4.4 Temperature dependent parameters used in the calculations

Property	Expression
$k_{Cu}(Wm^{-1}K^{-1})$	$393.688 + 0.0096T - 0.0002T^2 \ (T \leq T_M)$ $\left.\begin{array}{l}47.56903 + 0.185042T - 8.4054\times10^{-5}T^2 + \\ 1.25748\times10^{-8}T^3\end{array}\right\}(T_M < T < T_{BOIL})$
$k_{Ni}(Wm^{-1}K^{-1})$	$90.420288 - 0.1097862T + 1.1856\times10^{-4}T^2 -$ $4.997\times10^{-8}T^3 + 7.196\times10^{-12}T^4$
$c_{Cu}(JKg^{-1}K^{-1})$	$376.7528 + 0.143199T - 4.9657144\times10^{-5}T^2 +$ $4.6515071\times10^{-9}T^3$
$c_{Ni}(JKg^{-1}K^{-1})$	$452.725 + 0.2895T - 1.63786\times10^{-4}T^2 -$ $4.997\times10^{-8}T^3 + 7.1961\times10^{-12}T^4$
$\mu_{Cu}(Nsm^{-2})$	$0.309\times10^{-3}e^{\left(30500/8.314T\right)}$
$\mu_{Ni}(Nsm^{-2})$	$0.1663\times10^{-3}e^{\left(50200/8.314T\right)}$
$\sigma_{Cu}(Nm^{-1})$	$1.285 - 0.13\times10^{-3}(T - T_M)$
$\sigma_{Ni}(Nm^{-1})$	$1.778 - 0.38\times10^{-3}(T - T_M)$
ϕ (any property)	$\phi = \phi_{Cu}C + \phi_{Ni}(1-C)$

The copper nickel system chosen is very close to an ideal binary system with complete miscibility in liquid and solid states, and hence it justifies most of the assumptions made with regard to the mixture model. One important property that is very difficult to estimate for the simulation is the efficiency of absorption of heat from the laser beam. While the surface finish and emissivity reduce the coupling efficiency, vapour and plasma formation on the surface of melt pool enhance the same. It is very difficult to determine the coupling efficiency from experiments, and published studies on this issue are not adequate. An

efficiency value close to what is generally found in the literature of laser welding of similar metals is used. In this context, it should be noted that the weld pool shape and qualitative details will be unaffected by small changes in the coupling efficiency and quantitative agreement with experimental results is not aimed at in the present modelling attempt.

Phase change is modelled using an enthalpy-porosity technique [99]. As discussed earlier, only melting of pure metals need to be considered if one models the melting phenomenon in a stationary spot weld. For a given control volume, pure metal properties (including latent heat of fusion) are used until melting takes place. Once melting occurs, followed by transport of material from one zone to another and subsequent mixing of the two metals, mixture rules for the properties are applied.

An explanation of various terms in the equations for conservation of mass, momentum, enthalpy and species is given in the Appendix at the end of the thesis. The final set of governing equations are given below:

Continuity:

$$\frac{\partial \rho}{\partial t} + \nabla \cdot (\rho \vec{u}) = 0 \tag{4.1}$$

Momentum:

$$\frac{\partial}{\partial t}(\rho u) + \nabla \cdot (\rho \vec{u} u) = \nabla \cdot (\mu \nabla u) - \frac{\partial p}{\partial x} + S_x \tag{4.2}$$

$$\frac{\partial}{\partial t}(\rho v) + \nabla \cdot (\rho \vec{u} v) = \nabla \cdot (\mu \nabla u) - \frac{\partial p}{\partial y} + S_y \tag{4.3}$$

$$\frac{\partial}{\partial t}(\rho w) + \nabla \cdot (\rho \vec{u} w) = \nabla \cdot (\mu \nabla w) - \frac{\partial p}{\partial z} + S_z \tag{4.4}$$

Energy:

$$\frac{\partial}{\partial t}(\rho c T) + \nabla \cdot (\rho c T \vec{u}) = \nabla \cdot (k \nabla T) - \frac{\partial}{\partial t}(\rho \Delta H) \tag{4.5}$$

Mass fraction:

$$\frac{\partial}{\partial t}(C) + \nabla \cdot (\vec{u} C) = \nabla \cdot (D \nabla C) \tag{4.6}$$

where, t is time, ρ is density, u,v and w are velocities along x,y and z directions, $\vec{u}$ is the velocity field in vector notation, μ is viscosity, p is pressure, k is thermal conductivity, c is specific heat, ΔH is latent heat content, C is species and D is species diffusivity coefficient.

Boundary and initial conditions:

At time $t = 0$, the entire domain is in the solid state at room temperature. At time $t > 0$, the following boundary conditions are applied:

At the top surface of the work piece, a heat flux with a Gaussian distribution is applied, as given by:

$$q''(r) = \frac{\eta Q}{\pi r_q^2} \exp\left(-\frac{r^2}{r_q^2}\right) \tag{4.7}$$

where η is efficiency of absorption of laser, Q is laser power and r_q is radius of the laser beam. No mass transfer is considered at the top surface. All the sides are subjected to convective and radiative heat loss. At the flat free surface of the liquid, shear force due to surface tension (Marangoni force) is expressed as:

$$\mu \frac{\partial u}{\partial y}\bigg|_{y=h} = \frac{\partial \sigma}{\partial x}\bigg|_{y=h} \tag{4.8}$$

$$\mu \frac{\partial w}{\partial y}\bigg|_{y=h} = \frac{\partial \sigma}{\partial z}\bigg|_{y=h} \tag{4.9}$$

The surface tension for a mixture of copper and nickel is given by Butler's equation as indicated in table 4.4. The surface tension of a liquid is a function of surface active elements such as oxygen and sulphur [100]. The surface tension of copper is found to decrease with increase in the concentration of oxygen [101,102] and sulphur [103]. Similarly surface tension of nickel is also found to decrease with alloying elements [104]. Studies on the effect of the presence of surface active elements on the weld pool shape exist [105]. Weld pool diameter and the frequency of oscillation due to Marangoni flow were used to back calculate the surface tension [106]. It is very difficult to measure the composition of the surface active elements in the liquid weld pool. However, the present study does not aim at a quantitative matching of weld pool shape but only to study the physical phenomena that take place. The simulations were all performed assuming no

presence of surface active elements as it would introduce an additional variable whose value is unknown.

As shown in equations (4.8) and (4.9), the Marangoni force is balanced by viscous shear force at the top surface. Since fluid is pulled in the direction of increasing surface tension, a negative surface tension coefficient would result in a surface flow away form the laser centre towards the pool edges. The thermal Marangoni number (based on temperature gradient) for this problem can be defined as:

$$Ma = \frac{\sigma_T L r_q}{\alpha C_{pl} \mu} \tag{4.10}$$

Where, σ_T is temperature coefficient of surface tension, L is latent heat, α is thermal diffusivity, C_{pl} is specific heat in the liquid state and μ is viscosity. Since variable properties are used in this work, the governing equations are not non-dimensionalised with the Marangoni number, which is not a fixed quantity for the problem. Representative values of Marangoni number for the copper and nickel at 1600 °C are 625 and 3863, respectively. All parameters used in the present work are in a dimensional form.

4.5.3 Numerical Procedure

The three dimensional coupled continuity, momentum, energy, and mass fraction equations along with the boundary conditions are solved numerically using a finite volume technique. The general framework of the numerical solution rests on SIMPLER algorithm [60], modified appropriately to accommodate phase change processes and mixing of dissimilar metals. The set of linear equations obtained were solved using a tridiagonal matrix algorithm (TDMA). The values of thermophysical data used are listed in table 4.4, and the process parameters used for the case study are given in table 2. A non-uniform grid of $64 \times 48 \times 64$ is used to discretise the computational domain, with a high concentration of grids inside the weld pool.

The time steps for computations are varied according to the stages of the melting process. The large temperature gradients in the melt pool set up a strong Marangoni convection, leading to high fluid velocities, typically of the order of 1 m/s. During the initial phase during which the weld pool shape develops, the time steps used are small (about 0.05 ms).

The problem formulated here consists of solving several variables simultaneously. The properties are dependent on two of the variables solved for, namely, temperature and composition. Thus, the equations are highly nonlinear and coupled. The small time steps chosen (~0.1ms) to ensure convergence within a reasonable number of iterations (~100) increase the total number of times steps required to complete a run. The computational time required to solve for one set of input parameters is more than 100 hrs on an IBM 570 machine. The final set of linear equations, solved by the TDMA algorithm, is of the kind below:

$$\phi_p = \sum_{neighbors} a_i \phi_i + b_i \qquad (4.11)$$

Since the solution of a parameter ϕ at a node p depends on its nearest neighbours only, the equation set is amenable to parallelisation. In order to perform calculations within a reasonable time frame, the program has been modified to run on a multi processor machine using MPI library [107].

The descretised conservation equations are solved at each times step and convergence is declared when the maximum of residuals in two consecutive time steps falls below a small number, say, 5×10^{-5}. The results obtained in terms of distribution of temperature, composition and velocity field at the grid locations in the whole domain are analysed after post-processing to plot sections of the various parameters for analysis. The parameters used for the case study are given in the table 4.5.

Table 4.5 Parameters used in the computation

Laser power (kW)	3.5
Efficiency η	0.22
Radius of laser (mm)	0.5
Box dimensions ($mm \times mm \times mm$)	$12 \times 10 \times 12$
Number of Grids	$64 \times 48 \times 64$

4.5.4 Results and discussion

Due to the difference in thermal diffusivity of copper and nickel, heat diffusion in copper will be more during the conduction phase of the heating process. Nickel, which has a lower thermal conductivity, will be experiencing a quicker temperature rise than copper. As a result, the location of maximum temperature will be shifted towards the nickel side. Depending on the rate of heating of the two metals and their respective melting points, one can expect either of the two metals to melt first. In the present case, the low thermal conductivity of nickel more than compensates for its high melting point and melts first. Figure 4.22 shows the evolution of the weld pool as the laser heating takes place. The velocity profile is superimposed on the temperature contours to show the flow pattern that leads to transport of heat and further evolution of the weld pool shape. Since the temperature coefficient of surface tension, σ_T, is negative, the value of surface tension at the maximum temperature location is lower than that at the edges of the weld pool. Hence, the fluid in the centre is pulled radially outward. This leads to the melt spreading towards the copper side due to the flow. The heat is transported from the nickel side to the copper side by the convective flow. This information is not easily obtainable from experiments alone, and hence it is considered to be an important contribution from our numerical modelling. During the initial stages when copper starts melting at the interface of copper and nickel, as shown in figure 5.22 (c,d), the dependence of surface tension on composition leads to instabilities in the flow pattern.

However, at later times, the flow pattern is dominated by the strong convection originating from the nickel side. The fully developed pool shown in figure 4.22 (f) depicts an asymmetric pool shape. The evolution of the pool shape in a transverse section is shown in figure 4.23. It can be seen that due to asymmetric heating and convection, isotherms bend and become non-circular. On the free surface, convection brings the hot liquid from the maximum temperature location to the edges of the weld pool, thus increasing the width of the weld pool. By continuity, this flow also brings the cold fluid up from the bottom of the pool to the surface. The amount of heat transported in the vertical direction is therefore relatively small. Hence, the melt pool tends to be shallow and wide. Since surface tension forces are dominant, the maximum velocity occurs on the free surface. The eye of the convection cell is close to the surface. The radially outward flow and formation of two loops, a large one on the nickel side and a small one on copper side could be easily observed. The strong radially outward convection due to Marangoni forces leads to a

shallow pool. The composition of copper on the top view at three different time steps during heating (figure 4.24) shows increased mixing as heating progresses. It could be noticed that the nickel side is well mixed and the composition gradients at the molten copper/substrate interface are large.

The laser is switched off when the pool shape is fully developed to follow the phenomena that take place during the cooling stage. Due to the small size of the weld pool and a large base metal acting as heat sink, cooling takes place rapidly and the weld pool shrinks, eventually leading to a completely solid domain. The pool shapes at different time steps after the laser is switched off are shown in figure 4.25. Copper solidifies first, as its thermal diffusivity is higher that that of nickel. The pool shrinks from the copper side, finally leading to a small pool on the nickel side. The shape of the pool on nickel side resembles very much the one during initial stages of heating. This shows that the pool shape development is governed more or less by the nickel side. The cooling cycle is analysed using the transverse section also, as shown in figure 4.26. Even after the pool shrinks from copper side, the melt pool shape in transverse section is asymmetric with a flat side towards the copper side, showing the effect of high thermal diffusivity of copper on that side. Solidification of the melt pool takes place to completion by heat extraction by the base metals. The composition of the solidified spot weld is shown in figure 4.27. It could be noticed that the composition is nearly uniform on the nickel side and has sharp gradients on the copper side. Solidification phase after the laser is switched off does not lead to major changes in the composition profile at a macro level. The solidified weld composition contours could be compared to those of the experimentally determined ones, shown in figure 4.18. The composition across the weld near the top is shown in figure 4.27(c) which could be compared to the corresponding experimental plots shown in figures 4.3(b) and 4.4(b). The experimental and numerical plots are superimposed on figure 4.27 (c). The qualitative agreement between the calculated and experimental profiles is good.

In this simulation, the same value of efficiency of laser absorption was used for both the metals, and hence the observed asymmetry in the melt pool is entirely due to difference in thermal transport properties of the two metals. Simulations were run using differential laser absorption efficiencies for the two metals, but the effect is found to be less significant.

4.5.5 Scale analysis

In the previous section, it was observed that nickel melts before copper does, although the former has a higher melting point. A possible cause identified for this phenomenon is the higher thermal conductivity of copper. There are several other properties such as density, specific heat, and latent heat, each of which could also play a role in determining the time for initiation of melting after the laser is switched on. In this section, a systematic scale analysis is performed, from which one may be able to predict time scales for initiation of melting of each metal in a dissimilar couple.

Before melting occurs, the mode of energy transport is pure conduction. Accordingly, the energy equation (4.5) takes the following form in this regime:

$$\frac{\partial}{\partial t}(\rho c T) = \frac{\partial}{\partial x}\left(k\frac{\partial T}{\partial x}\right) + \frac{\partial}{\partial y}\left(k\frac{\partial T}{\partial y}\right) + \frac{\partial}{\partial z}\left(k\frac{\partial T}{\partial z}\right) \tag{4.12}$$

The diffusion terms on the right hand side of equation (4.12) are all of the same order of magnitude. Let us consider only the term $\frac{\partial}{\partial y}\left(k\frac{\partial T}{\partial y}\right)$. The transient heating term on the left side of equation (4.12) should also be of the same order of magnitude. In other words,

$$\frac{\partial}{\partial t}(\rho c T) \sim \frac{\partial}{\partial y}\left(k\frac{\partial T}{\partial y}\right) \tag{4.13}$$

A length scale, y_{ref}, is defined, representing the penetration of heat by diffusion as a result of the laser heat flux acting on the top of the work piece. With this definition, the rate of energy absorption per unit volume can also be scaled as $\frac{q}{y_{ref}}$. Hence, one can write:

$$\frac{\partial}{\partial t}(\rho c T) \sim \frac{\partial}{\partial y}\left(k\frac{\partial T}{\partial y}\right) \sim \frac{q}{y_{ref}} \tag{4.14}$$

When melting initiates, the temperature at the top surface is T_m, while the temperature at a distance y_{ref} from the top surface will be nearly that of ambient (since y_{ref} represents a diffusion length scale). Defining $\Delta T = T_m - T_{ambient}$, one can rewrite equation (17) as:

$$\frac{\rho c \Delta T}{t_{ref}} \sim \frac{k\Delta T}{(y_{ref})^2} \sim \frac{q}{y_{ref}} \tag{4.15}$$

where t_{ref} is the time scale for initiation of melting. Eliminating y_{ref} from the above equation, one gets:

$$t_{ref} \sim \rho c k \left(\tfrac{\Delta T}{q}\right)^2 \qquad\qquad (4.16)$$

The above expression suggests that, for the same laser heat flux, q, the time for initiation of increases with density, specific heat, thermal conductivity, and the melting temperature of the particular material. Substituting the average property values of copper and nickel into the above expression and using average laser intensity, it is found that $(t_{ref})_{nickel} \sim 0.2$ ms and $(t_{ref})_{copper} \sim 0.4$ ms.

4.6 Computational Modelling of continuous welding

A full scale modelling of a moving dissimilar weld pool (i.e. produced by a continuous laser welding) requires modelling of the melting, mixing and solidification at both micro and macro scales. Solidification and melting take place at the two ends of the weld pool and have to be modelled simultaneously. Modelling such a situation is a very difficult task, since the composition can vary sharply at any location. In addition, the solidification process would depend on the scale of mixing of the two metals at the interface, which may be very difficult to determine using present modelling tools. In the present case, an attempt is made to model the melting and mixing processes at a macroscopic level.

4.6.1 Mathematical Formulation

A schematic of the computational domain used for numerical simulation is shown in figure 4.1. Continuous welding is taken in to account by the motion of a Gaussian heat source moves along the z-axis at a velocity w_{scan}. The assumptions made in the computational model of the spot welding also apply for continuous weld. Since the laser heat source is moving, the problem is analysed in a reference frame fixed to the laser itself. The details of the governing equations are given in the appendix at the end of the thesis. The governing equations for mass, momentum, energy and species equations are as follows:

Continuity:

$$\frac{\partial \rho}{\partial t} + \nabla \cdot (\rho U) = 0 \qquad\qquad (4.17)$$

Momentum:

$$\frac{\partial}{\partial t}(\rho u) + \nabla \cdot (\rho \vec{u} u) = \nabla \cdot (\mu \nabla u) - \frac{\partial p}{\partial x} - \left(\frac{K(1-\varepsilon)^2}{\varepsilon^3 + b}\right) u - \frac{\partial}{\partial z}(\rho u w_{scan}) \tag{4.18}$$

$$\frac{\partial}{\partial t}(\rho v) + \nabla \cdot (\rho \vec{u} v) = \nabla \cdot (\mu \nabla v) - \frac{\partial p}{\partial y} - \left(\frac{K(1-\varepsilon)^2}{\varepsilon^3 + b}\right) v$$
$$+ \rho g [\beta_T (T - T_r) - \beta_C (C - C_r)] - \frac{\partial}{\partial z}(\rho v w_{scan}) \tag{4.19}$$

$$\frac{\partial}{\partial t}(\rho w) + \nabla \cdot (\rho \vec{u} w) = \nabla \cdot (\mu \nabla w) - \frac{\partial p}{\partial z} - \left(\frac{K(1-\varepsilon)^2}{\varepsilon^3 + b}\right) w - \frac{\partial}{\partial z}(\rho w w_{scan}) \tag{4.20}$$

Energy:

$$\frac{\partial}{\partial t}(\rho c T) + \nabla \cdot (\rho \vec{u} c T) = \nabla \cdot (c \nabla T) - \frac{\partial}{\partial t}(\rho \Delta H) - \frac{\partial}{\partial z}(\rho c T w_{scan}) - \frac{\partial}{\partial z}(\rho w_{scan} \Delta H) \tag{4.21}$$

Mass fraction:

$$\frac{\partial C}{\partial t} + \nabla \cdot (\vec{u} C) = \nabla \cdot (D \nabla C) - \frac{\partial}{\partial z}(C w_{scan}) \tag{4.22}$$

Where, μ is viscosity, u,v,w are velocity components along x,y,z, $\vec{u}$ is the total velocity vector, T is Temperature, σ is surface tension, C is solutal weight fraction, ρ is density, t is time, p is pressure, H is enthalpy, k is thermal conductivity and D is solutal diffusivity. K is a morphological constant, b is an arbitrary small number to prevent division by zero, ΔH is the latent heat content of a control volume, and ε is the liquid fraction.

Initial and boundary conditions:

At time $t=0$, the entire domain is in the solid state at room temperature. At time $t>0$, at the top surface of the work piece, a heat flux with a Gaussian distribution is applied symmetric about the centreline. At the flat free surface of the liquid, shear force due to surface tension is applied to take Marangoni convection into account. No mass transfer is considered at the top surface. The bottom surface is insulated, while the four sides are subjected to convective and radiative heat loss. At the melting front, the flux of species in to the weld pool is given by

$$v_n C_l = -D_l \frac{\partial C_l}{\partial y}$$
(4.23)

where v_n is the projection of the traverse speed onto the normal to the solid-liquid boundary, C_l is the species concentration in the liquid and D_l is the diffusivity . The flux of species due to partitioning at the solidification interface is given by the equation 4.24. k_p is partition coefficient.

$$(1 - k_p) v_n C_l = -D_l \frac{\partial C_l}{\partial y}$$
(4.24)

4.6.1 Numerical Procedure

The three-dimensional coupled continuity, momentum, energy, and mass fraction equations along with the boundary conditions are solved numerically using a finite volume technique. The general framework of the numerical solution rests on the SIMPLER algorithm, modified appropriately to accommodate phase change processes and mixing of dissimilar metals. Transient studies were carried out until some mixing patterns are obtained. The thermophysical data for the case study is given in table 4.6. A grids used are non uniform to ensure high concentration of grids inside the weld pool.

Table 4.6 Parameters used in the computation

Laser power (kW)	3.5
Efficiency η	0.22
Radius of laser (mm)	0.5
Laser scan speed (mm/s)	8
Box dimensions $(mm \times mm \times mm)$	$12 \times 10 \times 12$
Number of Grids	$64 \times 48 \times 64$

4.6.2 Discussion of Computational Results

The weld pool shape evolution during continuous welding was similar to that during spot welding. The fully developed weld pool is analysed using temperature and velocity profiles at a snapshot of time. Figure 4.28 shows the temperature contours and velocity profile on the top view as well as cross sectional view. The weld pool is asymmetric with more melting of nickel than copper. The spacing between temperature contours indicates the temperature gradient and thus, heat extraction rate on each side. The closely spaced contours on the nickel side and widely spaced contours on the copper side could be clearly seen. Nickel has more sensible heat than copper. The velocity profile extends to the temperature contour at 1085 ^{o}C on the copper side and to the contour at 1450 ^{o}C on the nickel side showing the extend of melt pool on each side. The maximum velocity in the weld pool is nearly 2 m/s which is much larger than the laser scan speed. Thus, we do not expect much trailing of weld pool in the direction of laser scan speed. The velocity profile shows a strong vortex on the nickel side indicating that the weld pool shape is governed primarily by the convection on the nickel side. The microstructural bands shown in figure 4.8 (c) also show the 'eye' of the vortex on the nickel side. The width of the melt pool along the z-axis is a measure of the amount of time spent by a given region in the molten state. It could be noticed that copper side has much less melt pool width than nickel side. Thus, the mixing on copper side is not expected to be complete, leading to sharp composition gradients on that side. However, the nickel side is well mixed due to strong convection and extended time spent in the molten state before solidification.

The microstructural features observed in the experiments, such as asymmetric weld pool shape, good mixing on nickel side and high composition gradients on the copper side are well reproduced by the computation. Thermal transport arguments are used successfully to explain these features. The coupling coefficient being different for copper and nickel would only enhance the asymmetry we noticed. The melting and solidification sequence, namely that copper melts later and solidifies first, leads to lack of mixing on copper side. This information is not easily determined in experiments and is thus an important contribution from the computation.

4.7 Summary

Detailed analysis of laser welding of copper and nickel was presented. Welding have been performed at different scanning speeds such that the welding mode changes from conduction mode at high scan speed to keyhole mode at low scan speeds. The weld pool shape was found to be asymmetric and the microstructural features observed for the case of iron-copper system were found to be similar to those of copper-nickel system. Cellular microstructure was observed in the weld pool at all welding speeds. Composition across the weld indicates good mixing on the nickel side in the weld pool. The growth of nickel was continuous into the weld pool with a gradual increase in composition. On the copper side, such a continuous growth was not observed. The bands near the copper side were similar in nature to those at the nickel side. They originate due to growth rate fluctuations. Microstructural banding with fluctuations in length scale and composition were observed. TEM study shows that the weld pool is highly strained.

A computational model of the transport phenomena that take place during laser welding of dissimilar metals was developed using a finite volume formulation. Nickel was observed to melt first and the heat is transported to the copper side by convection in the molten nickel due to Marangoni and buoyancy forces. The final shape of the weld pool is dictated by the convective flow and is observed to be asymmetric. The copper side spends less time in the liquid state with insufficient mixing whereas the nickel side is well mixed. The composition profile across the weld pool shows good qualitative agreement with the experimentally observed one.

Figure 4.1 Phase diagram of copper nickel system [88].

(a)

(b)
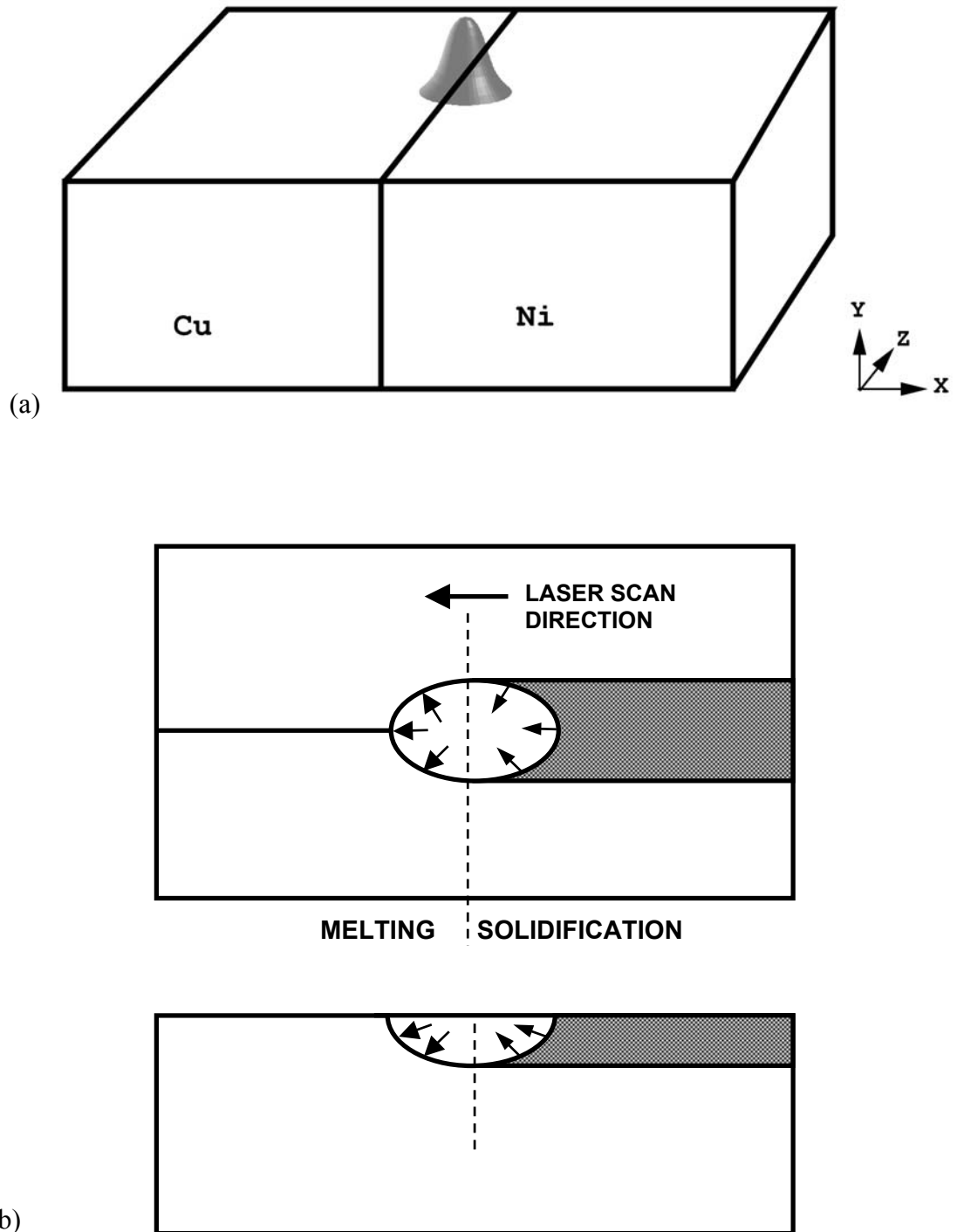
Figure 4.2. (a)Schematic of Laser welding setup. (b) Schematic illustrating simultaneous melting and solidification during continuous welding.
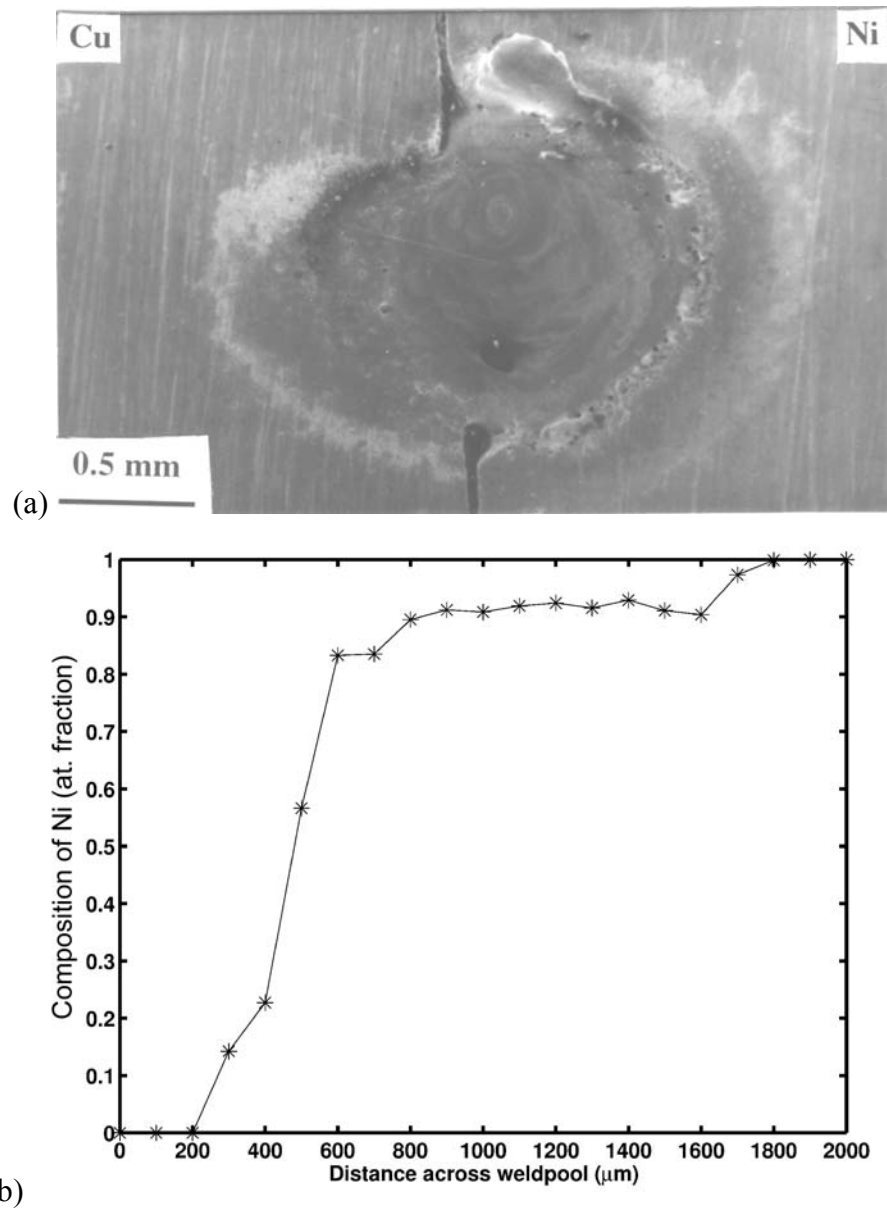
Figure 4.3 (a) Top view of a Cu-Ni spot weld done with Nd-YAG laser (20J, 0.1ms) (b) Composition plot across the weld.

(a)

(b)
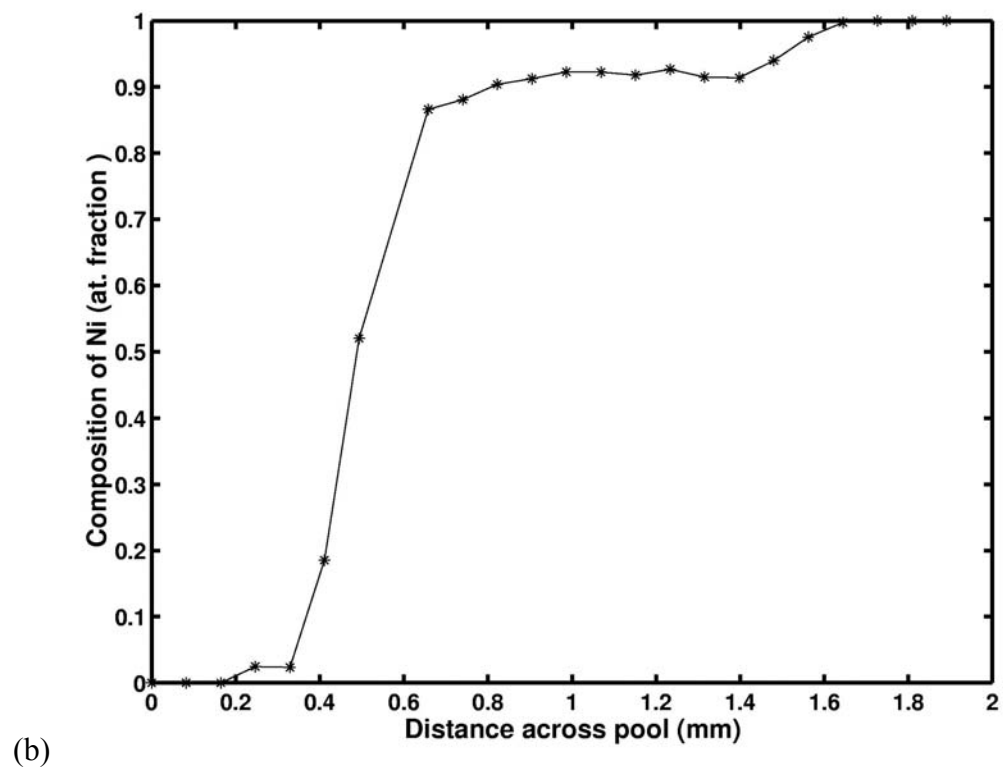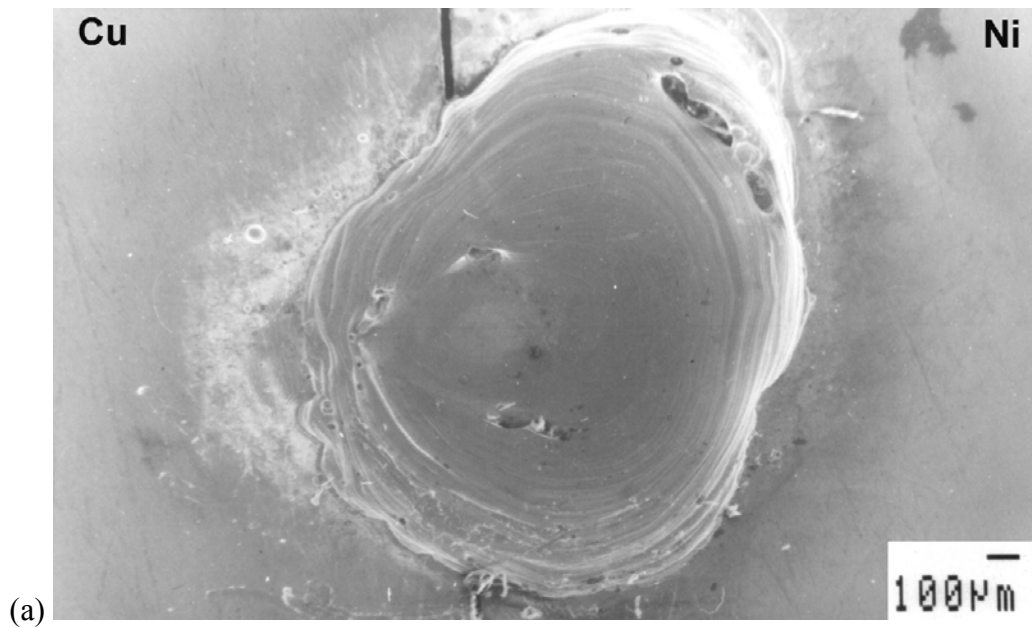
Figure 4.4 (a) Top view of Cu-Ni spot weld (power = 4.5 kW, time = 0.4 s)
(b) Composition across the above spot weld.
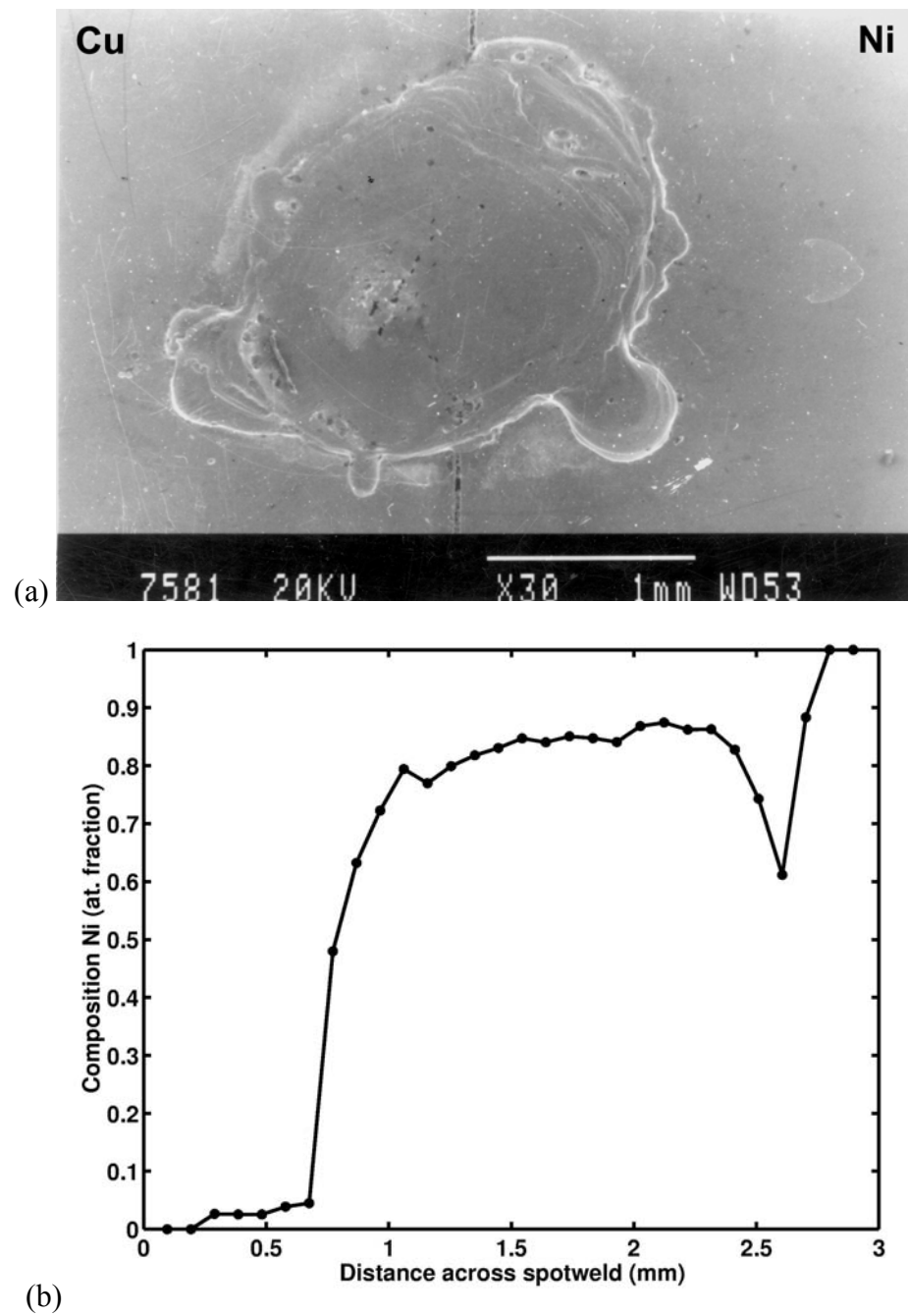
Figure 4.5 (a) Top view of spot weld (Power = 3.5 kW, time = 0.8 s) (b) Composition across the spot weld.
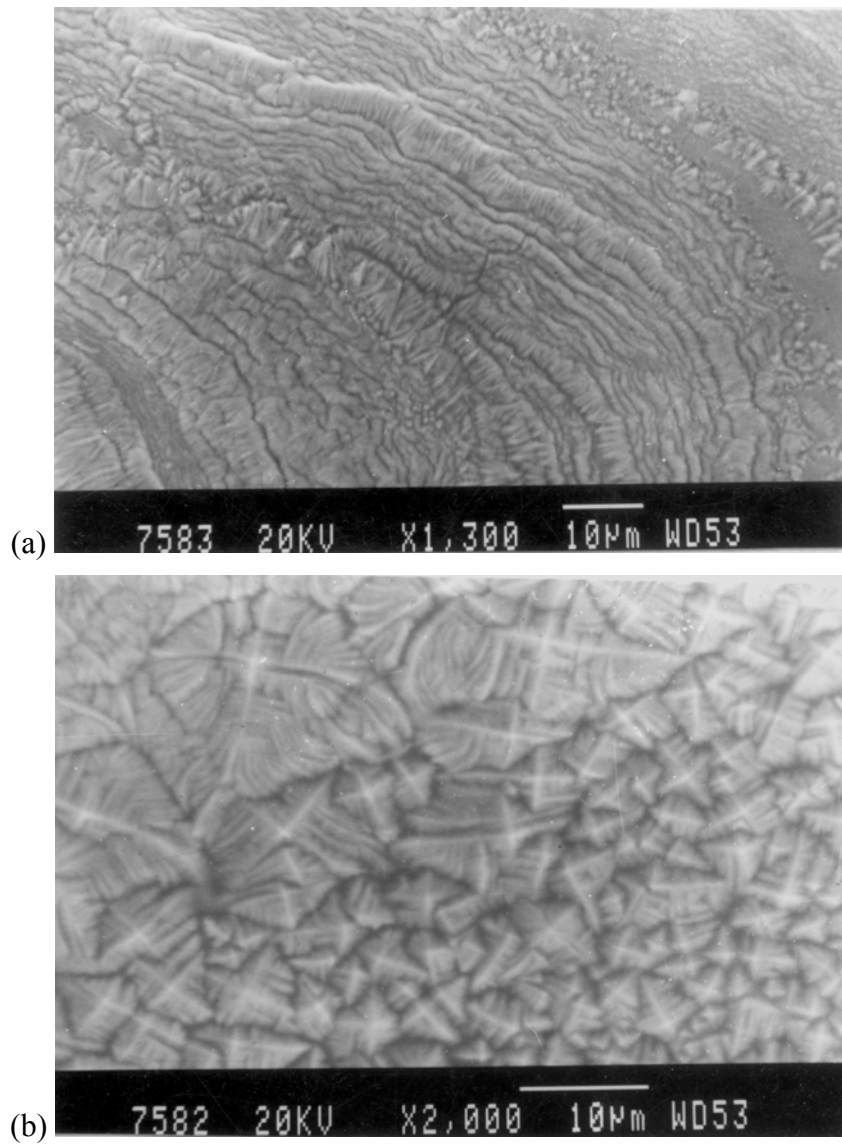
Figure 4.6 (a) Frozen in ripples on the top surface (b) Unetched dendrites on the top surface of the spot weld (Power = 3.5 kW, time = 0.8 s).

(a)

(b)

(c)
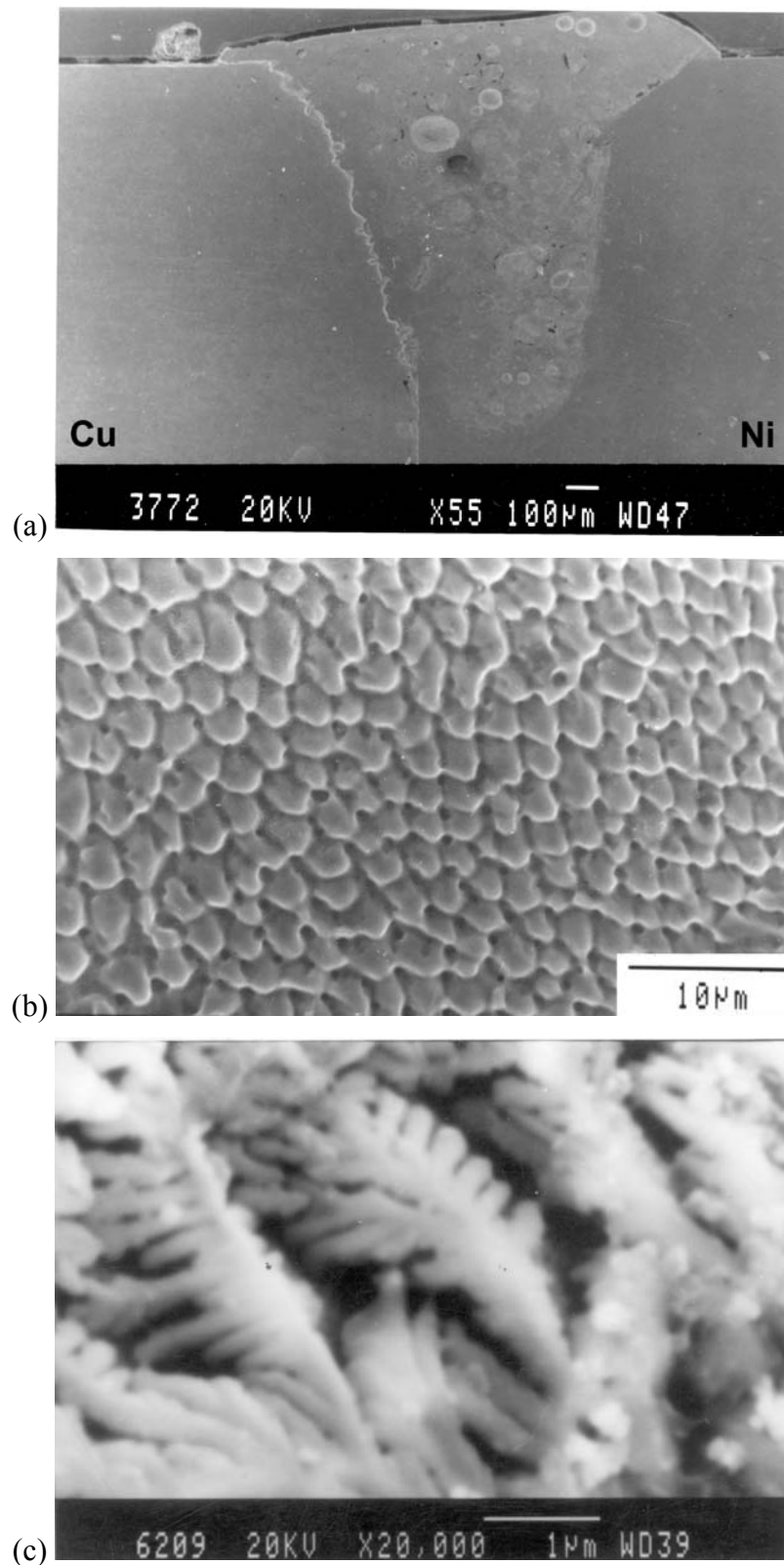
Figure 4.7 (a) Cross section view of spot weld (power = 3.5 kW, time = 0.5s)
(b) Cellular microstructure observed in the weld cross section. (c) Dendrites of Cu-Ni
(~15at%Cu) found in pores.

Cu   **Ni**

1mm

(a)
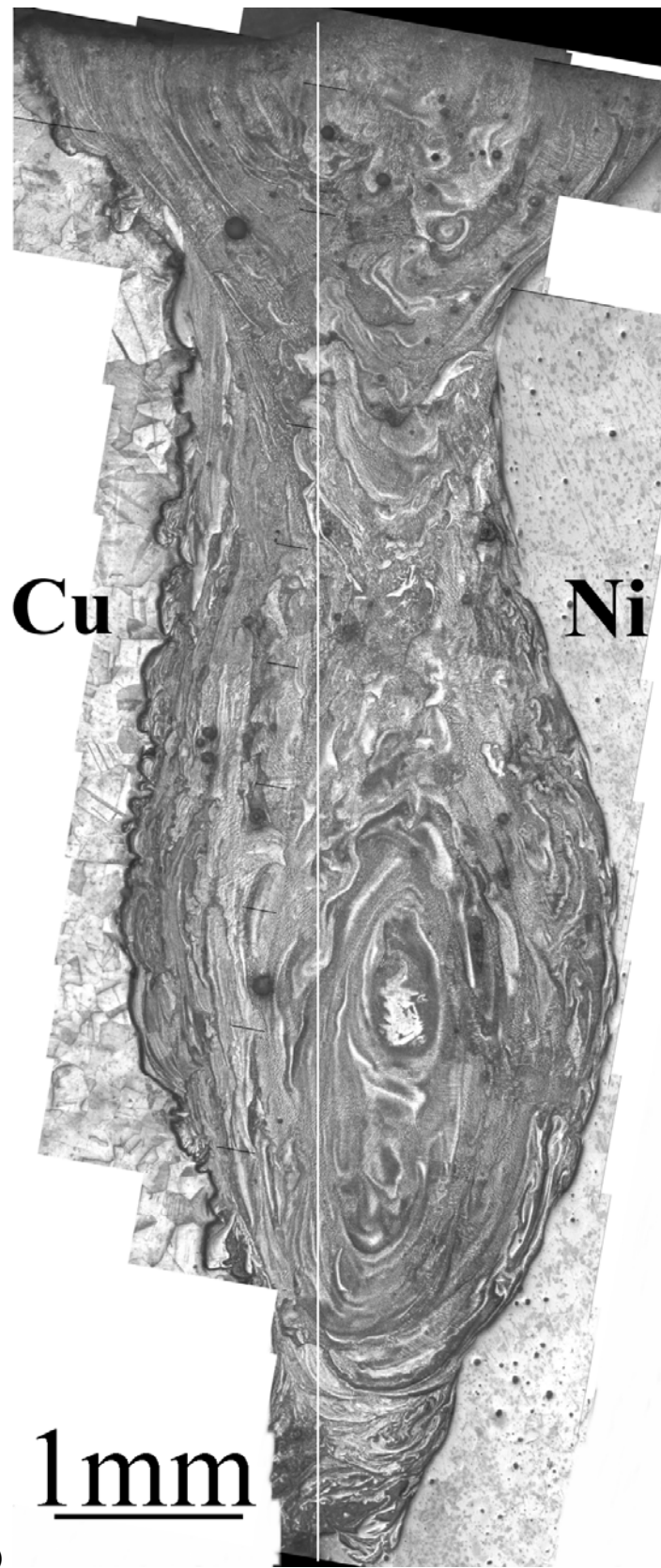
Figure 4.8 Cross section view of the Cu-Ni weld pool processed at a laser power of 5.5 kW and scan speeds of (a) 21 mm/s
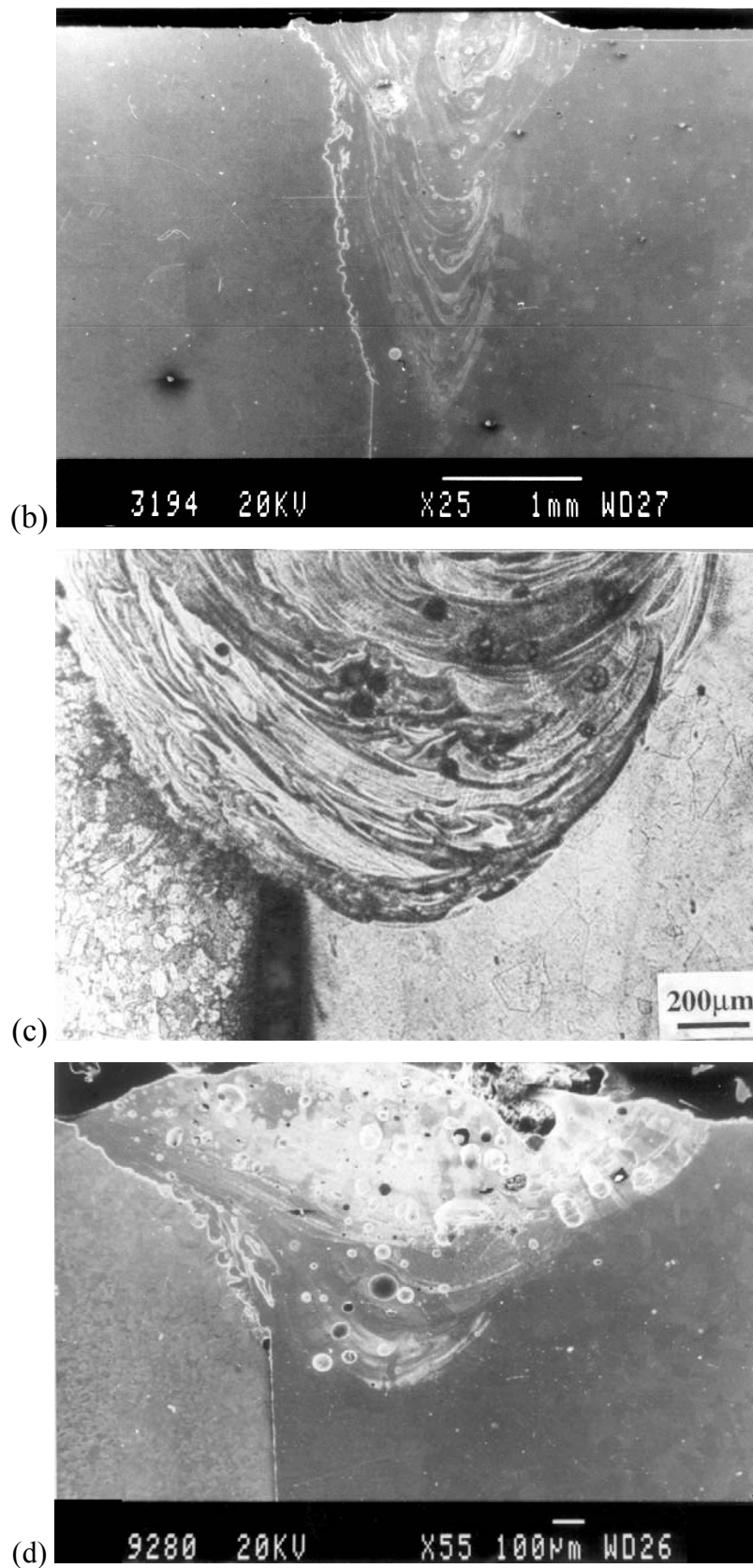
(b)

(c)

(d)

Figure 4.8 (contd.) Cross section view of the Cu-Ni weld pool processed at a laser power of 5.5 kW and scan speeds of (b) 42 mm/s (c) 84 mm/s and at (d) a laser power of 4.5 kW and scan speeds of 4 mm/s. Copper is on the left side and nickel is on right.
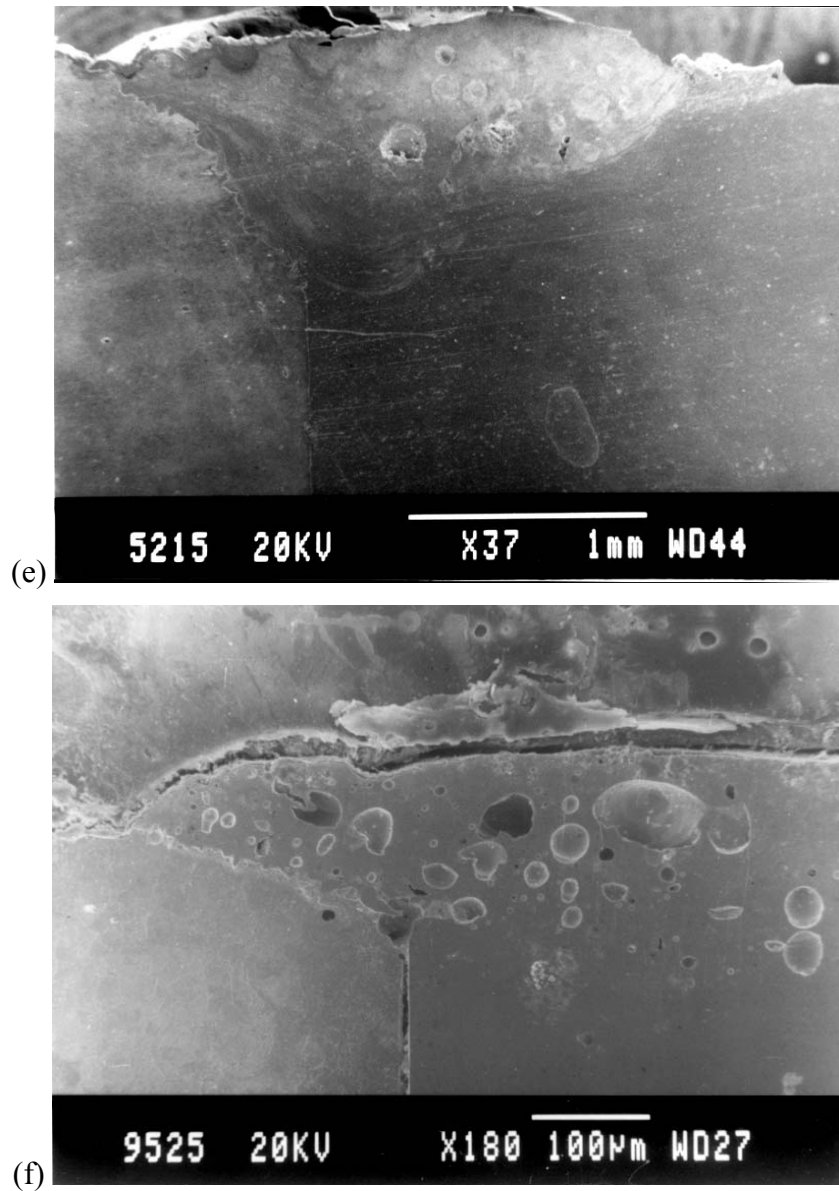
(e)

(f)

Figure 4.8 (contd.) Cross section view of the Cu-Ni weld pool processed at a laser power of 4.5 kW and scan speeds of (e) 12 mm/s and (f) 16 mm/s. In all the micrographs, copper is on the left side and nickel is on right side.
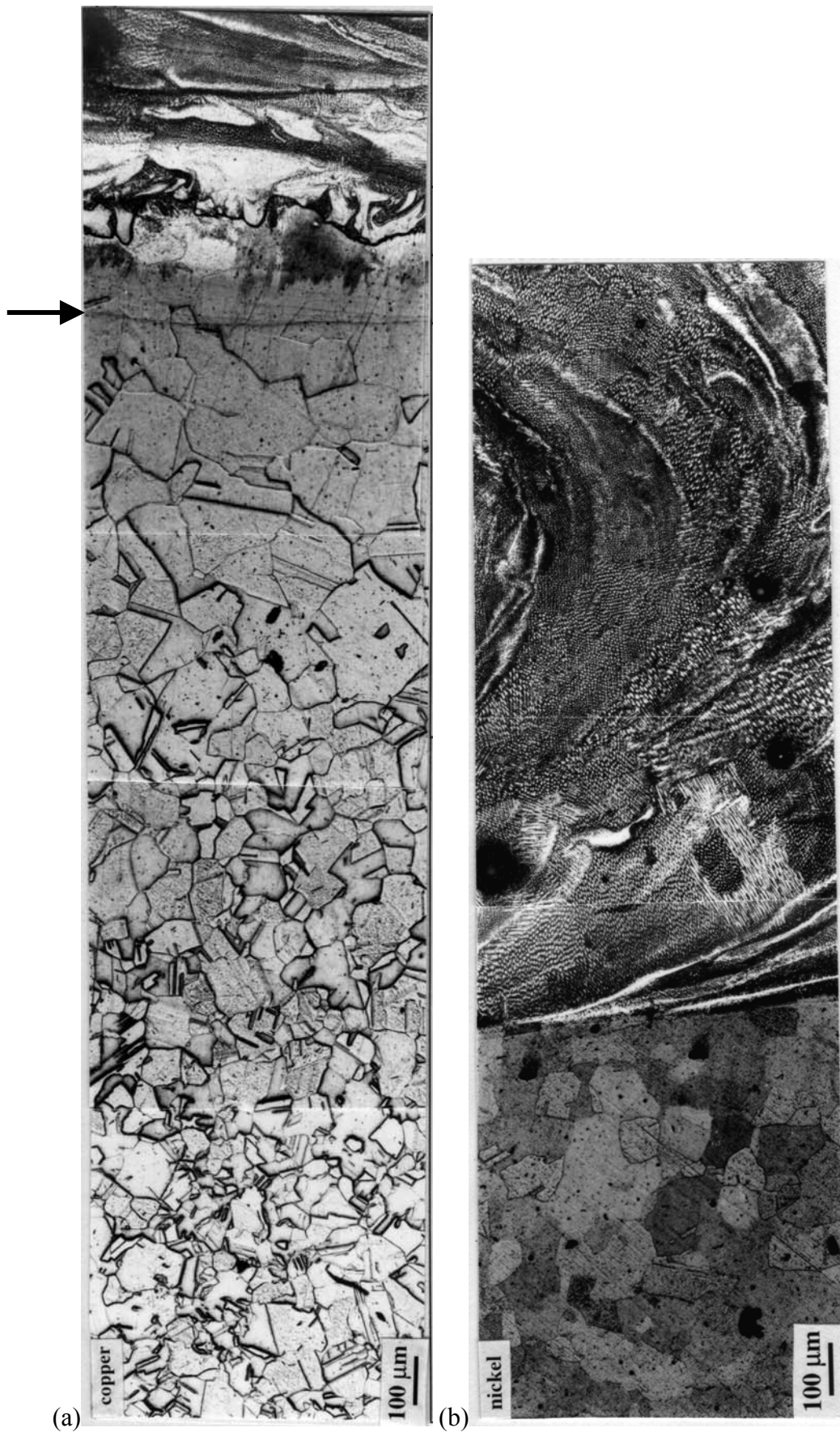
Figure 4.9 Microstructure on the top view (a) copper side (b) nickel side of the weld at a laser power of 5.5 kW and scan speed of 21 mm/s.

(a)

(b)

(c)
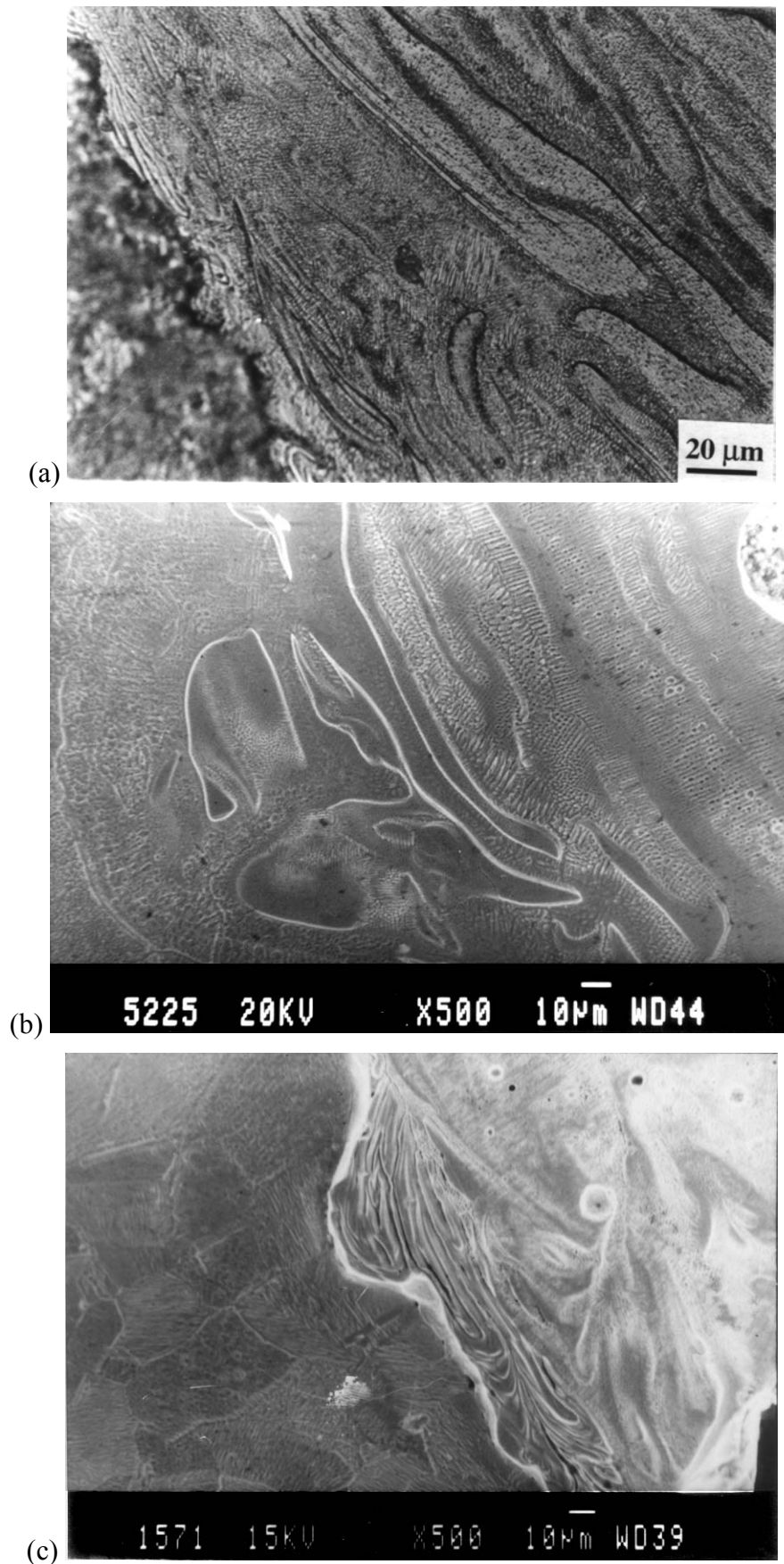
Figure 4.10 Microstructures of the copper side interface of Cu-Ni weld at (a) 5.5 kW, 42mm/s. (b &c) 3.5 kW, 4 mm/s

(d)

(e)
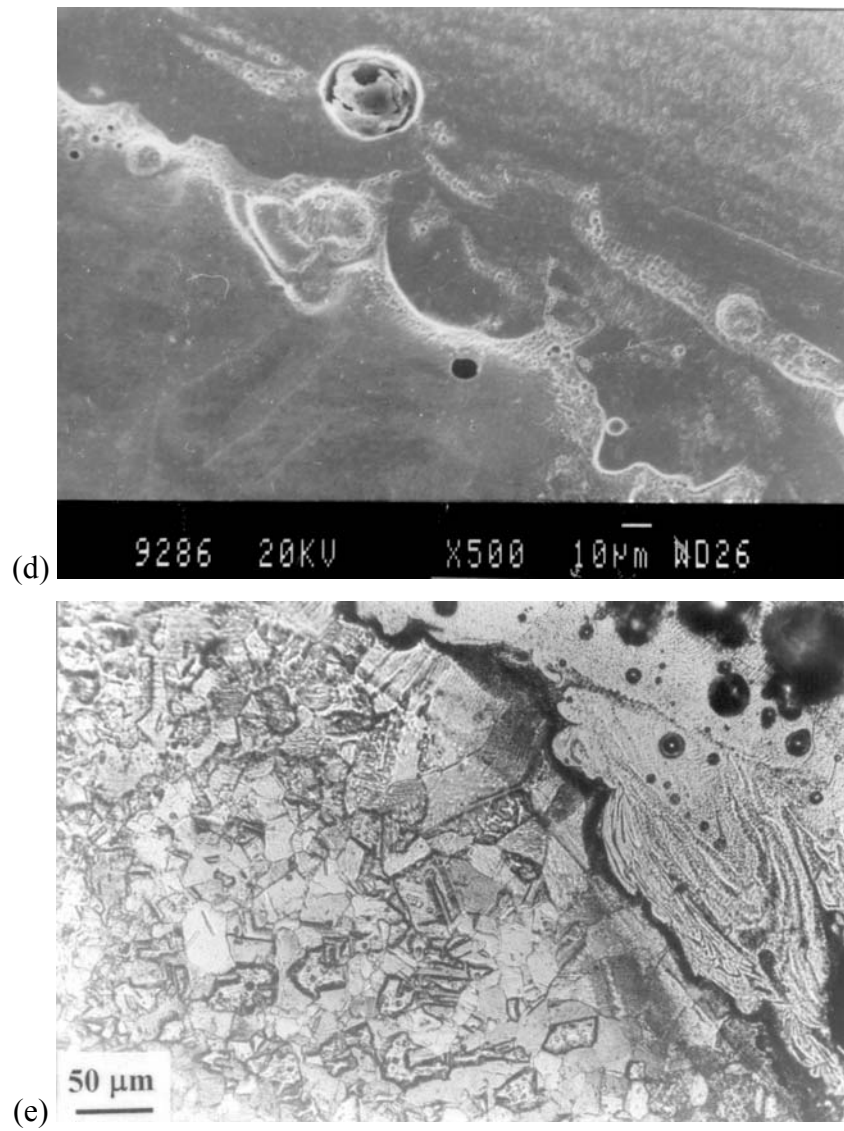
Figure 4.10 (contd.) Microstructures of the copper side interface of Cu-Ni weld at 4.5 kW, (d) 8 mm/s and (e) 12 mm/s.

(a)

(c)

(b)

(d)
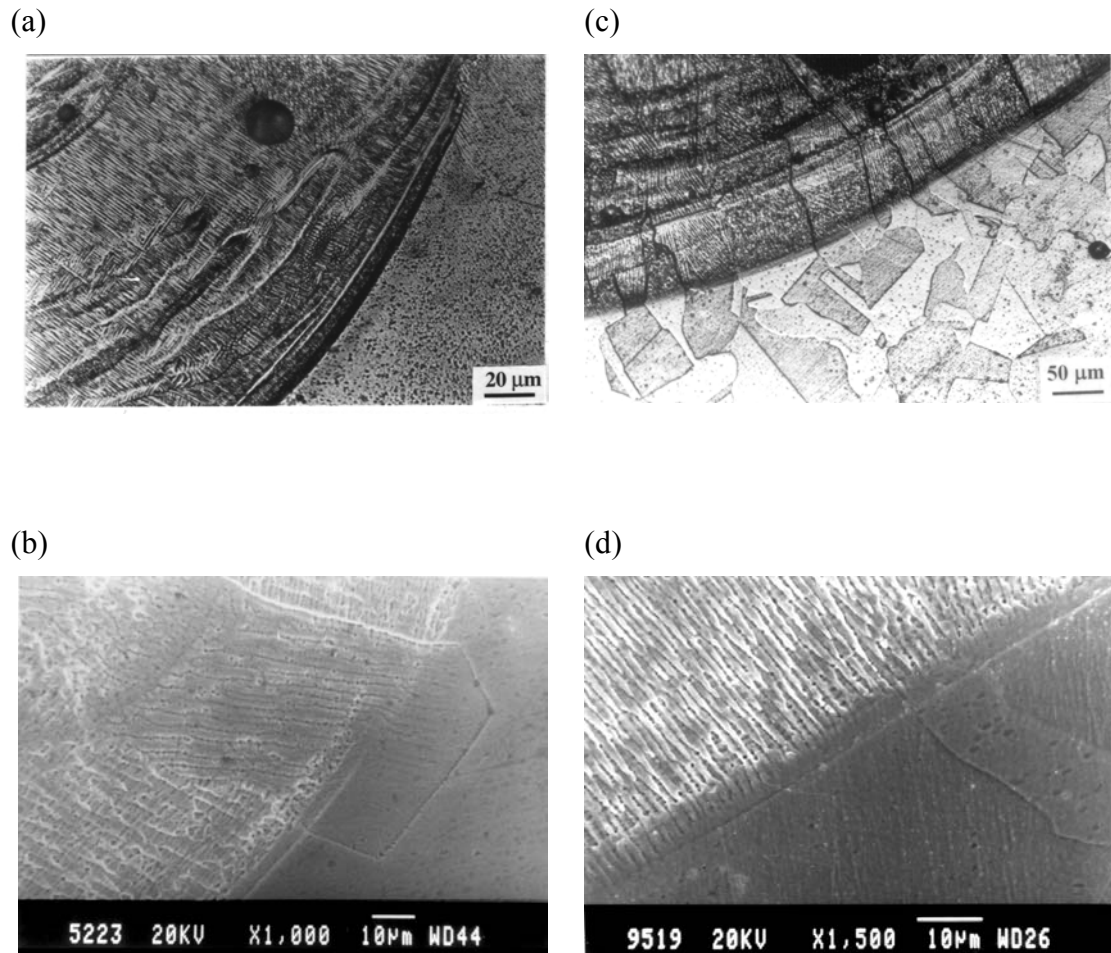
Figure 4.11 Microstructures of the nickel side interface of Cu-Ni weld at (a) 5.5 kW, 42mm/s. (b) 4.5 kW, 4 mm/s (c) 4.5 kW, 8 mm/s and (d) 4.5 kW, 12 mm/s.
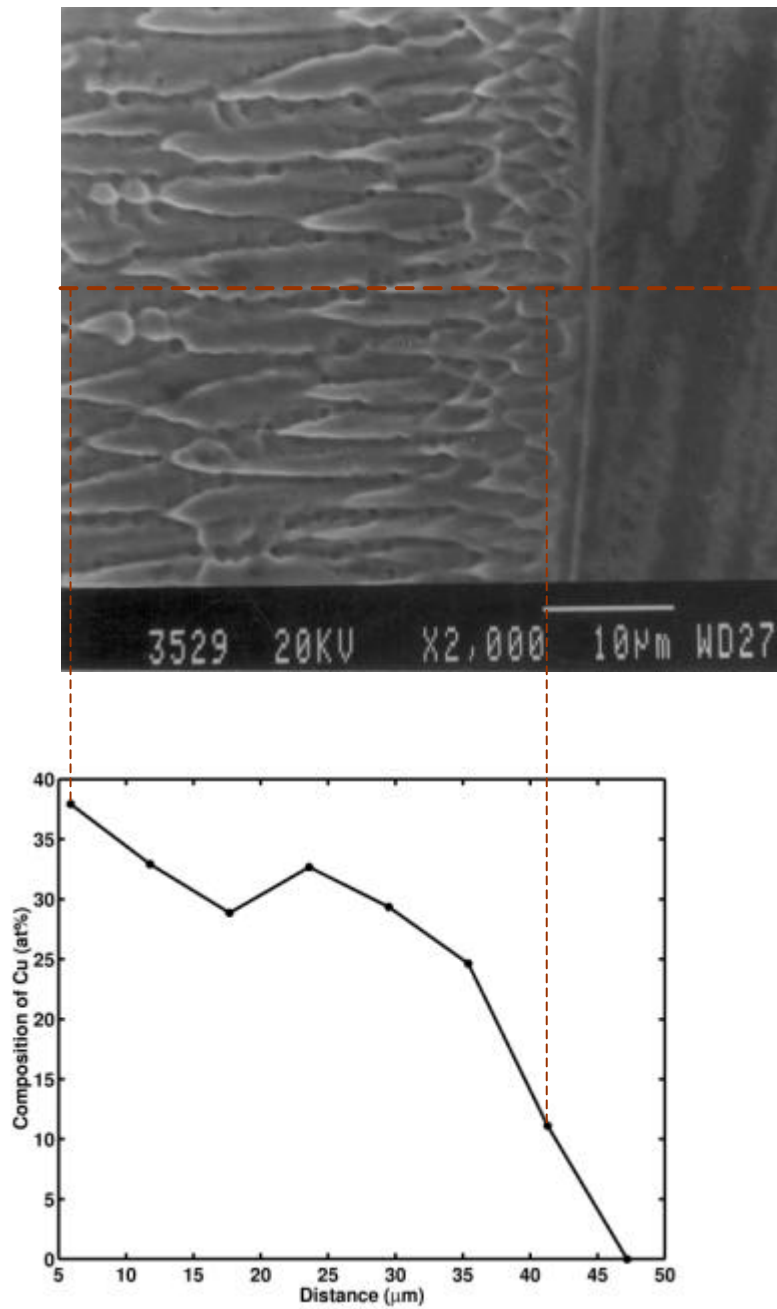
(a)

Figure 4.12 Composition variation from the nickel interface in to the weld for laser power of 5.5 kW and scan speed of (a) 42 mm/s.
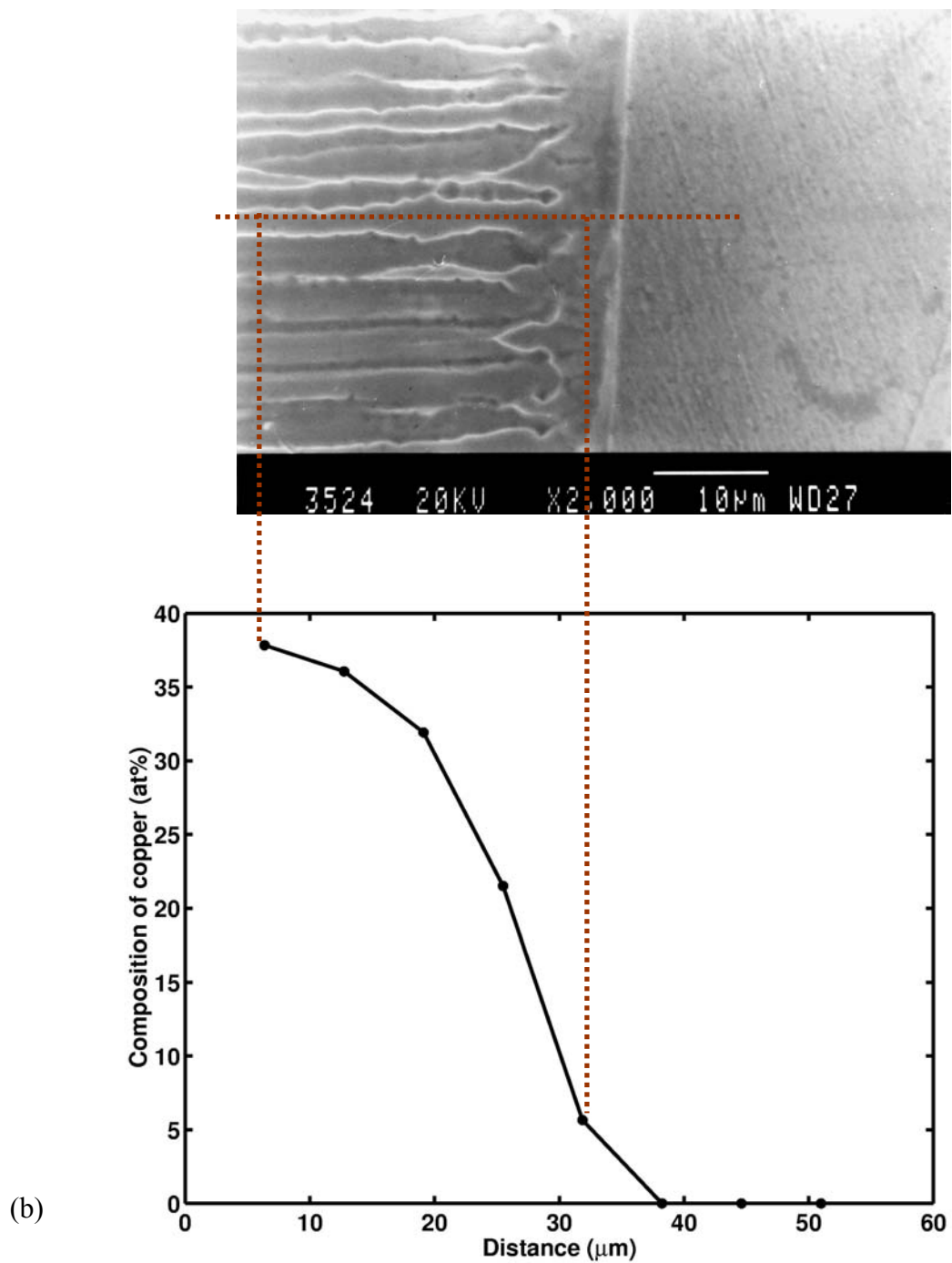
Figure 4.12 (contd.) Composition variation from the nickel interface in to the weld for laser power of 5.5 kW and scan speed of (b) 10.6 mm/s.
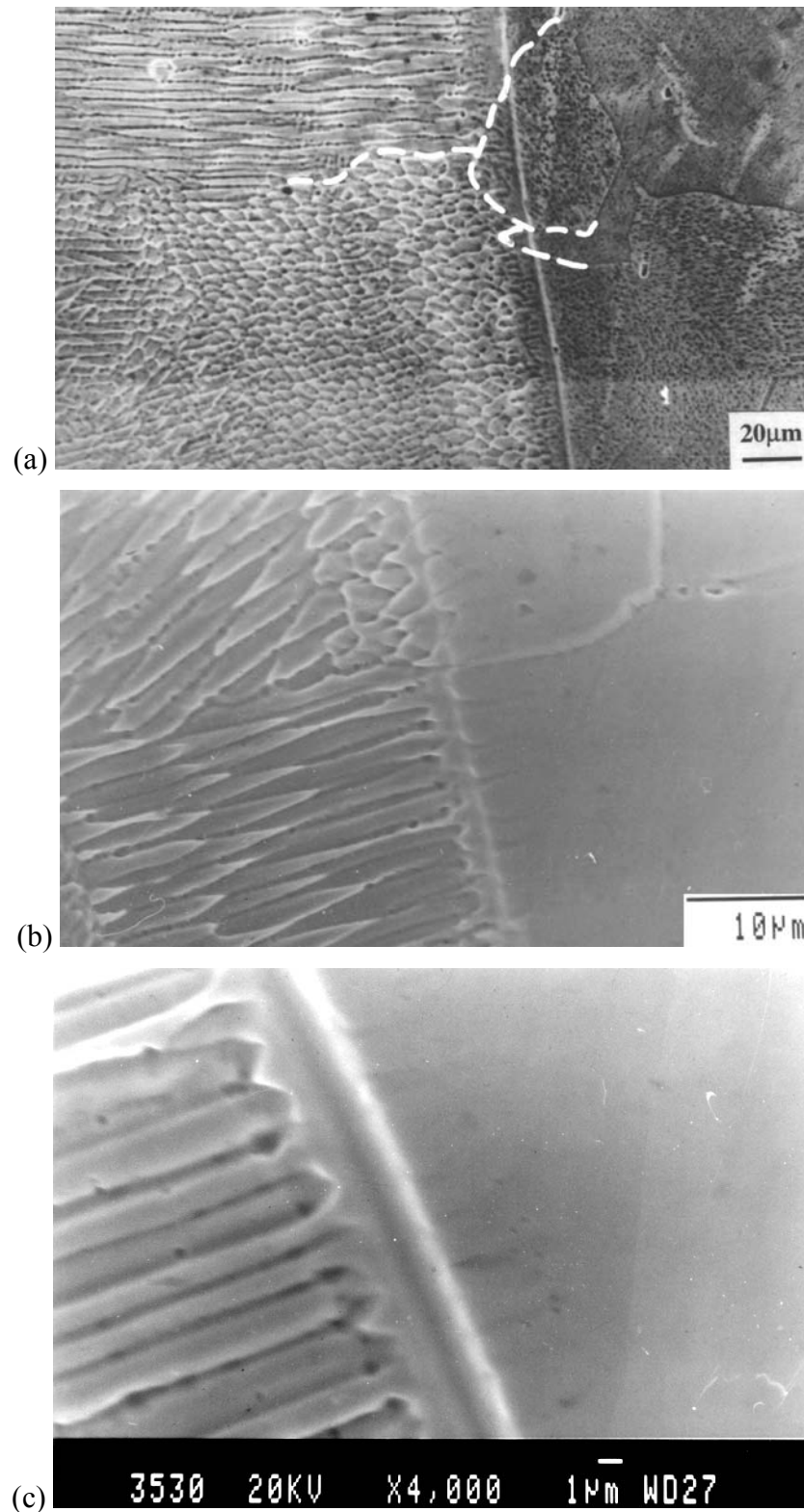
Figure 4.13 Interface microstructures on the nickel side of Cu-Ni weld showing transition from planar to cellular growth mode. The laser power is 5.5 kW and scan speeds used are (a) 21 mm/s and (b&c) 42 mm/s. The white line in (a) shows possible extent of growth from each grain on the nickel side.
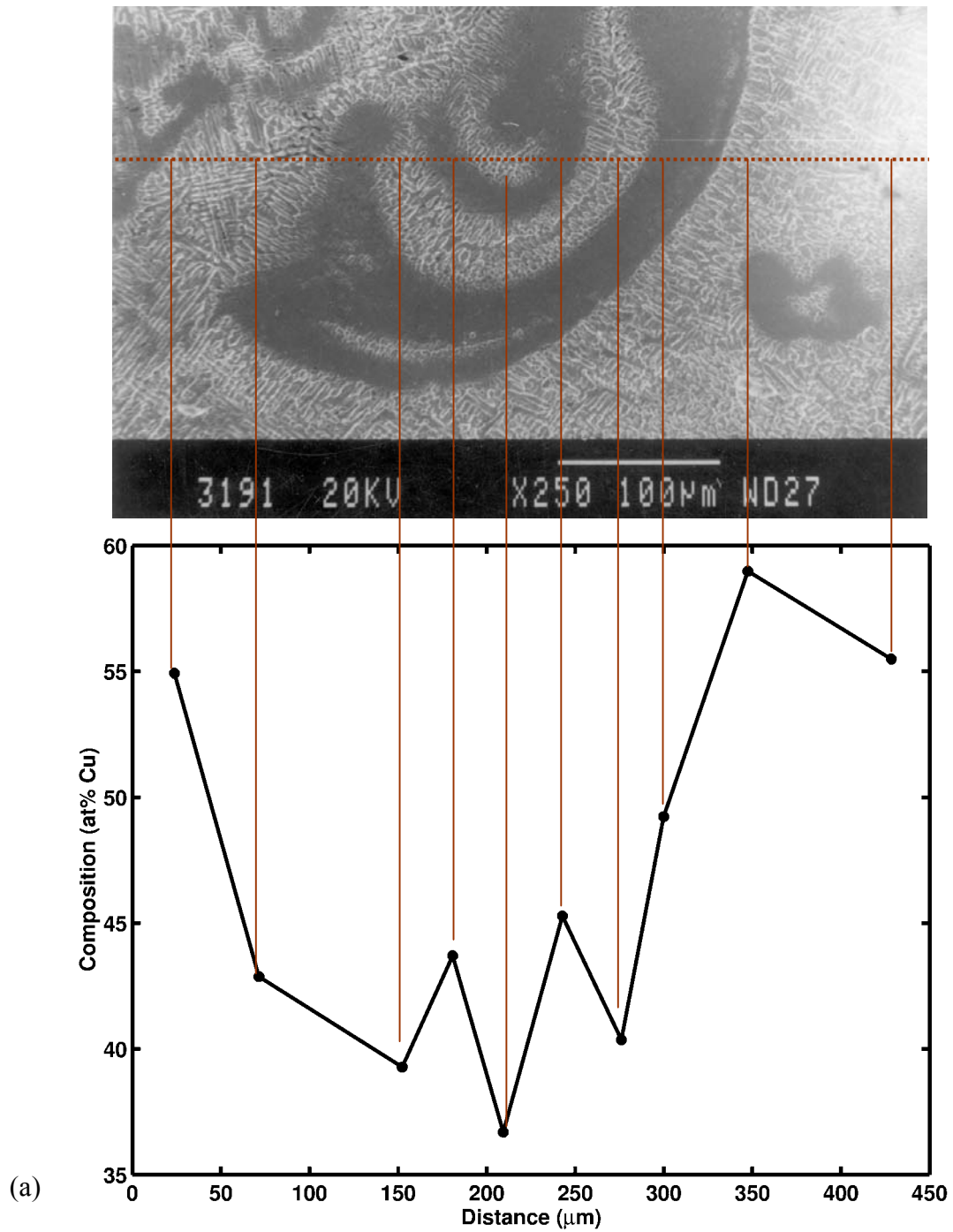
Figure 4.14 Microstructural banding in the Cu-Ni weld at a laser power of 5.5 kW and (a) 10.6 mm/s, at the center of the weld.
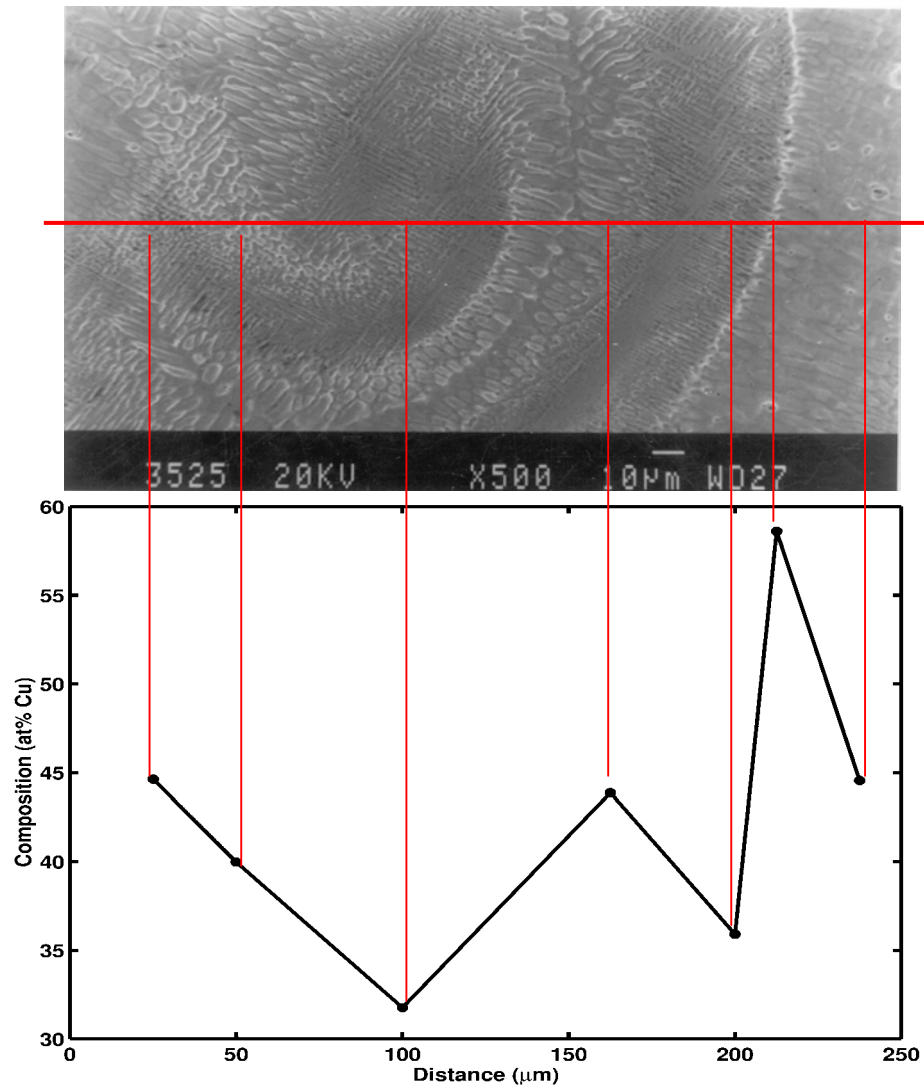
(b)

Figure 4.14 (contd.) Microstructural banding in the centre of the weld Cu-Ni weld done at power of 5.5 kW, (b) 10.6 mm/s within the weld.

(a)

(b)
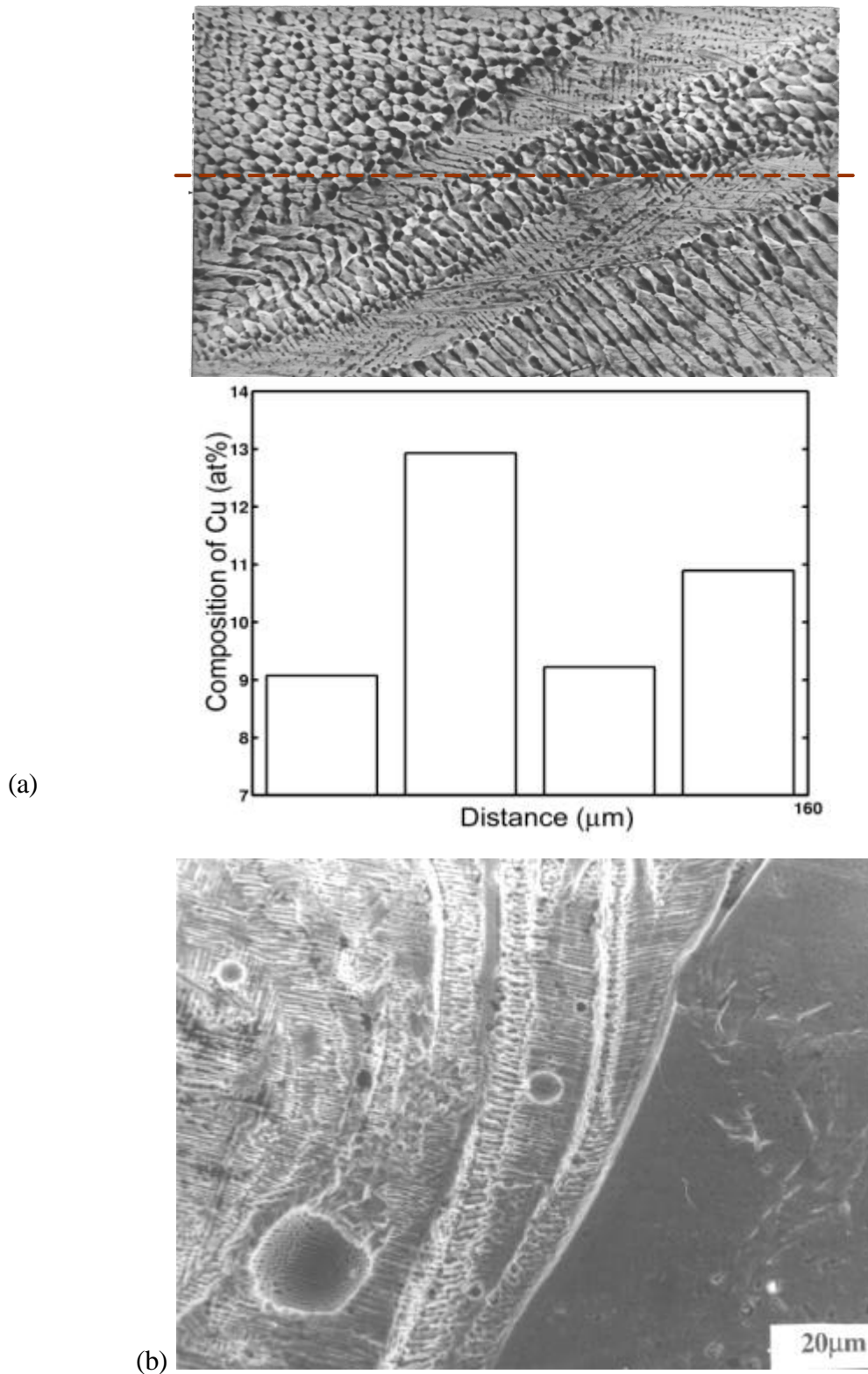
Figure 4.15 Microstructural banding in the Cu-Ni weld at a laser power of 5.5 kW (a) 21 mm/s within the weld and (b) 84 mm/s, ahead of the nickel interface near the top.

(a)

(b)

(c)
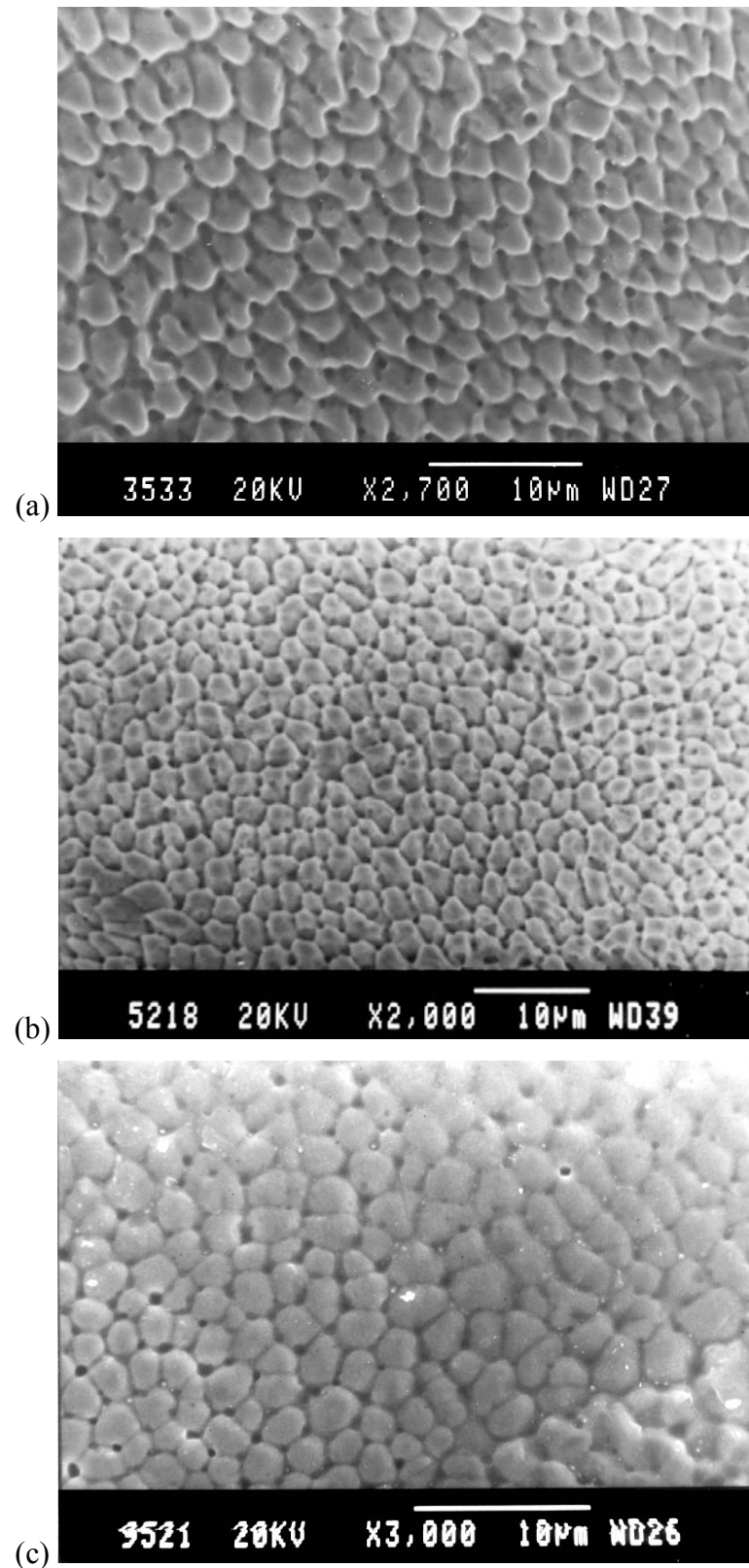
Figure 4.16 Cellular microstructures observed through out the weld regions for laser power and scan speeds of (a) 5.5 kW, 42 mm/s and (b) 4.5 kW, 12 mm/s (c) 4.5 kW, 12 mm/s. near the top of the weld.

(a)

(b)
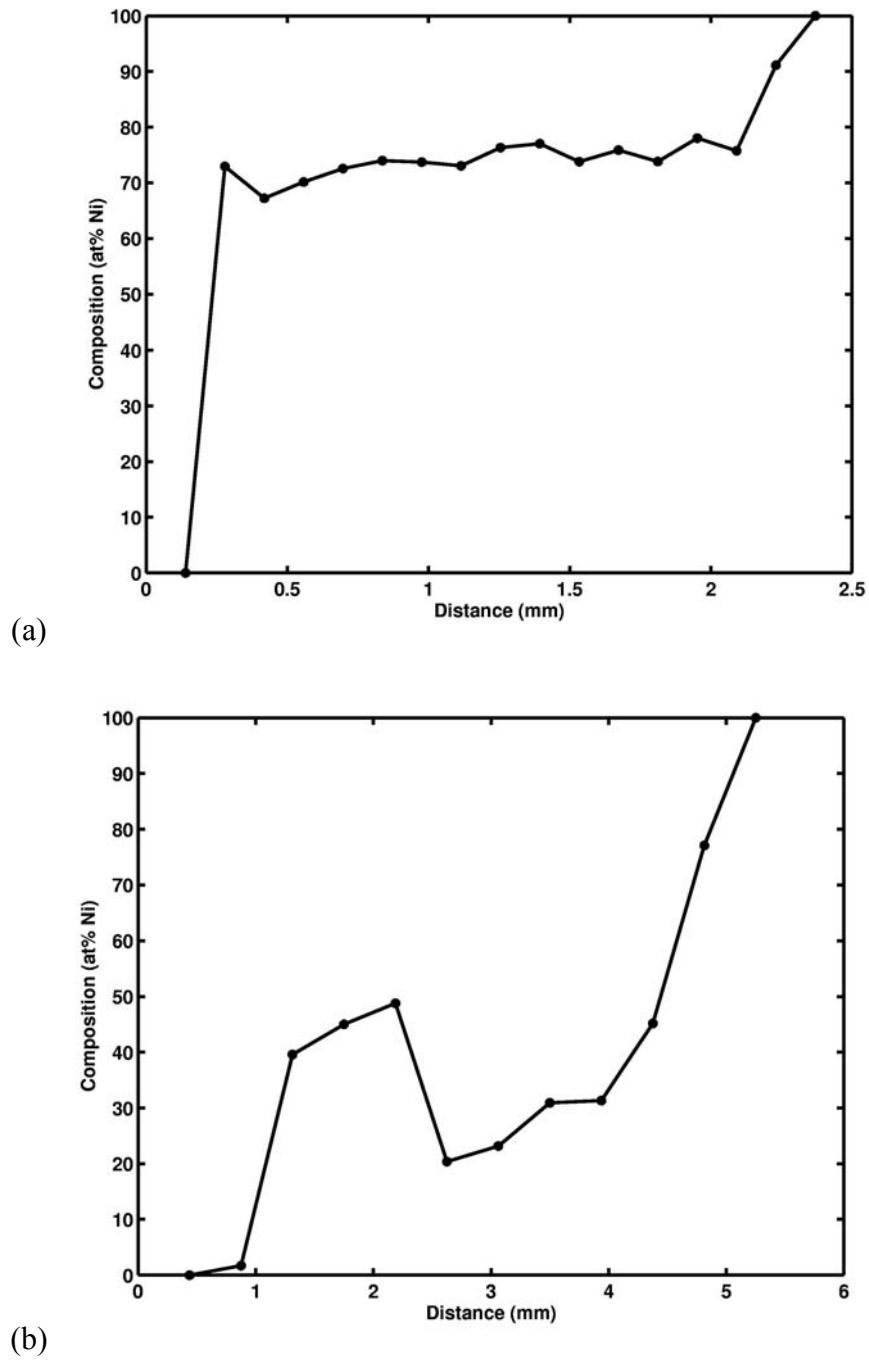
Figure 4.17 Composition across the weld from copper side on the left to nickel side on the right for welds of (a) 4.5 kW, defocussed beam, 12 mm/s and (b) 5.5 kW, focussed beam, 10.6 mm/s.

(a)

(b)
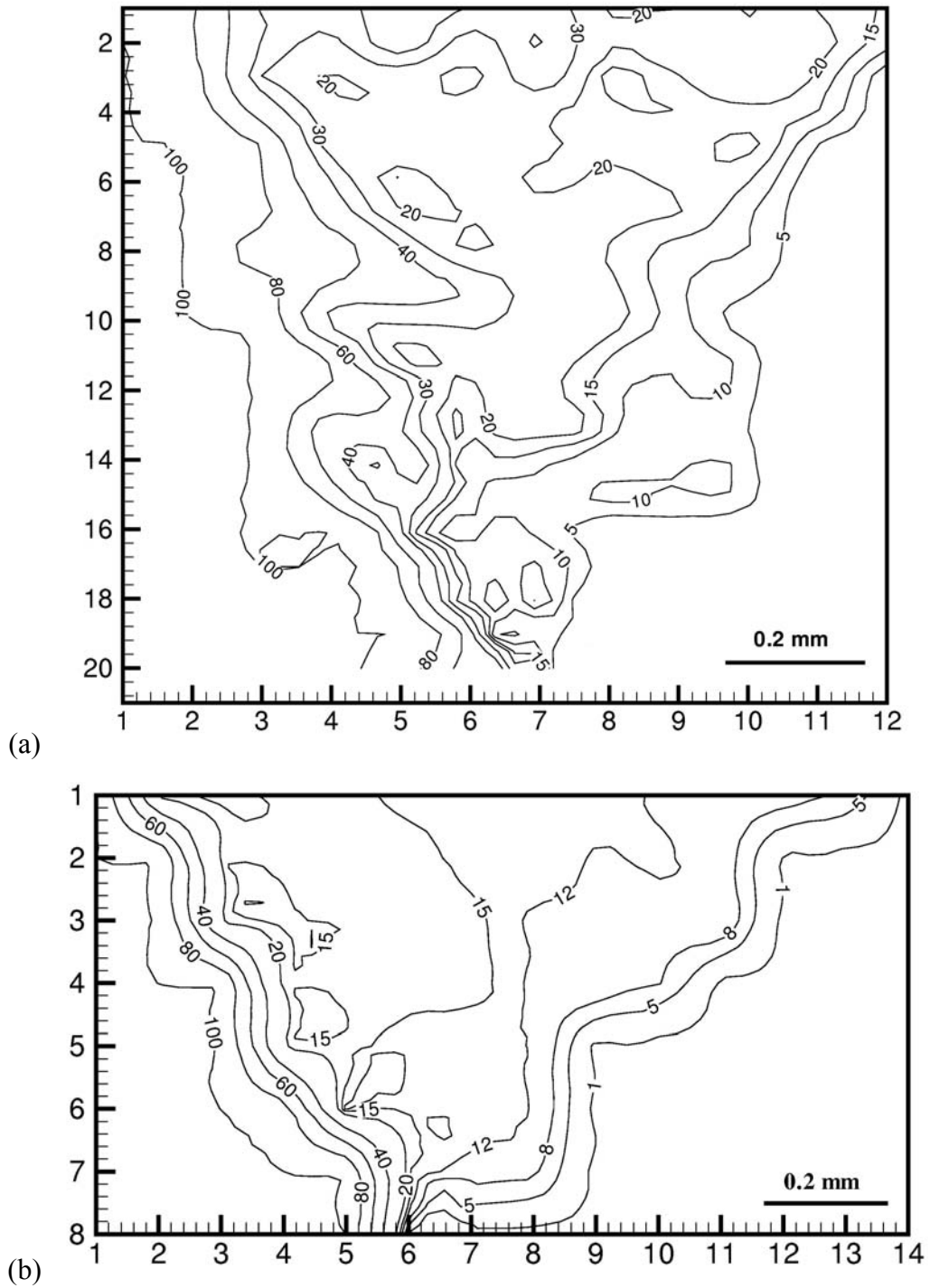
Figure 4.18 Composition map in the whole of weld pool with copper on the left and nickel on the right for welds of (a) 5.5 kW, 84 mm/s and (b) 4.5 kW, 8 mm/s. The contour levels shown are in at% Cu.

(a)

(c)

(b)
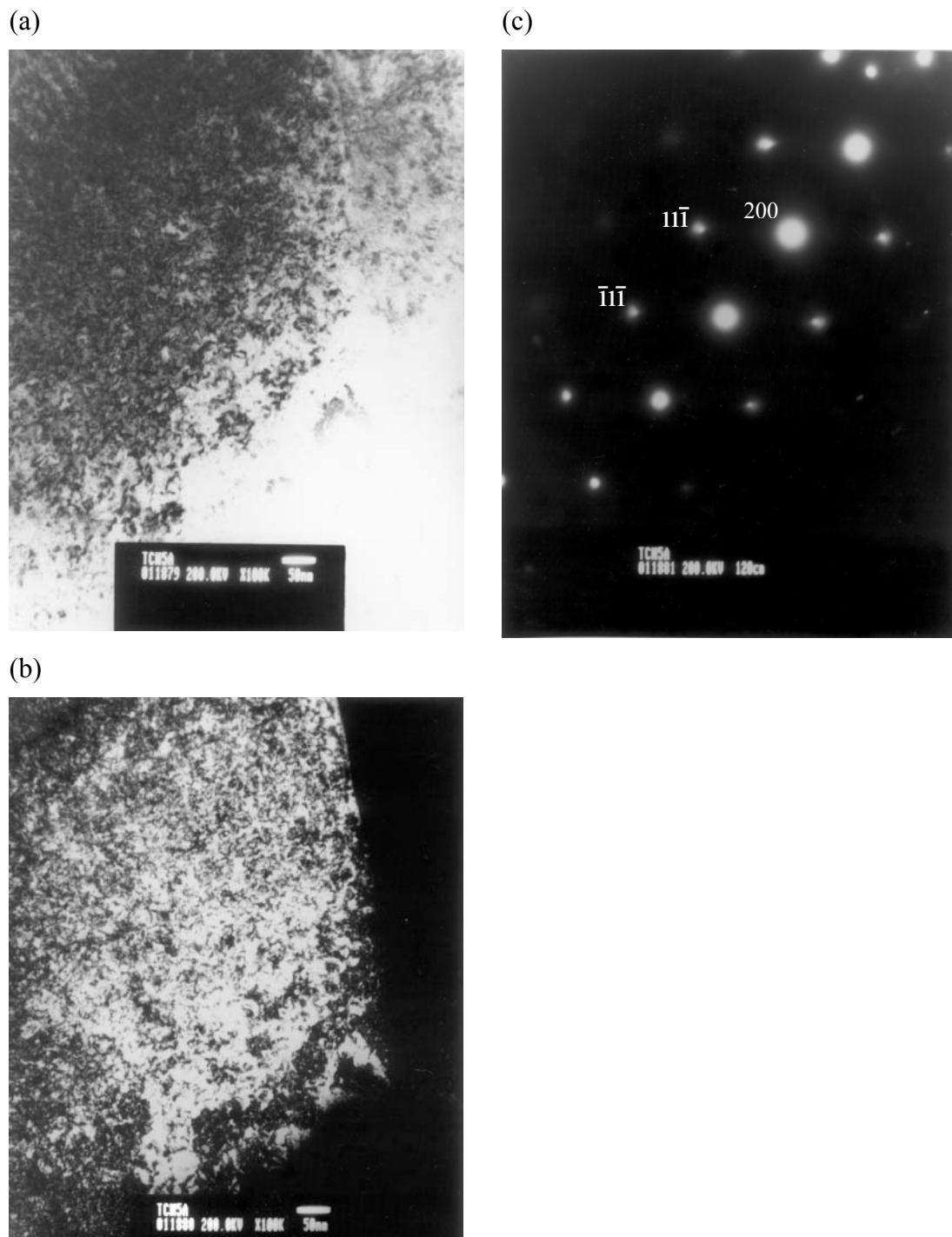
Figure 4.19 Transmission electron microscopy of Cu-Ni weld at 4.5 kW, 16 mm/s. (a) Bright field in [011] zone and (b) Dark field (from 200 reflection) images showing strain contrast. The corresponding diffraction pattern is shown in (c).

(a)

(c)

(b)

(d)
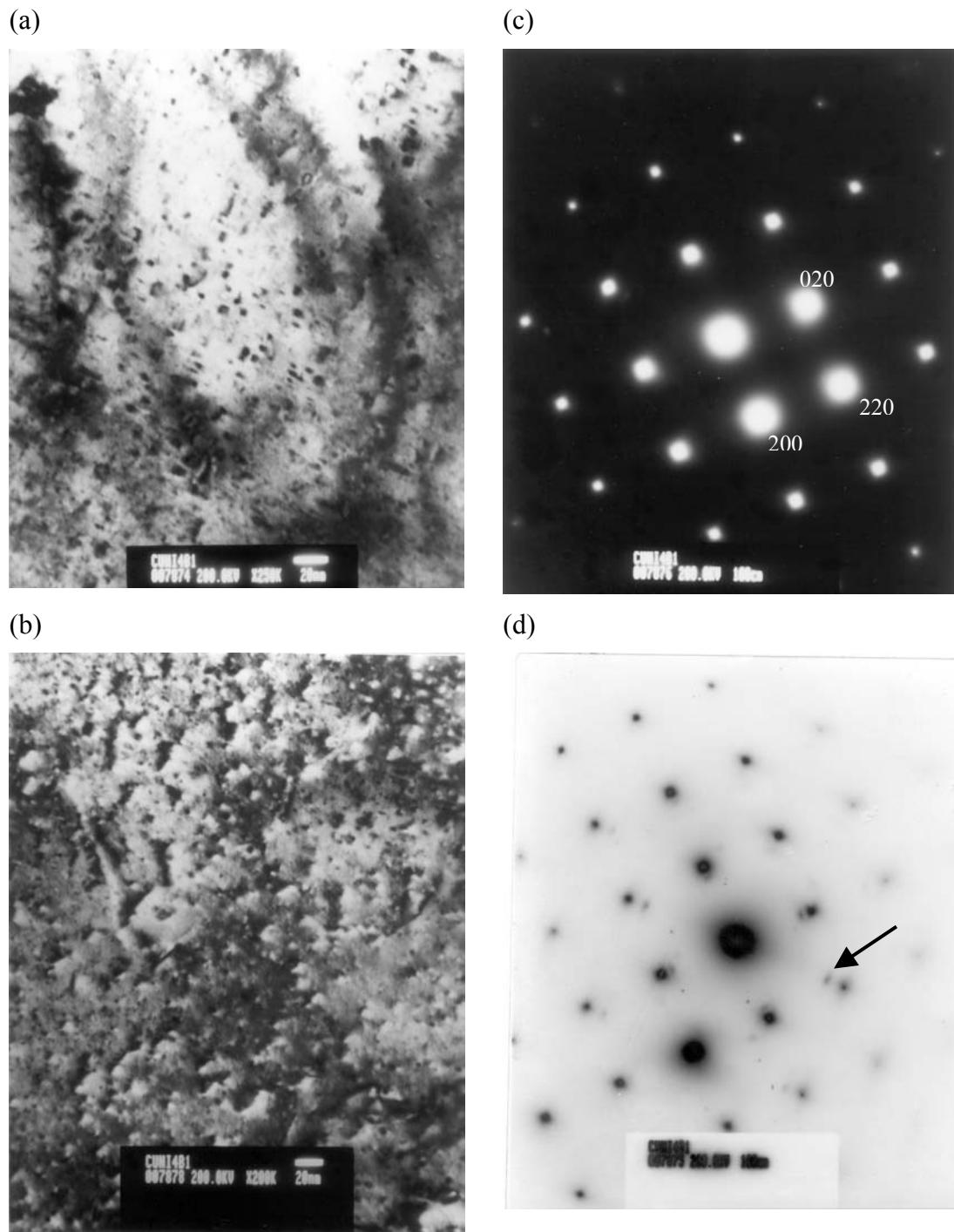
Figure 4.20 Transmission electron microscopy of Cu-Ni weld at 5.5 kW, 16 mm/s.
(a) shows bright field image taken in [001] zone. (b) Dark field taken from (200)
reflection. The Corresponding diffraction pattern is shown in (c). (d) SADP taken from
the region in (a). The arrow points towards extra spots.

(a)

(b)
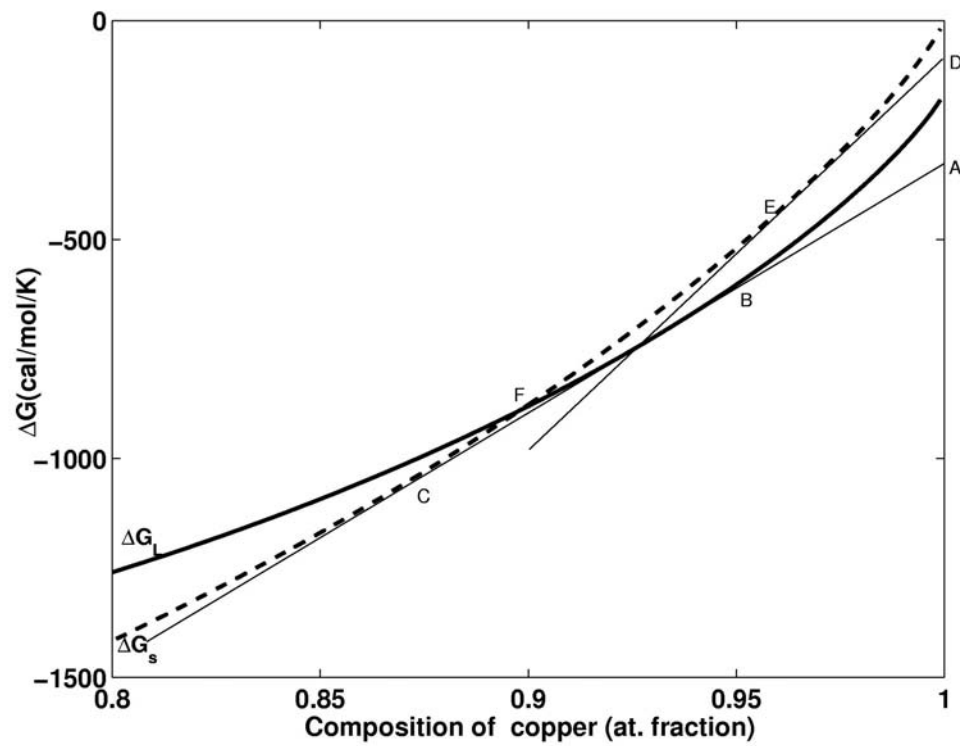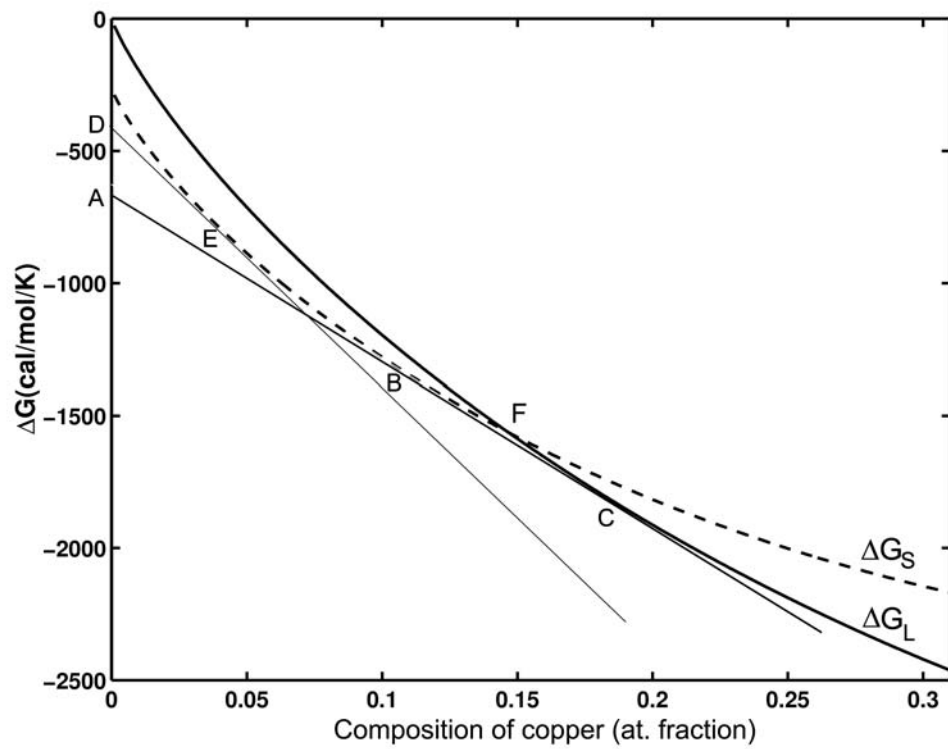
Figure 4.21 Free energy vs. composition plots for (a) T=1400 $^\circ$C shown on nickel rich side and (b) T=1140 $^\circ$C shown on copper rich side.
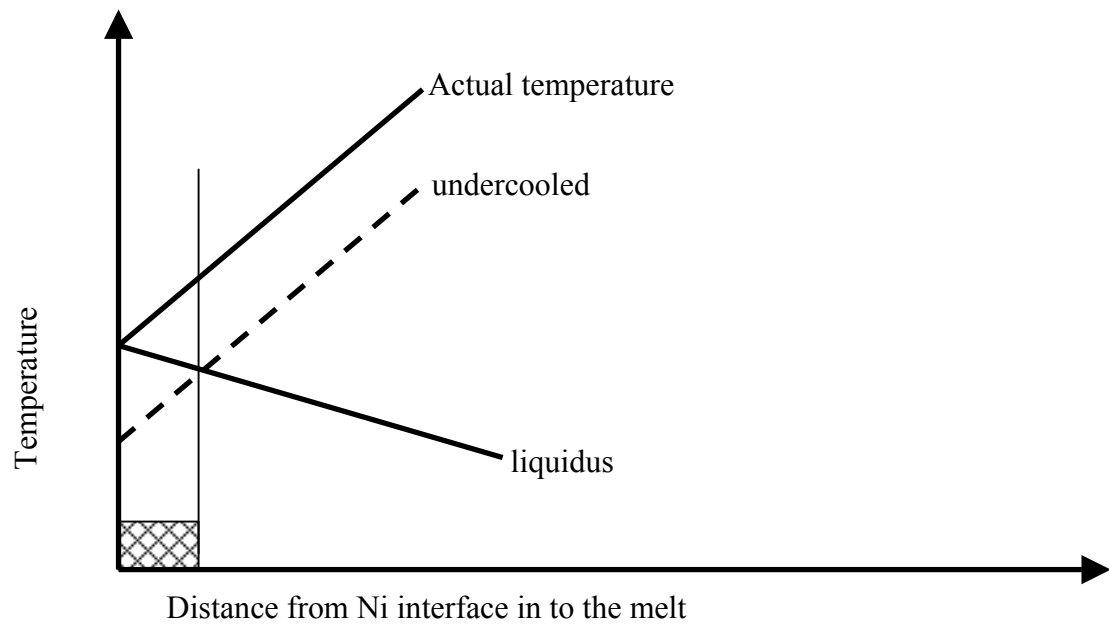
Figure 4.21 (contd.) (c) Schematic showing possibility of undercooled region (shaded) ahead of nickel interface.
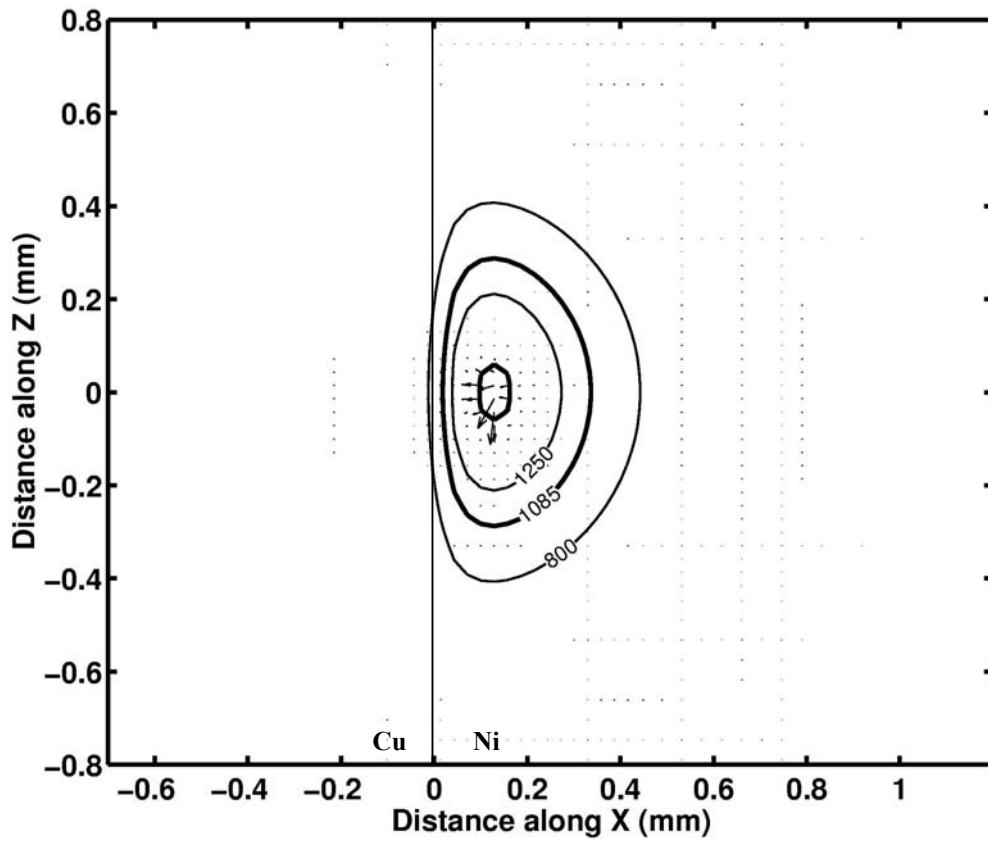
(a)
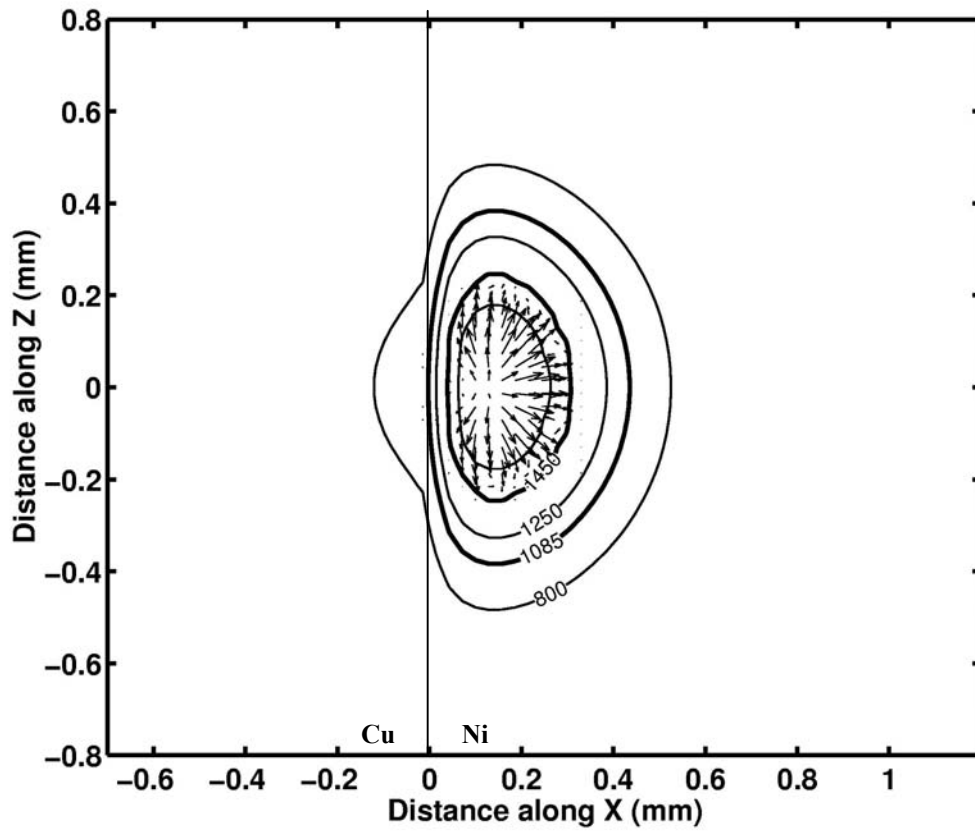
(b)

Figure 4.22 Temperature contours and velocity profile of the top view of weld pool after (a) 1 ms and (b) 1.8 ms. Values shown on the contours are in ^{o}C and the bold contours refer to the melting points of copper and nickel.
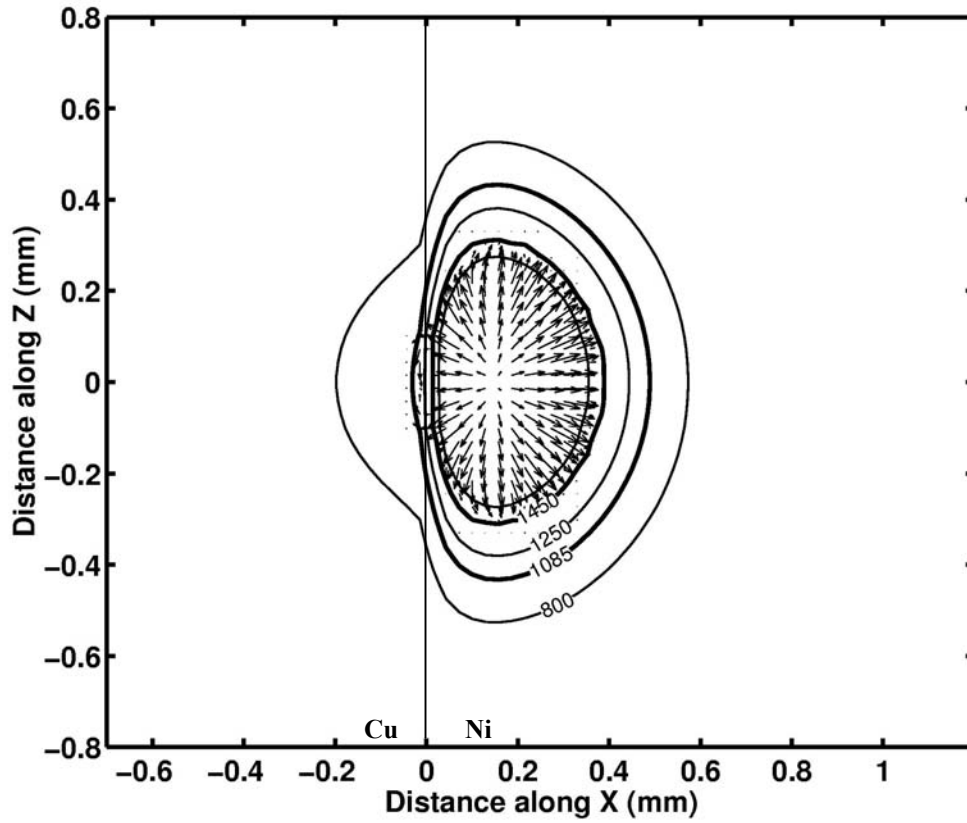
(c)
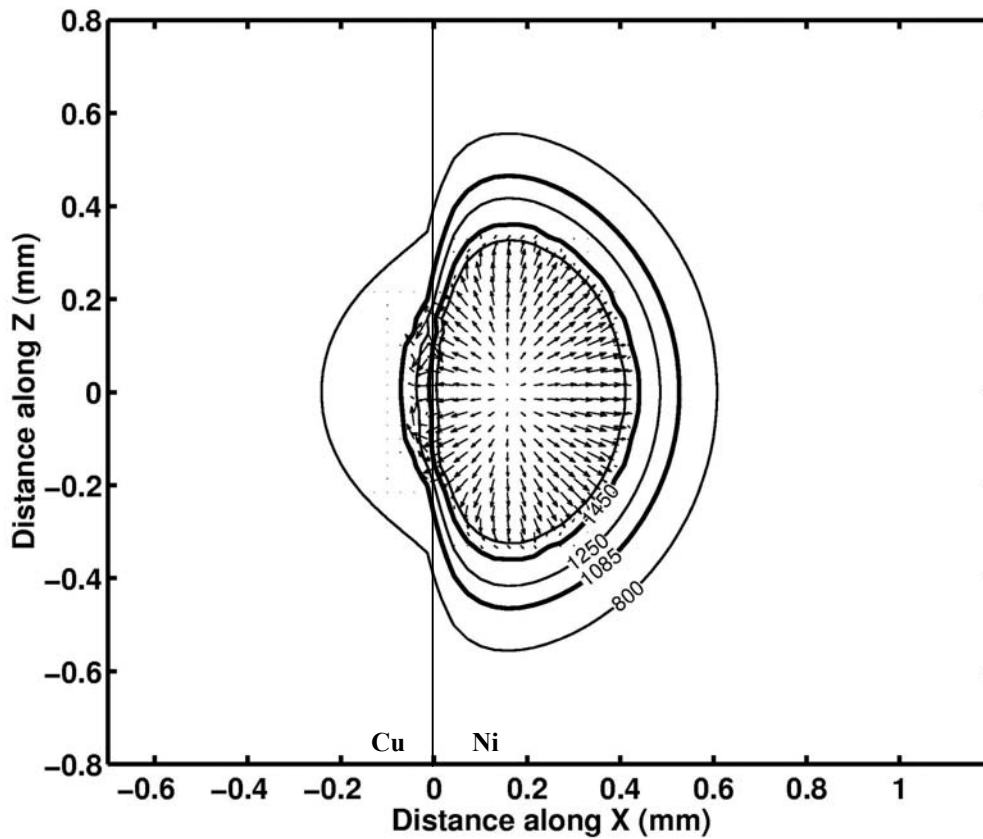
(d)

Figure 4.22 (contd.) Temperature contours and velocity profile of the top view of weld pool after (c) 2.6 ms and (d) 3.4 ms. Values shown on the contours are in ^{o}C and the bold contours refer to the melting points of copper and nickel.
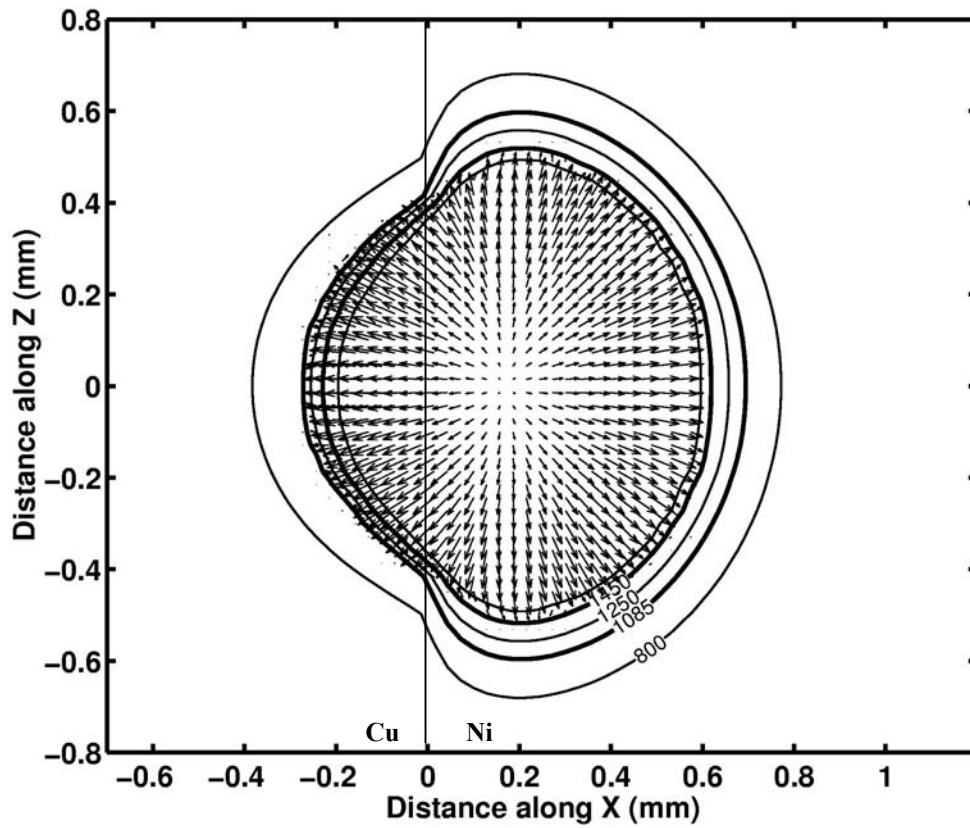
(e)
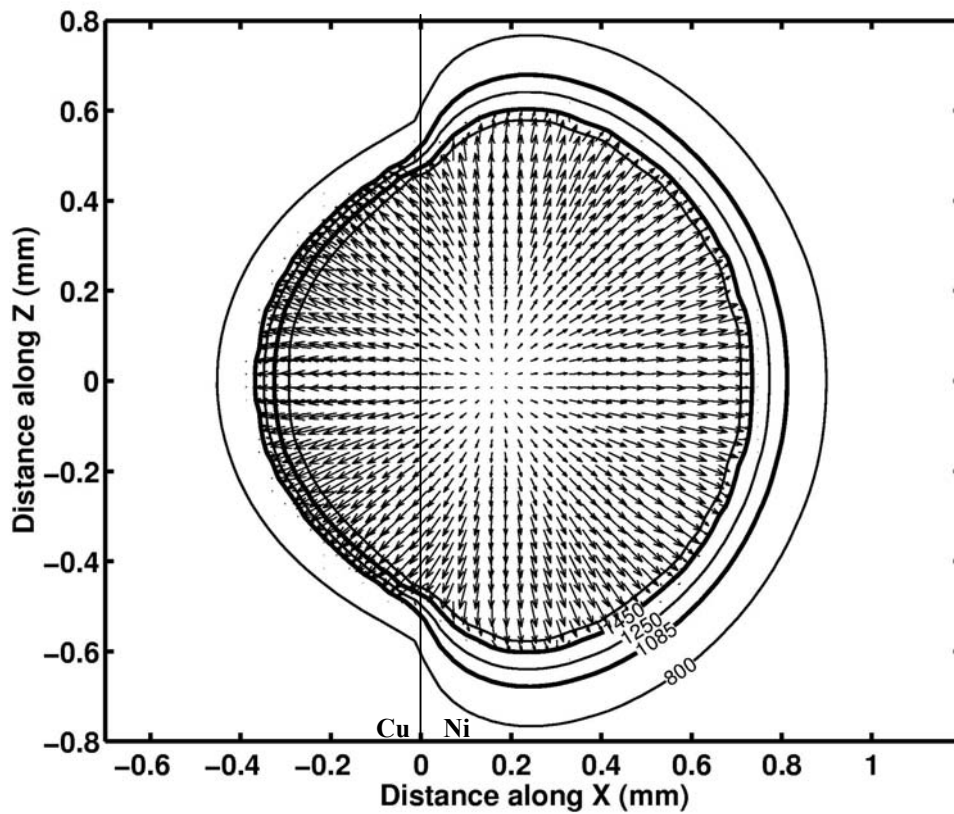
(f)

Figure 4.22 (contd.) Temperature contours and velocity profile of the top view of weld pool after (e) 11 ms and (f) 25 ms. Values shown on the contours are in ^{o}C and the bold contours refer to the melting points of copper and nickel.
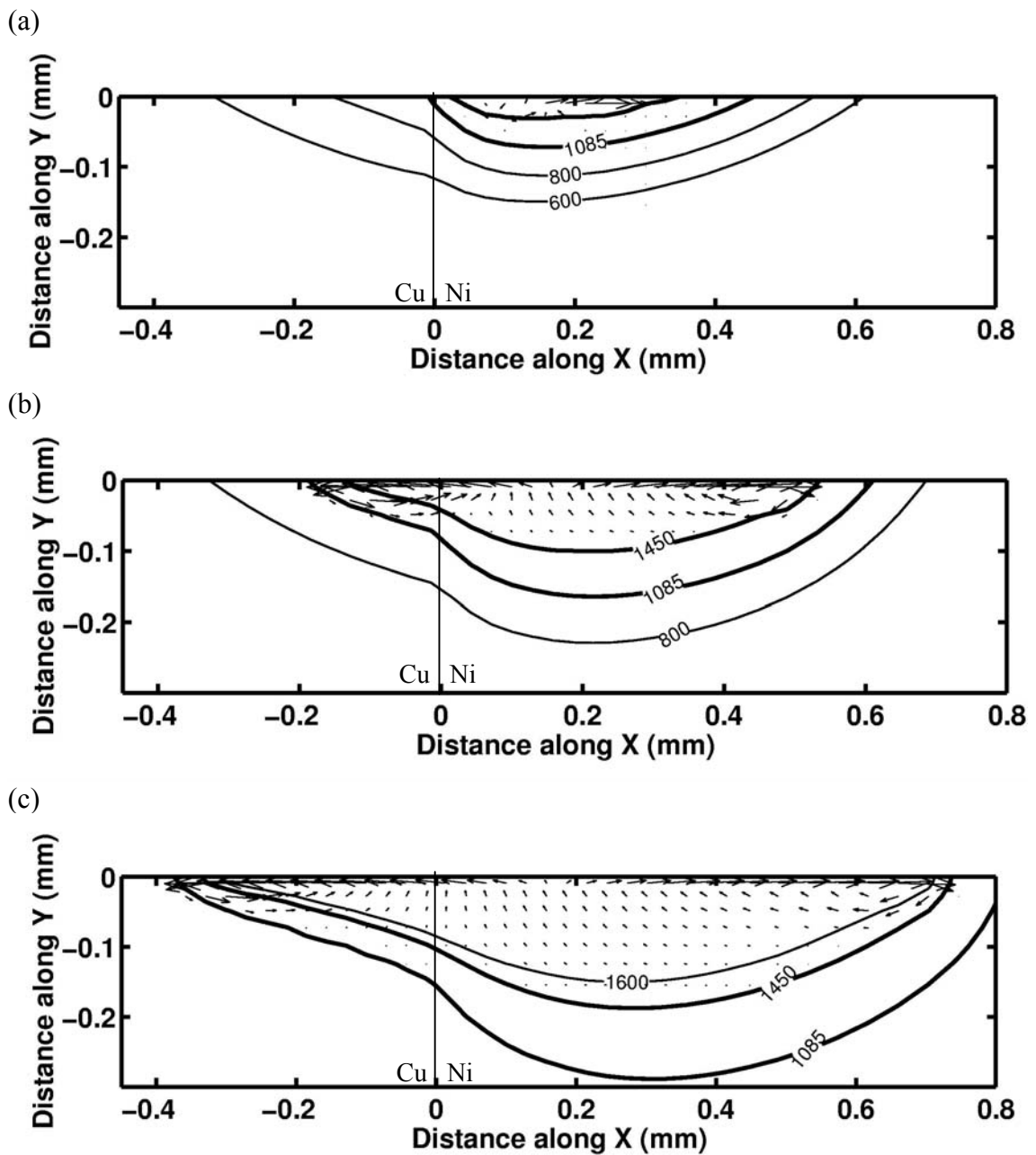
Figure 4.23 Contours of temperature and velocity profile of the cross section view of weld pool after (a) 3.4 ms, (b) 11 ms and (c) 25 ms. Values shown on the temperature contours are in ^{o}C.

(a)

(b)

(c)
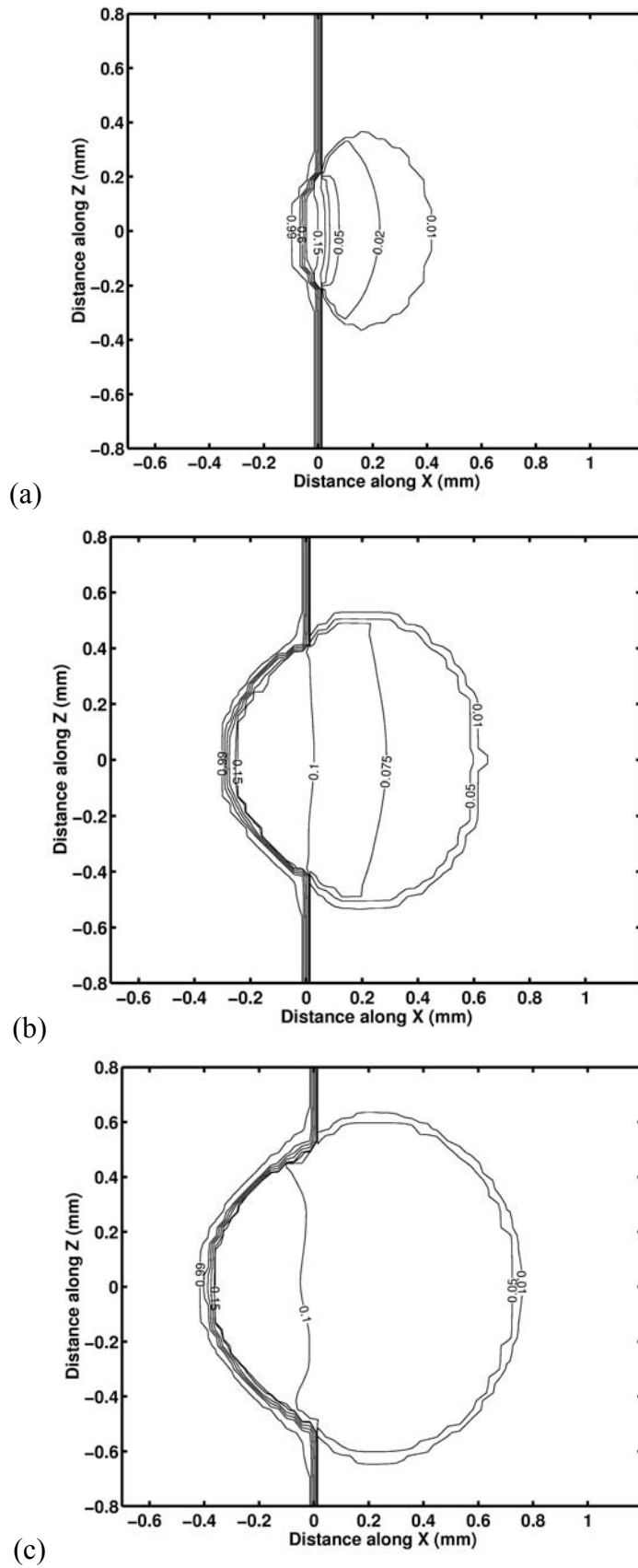
Figure 4.24 Composition contours and velocity profile of the top view of weld pool after (a) 3.4 ms, (b) 11 ms and (c) 25 ms. Values shown on the contours are wt% copper.
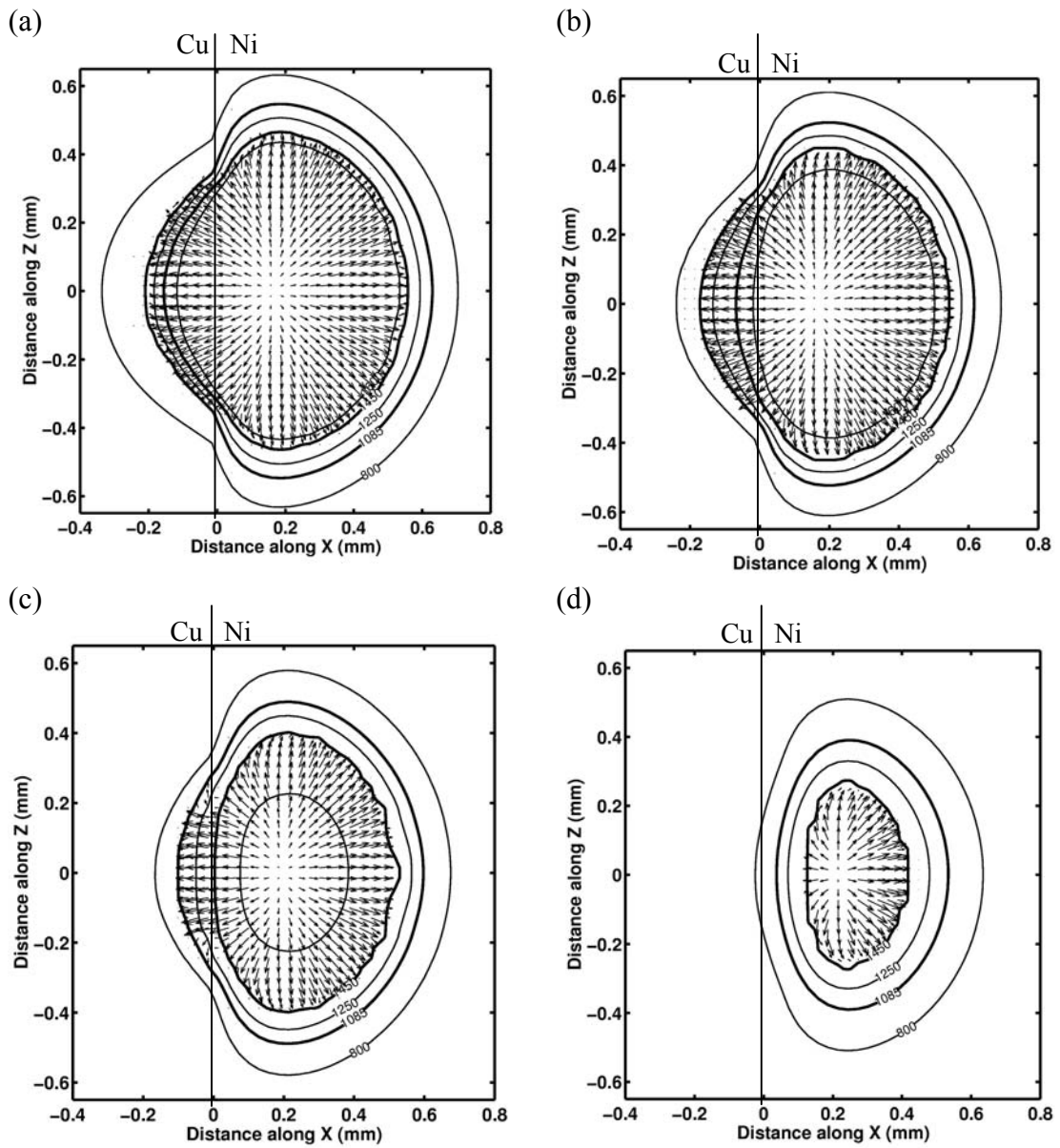
Figure 4.25 Temperature contours and velocity profile in the top view during the cooling cycle: (a) 0 ms (b) 0.3 ms (c) 0.5 and (d) 1.1 ms after the laser is switched off.

(a)

(b)

(c)

(d)
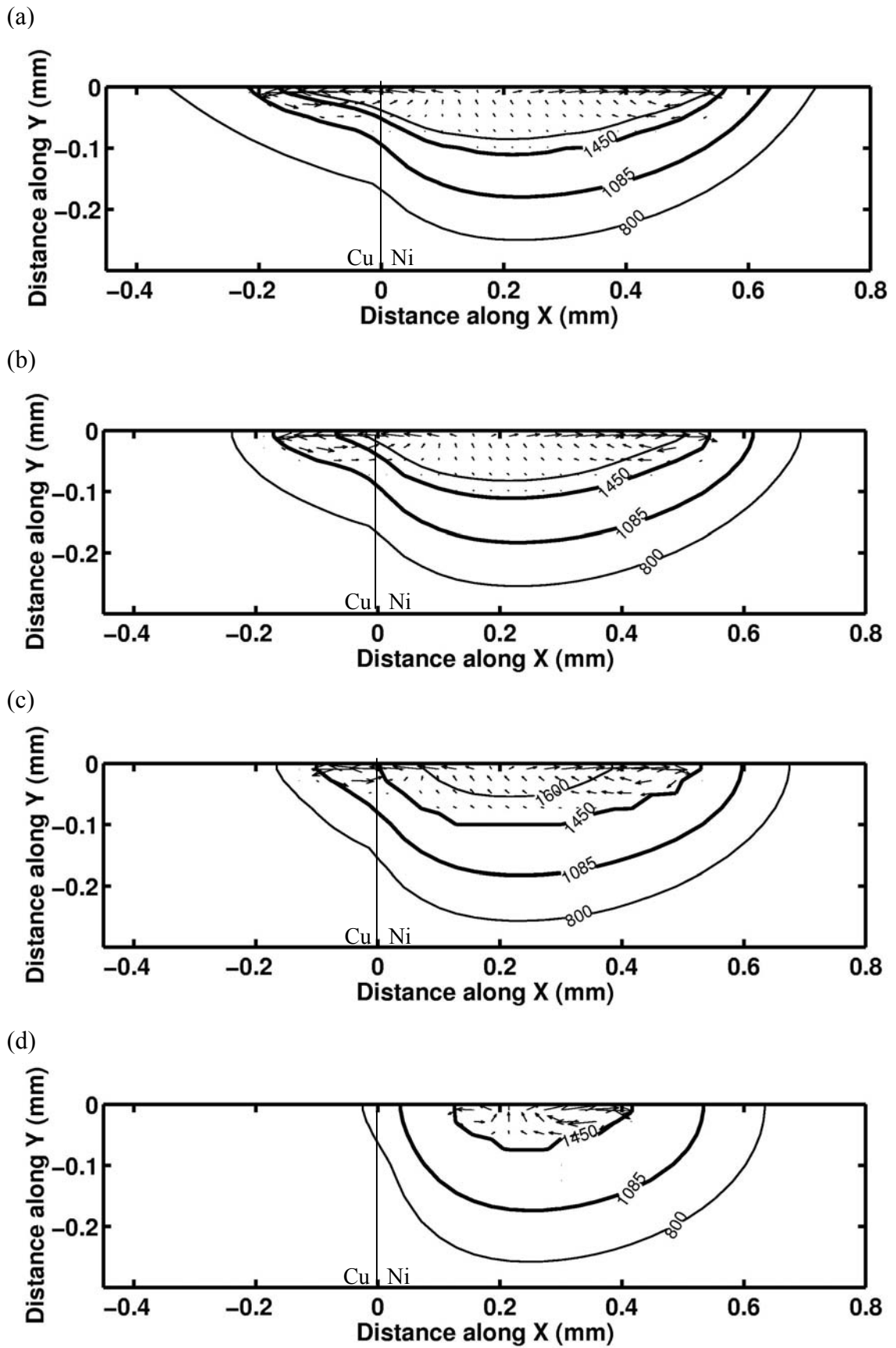
Figure 4.26 Temperature contours and velocity profile in the cross section view during the cooling cycle (a) 0 ms (b) 0.3 ms (c) 0.5 and (d) 1.1 ms after the laser is switched off.

(a)

(b)

(c)
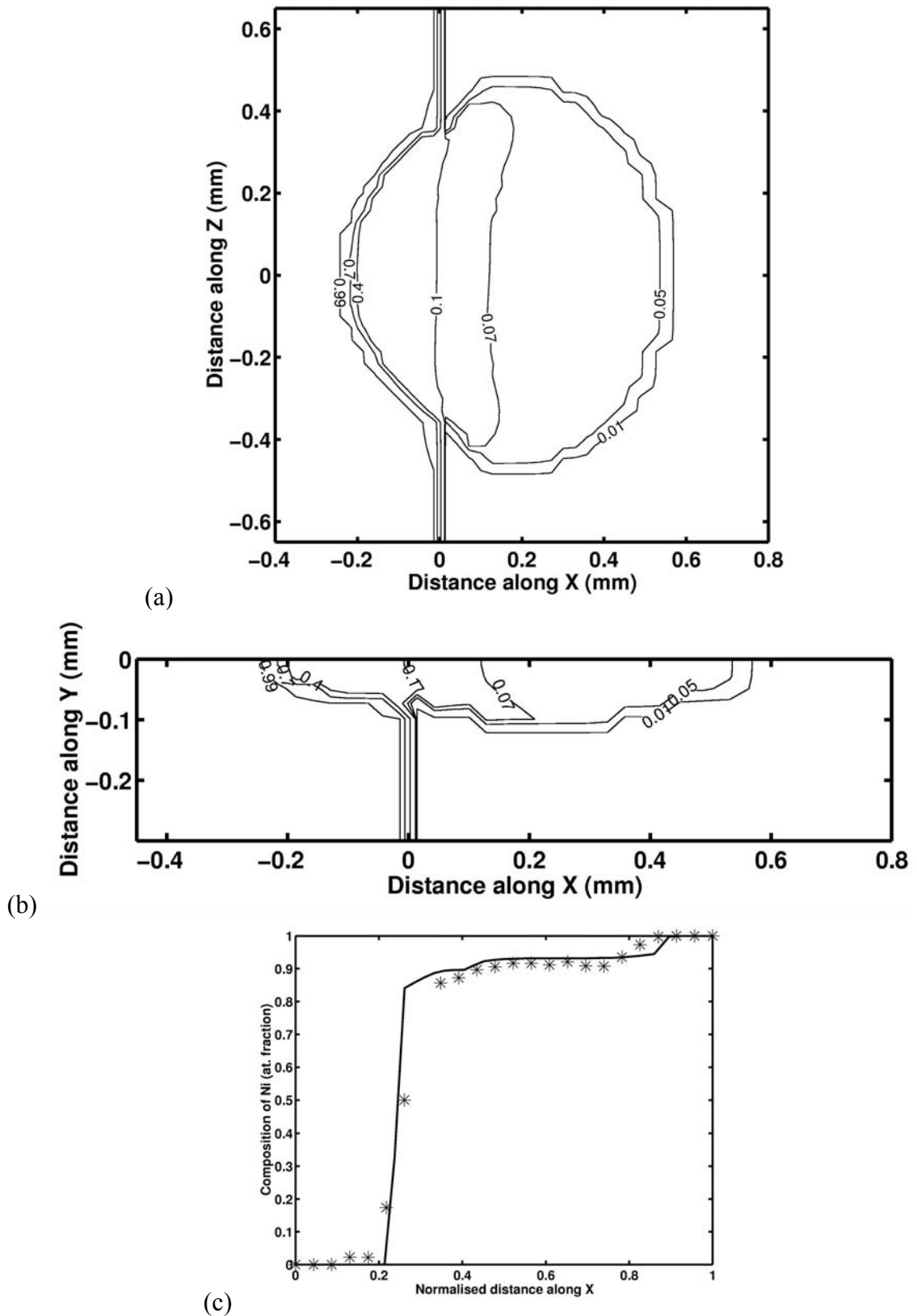
Figure 4.27 Composition contours of the solidified spot weld in (a) top view and (b) cross section view. The values on the contours are wt% Cu. (c) along a line across the weld near the top. The asterisks superimposed are the experimental compositions of nickel taken from figure 4.4(b).

(a)

(b)
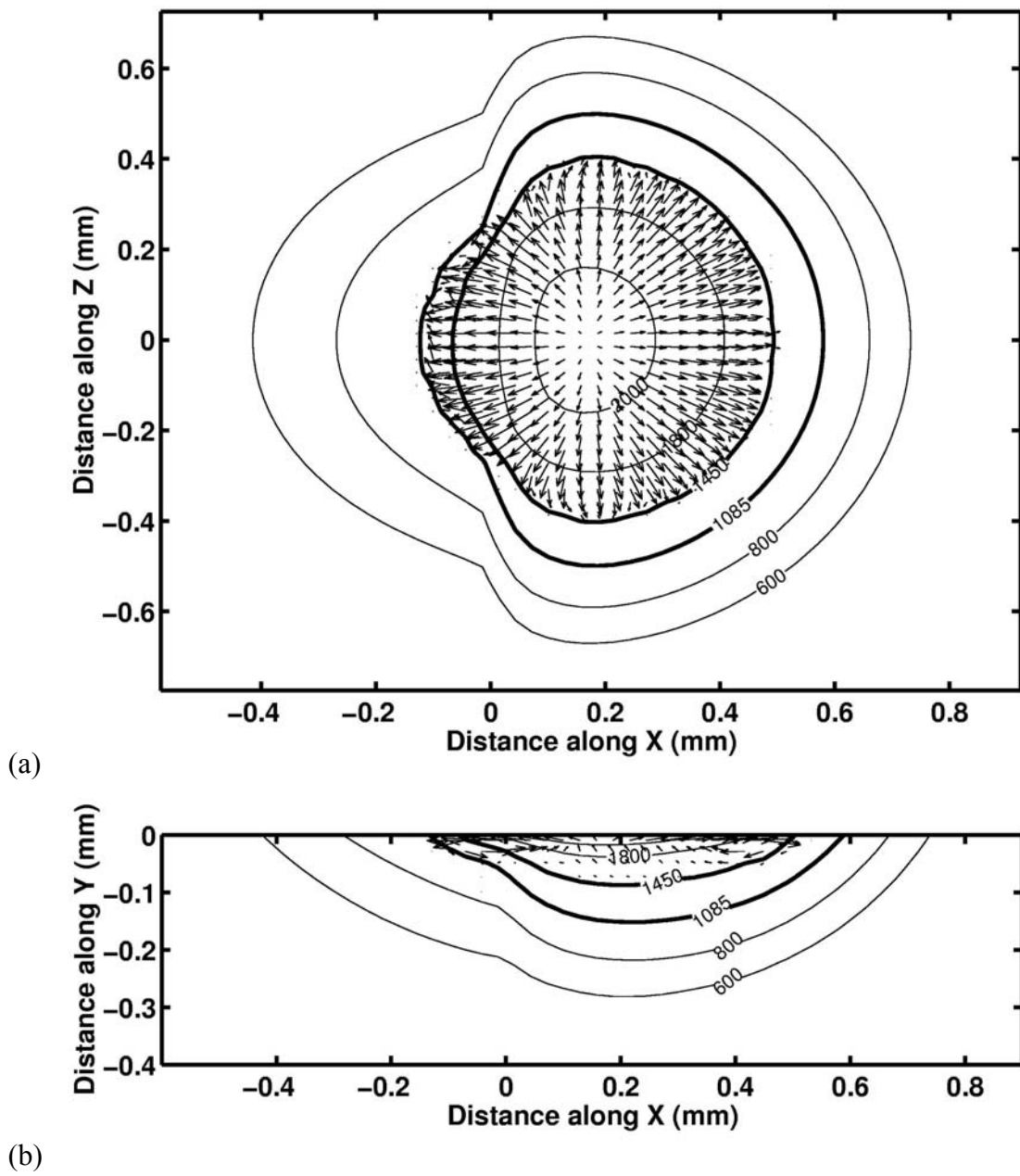
Figure 4.28 Temperature contours and velocity profile in (a) top view and (b) transverse section at a snapshot after 7 ms.
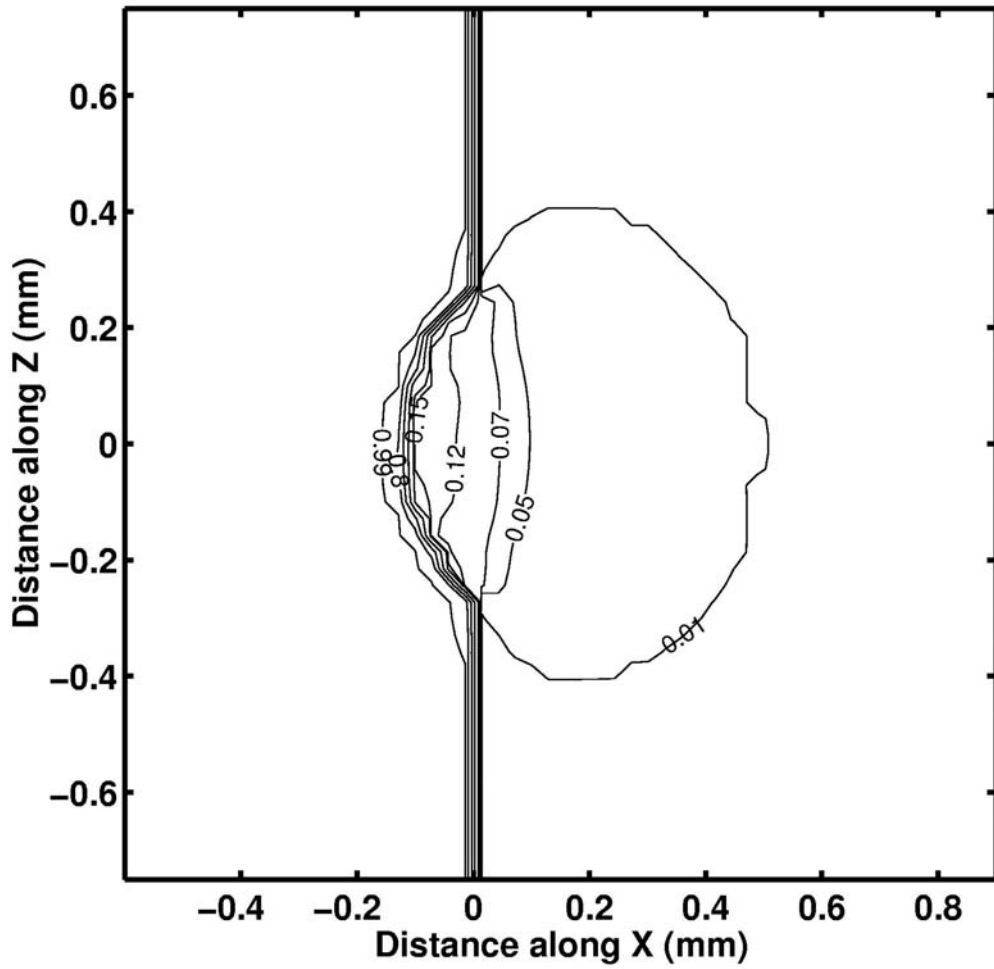
(a)
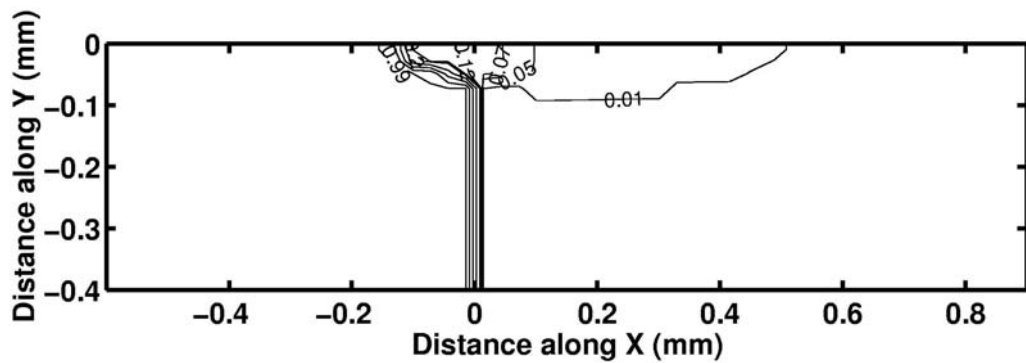
(b)

Figure 4.28 (contd.) Composition contours in (a) top view and (b) transverse view at a snapshot after 7 ms. The values on the contours are wt% Cu.

Chapter 5

Laser remelting of Al-Bi alloy

5.1 Introduction

The process of laser cladding to produce alloy coatings on surfaces has several similarities with laser welding. Issues such as size and shape of fusion zone, temperature history and fluid flow that play an important role in the microstructural evolution, are common to both the processes. Aluminium alloys with soft dispersions such as lead, bismuth and tin show promising applications in tribology of automotive components [108]. Conventional casting route to produce alloys of Al-X (X=Pb/Bi/Sn) leads to coarse microstructure with segregation and settling down of the heavier phase at the bottom [109,110]. Vigorous convection could be used to avoid the same. Magnetohydrodynamics is one such technique that employs Lorentz force induced convection to compensate for buoyancy induced flow to produce bulk alloys of uniform dispersion of soft heavy phase in a metallic melt [111,112]. In this work, laser cladding is being investigated as a technique to produce uniform dispersions of soft phase on the surface of the desired material.

The binary phase diagram of aluminium-bismuth [113] (figure 5.1) shows a monotectic reaction due to liquid immiscibility. Thus, upon cooling from a temperature above the monotectic temperature (930 K), a hyper monotectic alloy liquid separates into globules of bismuth dispersed in a matrix of aluminium. The work presented here aims at determining experimentally the size distribution of bismuth particles in the aluminium matrix and to develop a computational model to understand the factors that govern the distribution. In this chapter, the first section deals with the laser cladding and remelting experiments to produce an Al-Bi alloy solidified at several growth rates. Characterisation and experimental results are detailed in the next section. Section 5.4 presents an outline of the modelling strategy adapted and the details of laser melting program. Section 5.5 deals with the particle

nucleation and growth. In the next section, coalescence of particles by particle tracking and collision is discussed. The chapter is concluded with a summary of results in the last section.

5.2 Experiments

A schematic of the laser cladding process is shown in figure 5.2. The laser cladding setup consists of a powder feeding system in addition to the laser. Elemental powders of commercial purity aluminium and bismuth are blended in 9:1 wt/wt ratio. The powder is fed into the laser melt pool using a powder feeder. When the base metal is moved at a prescribed speed, the alloy powder mixes in the laser melt pool of the base metal and forms the alloy clad. Rofin Sinar R10000 Continuous wave CO_2 laser with a peak power of 10kW is used for the cladding processes. The laser is focussed 30 mm above the focal point to give a beam diameter greater than 2 mm. This results in a broad distribution of intensity that does not lead to vaporization and is thus well suited for cladding.

Initial experiments of laser cladding with a laser power around 3-4 kW produced clads without good adherence to the base metal and uniformity along the length of the clad. Several cladding experiments have been performed to determine the optimum conditions for a smooth clad on the surface without any porosity. No surface coating was used to leave the surface as pure aluminium. A high power of about 8.5 kW was employed to obtain good clads that were used for the characterization studies. The alloy clad was then remelted using the same laser at higher speeds to simulate higher solidification rates. The relation between laser scan speed and the solidification rate is illustrated in figure 2.10 [85]. Thus remelting could be used to simulate higher solidification rates to study microstructural evolution as a function of growth rate.

The process conditions used in this study are as follows:

Powder Composition	Al + 10 wt% Bi (Al+1.414at%Bi)
Laser Power	8.5 kW
Laser scan speeds	5 mm/s (cladding) 5 mm/s, 13.3 mm/s and 20 mm/s (remelting)

5.3 Characterisation

5.3.1 Microstructure

Transverse and longitudinal sections are taken from the laser clad and remelt samples. The transverse sections are used for microstructural analysis using optical microscopy and scanning electron microscopy. Longitudinal sections are used to determine the growth rate of the alloy as a function of height from the bottom of the remelt pool.

Figure 5.3 shows a composite X-Ray Diffraction pattern of the clad and remelted alloys. Only elemental peaks of aluminium and bismuth can be seen confirming the presence of bismuth as the second phase in the alloy. Spot EDAX was done on several bismuth particles seen in the SEM images to confirm that the particles are of bismuth. Figure 5.4(a) presents an EDAX spectrum of a bismuth particle shown in the inset. Figure 5.4(b) shows EDAX taken from a large area to reveal an approximate proportion of bismuth present in the alloy. Several such spectra are taken on unetched samples for quantitative analysis showing that the effective bismuth content in the remelted alloys is about 0.78 at% Bi.

The transverse section of a clad layer of Al-Bi alloy is shown in figure 5.5. The clad region is about 6 mm wide and 2 mm deep and has a distinct feature of directional growth of aluminium grains of substrate into the clad region. The remelted regions for the three speeds is shown in figure 5.6. The shape of the remelted region could be noticed within the clad region due to a trace of the bottom of the remelted pool left after solidification. The longitudinal section of the clad and remelted alloy region is shown in figure 5.7. The three regions *i.e.*, base metal, clad region and the remelted region could be identified easily in the micrograph. The grains are oriented in the direction of growth. The change in the orientation of grains at the bottom of the remelted region shows a change in the growth rate in the alloy at that position due to remelting. As illustrated in the figure 2.10, the growth rate could be calculated from the orientation of the grains as a function of height from the bottom of the remelted region (figure 5.8). Since the grains near the top of the remelted region are oriented almost along the laser scan direction, the growth rate approaches close to the laser scan rate itself at the top.

5.3.2 Size distribution

Back scattered electron microscopy (BSE) was used to image the distribution of bismuth particles in the remelted alloy region. Figure 5.9 shows the typical BSE micrographs of the cross-sections of laser remelt regions, showing fine dispersion of bismuth particles. It could be noticed that the bismuth particles are quite large at low scan speed. During metallographic preparation, some of the bismuth particles fall off and pits form during etching, leading to formation dark spots in the back scattered electron micrographs. The microstructures at low magnification, shown in figure 5.10, depict the uniform nature of the distribution of bismuth particles. At higher magnification, it can be seen that most of the particles are fine and nearly uniform in size. However, there were a few particles which are much larger in size than the average (figure 5.11). Since the particles were nearly uniform within the remelted region, size distribution analysis was confined to the top of the region. Several microstructures were taken in both transverse and longitudinal sections to determine the size distribution of the particles. The BSE images were digitised and a software 'SigmaScan Pro' was used to estimate the diameter of the particles. Since the particles are nearly circular in shape, Feret diameter (diameter of a circle of same area as that of the particle) is used as the representative parameter for the diameter of the particles. A large number of particles (between 300 and 700) are taken to ensure meaningful statistical analysis. Distribution of particle sizes plotted for the clad and remelt alloys is shown in figure 5.12. Average sizes are given in table 5.1. As can be noted, with increasing laser scan speed, the average size of the particles decreases. However, there are particles much larger than the average size indicating a bimodal distribution. The microstructures of remelted alloys show one other feature namely, network formation of bismuth towards one side of the bottom of the pool (figure 5.13). Such a network formation was found to be throughout the clad/remelt regions for the alloys processed at low laser power. A possible explanation for this phenomenon could be that, when the laser power is low, the temperature does not increase significantly beyond the liquidus temperature given by the phase diagram. Since the laser scan velocities are large, the time spent by the laser melted alloy region above the liquidus could be too small for dissolution of bismuth particles in the liquid. When the laser power was increased, such network formation was generally absent, thus supporting this explanation. However, such a network formation was observed in a small region for the samples processed at 8.5 kW laser power. This could be due to non-uniformity of the laser intensity distribution leading to a lower intensity at such locations.

Table 5.1. Average bismuth particle size of the clad/remelt alloys.

Laser scan speed	Average size
5 mm/s (as clad)	0.73 µm
5 mm/s	0.80 µm
13.3 mm/s	0.51 µm
20 mm/s	0.44 µm

As shown in the schematic diagram given in the figure 5.14, the grains of aluminium grow from the bottom of the remelt region towards the top, continuously changing the direction such that the growth direction, normal to the solid-liquid interface, is along the direction of the maximum temperature gradient. The dashed line shows the trace left by the moving solid-liquid front due to small fluctuations in the growth rate as also shown in the figure 5.7. A series of the microstructures of the remelted alloy taken for a single grain from the top to the bottom of the remelt region (shown by the dots in the schematic of figure 5.14) shows interesting features for the three remelting speeds. It is clear that the particles are all embedded in the grain, showing that they are entrapped by the growing aluminium grains. The alloy remelted at 5 mm/s shows bismuth particles aligned along the direction of growth near the top (figure 5.15). However, particles appear randomly distributed at the middle and bottom of the remelted region. In case of the alloy remelted at 13 mm/s, the aligned nature of particles is clear at the middle and top of the remelt region and is absent at the bottom (figure 5.16). For the case of 20 mm/s as shown in figure (5.17), except very close to the bottom of the remelt region, the particles seem to be aligned through out the grain up to the top.

5.3.3 Summary of experimental results

Laser processing conditions were optimised to produce clads of aluminium-bismuth alloy of hypermonotectic composition. Alloy clads were remelted at three different speeds to simulate different growth rates. Bismuth was observed to have precipitated out of the alloy liquid in a uniform manner throughout the remelted region. Particle size distribution was determined to characterise the microstructure of the remelt alloys at the three laser scan

rates. Higher scan rate produced a finer dispersion of bismuth particles. Particles much larger than the average size were observed, indicating a bimodal distribution of particle sizes.

5.4 Modelling

5.4.1 Outline of the model

The process of microstructural evolution in laser cladding could be visualized in two stages. At the macro level, the laser melting with heat transfer and fluid flow dictates the size and shape of the liquid zone. The temperature history of various locations in the clad region is given by the solution of the laser melting problem. At the micro level, the microstructure is determined by the nucleation, growth, coarsening and coalescence of the soft dispersion phase in the melt pool. These processes are determined by the temperature history. Thus one has an option of modelling the problem in two stages to arrive at the final picture of the microstructure in terms of size distribution of the dispersed phase. A flow sheet of the computational model is shown in figure 5.18.

5.4.2 Laser Melting

The computational model developed for the laser welding problem could be used for laser remelting with minor modifications. The formulation is presented below for the sake of completeness. The laser melting process involves a continuous beam of laser moving with a constant scanning speed, w_{scan}, along the z-direction. As the laser strikes the base metal, part of the laser energy is absorbed and the temperature of the base increases, leading to melting under the laser. When the laser moves away, heat is extracted by the base metal and resolidification of molten region takes place.

In the present formulation, the following assumptions are made:

    (i)   The top surface of the pool is flat.

    (ii)   The heat source on the top is assumed to be Gaussian in nature.

(iii)   The Al-Bi alloy exists as a dilute solution in the molten pool. In order to reduce the complexity of the problem, in the laser melt pool is assumed to be well mixed and hence species equation is not solved.

(iv)   Melting and solidification of the base metal is formulated using a pure metal assumption.

(v)   Evaporation at the top surface is neglected.

5.4.2.1 Governing equations

Since the molten pool moves with the laser beam, the problem is more conveniently studied in a reference frame fixed to the laser. Continuity, momentum conservation and enthalpy conservation equations are solved to obtain the temperature and velocity distribution in the laser remelted region. The fundamental variables solved for are temperature (T) and velocity of liquid in the laser melt pool (u,v,w). The governing equations for the process are given below.

Continuity:

$$\frac{\partial \rho}{\partial t} + \nabla \cdot (\rho \vec{u}) = 0 \tag{5.1}$$

Momentum:

$$\frac{\partial}{\partial t}(\rho u) + \nabla \cdot (\rho u \vec{u}) = \nabla \cdot (\mu \nabla u) - \frac{\partial p}{\partial x} - \frac{\partial}{\partial z}(\rho w_{scan} u) - \left(\frac{K(1-\varepsilon)^2}{\varepsilon^3 + b} \right) u \tag{5.2}$$

$$\frac{\partial}{\partial t}(\rho v) + \nabla \cdot (\rho v \vec{u}) = \nabla \cdot (\mu \nabla v) - \frac{\partial p}{\partial y} - \frac{\partial}{\partial z}(\rho w_{scan} v) - \left(\frac{K(1-\varepsilon)^2}{\varepsilon^3 + b} \right) v + \rho g \beta_T (T - T_r) \tag{5.3}$$

$$\frac{\partial}{\partial t}(\rho w) + \nabla \cdot (\rho w \vec{u}) = \nabla \cdot (\mu \nabla w) - \frac{\partial p}{\partial z} - \frac{\partial}{\partial z}(\rho w_{scan} w) - \left(\frac{K(1-\varepsilon)^2}{\varepsilon^3 + b} \right) w \tag{5.4}$$

Energy:

$$\frac{\partial}{\partial t}(\rho H) + \nabla \cdot (\rho \vec{u} H) = \nabla \cdot (k \nabla T) - \frac{\partial}{\partial z}(\rho w_{scan} H) - \frac{\partial}{\partial t}(\rho \Delta H) \tag{5.5}$$

In the above equations, T is temperature, t is time, ρ is density, u, v and w are velocities along x, y and z directions, $\vec{u}$ is the velocity field in vector notation, μ is viscosity, p is pressure, K is permeability, b is a small number to avoid division by zero, w_{scan} is the laser scanning velocity, g is acceleration due to gravity, β_T is compressibility, T_r is the reference temperature for buoyancy, ε is liquid fraction and k is thermal conductivity.

The enthalpy, H, of a material can be expressed as:

$$H = h_s + \Delta H \tag{5.6}$$

$$h_s = cT \tag{5.7}$$

where h_s is the sensible heat, and ΔH is the latent heat content and c is specific heat. In order to simulate a phase change, the latent heat contribution is specified as a function of temperature, T, and the resulting expression is:

$$\Delta H = f(T) \tag{5.8}$$

Since latent heat is associated with the liquid fraction, f_l, one can write:

$$\Delta H = f(T) = \begin{cases} L & for & T > T_l \\ Lf_l & for & T_s \leq T \leq T_l \\ 0 & for & T < T_s \end{cases} \tag{5.9}$$

where T_l is the liquidus temperature at which solid formation begins, T_s is the solidus temperature at which full solidification occurs, and L is the latent heat of fusion. In the present problem, the substrate is pure aluminium. The range of temperature over which phase change takes places is taken to be numerically small for this purpose. Substituting the expression for H from equation (5.9) and equation (5.6) in the energy equation (5.5), one arrives at the following final form of the energy equation:

$$\frac{\partial}{\partial t}(\rho cT) + \nabla \cdot (\rho cT\vec{u}) = \nabla \cdot (k\nabla T) - \frac{\partial}{\partial x}(\rho u_{scan}cT) - \frac{\partial}{\partial t}(\rho \Delta H) \tag{5.10}$$

5.4.2.2 Boundary Conditions

Since a single domain analysis is used here for solving the energy and momentum equations, the solid-liquid interface comes out as a solution. There is no need to explicitly track the solid-liquid interface and put a boundary condition there. Hence, the boundary

conditions for momentum and energy equations are applied on the boundaries of the work-piece domain as follows:

Top Surface:

A Gaussian heat flux distribution is assumed at the top surface which is given by:

$$q''(r) = \frac{q}{\pi r_q^2} \exp\left(-\frac{r^2}{r_q^2}\right) \qquad (5.11)$$

where, r is the distance from the laser centre, q is laser power and r_q is half the laser beam width. Considering heat losses due to convection and radiation, one arrives at the following boundary condition:

$$-q''(r) + h(T - T_\infty) + \sigma_e \varepsilon_e (T^4 - T_\infty^4) = -k\left(\frac{\partial T}{\partial y}\right)_{top} \qquad (5.12)$$

where, σ_e is the Stefan-Boltzman constant, ε_e is emissivity, T_∞ is the ambient temperature and h is the convective heat transfer coefficient. The top surface is assumed to remain flat:

$$v_{top} = 0 \qquad (5.13)$$

From the balance between shear force and surface tension at the free surface:

$$\tau_{yx} = -\mu\left(\frac{\partial u}{\partial y}\right)_{top} = \frac{\partial \sigma}{\partial T}\left(\frac{\partial T}{\partial x}\right)_{top} \qquad (5.14)$$

$$\tau_{zx} = -\mu\left(\frac{\partial w}{\partial y}\right)_{top} = \frac{\partial \sigma}{\partial T}\left(\frac{\partial T}{\partial z}\right)_{top} \qquad (5.15)$$

where, $\dfrac{\partial \sigma}{\partial T}$ is the temperature coefficient of surface tension.

Faces:

The four side faces and the bottom face are subjected to convective heat transfer boundary condition:

$$-k\left(\frac{\partial T}{\partial n}\right)_{wall} = h(T - T_\infty) + \sigma_e \varepsilon_e (T^4 - T_\infty^4) \qquad (5.16)$$

where n is in the direction of the outward normal to any side and the bottom face.

5.4.2.3 Results and Discussion

The governing equations described in the previous section are solved under the respective boundary conditions simultaneously using a control volume technique. SIMPLER procedure [60] with a tri-diagonal-matrix algorithm is used for the solution. Convergence is declared when the maximum value of residuals of each parameter drops below 0.01% of the maximum value for each time step. The parameters used for the simulation are given in table 5.2. Since the cooling rate obtained from the laser melting program is used as an input parameter for the microstructure calculation, the value of efficiency is chosen such that the pool shape matches with that of the experimental remelt pool shape for one of the remelting speeds. The efficiency is then kept constant for the remaining two remelt speeds. Results of modelling of laser melting are shown by the snap shots of temperature contours and velocity profiles of the laser melt pool at any instant.

Table 5.2 Parameters used in the laser melting program

Laser Power q (W)	8500
Efficiency η	0.20
Radius of laser r_q (mm)	1.5
Dimensions of domain $X \times Y \times Z$ ($mm \times mm \times mm$)	$30 \times 10 \times 30$
Number of grids	$64 \times 48 \times 64$
Laser scan speeds (mm/s)	5, 13, 20

Figure 5.19 shows the temperature contours in the longitudinal section, top view and transverse section of the remelt region. It could be noticed that the pool has a trailing shape towards the solidification front (in the $+z$ direction) due to the laser scanning velocity. The trailing is not significant due to high thermal diffusivity of aluminium. The shape of the solidification front is similar to the trace left by the moving solidification front shown in the figure 5.7. The transverse section shows laser remelt pool in the plane normal to the laser scan direction and thus the shape of remelt pool is symmetric about the $y=0$ line. Figure 5.20(a-c) and 5.21(a-c) show temperature contours for the laser remelting speeds of 13 mm/s and 20 mm/s, respectively. The velocity profiles for laser remelting speed of 20 mm/s

are shown in the three sections in figure 5.21(d-f). It could be noticed that due to negative coefficient of surface tension of aluminium, the liquid flows radially outward from the laser centre on the top surface. The maximum velocity is on the top of the pool near the solid-liquid interface and is about 2 m/s in magnitude. The strong dependence of viscosity on temperature and the high temperature near the top surface lead to a recirculation of the fluid within a small depth from the top surface. The remaining fluid in the remelt pool has a counter circulation leading to transport of heat towards the bottom of the pool. The final shape of melt pool is shallow, as desired for cladding.

After the temperature field reaches a quasi steady state, the temperature history of any point (x,y,z_1) in the computational domain could be obtained by the following equation.

$$T(x,y,z_1,t_1) = T(x,y,z_1) + \frac{T(x,y,z_2) - T(x,y,z_1)}{z_2 - z_1} w_{scan}(t_2 - t_1) \qquad (5.17)$$

where, (x,y,z_2) is the position to which the laser moves after the time interval (t_2-t_1).

The cooling rate can then be obtained within a given temperature interval by interpolation. Figure 5.22(a) shows the temperature history of a point at the top of the remelted region for the three laser scan speeds. In the zoomed plot shown in figure 5.22(b), one can note the time intervals allowed in the range of temperature from the start of liquid immiscibility to the monotectic point for the composition of Al + 0.78 at% Bi. Table 5.3 shows the time intervals for the three scan speeds. The cooling rates thus calculated form the input for the nucleation and growth calculations detailed in the next section.

Table 5.3 Time intervals spent in the temperature range of phase separation
(733°C to 660 $^{\circ}$C)

Laser scan speed (mm/s)	Time interval (ms)	Effective cooling rate (K/s)
5	25	2920
13	13	5600
20	12	6010

5.5 Microstructure Evolution

5.5.1 Nucleation of Bi particles

Nucleation of second phase in the liquid immiscible systems can be adequately described by homogeneous nucleation theory as shown by Granasy and Ratke [114]. The phase diagram is shown in figure 5.1 [115]. A thermodynamic description of the Al-Bi binary system is required to arrive at the driving force for nucleation of the Bi particles. The free energy of the Al-Bi system, for the temperature range (930K to 1310K) within which immiscibility exists, is given by a subregular solution model [116]. The free energy expression used is given by the following equation and the corresponding coefficients are given in table 5.4.

$$\Delta G = \sum_{i=0}^{n} K_i x_1 x_2 (x_1 - x_2)^i + RT(x_1 \log x_1 + x_2 \log x_2)$$
$$K_i = A_i + B_i T$$

(5.18)

Table 5.4. Coefficients used in the equation 5.18.

i	A_i (J/mol)	B_i (J/(mol.K)
0	24649.18	-3.04970
1	13282.64	-5.92753
2	18519.75	-12.33873
3	6959.30	-2.24613

The free energy vs. composition curve for any given temperature is used to arrive at the driving force for phase separation, as illustrated by Thompson and Spaepen [117]. At any given temperature within the range of phase separation, a tangent is drawn to the free energy versus composition curve at a composition C_1 corresponding to that of the liquid. A tangent parallel to it is drawn such that it meets the free energy curve at C_2. The vertical difference between the two tangents gives the free energy difference of a nucleus of composition C_2 formed from a liquid of composition C_1 such that the difference in the chemical potentials for Al and Bi components is same for both the liquid and the nucleus.

An illustration of the construction for 1.414 at% Bi at 1055K is shown in the figure 5.23. Numerous such constructions were made at temperatures of 5K interval and compositions of ~ 0.05 at% interval to obtain the driving force for nucleation as a function of temperature and composition within the range of phase separation. Figure 5.24(a) shows contours of driving force for nucleation in J/mol as a function of temperature and composition. Similarly, the composition of the nucleus is shown in the figure 5.24(b).

The surface energy of a critical system such as the immiscible liquid system Al-Bi is described by the following relation [118].

$$\sigma = \sigma_O\left(1 - \frac{T}{T_C}\right)^{\mu} \tag{5.19}$$

where, σ_O is a constant, T_c is the critical temperature, and μ is the critical exponent. σ is taken to be 0.06 J/m^2 at the monotectic temperature, as reported in the literature [119]. Homogeneous nucleation rate for phase separation is given by:

$$I = I_O \exp\left(-\frac{\Delta G^*}{k_B T}\right) \tag{5.20}$$

where, $\Delta G^* = \frac{16\pi}{3}\frac{\sigma^3}{\Delta G_V^2}$ and ΔG_V is the volume free energy given by $\Delta G_V = \Delta G / V_m$ where, V_m is the molar volume. The pre-exponent factor I_o was evaluated using the classical expression for nucleation rate [114].

$$I_0 = N_0 O\Gamma Z \exp(-\Delta G^* / kT) \tag{5.21}$$

where, N_0 is the number density of atoms in the liquid, $O = 4n^{2/3}$ with n being the number of atoms in the droplet of critical size, $\Gamma = 6D / \lambda^2$, λ being the average jump distance of atoms in the liquid and D being the diffusivity. Diffusivity values are unavailable for most monotectic systems in the literature and for the present case of Al-Bi, it is estimated using Stokes-Einstein's relation given by the equation (5.22), where k is Boltzman constant, η is viscosity, and a_0 is the diameter of diffusing particle (bismuth atom, in this case).

$$D = kT(3\pi a_0 \eta)^{-1} \tag{5.22}$$

The critical radius of the nucleus is given by $R^* = \dfrac{2\sigma}{\Delta G_V}$ [120]. The parameters used for the calculations are taken from Smithells' Handbook [88] and are listed at the end of this section. Steady state nucleation rates were calculated as a function of temperature and composition using equation 5.20. The contours of the same are shown in the figure 5.24(c). It could be observed that the nucleation rate increases exponentially with decrease of temperature. At lower compositions, the liquidus temperature is lower and the undercooling for phase separation is smaller. Thus, at a given temperature, nucleation rate is lower at lower compositions of bismuth in the liquid. The contour labels show nucleation rate in number per unit volume per unit time.

Table 5.5 Parameters used in the nucleation and growth calculations

Surface tension σ (Nm^{-1})	$0.2854\left(1.0 - \dfrac{T}{1310}\right)^{1.26}$
Average jump distance λ (m)	3.64×10^{-10}
Atomic volume of Al Ω (m^3)	1.2249×10^{-29}
Atomic volume of Bi Ω (m^3)	2.5252×10^{-29}
Viscosity of Al μ (Nm^{-2}s)	$0.1492 \times 10^{-3}\exp(16500/8.314T)$
Viscosity of Bi μ (Nm^{-2}s)	$0.4458 \times 10^{-3}\exp(6450/8.314T)$
Molar weight of Al (kg)	0.02698
Molar weight of Bi (kg)	0.20898
Density of Al (kgm^{-3})	2700
Density of Bi (kgm^{-3})	9550

5.5.2 Growth of Bi particles

Growth of Bi particles takes place via diffusion [121] and LSW coarsening [122,123]. The time scale of these processes is on the order of a few milliseconds for the laser remelting conditions used in this work. An order of magnitude analysis is performed to determine which of the two processes is dominant.

Transport constant for LSW coarsening [124] is given by equation (5.23) below.

$$K_{LSW} = \frac{8\sigma\Omega C_\infty D}{9k_B T \Delta C} \tag{5.23}$$

At T=1030K, $K_{LSW} \approx 4 \times 10^{-19}\, m^3 s^{-1}$.

The increase in diameter of particle due to diffusion is approximated by the following expression:

$$\Delta R \approx \sqrt{2D\Delta t \left(\frac{C_0 - C_{Al}}{C_{Bi} - C_{Al}} \right)} \qquad (5.24)$$

C_{Al}, C_{Bi} are concentrations of the two liquids at equilibrium during nucleation and C_0 is the concentration of the decomposing liquid. Diffusivity was estimated using equation (5.22) at the same temperature ($D = k_B T (3\pi a_o \eta)^{-1} \approx 4.7 \times 10^{-9} m^2 s^{-1}$). It can be seen that diffusional growth of particles in the liquid for the time scale involved gives almost two orders higher value than coarsening. Hence, the LSW coarsening is neglected in the present calculations. However, for long time scales and lower temperatures, this would be of importance.

Growth by diffusion can take place only till the supersaturation is exhausted. The growth of bismuth particles is calculated using the following expression [120]:

$$\frac{dR}{dt} = D \left(\frac{C_0 - C_{Al}}{C_{Bi} - C_{Al}} \right) \frac{1}{R} \qquad (5.25)$$

The temperature at which the nucleation and growth of bismuth particles takes place, continuously decreases at a rate given by the cooling rate. Thus, to obtain the number of nuclei and the final size distribution of the bismuth particles, nucleation rate and increase in particle size by diffusional growth should be calculated simultaneously. The calculations are done for a unit volume in which the mass of bismuth is balanced after every time step. Thus, the composition of bismuth in the control volume decreases during the process and calculations are stopped once the supersaturation is exhausted i.e., composition reaches the value corresponding to the solid solubility limit of bismuth in aluminium.

Size distribution is investigated as a function of three parameters, surface tension, composition and cooling rate. The calculations take several parameters as input, the accuracies of most of which are not easily determined. The parameter most sensitive to presence of impurities and measured least is surface tension. Figure 5.25(a) shows the size distribution of the bismuth particles that nucleate and grow during phase separation of a liquid of composition 0.78 at% bismuth at a cooling rate of 6000 K/s. Three values of surface tension *viz.*, 20% higher, 20% lower and equal to the value available in literature were used in the calculations, keeping all the other parameters constant. Lower surface tension increases the nucleation rate and leads to higher number of nuclei, narrower size

distribution due to lack of supersaturation for growth. As could be noted, there is a significant change in the size distribution demonstrating the importance of correct input parameters for physical properties.

Figure 5.25(b) shows size distribution of bismuth particles after phase separation of a liquid at a cooling rate of 6000 K/s for different initial compositions of liquid. The size distribution is broader and the total number of nuclei is smaller for lower initial composition of bismuth. This is understandable since at lower compositions of bismuth, the steady state nucleation is lower, leading to an increase in the size of particles before the supersaturation is exhausted. However, the size distribution does not seem to be a strong function of composition.

While all the parameters are kept constant, at different laser remelting speeds, the parameter that changes is the cooling rate. Size distribution of bismuth particles was studied at three different cooling rates: 10^2, 10^3 and 10^4 K/s, as shown in figure 5.25(c). The distribution was normalised with the maximum nuclei for comparison within the same plot. The number of nuclei is large for higher cooling rate and accordingly, the average size of the particles is also lower. The development of distribution at different cooling rates could be understood by the path taken by a control volume in the temperature-composition map. Figure 5.26 shows such a path for different cooling rates superimposed with the contours of nucleation rates as a function of temperature and composition. At higher cooling rates, the temperature of a control volume decreases considerably before the supersaturation starts decreasing due to high nucleation rate and growth of particles, leading to a decrease in composition of bismuth. At lower cooling rates, the control volume spends more time at a given temperature and thus, the composition starts decreasing before the temperature drops much. The figure also shows such paths for the cooling rates corresponding to the three laser remelting speeds used in the present work. The size distribution after nucleation and growth of particles at these three cooling rates is shown in figure 5.27.

5.5.3 Collision and coalescence of particles

The nucleation and growth of the bismuth particles take place in a liquid pool that undergoes vigorous convection driven by Marangoni forces [125]. It is clear that coalescence due to collision of particles will be present during the process. Coalescence during sedimentation is negligible as the velocities for convection in a laser melt pool are

large (of the order of 1 m/s) and thus, significantly higher than Stokes velocities (which is of the order of 1 mm/s).

Coagulation and coalescence of particles under motion is well studied and a review by Drake [126] provides a comprehensive analysis of models in use for processes involving aerosols and colloids. However, coalescence of particles during solidification is not so well understood [124]. The models discussed by Drake and Ratke involve collision frequency as a function of velocity of the particles. This term is nearly impossible to evaluate for laser melting process, for which, the velocity profile is solved numerically. The velocity of the fluid varies as a function of position and time apart from the process conditions. Thus, a method outlined below is used to take coalescence into account.

The following assumptions are made:

- Particles move along with the liquid and the effect of drag is negligible. Collision takes place due to finite sizes of the particles.

- Particles are small enough in volume fraction so that they have no effect on the liquid flow profile.

- Particles that have undergone diffusional growth are taken for coalescence study during which they only collide and coalesce but do not grow. Growth and coalescence are thus treated as discrete steps in the process.

The first two assumptions are justifiable, as the volume fraction of the particles is less than 2%. Since this complex model is attempted for the first time, the growth and coalescence are treated as discrete stages. In principle, it could be done simultaneously, but it will increase the complexity of the problem.

Figure 5.28 shows velocity profile on the solidification front for laser remelting at 20 mm/s. The laser scan direction is indicated by an arrow at the top of the figure. The temperature contours shown are in ^{o}C and correspond to the range within which phase separation takes place for the composition of the alloy under study. The box shown at the right top of the figure is the control volume chosen to study collision of particles. The total number of particles introduced in the control volume during a time interval Δt_1 (figure 5.29) are such that the number of particles per unit volume corresponds to the number of nuclei calculated for exhaustion of supersaturation as detailed in the previous section. The particles are

introduced with their sizes corresponding to the distribution after nucleation and growth. The locations of particles within the control volume are chosen by a random number generation program. The particles are then tracked by integrating the fluid velocities at the respective locations using a fourth order Runge-Kutta method. Two particles (labelled 1,2) are coalesced and the size of #1 increased for volume conservation when they come close enough by the following criterion:

$$\left|(x_1 - x_2)^2 + (y_1 - y_2)^2 + (z_1 - z_2)^2\right| \leq (r_1 + r_2)^2 \qquad (5.26)$$

where (x_1, y_1, z_1) and (x_2, y_2, z_2) are positions of the two particles with radii r_1 and r_2, respectively. The collision and coalescence is allowed during a time interval Δt_2 allowed for the process.

Figure 5.30 shows the particle size distributions before and after collision. The size distribution after nucleation and growth, is narrow and nearly symmetric about the mean size. Collision leads to increase in average particle size. The larger particles have more probability of collision due to size effect and thus the size distribution shows a gradual decrease of number of particles at the higher sizes. It could be noticed that the experimental size distribution also shows a similar feature of sharp increase and a gradual decrease of number of particles with size. The total number of particles decreases during the coalescence. The calculated sizes are slightly higher compared to the experimentally determined ones. As noted in the previous section, the size distribution is sensitive to several parameters that include surface tension and composition. Some of the parameters, such as surface tension, are sensitive to presence of impurities and are difficult to determine experimentally. Inaccuracy of values of such parameters borrowed from the experimental data could be one of the reasons for the discrepancy between the computed and calculated size distributions. However, the computed sizes of particles are quite close to the experimentally observed ones and the nature of computed distribution is depicted closely matching the trend of experimental distribution. Hence, it could be concluded that the agreement between the computational and experimental size distributions is satisfactory experiments.

5.6 Summary

Microstructure development as a function of laser remelting rate was studied for aluminium-bismuth system. The alloy which was made using laser cladding of elemental powders, was remelted at 5mm/s, 13 mm/s and 20 mm/s. The microstructures in transverse and longitudinal sections observed in SEM showed uniform distribution of bismuth particles in the matrix of aluminium. The miscibility gap of liquid Al-Bi alloy led to precipitation of nearly globular particles of bismuth. Size distribution of bismuth particles for alloys remelt at the three different scanning speeds, was determined using image analysis. Higher scan speeds led to a finer size distribution.

A computational model was developed to calculate the size distribution of bismuth particles during laser remelting. The remelted pool shape and cooling rates during laser surface remelting were calculated. The driving force for nucleation was calculated and a map of nucleation rate was constructed as a function of composition and temperature. Size distribution of bismuth was calculated at different cooling rates taking into consideration, simultaneous nucleation and growth by diffusion in the melt, till the super saturation is exhausted. Cooling rates used were obtained from the laser remelting program. Collision of particles due to convection in the laser melt pool is taken into account by a particle tracking algorithm. Final size distribution of bismuth particles showed a good agreement with the experimental particle size distribution.

Figure 5.1 Phase diagram of the aluminium-bismuth system [88].
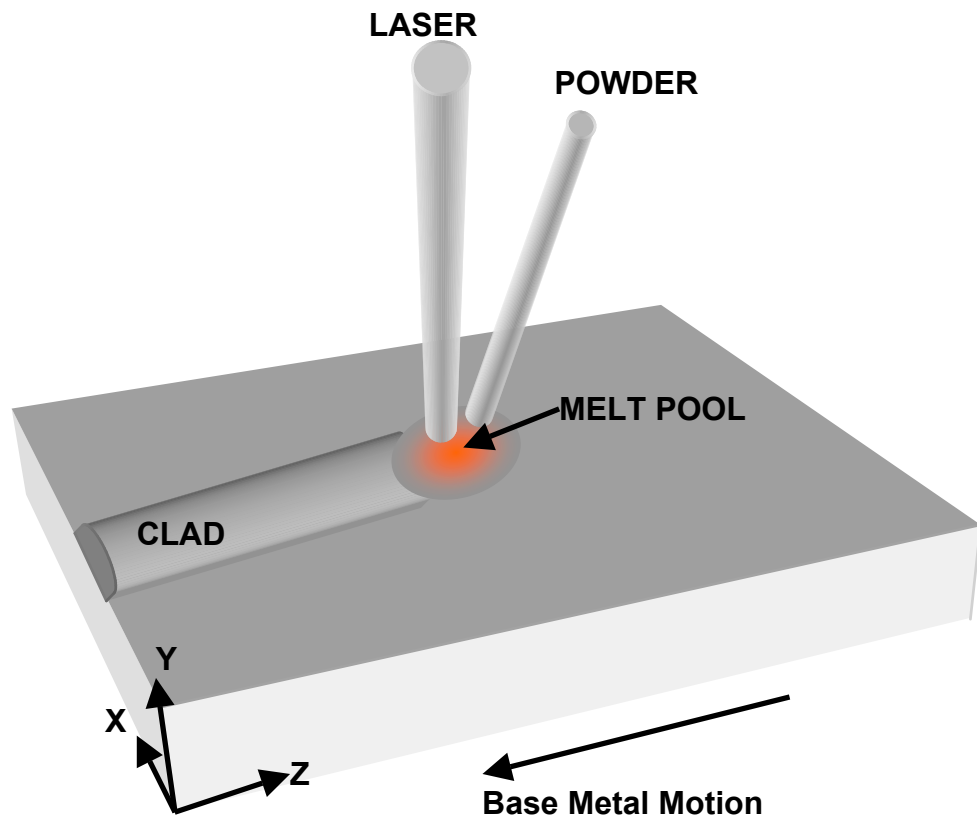
Figure 5.2 Schematic of the laser cladding process.
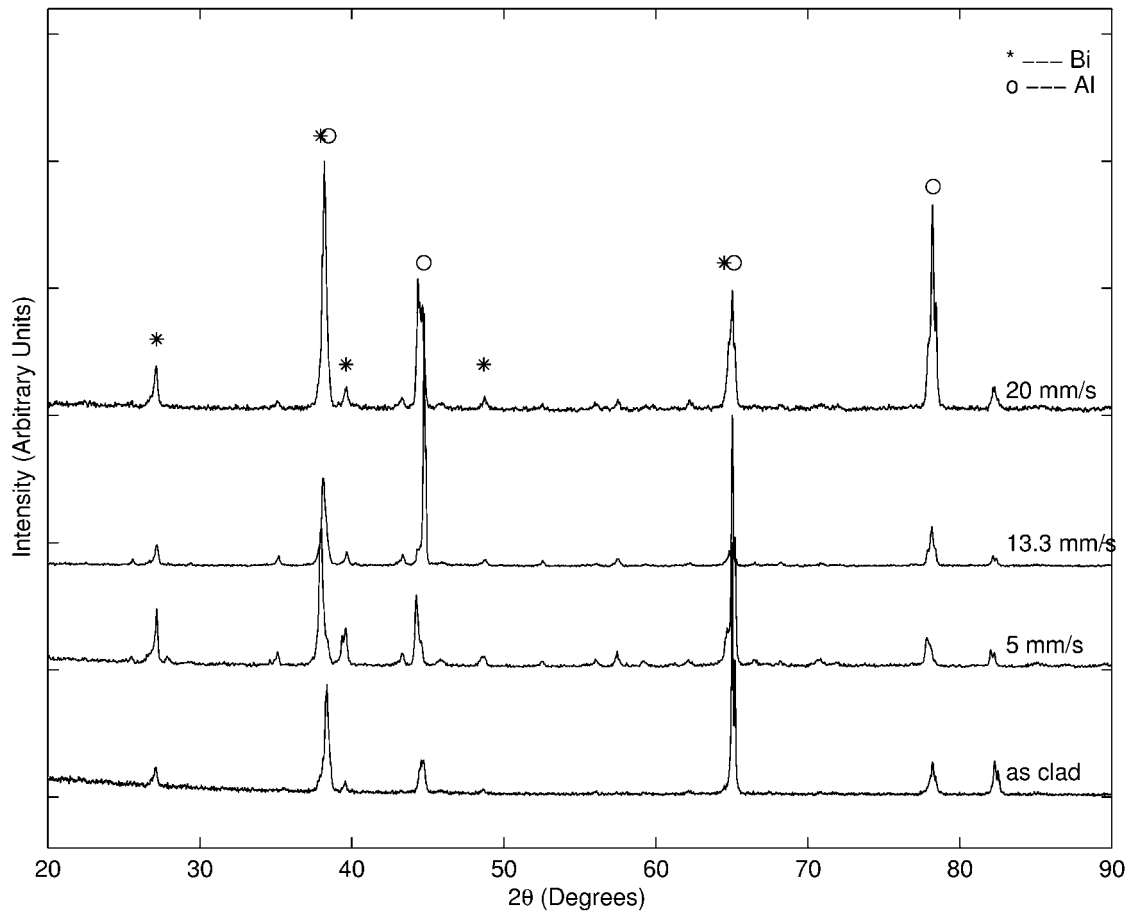
Figure 5.3 Composite X-Ray (Cu k$_\alpha$) Diffraction pattern of Al-Bi alloys showing elemental peaks of aluminium and bismuth for the clad and remelted alloys.

(a)

(b)
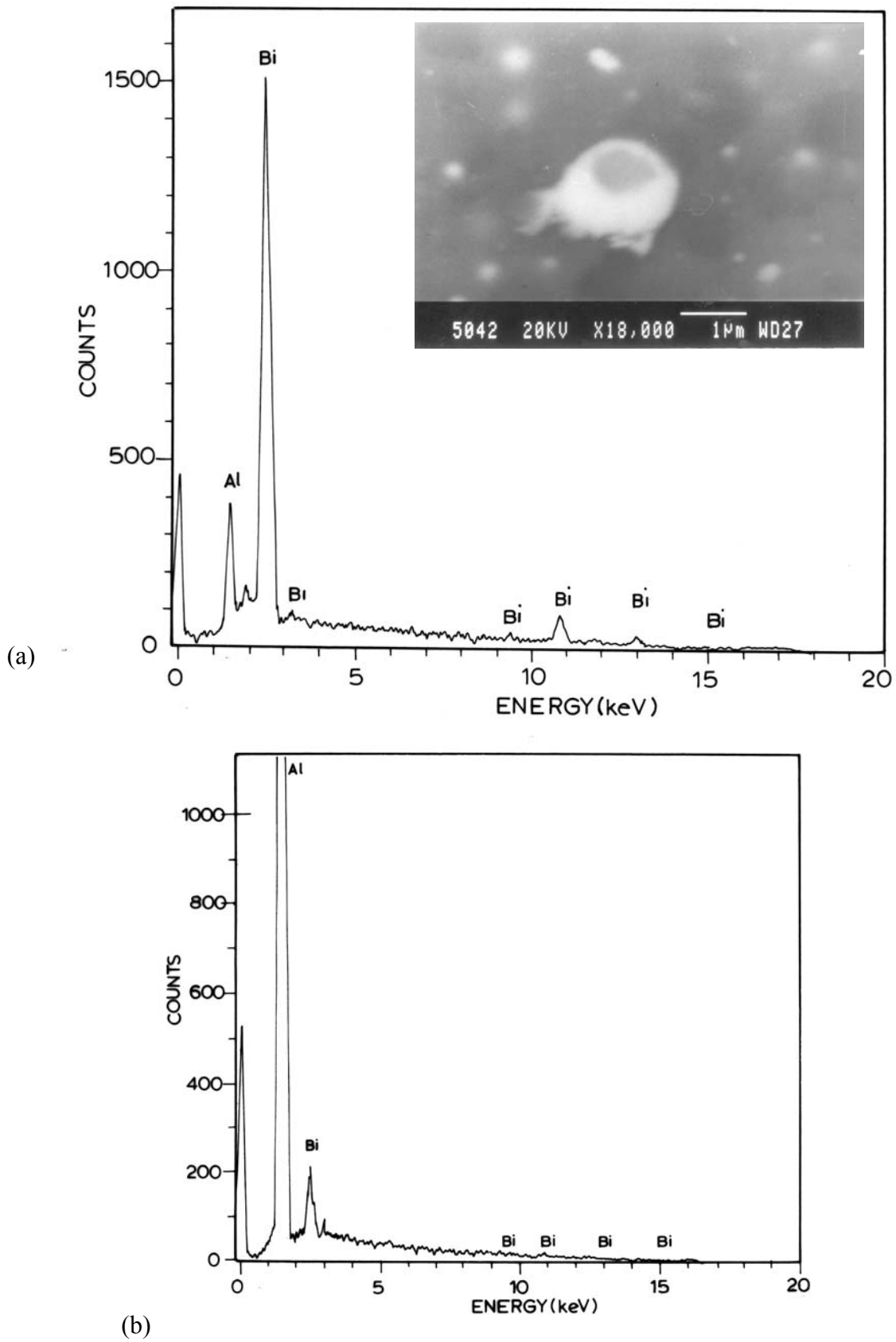
Figure 5.4 (a) Spot EDAX of a Bismuth particle (shown in inset). (b) EDAX of a large region in the alloy remelted at a scan speed of 20 mm/s.
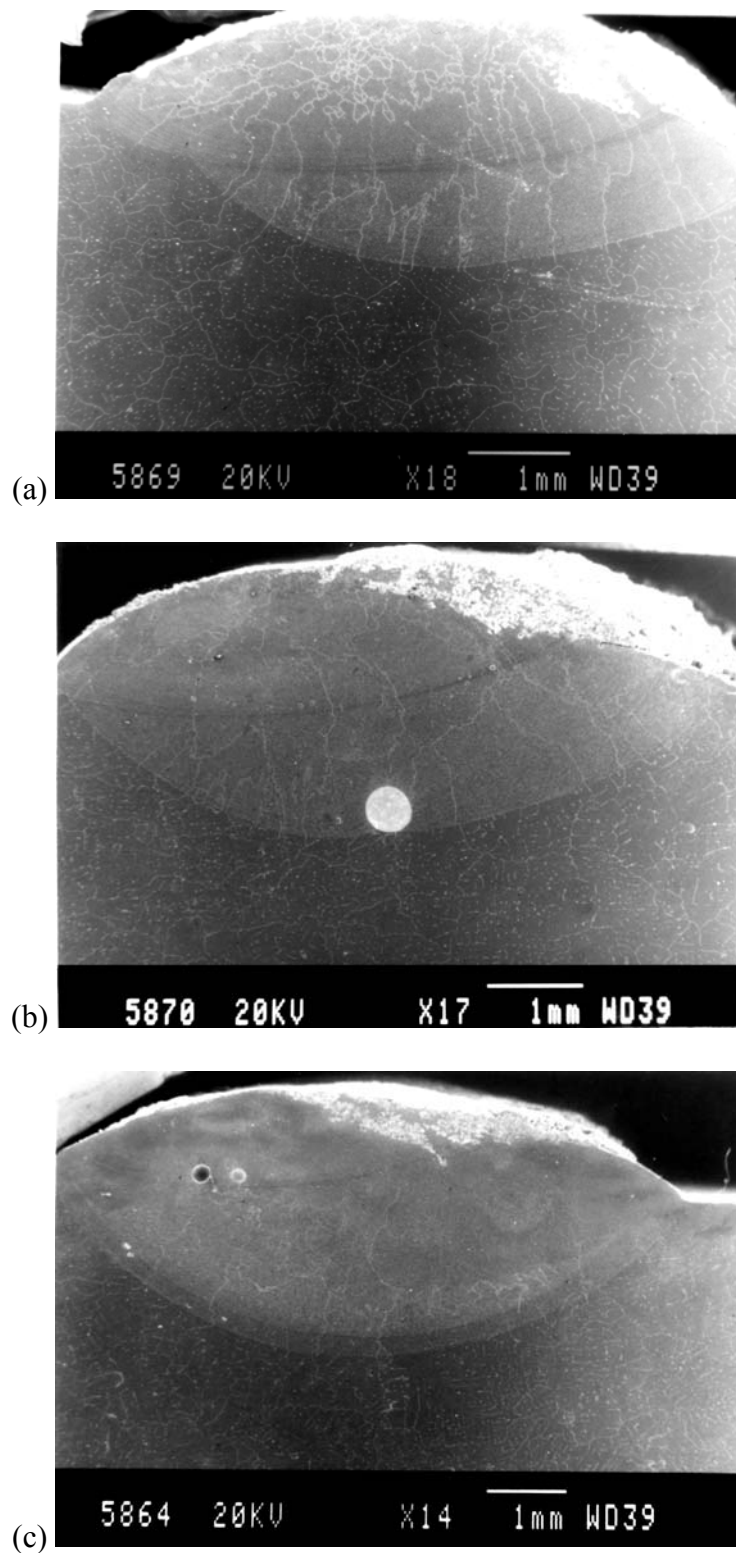
Figure 5.5 Transverse sections of the clad and remelted regions for the laser scan speed of 5 mm/s for cladding and (a) 5 mm/s (b) 13 mm/s (c) 20 mm/s for remelting.

(a)

(b)

(c)
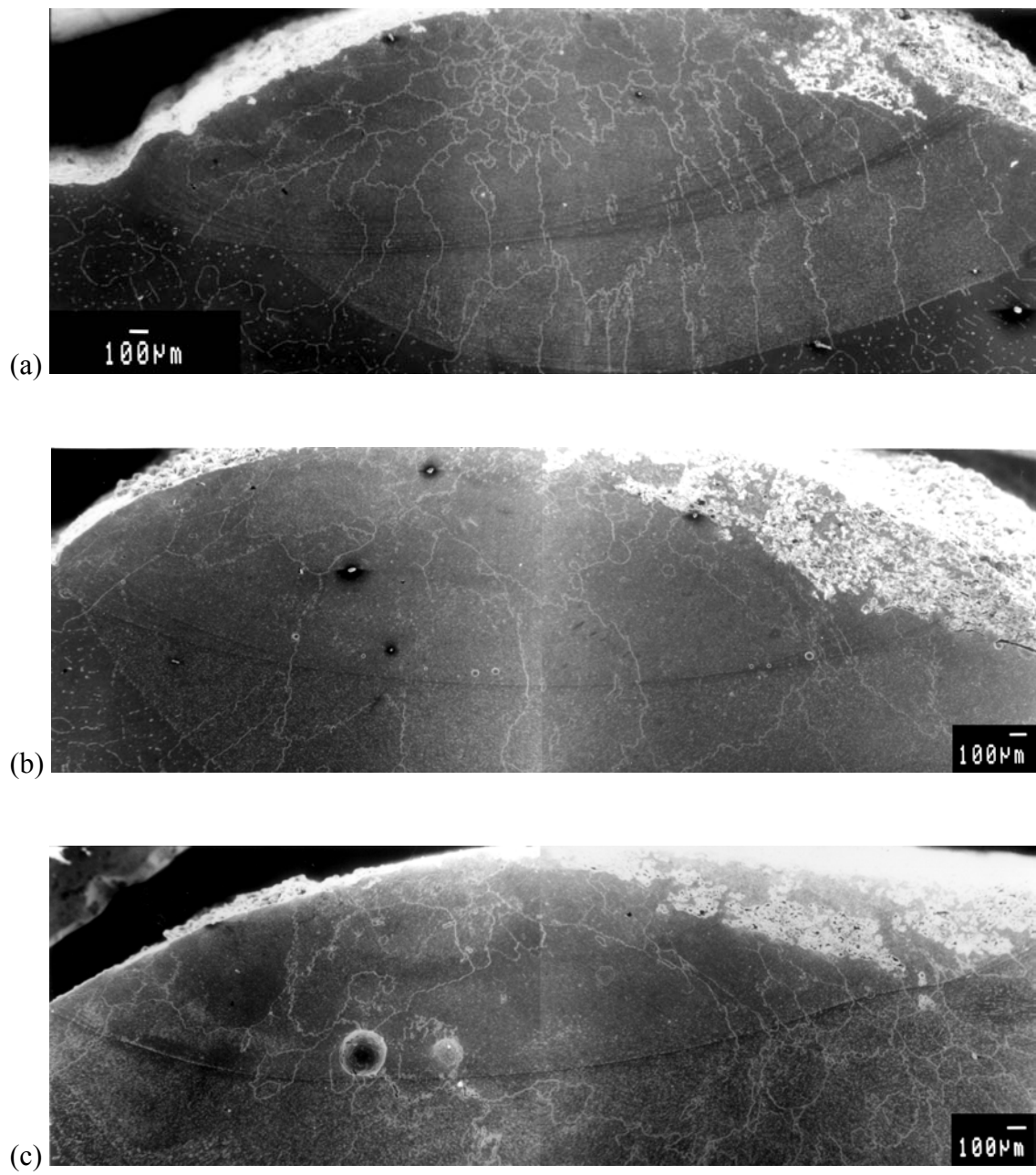
Figure 5.6 Remelted regions for laser scan speeds of (a) 5 mm/s (b) 13 mm/s (c) 20 mm/s
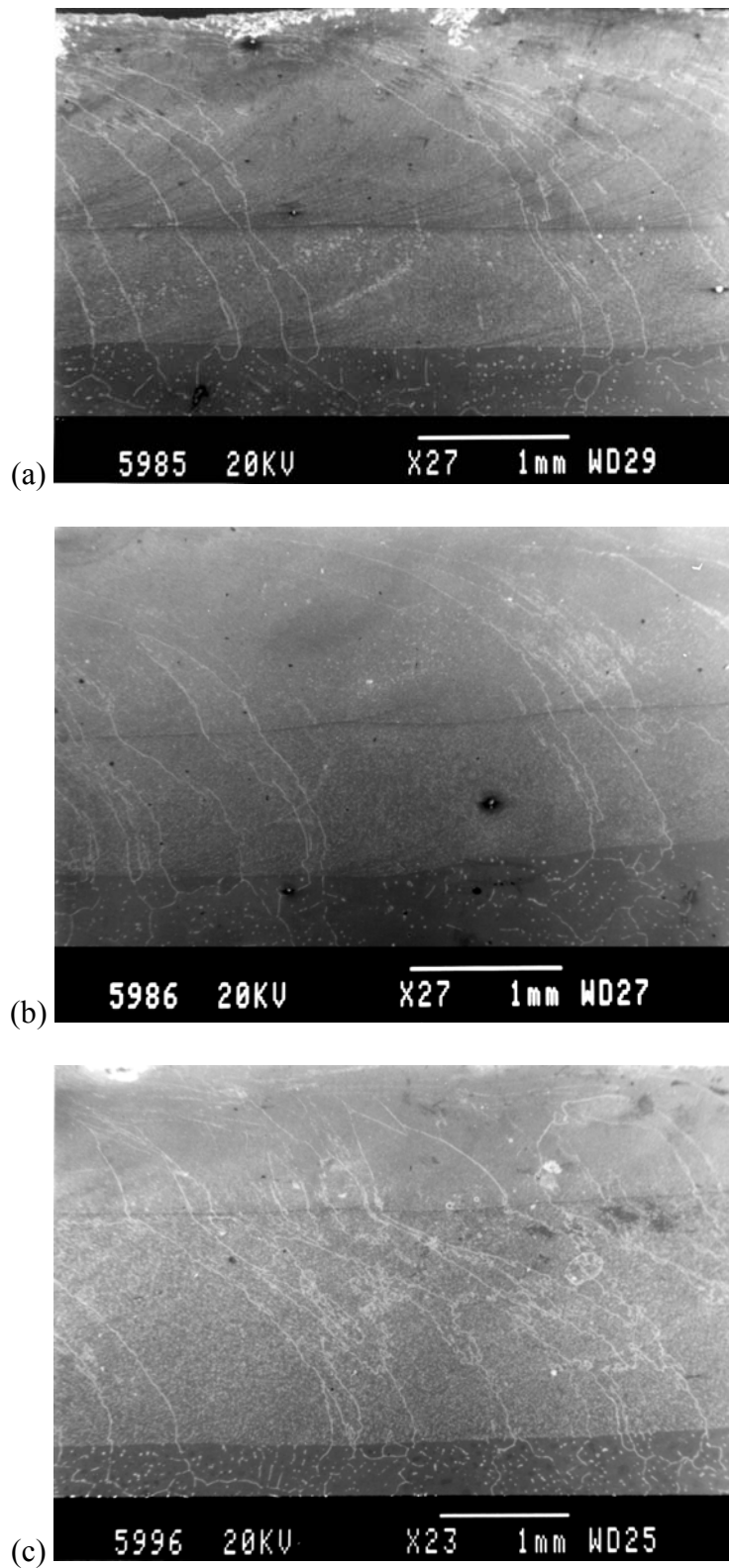
Figure 5.7 Longitudinal sections showing the base metal, clad and remelt regions for scan speeds of (a) 5 mm/s (b) 13 mm/s (c) 20 mm/s.

(a)

(b)

(c)
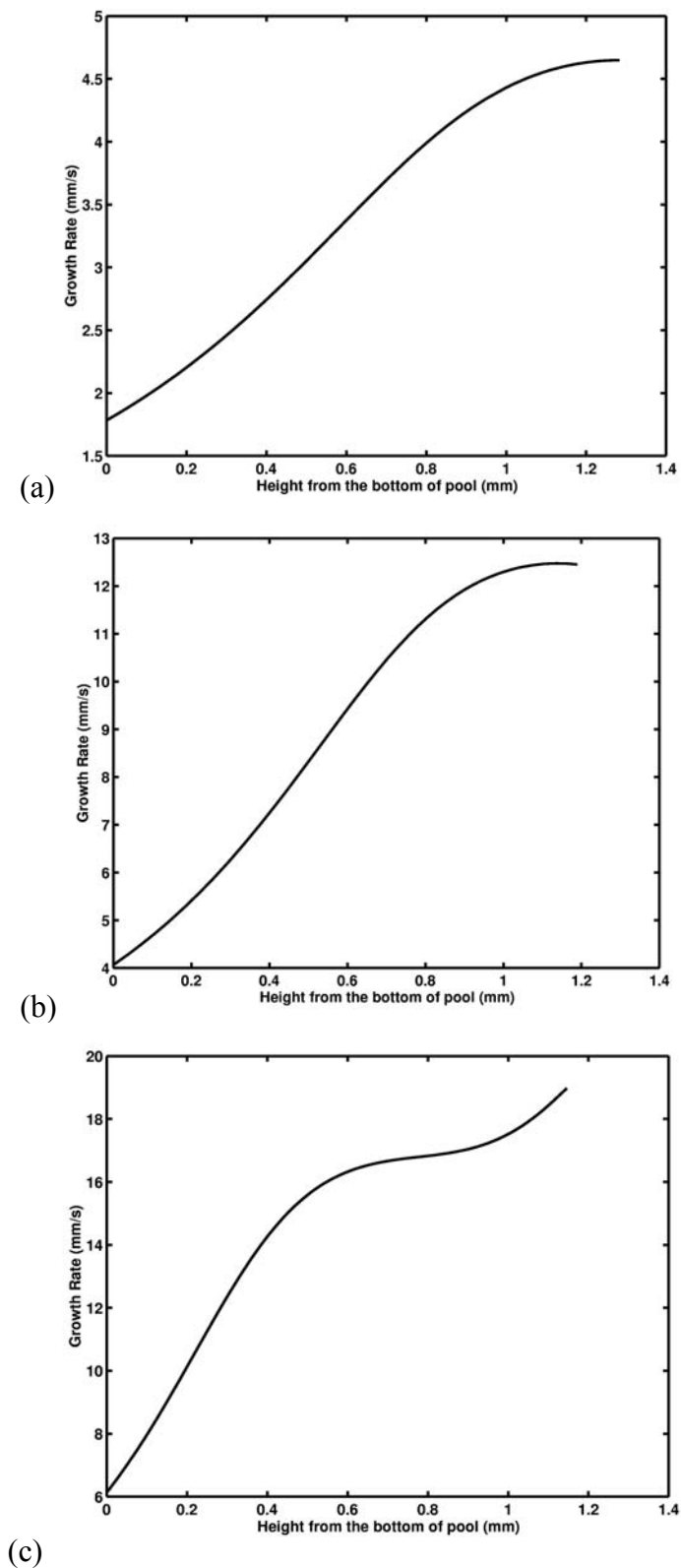
Figure 5.8 Growth rates calculated from the orientation of grains as a function of height from the bottom of the pool for laser remelt speeds of (a) 5 mm/s (b) 13 mm/s and (c) 20 mm/s.

(a)

(b)

(c)
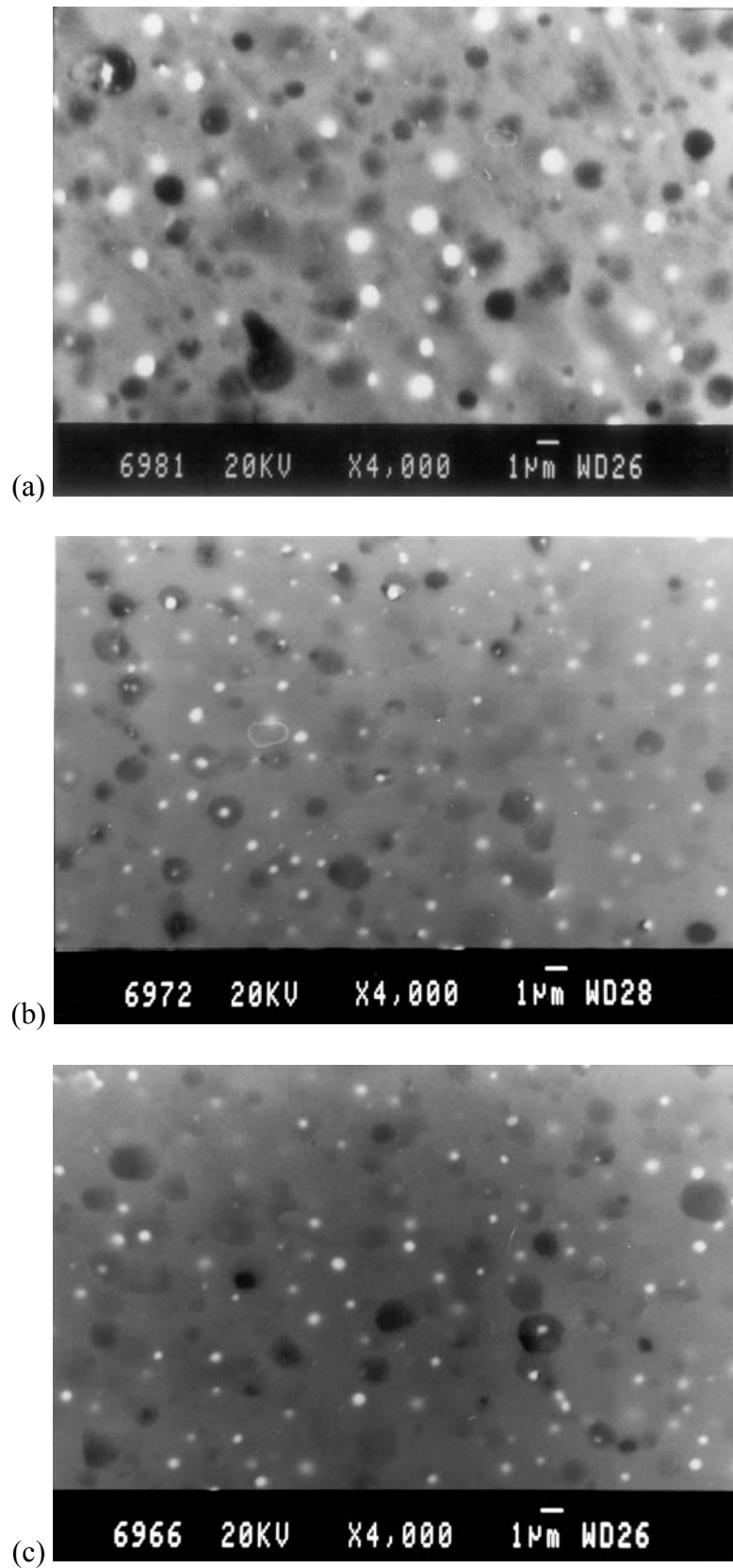
Figure 5.9. Typical back scattered images of remelt regions showing Bismuth (white) particles in aluminium matrix for scan speeds of (a) 5 mm/s (b) 13 mm/s (c) 20 mm/s.

(a)

(b)
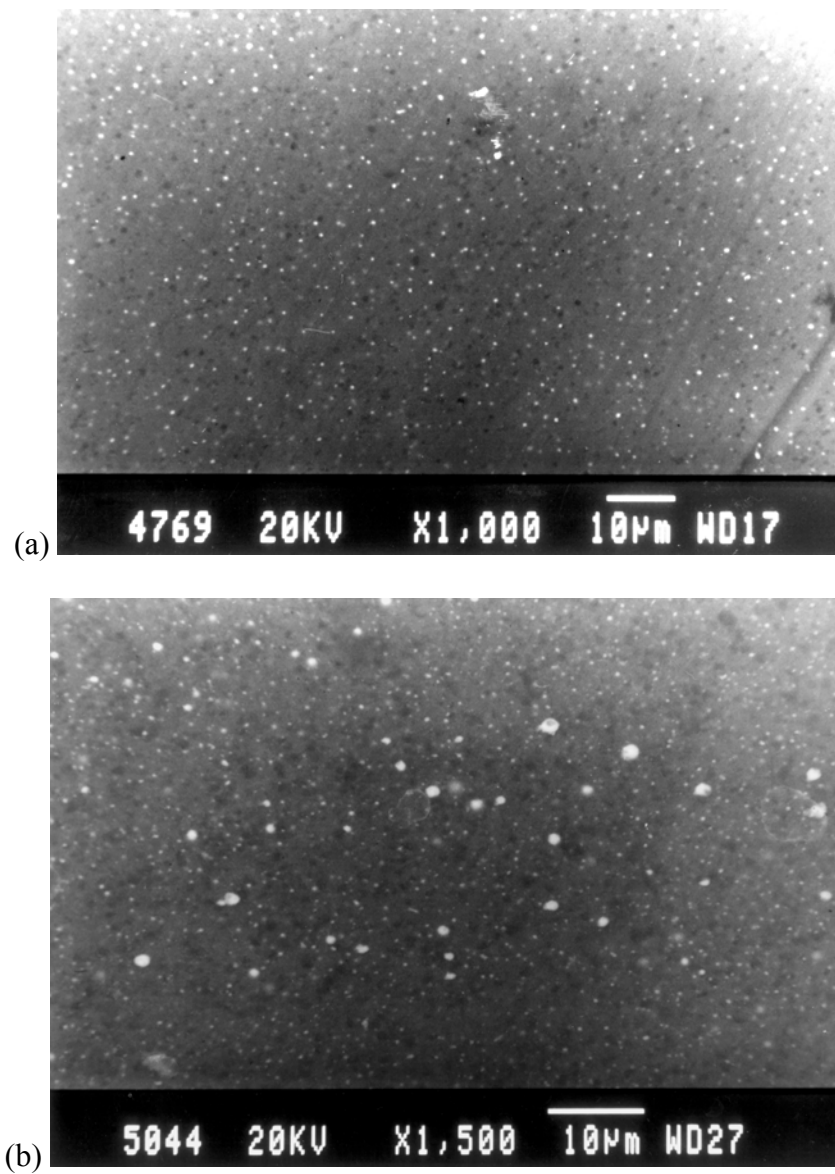
Figure 5.10 Back scattered electron images at low magnification showing uniform
distribution of Bismuth particles in the regions remelted at (a) 13.3 mm/s and (b) 20 mm/s.

(a)

(b)
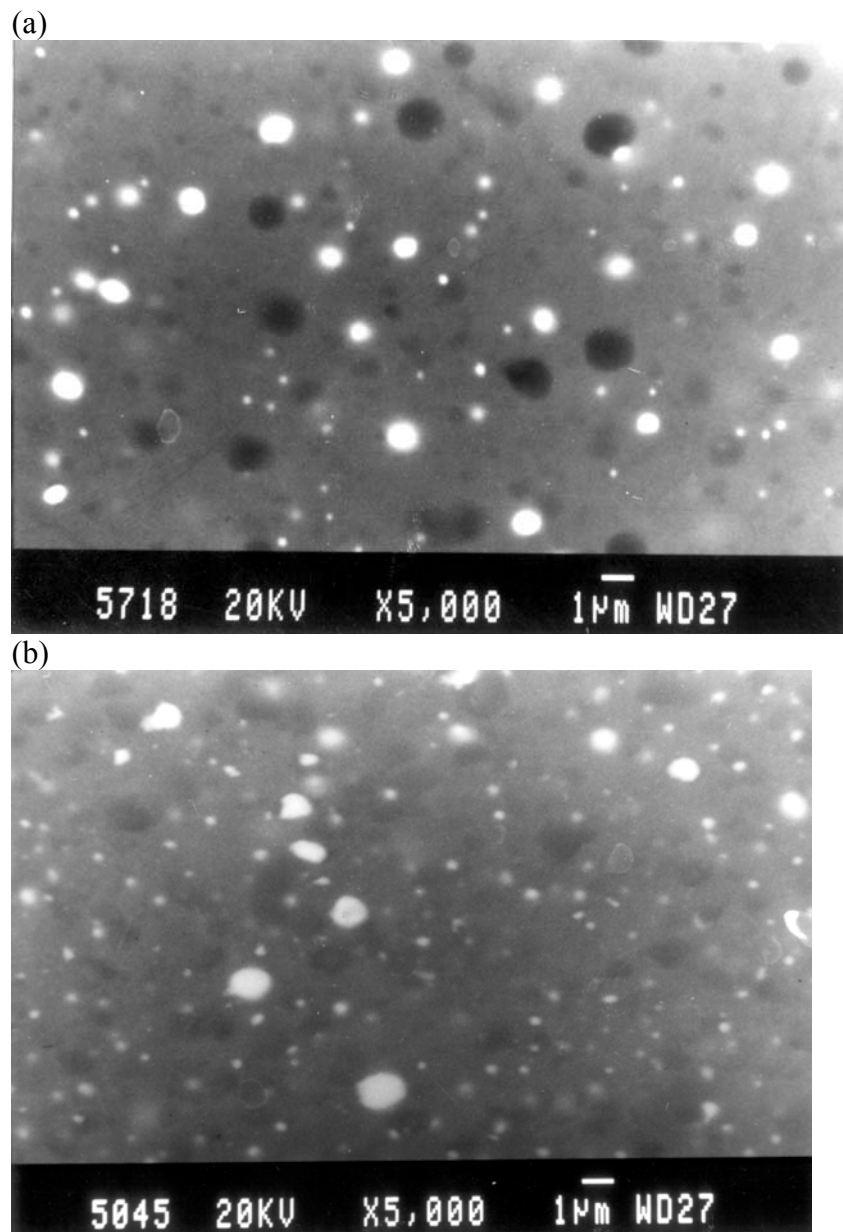
Figure 5.11 BSE images showing two sizes of Bismuth particles for remelting speeds of
(a) 13 mm/s (b) 20 mm/s.
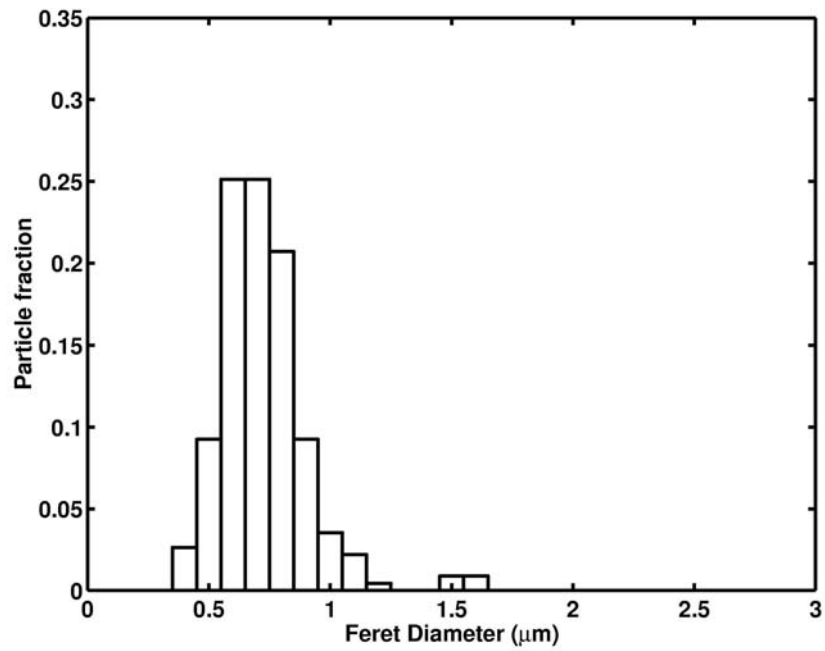
(a)
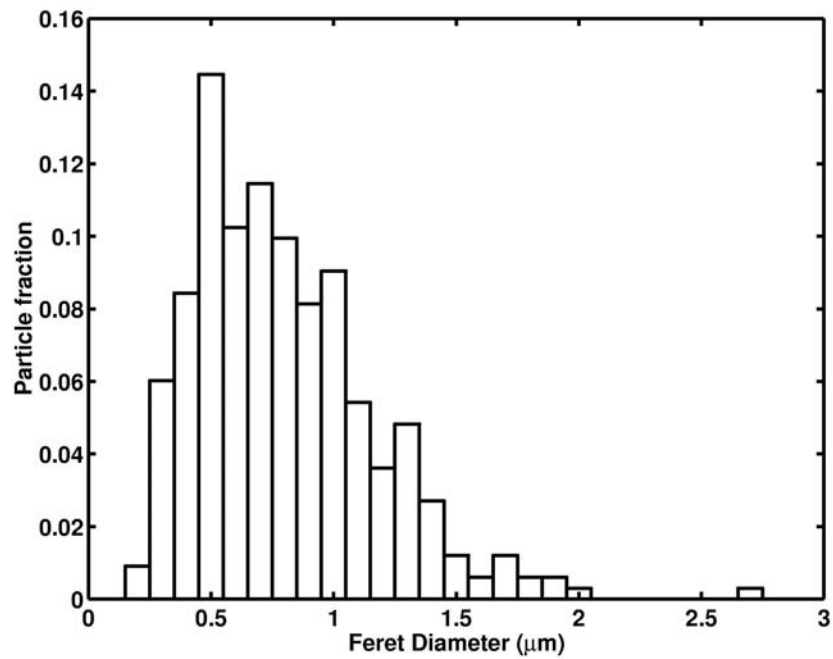
(b)

Figure 5.12 Distribution of Bismuth particle size (Feret Diameter) for (a) as clad at 5 mm/s (b) remelt at 5 mm/s.
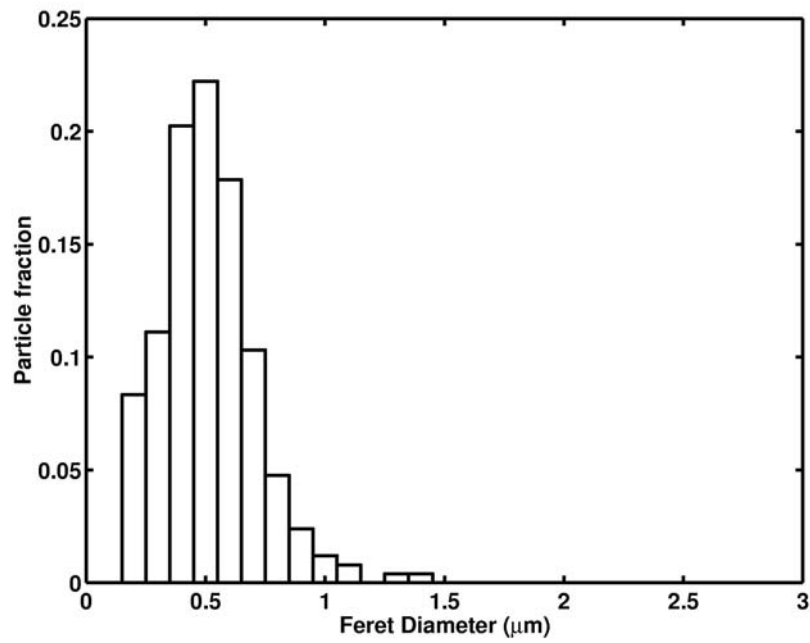
(c)
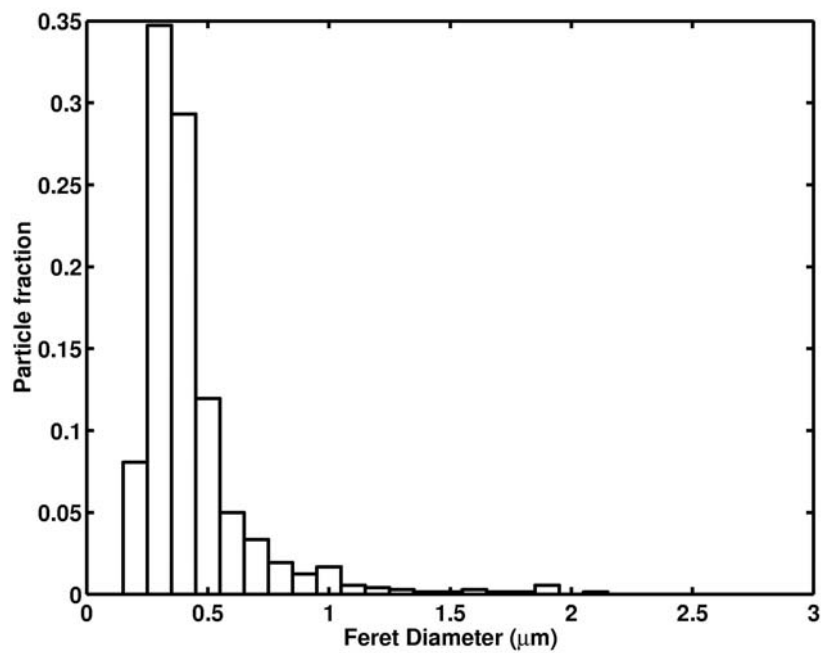
(d)

Figure 5.12 (contd.) Distribution of Bismuth particle size (Feret Diameter) for (c) remelt at 13.3 mm/s and (d) remelt at 20 mm/s.
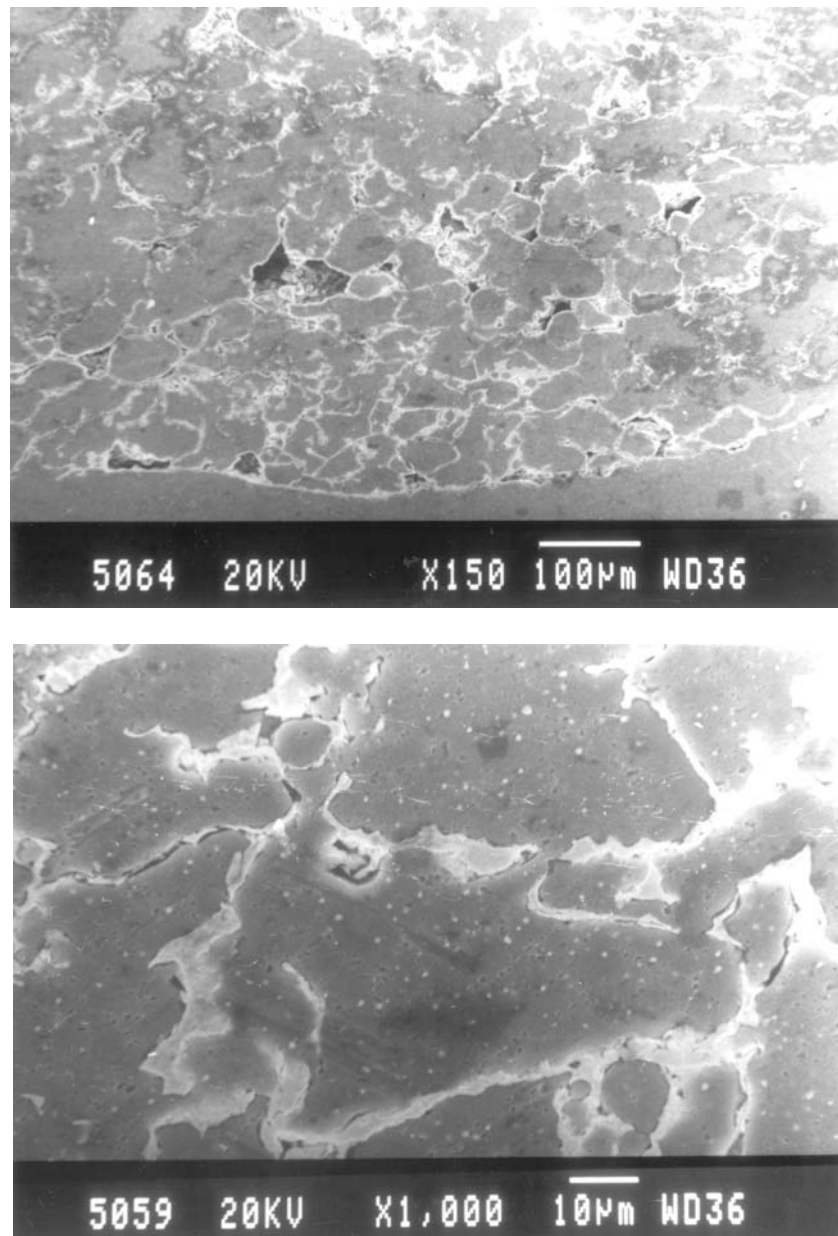
Figure 5.13 (a) Network formation of bismuth at the bottom of pool. (b) Bismuth in particle morphology and as a network in the aluminium matrix.
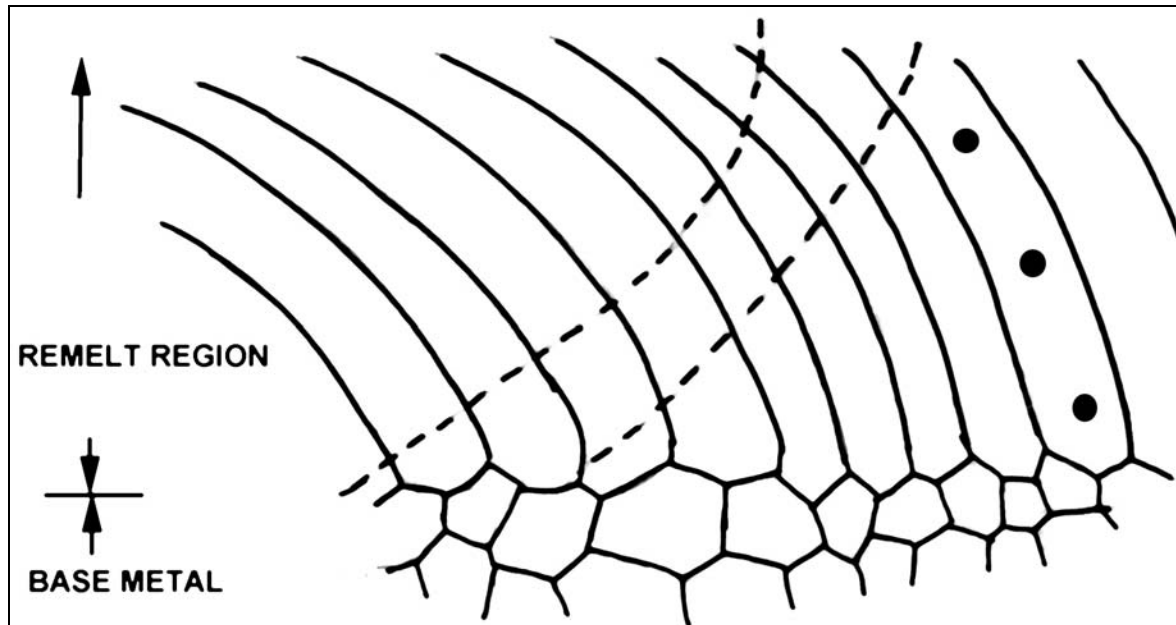
Figure 5.14 Schematic of aluminium grain growth in to the remelt region. The dark cirles show locations where the BSE microstructures were taken.
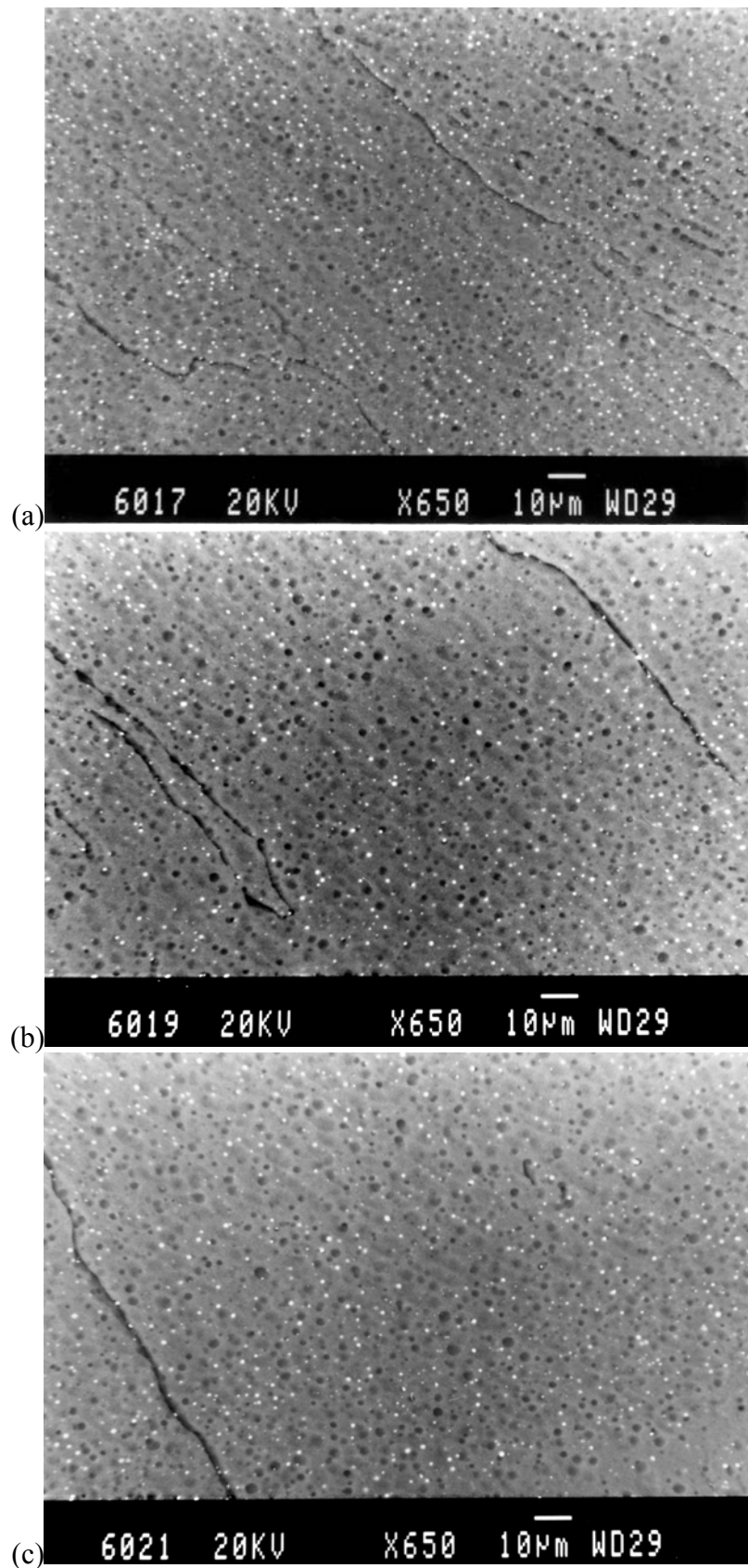
Figure 5.15 Back scattered images showing distribution of bismuth particles at a distance of (a) 1 mm (b) 0.5 mm and (c) 0 mm from the bottom of a single grain in the longitudinal section for laser remelt speed of 5 mm/s.
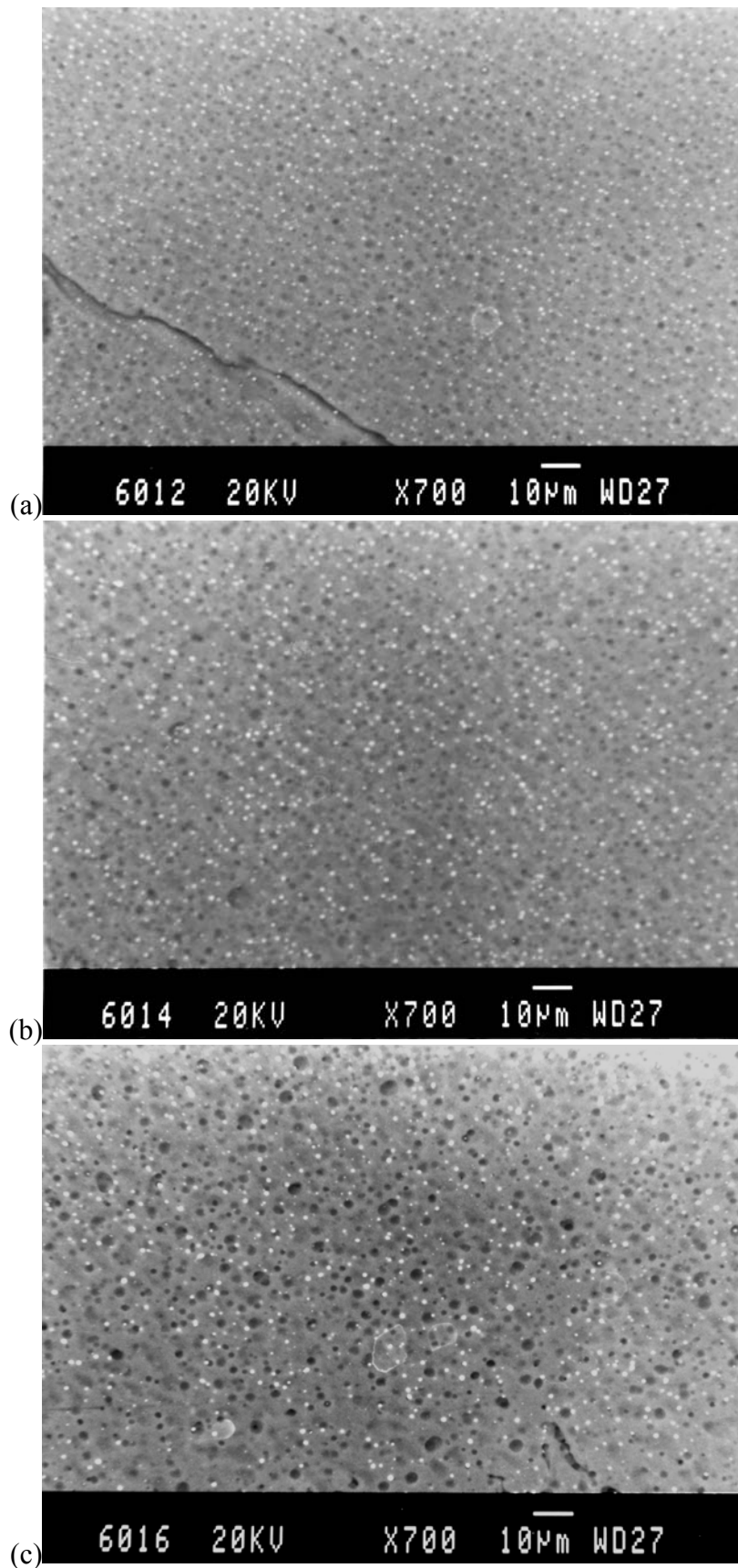
Figure 5.16 Back scattered images showing distribution of bismuth particles at the (a) 1 mm (b) 0.5 mm and (c) 0 mm from the bottom of a single grain in the longitudinal section for laser remelt speed of 13 mm/s.
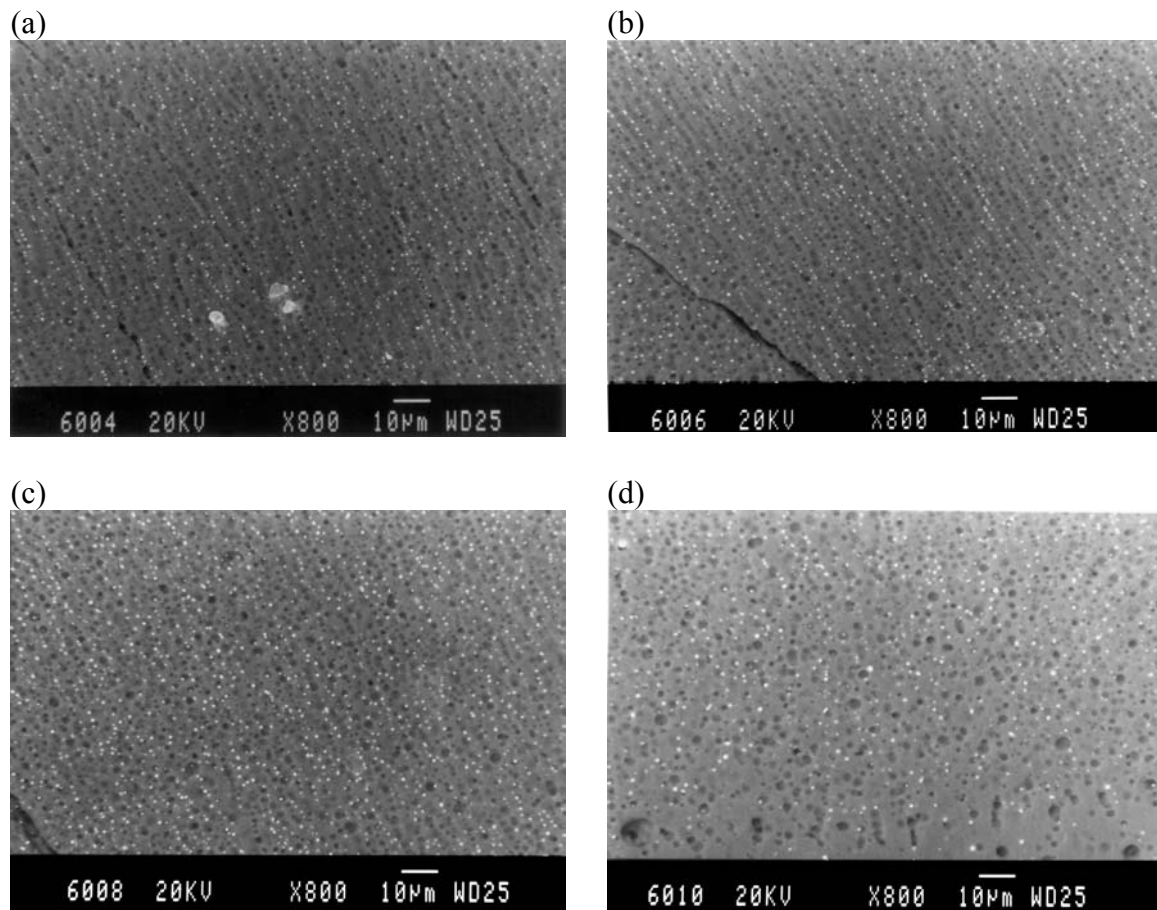
Figure 5.17 Back scattered images showing distribution of bismuth particles at a distance of (a) 1 mm (b) 0.6 mm (c) 0.3 mm and (d) 0 mm from the bottom of a single grain in the longitudinal section for laser remelt speed of 20 mm/s.
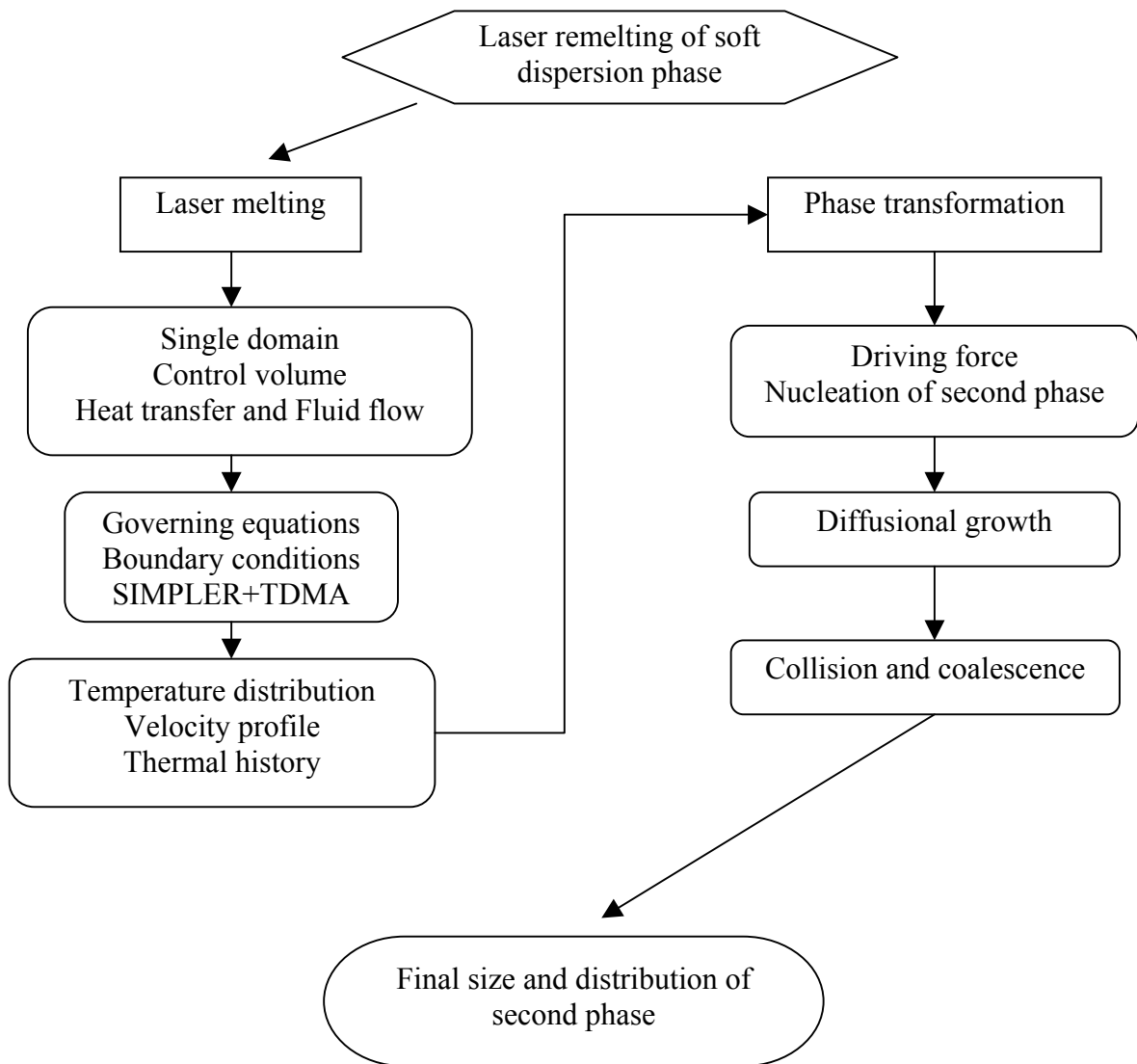
Figure 5.18 Flow chart of the modelling scheme.

(a)

(b)

(c)
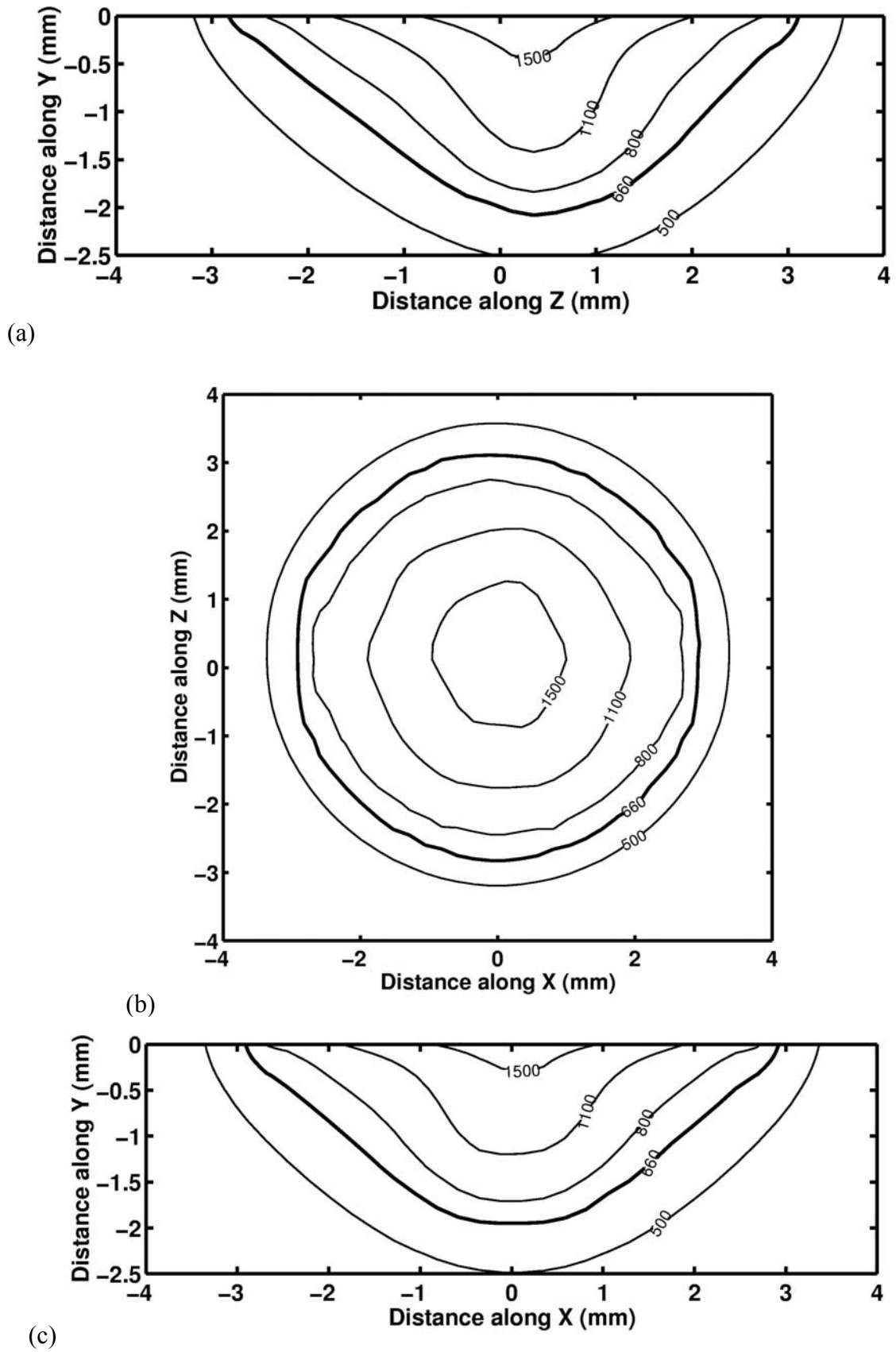
Figure 5.19 (a) Longitudinal section, (b) Top view and (c) Transverse section of temperature contours for laser scan speed of 5 mm/s.

(a)

(b)

(c)
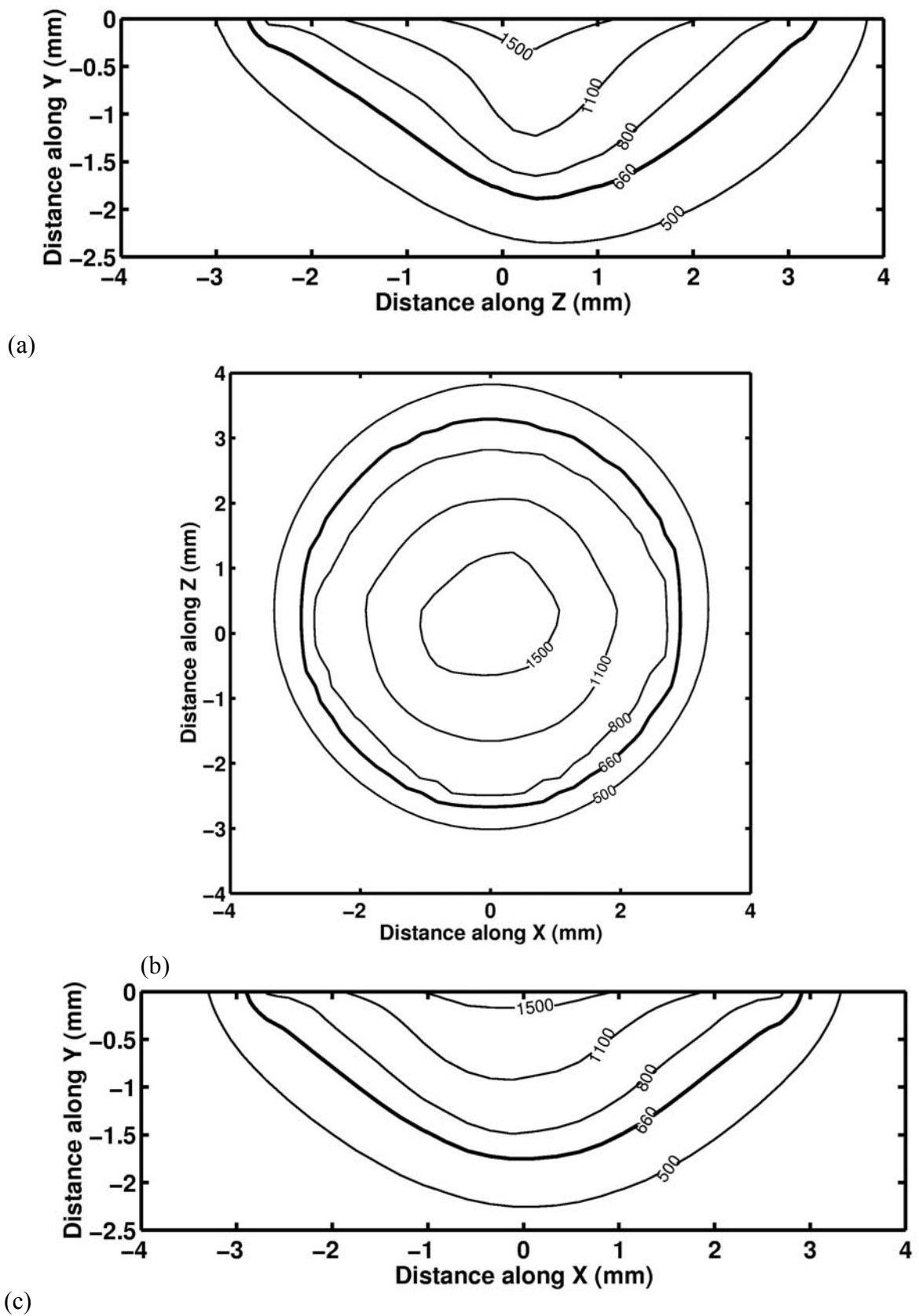
Figure 5.20 (a) Longitudinal section, (b) Top view and (c) Transverse section of temperature contours for laser scan speed of 13 mm/s.

(a)

(b)

(c)
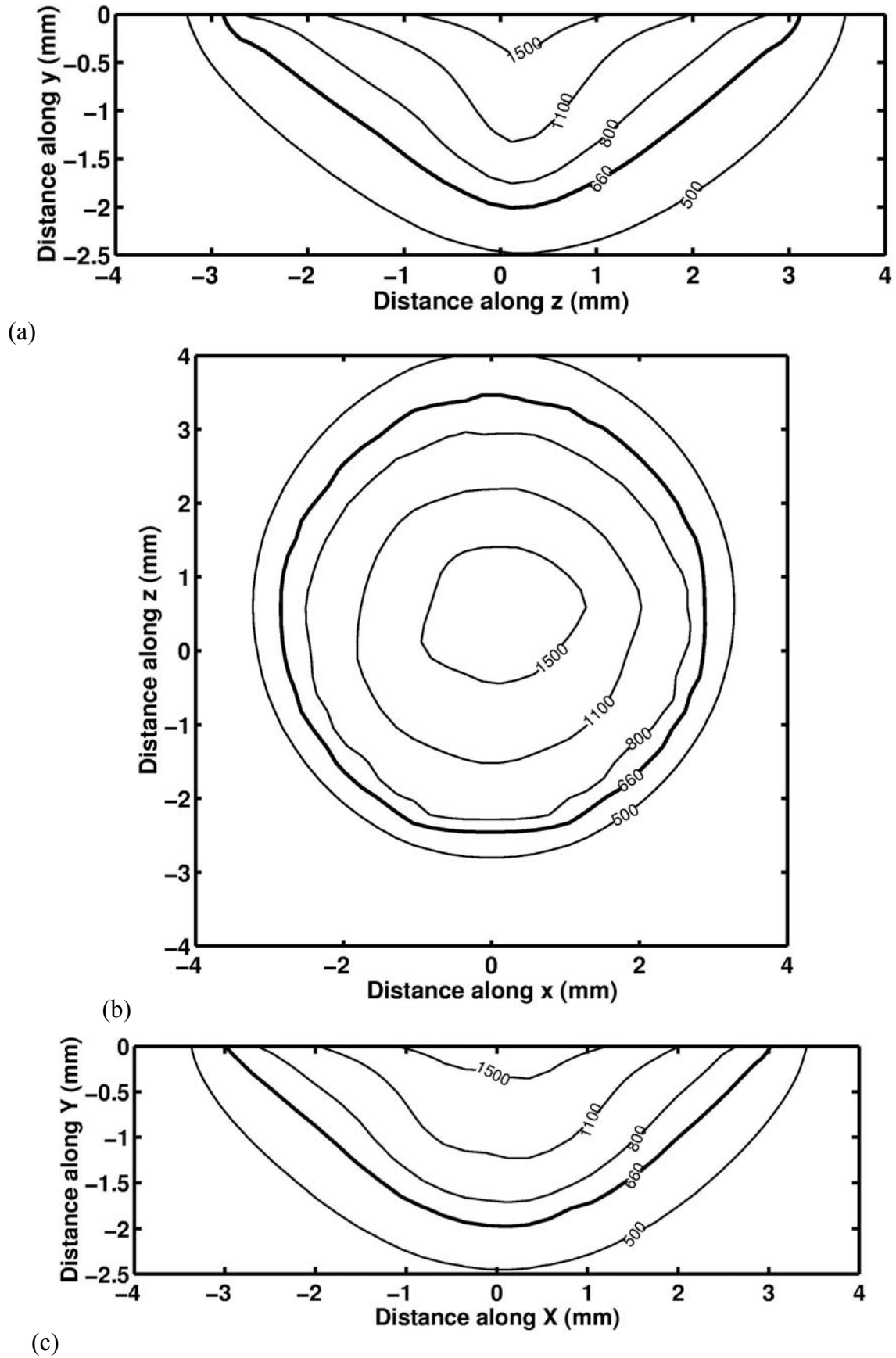
Figure 5.21(a) Longitudinal section, (b) Top view and (c) Transverse section of temperature contours for laser scan speed of 20 mm/s.

(a)

(b)

(c)
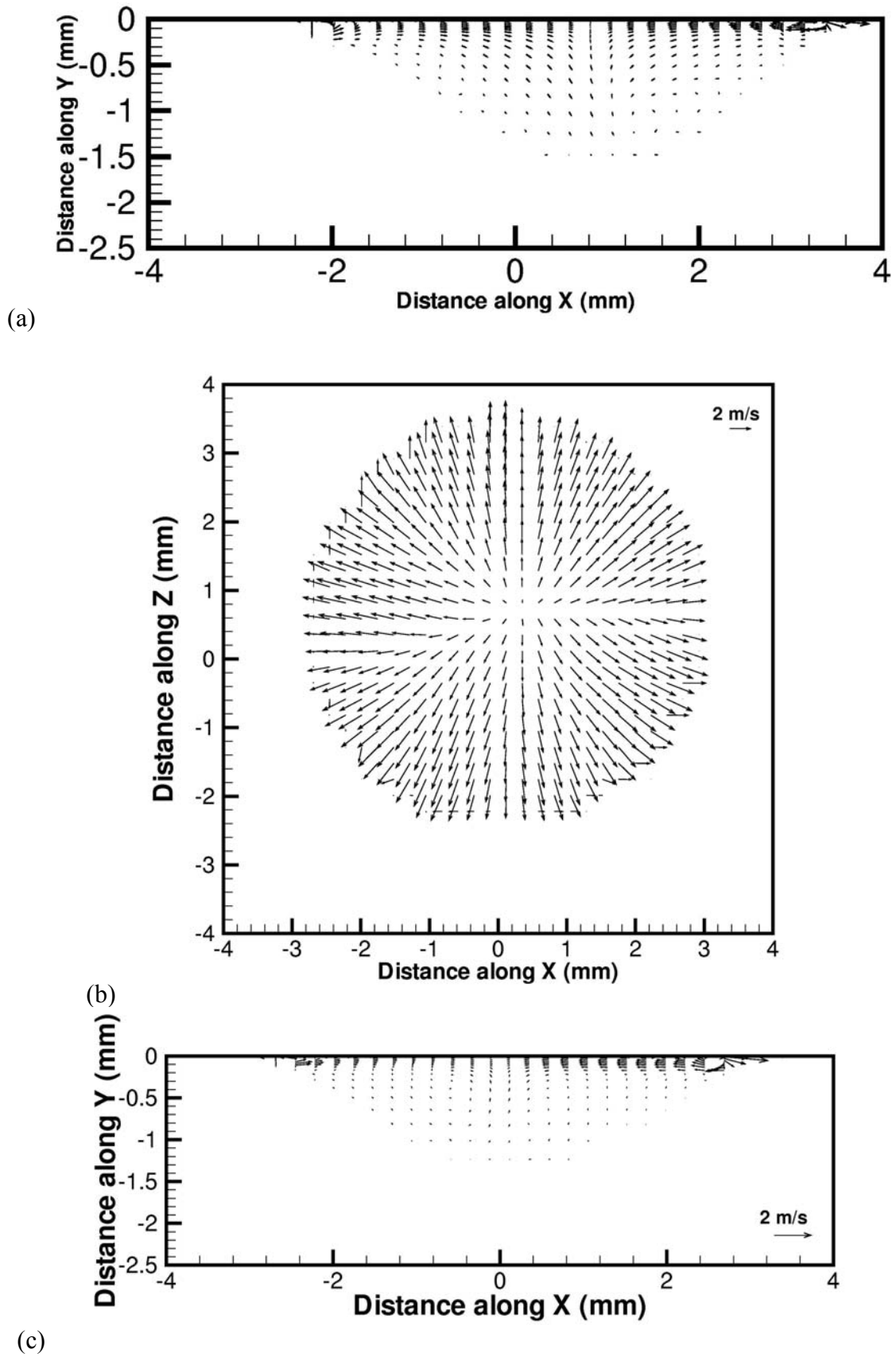
Figure 5.21 (d) Longitudinal section, (e) Top view and (f) Transverse section of velocity profiles for laser scan speed of 20 mm/s.
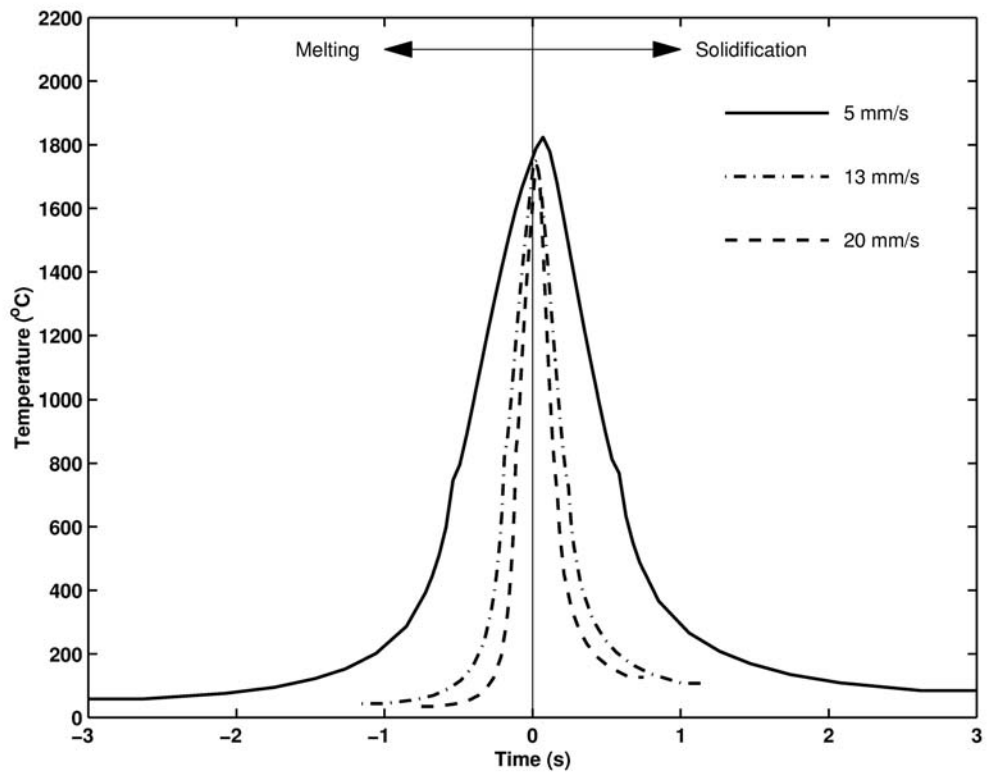
(a)
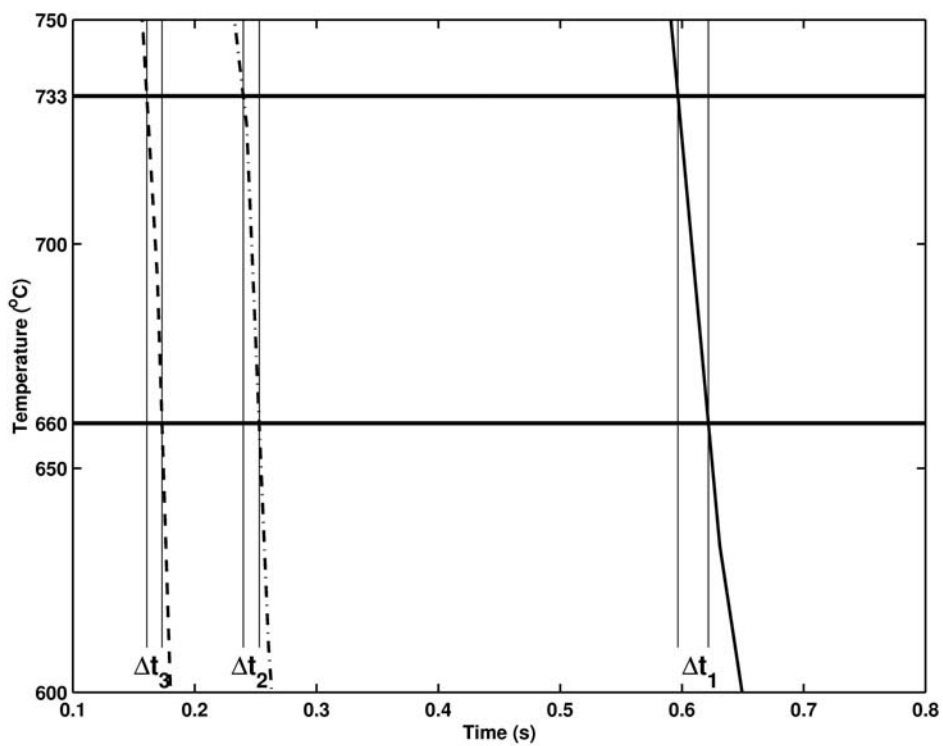
(b)

Figure 5.22 A profile of temperature showing the time of residence in the range of phase separation for three laser scan speeds used in the work.
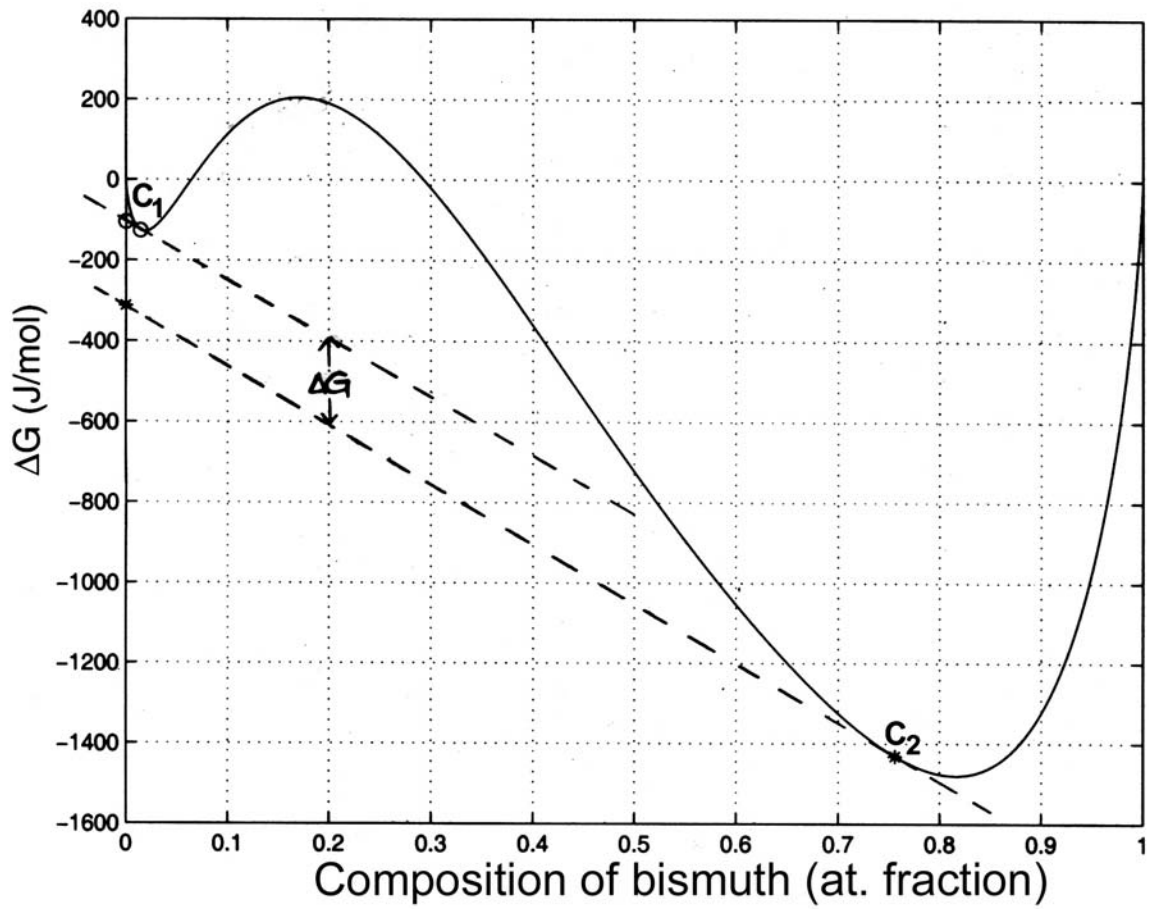
Figure 5.23 An illustration of Thomson-Spaepen construction to calculate driving force for nucleation. The plot shown is for Al+1.414at%Bi at 1055K.
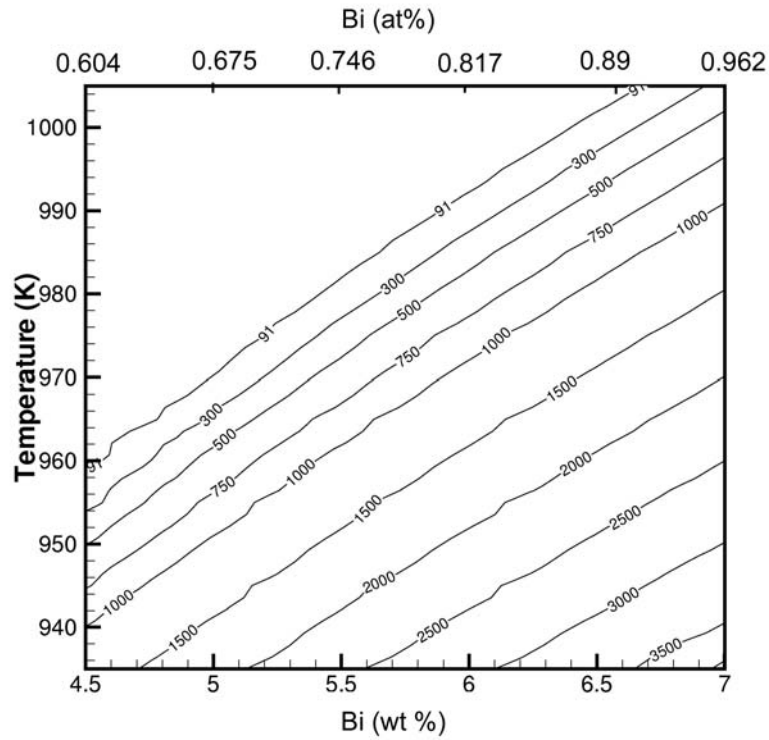
(a)
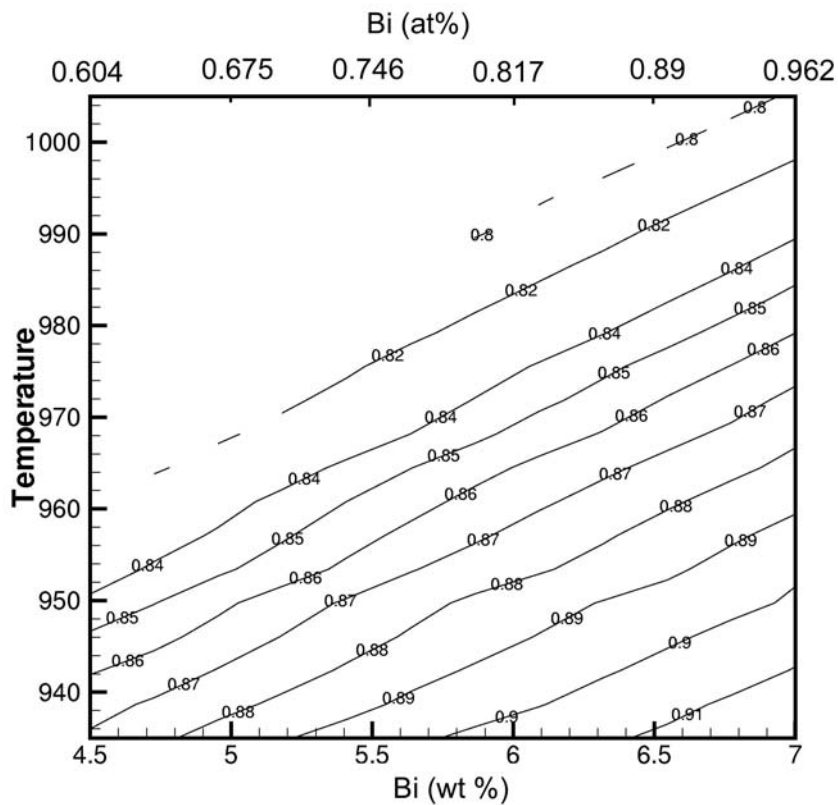
(b)

Figure 5.24 Contours of (a) driving force for nucleation (b) composition of nucleating particle as a function of temperature of phase separation and composition of the liquid.
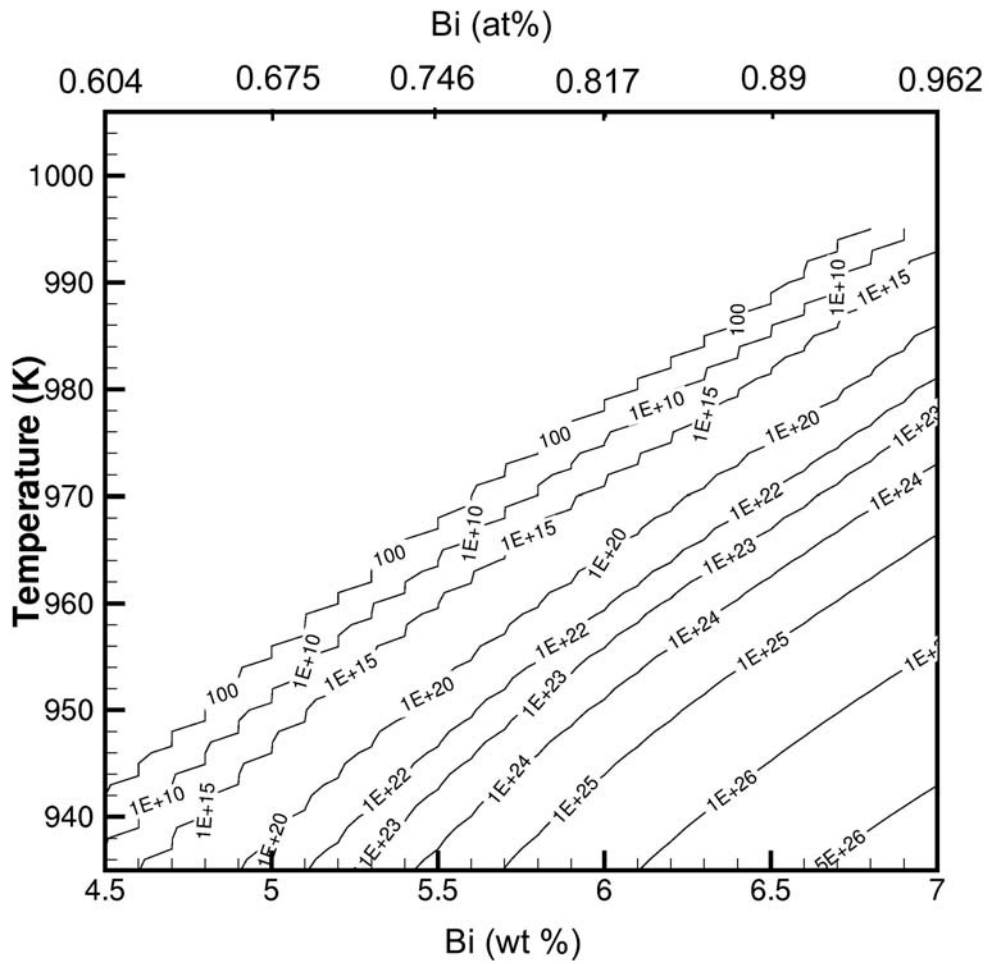
(c)

Figure 5.24 (contd.) Contours of nucleation rate a function of temperature of phase separation and composition of the bismuth in the Al-Bi alloy.
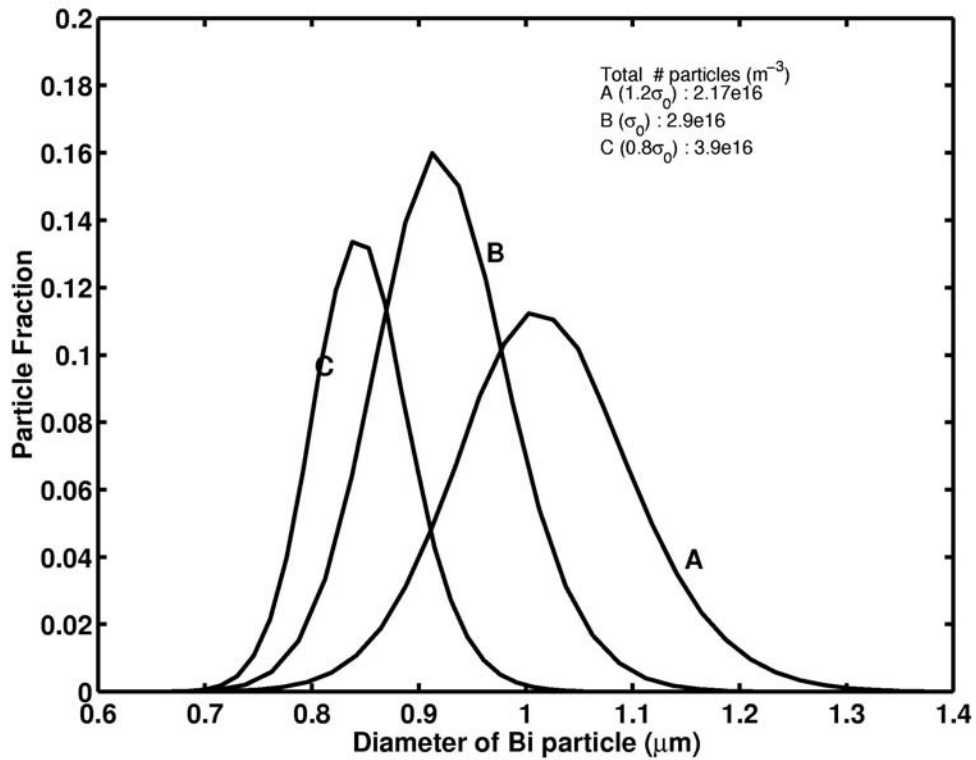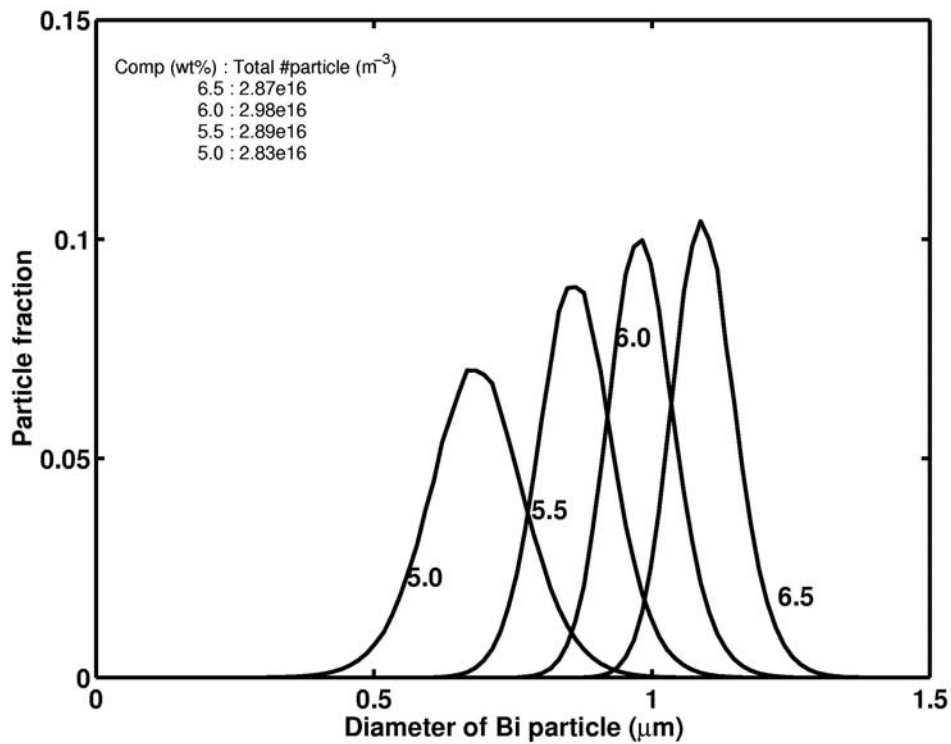
Figure 5.25 Size distribution of bismuth particles after nucleation and simultaneous diffusional growth evaluated till exhaustion of supersaturation, as a function of change in (a) surface tension of liquid Al-Bi and (b) composition of liquid.
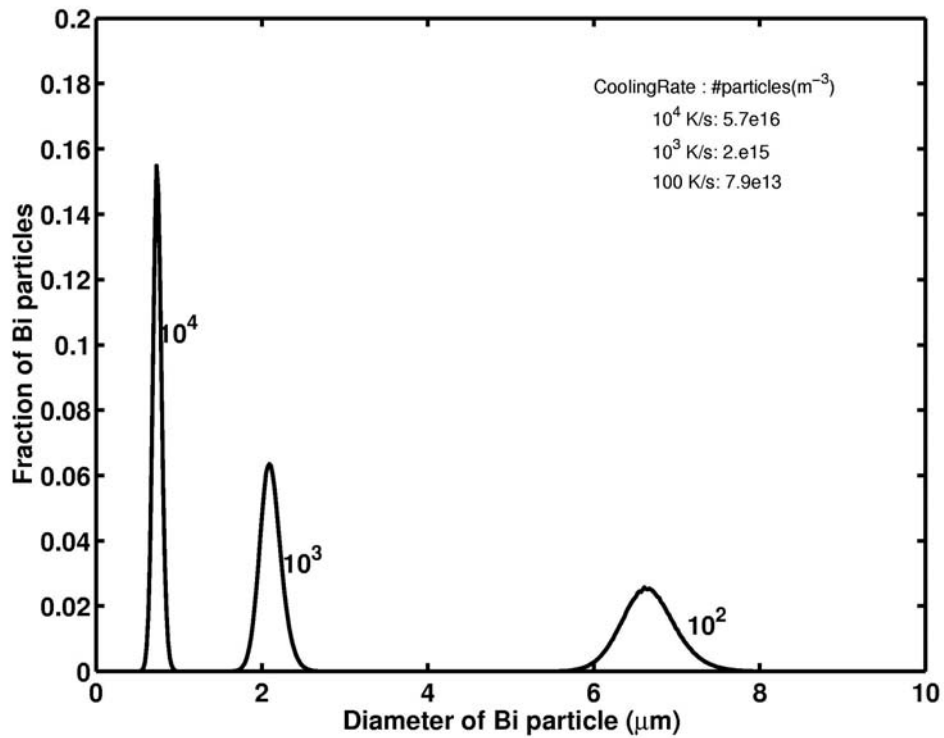
(c)

Figure 5.25 (contd.) Size distribution of bismuth particles after nucleation and simultaneous diffusional growth evaluated till exhaustion of supersaturation, as a function of cooling rate. The maximum number of nuclei used to normalise the plots are shown in the legend.
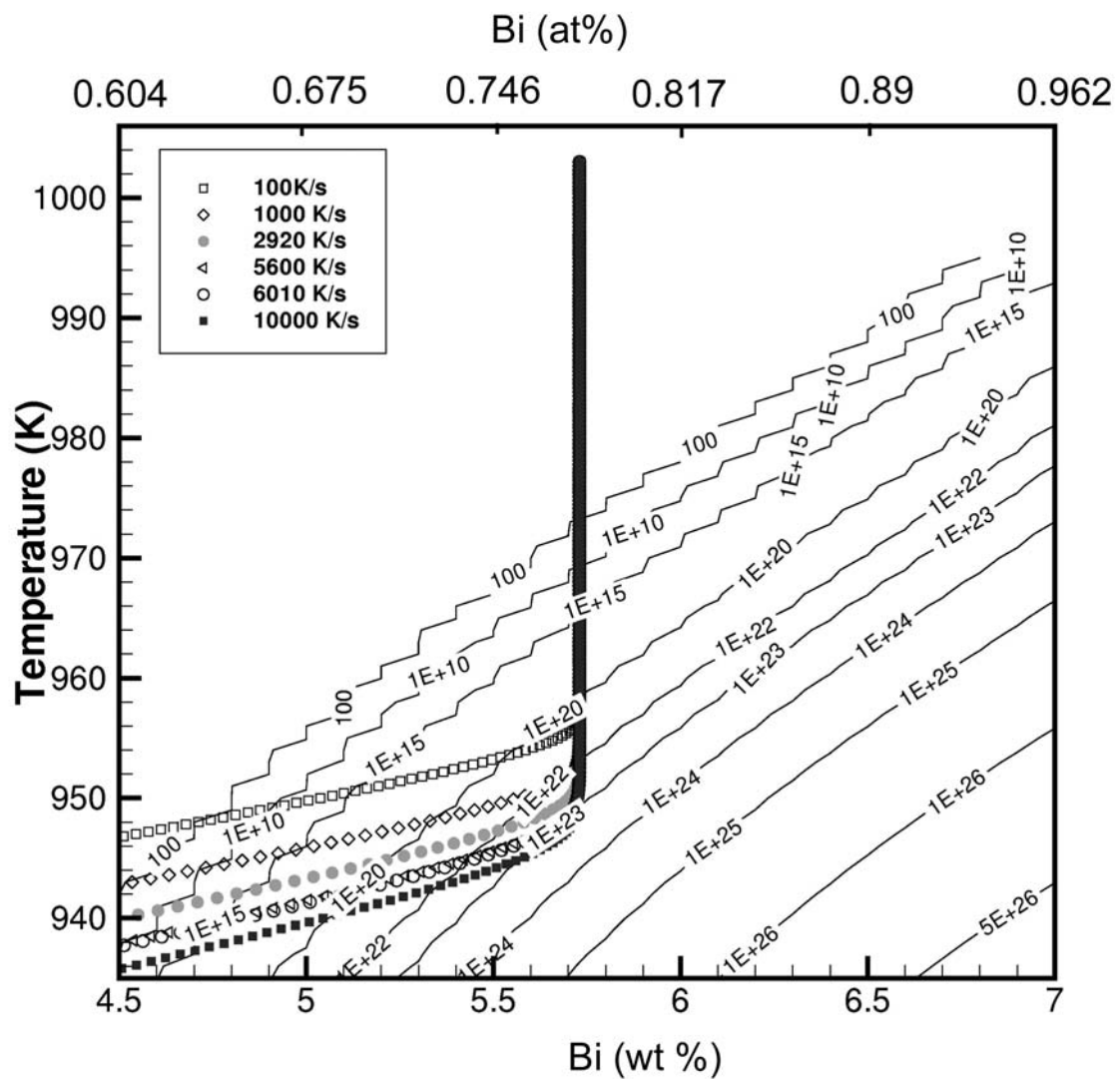
Figure 5.26 Temperature-composition values taken by a unit volume of constant initial composition for phase separation at different cooling rates evaluated till exhaustion of supersaturation. The path is superimposed on the contours of nucleation rate as a function of temperature and composition.
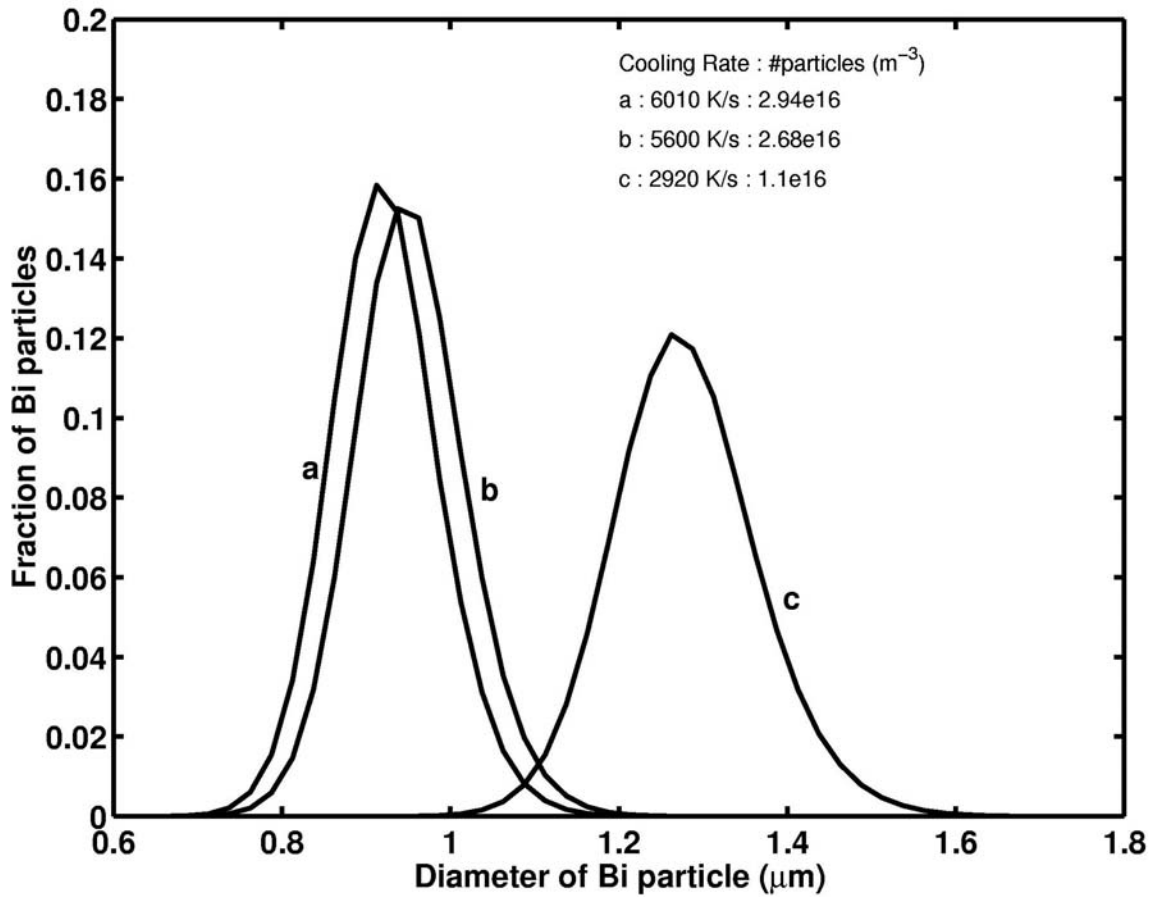
Figure 5.27 Size distribution of bismuth particles after simultaneous nucleation and growth evaluated till exhaustion of supersaturation, for the initial composition (0.78 at.% Bi) used in the experiments at cooling rates calculated from the laser melting calculation.
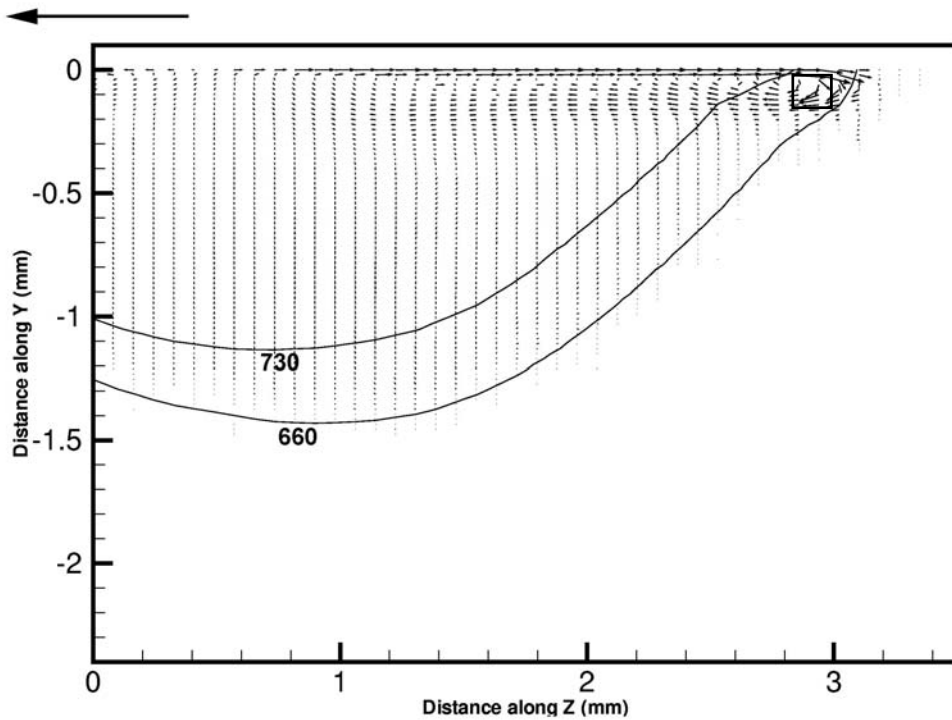
Figure 5.28 Velocity profile shown on the solidification front within the temperature range for phase separation. The laser remelting speed used is 20 mm/s. The arrow on the top of the figure shows the laser scan direction.
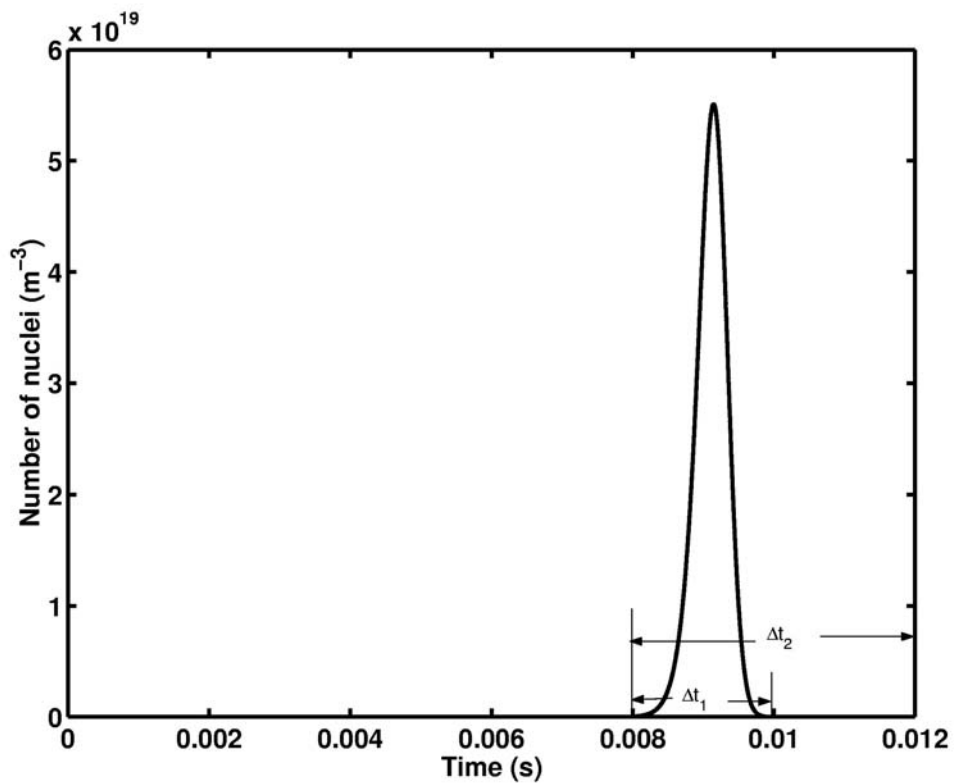
Figure 5.29 Number of nuclei precipitating out of Al-Bi alloy liquid during the time interval of phase separation. Δt_1 and Δt_2 are time intervals chosen to particles introduction in to the control volume and collision.
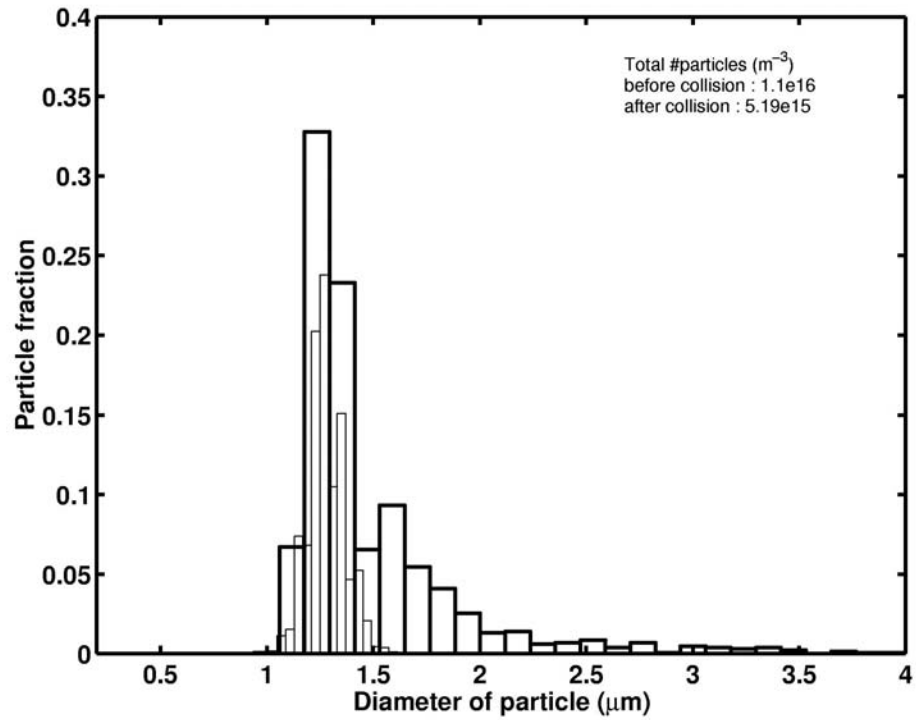
(a)
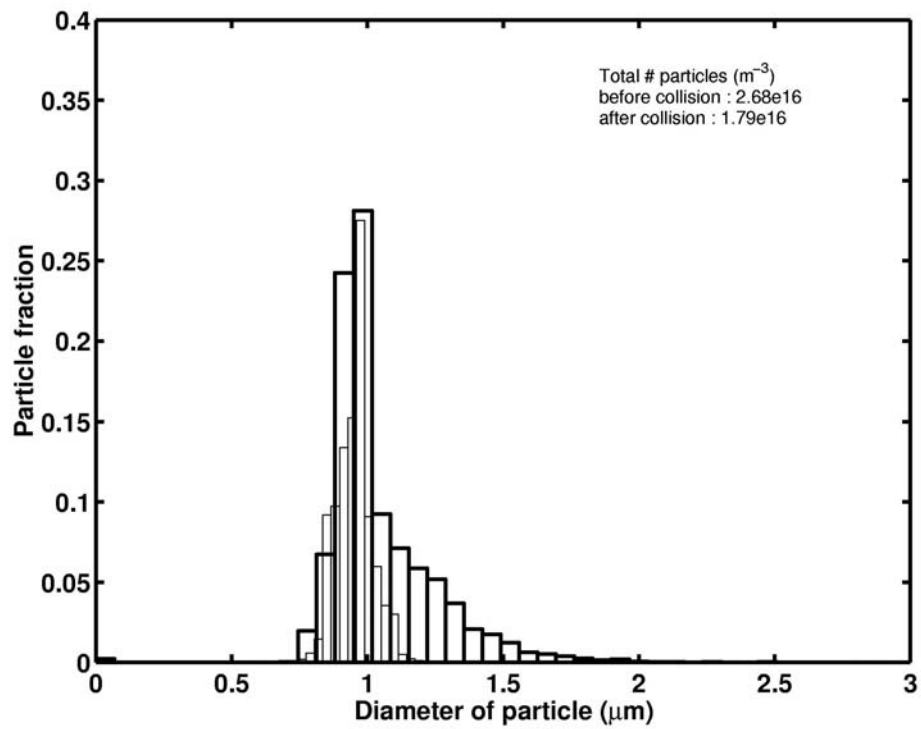
(b)

Figure 5.30 Size distribution of particles within a control volume before (thin line) and after (thick line) collision. The corresponding laser remelting speeds are (a) 20 mm/s (b) 13 mm/s.
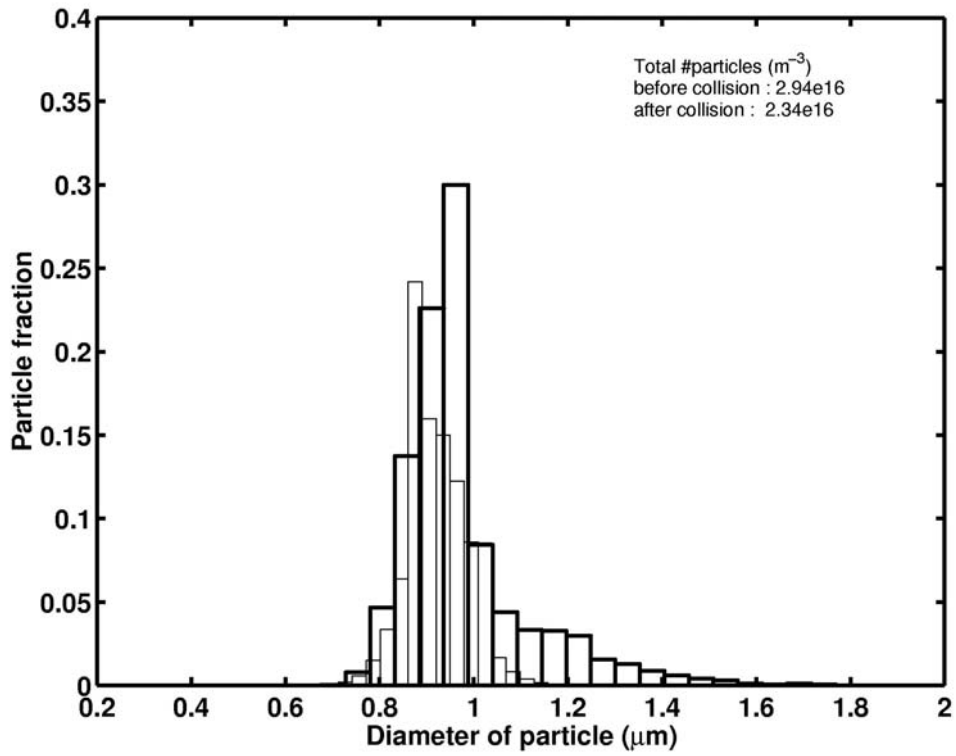
(c)

Figure 5.30 (contd.) Size distribution of particles within a control volume before (thin line) and after (thick line) collision. The corresponding laser remelting speed is (c) 20 mm/s.

Chapter 6
Summary

Laser welding of iron and copper at low and high scan speeds showed similar microstructural features. The weld pool shape is found to be asymmetric with more melting of iron, though the heat source is placed symmetrically on the butt joint. This phenomenon was attributed to differences in thermal diffusivity between the two metals. The overall composition is uniform at a macro scale. The weld interface also shows asymmetry. The iron side has a smooth interface with a transition from planar to cellular growth into the weld and a gradual increase in composition. The copper side showed a rough interface with extensive banding, indicating a peritectic reaction. Microstructural bands due to fluctuations in growth are present throughout the weld pool characterised by a change of length scale and composition. The difference in the growth mode from the copper side to iron side was explained using thermodynamic arguments. Droplet formation in the weld region, as shown by TEM studies, indicates access to submerged liquid miscibility gap during solidification of the weld.

Detailed analysis of laser welding of copper and nickel was presented. Welding have been performed at different scanning speeds such that the welding mode changes from conduction mode at high scan speed to keyhole mode at low scan speeds. The weld pool shape was found to be asymmetric and the microstructural features observed for the case of iron-copper system were found to be similar to those of copper-nickel system. Cellular microstructure was observed in the weld pool at all welding speeds. Composition across the weld indicates good mixing on the nickel side in the weld pool. The growth of nickel was continuous into the weld pool with a gradual increase in composition. On the copper side, such a continuous growth was not observed. The bands near the copper side were similar in nature to those at the nickel side. They originate due to growth rate fluctuations.

Microstructural banding with fluctuations in length scale and composition were observed. TEM study shows that the weld pool is highly strained.

A computational model of the transport phenomena that take place during laser welding of dissimilar metals was developed using a finite volume formulation. Nickel was observed to melt first and the heat is transported to the copper side by convection in the molten nickel due to Marangoni and buoyancy forces. The final shape of the weld pool is dictated by the convective flow and is observed to be asymmetric. The copper side spends less time in the liquid state with insufficient mixing whereas the nickel side is well mixed. The composition profile across the weld pool shows good qualitative agreement with the experimentally observed one.

Microstructure development as a function of laser remelting rate was studied for aluminium-bismuth system. The alloy which was made using laser cladding of elemental powders, was remelted at 5mm/s, 13 mm/s and 20 mm/s. The microstructures in transverse and longitudinal sections observed in SEM showed uniform distribution of bismuth particles in the matrix of aluminium. The miscibility gap of liquid Al-Bi alloy led to precipitation of nearly globular particles of bismuth. Size distribution of bismuth particles for alloys remelt at the three different scanning speeds, was determined using image analysis. Higher scan speeds led to a finer size distribution.

A computational model was developed to calculate the size distribution of bismuth particles during laser remelting. The remelted pool shape and cooling rates during laser surface remelting were calculated. The driving force for nucleation was calculated and a map of nucleation rate was constructed as a function of composition and temperature. Size distribution of bismuth was calculated at different cooling rates taking into consideration, simultaneous nucleation and growth by diffusion in the melt, till the super saturation is exhausted. Cooling rates used were obtained from the laser remelting program. Collision of particles due to convection in the laser melt pool is taken into account by a particle tracking algorithm. Final size distribution of bismuth particles showed a good agreement with the experimental particle size distribution.

Chapter 7
Scope for future work

The present work forms one of the early studies on the microstructure evolution during laser processing of dissimilar metals. The experimental studies are performed on chosen dissimilar metal combinations. On the experimental front, characterisation tools such as Electron Back Scattered Diffraction analysis (EBSD), composition analysis of very small areas and direct visualisation of the process could provide valuable information for a detailed analysis. The work could be extended to a careful analysis of dissimilar welding of metals that form intermetallic compounds. An understanding of formation of brittle intermetallic phases that lead to cracking and failure of the weld is important.

There are limitations of the computational work as outlined by the assumptions presented in the sections corresponding to the computational aspects. The computational work could be extended to take several features such as free surface deformation, porosity, remelting of solidified alloy and micro segregation in to account. The mixing patterns shown by banding are at a length scale much smaller, compared to the system scale. Studies using a two-fluid approach could lead to further insight in to formation of these patterns. The phase change temperature range is fixed *a priori* in most of the macro models that deal with heat transfer and solidification. Incorporation of interface undercooling from thermodynamic arguments would bring the macro model closer to reality. A micro model to study the microstructure evolution during laser processing of dissimilar metals using techniques such as phase field calculations is highly relevant.

Appendix

Spot welding

The conservation equations for mass, momentum, enthalpy and species during spot welding are given in their complete form in this section.

Continuity:

$$\frac{\partial \rho}{\partial t} + \frac{\partial}{\partial x}(\rho u) + \frac{\partial}{\partial y}(\rho v) + \frac{\partial}{\partial z}(\rho w) = 0 \tag{A.1}$$

Momentum:

$$\frac{\partial}{\partial t}(\rho u) + \overbrace{\frac{\partial}{\partial x}(\rho uu) + \frac{\partial}{\partial y}(\rho vu) + \frac{\partial}{\partial z}(\rho wu)}^{advective} = \overbrace{\frac{\partial}{\partial x}\left(\mu \frac{\partial u}{\partial x}\right) + \frac{\partial}{\partial y}\left(\mu \frac{\partial u}{\partial y}\right) + \frac{\partial}{\partial z}\left(\mu \frac{\partial u}{\partial z}\right)}^{viscous} \overbrace{- \frac{\partial p}{\partial x} + S_x}^{source} \tag{A.2}$$

$$\frac{\partial}{\partial t}(\rho v) + \frac{\partial}{\partial x}(\rho uv) + \frac{\partial}{\partial y}(\rho vv) + \frac{\partial}{\partial z}(\rho wv) =$$
$$\frac{\partial}{\partial x}\left(\mu \frac{\partial v}{\partial x}\right) + \frac{\partial}{\partial y}\left(\mu \frac{\partial v}{\partial y}\right) + \frac{\partial}{\partial z}\left(\mu \frac{\partial v}{\partial z}\right) - \frac{\partial p}{\partial y} + S_y \tag{A.3}$$

$$\frac{\partial}{\partial t}(\rho w) + \frac{\partial}{\partial x}(\rho uw) + \frac{\partial}{\partial y}(\rho vw) + \frac{\partial}{\partial z}(\rho ww) =$$
$$\frac{\partial}{\partial x}\left(\mu \frac{\partial w}{\partial x}\right) + \frac{\partial}{\partial y}\left(\mu \frac{\partial w}{\partial y}\right) + \frac{\partial}{\partial z}\left(\mu \frac{\partial w}{\partial z}\right) - \frac{\partial p}{\partial z} + S_z \tag{A.4}$$

The source terms in the above equations according to the enthalpy-porosity formulation are expressed as follows:

$$S_x = -\left(\frac{K(1-\varepsilon)^2}{\varepsilon^3 + b}\right) u \tag{A.5}$$

$$S_y = -\left(\frac{K(1-\varepsilon)^2}{\varepsilon^3 + b}\right)v + \rho g[\beta_T(T - T_r) - \beta_C(C - C_r)] \tag{A.6}$$

$$S_z = -\left(\frac{K(1-\varepsilon)^2}{\varepsilon^3 + b}\right)w \tag{A.7}$$

In the above equations, t is time, ρ is density, u,v and w are velocities along x,y and z directions, $\vec{u}$ is the velocity field in vector notation, μ is viscosity, p is pressure, K is permeability, b is a small number to avoid division by zero, g is acceleration due to gravity, β_T is compressibility, β_C is the difference in the densities of the two metal, T_r and C_r are reference temperature and composition for buoyancy and ε is liquid fraction. The first terms in each of the equations (A.5)-(A.7) represent the porous medium-like resistance in the mushy region at the solid-liquid interface. In the fully liquid region, the value of ε is 1, making the porous medium resistance terms zero. On the other hand, in the fully solid region, $\varepsilon = 0$, thus forcing the porous medium resistance terms in equations (A.5)-(A.7) to be very large. This large negative source term offers a high flow resistance, making the velocities in the entire solid region effectively zero. In the mushy region, however, ε lies between 0 and 1, and the porous medium resistance varies smoothly from zero in the liquid region to a high value in the solid region, thus making the velocities vary accordingly.

Energy:

$$\frac{\partial}{\partial t}(\rho H) + \frac{\partial}{\partial x}(\rho u H) + \frac{\partial}{\partial y}(\rho v H) + \frac{\partial}{\partial z}(\rho w H) =$$
$$\frac{\partial}{\partial x}\left(k\frac{\partial T}{\partial x}\right) + \frac{\partial}{\partial y}\left(k\frac{\partial T}{\partial y}\right) + \frac{\partial}{\partial z}\left(k\frac{\partial T}{\partial z}\right) + S_h \tag{A.8}$$

$$S_h = -\frac{\partial}{\partial t}(\rho \Delta H) \tag{A.9}$$

The enthalpy, H, of a material can be expressed as:

$$H = h_s + \Delta H \tag{A.10}$$

$$h_s = cT \tag{A.11}$$

where h_s is the sensible heat, and ΔH is the latent heat content and c is specific heat. In order to simulate a phase change, the latent heat contribution is specified as a function of temperature, T, and the resulting expression is:

$$\Delta H = f(T) \tag{A.12}$$

Since latent heat is associated with the liquid fraction, ε, one can write:

$$\Delta H = f(T) = \begin{cases} L & for & T > T_l \\ L\varepsilon & for & T_s \le T \le T_l \\ 0 & for & T < T_s \end{cases} \tag{A.13}$$

where T_l is the liquidus temperature at which solid formation begins, T_s is the solidus temperature at which full solidification occurs, and L is the latent heat of fusion. In the present problem, the domain consists of pure copper and nickel in a butt joint. During spot welding, melting and solidification take place one after other and not simultaneously. Also mixing occurs only after melting of pure components on each side takes place. Hence, pure metal melting only needs to be considered during the melting stage. The range of temperature over which phase change takes places is taken to be numerically small for this purpose. Substituting the expression for H from equation (A.10) and equation (A.11) in the energy equation (A.8), one arrives at the following final form of the energy equation:

$$\frac{\partial}{\partial t}(\rho c T) + \nabla \cdot (\rho c T \bar{u}) = \nabla \cdot (k \nabla T) - \frac{\partial}{\partial t}(\rho \Delta H) \tag{A.14}$$

where ΔH is the latent heat content of a control volume, and ε is the liquid fraction calculated as $\frac{\Delta H}{L}$, with L being the latent heat of melting for the corresponding metal. During solidification of spot weld, the enthalpy, H, used in equation (A.10) is defined in the liquid state at any location using mixture theory as given in the equation A.15 where, H_{Cu} and H_{Ni} are the enthalpy values of copper and nickel, respectively, at a given temperature. The melting point of any alloy is approximated, using equation A.16, to a weighted average of the melting points of copper and nickel as it closely follows the liquidus in the phase diagram. Since the solidification speed during spot welding is high, mushy zone could be neglected. This assumption is justifiable since we are interested only in the composition profile at a macro level.

$$H = H_{Cu}C + H_{Ni}(1-C) \tag{A.15}$$

$$T_{melt} = T_{melt,Cu}C + T_{melt,Ni}(1-C) \tag{A.16}$$

Mass fraction:

$$\frac{\partial C}{\partial t}+\frac{\partial}{\partial x}(uC)+\frac{\partial}{\partial y}(vC)+\frac{\partial}{\partial z}(wC)=\frac{\partial}{\partial x}(D\frac{\partial C}{\partial x})+\frac{\partial}{\partial y}(D\frac{\partial C}{\partial y})+\frac{\partial}{\partial z}(D\frac{\partial C}{\partial z}) \qquad \text{(A.17)}$$

Since no mass is added and mass transfer across all faces is assumed to be zero, there are no source terms for the species conservation equation.

Continuous welding

The reference frame used for the simulation of continuous welding is a moving frame fixed to the laser. The laser moves in the z-axis at a speed w_{scan}. If (x,y,z') is the stationary coordinate system and (x,y,z) is the system in reference to the laser, we can write the convection-diffusion equation for a general variable ϕ in a stationary coordinate system as

$$\frac{\partial}{\partial t}(\rho\phi)+\frac{\partial}{\partial x}(\rho\phi u)+\frac{\partial}{\partial y}(\rho\phi v)+\frac{\partial}{\partial z'}(\rho\phi w)=\frac{\partial}{\partial x}(\rho\Gamma\frac{\partial\phi}{\partial x})+\frac{\partial}{\partial y}(\rho\Gamma\frac{\partial\phi}{\partial y})+\frac{\partial}{\partial z'}(\rho\Gamma\frac{\partial\phi}{\partial z'})+S$$

$$\text{(A.18)}$$

$$\text{where,}\quad z'=z+w_{scan}t \qquad \text{(A.19)}$$

Differentiating equation A.19 with respect to time,

$$w'=w+w_{scan} \qquad \text{(A.20)}$$

Applying chain rule to convert the terms in equation A.18 to the moving frame,

$$\frac{\partial}{\partial z'}(\phi(x,y,z',t))=\frac{\partial z}{\partial z'}\cdot\frac{\partial}{\partial z}(\phi(x,y,z,t))=\frac{\partial}{\partial z}(\phi(x,y,z,t)) \qquad \text{(A.21)}$$

$$\frac{\partial}{\partial t}(\phi(x,y,z',t))=\frac{\partial}{\partial t}(\phi(x,y,z,t))+\frac{\partial z}{\partial t}\cdot\frac{\partial}{\partial z}(\phi(x,y,z,t))$$
$$=\frac{\partial}{\partial t}(\phi(x,y,z,t))+w_{scan}\frac{\partial}{\partial z}(\phi(x,y,z,t)) \qquad \text{(A.22)}$$

Substituting equation A.21 in to equation A.18,

$$\frac{\partial}{\partial t}(\rho\phi)+\frac{\partial}{\partial x}(\rho\phi u)+\frac{\partial}{\partial y}(\rho\phi v)+\frac{\partial}{\partial z'}(\rho\phi w)=\frac{\partial}{\partial x}(\rho\Gamma\frac{\partial\phi}{\partial x})+\frac{\partial}{\partial y}(\rho\Gamma\frac{\partial\phi}{\partial y})+\frac{\partial}{\partial z'}(\rho\Gamma\frac{\partial\phi}{\partial z'})$$
$$+S-\frac{\partial}{\partial z}(\rho\phi w_{scan})$$

$$\text{(A.23)}$$

Thus, the governing equations in the moving frame will be as given below:

Momentum:

$$\frac{\partial}{\partial t}(\rho u) + \frac{\partial}{\partial x}(\rho uu) + \frac{\partial}{\partial z}(\rho uv) + \frac{\partial}{\partial z}(\rho uw) = \frac{\partial}{\partial x}\left(\mu\frac{\partial u}{\partial x}\right) + \frac{\partial}{\partial y}\left(\mu\frac{\partial u}{\partial y}\right) + \frac{\partial}{\partial z}\left(\mu\frac{\partial u}{\partial z}\right)$$
$$-\frac{\partial p}{\partial x} - \left(\frac{K(1-\varepsilon)^2}{\varepsilon^3 + b}\right)u - \frac{\partial}{\partial z}(\rho uw_{scan})$$

(A.24)

$$\frac{\partial}{\partial t}(\rho v) + \frac{\partial}{\partial x}(\rho vu) + \frac{\partial}{\partial z}(\rho vv) + \frac{\partial}{\partial z}(\rho vw) = \frac{\partial}{\partial x}\left(\mu\frac{\partial v}{\partial x}\right) + \frac{\partial}{\partial y}\left(\mu\frac{\partial v}{\partial y}\right) + \frac{\partial}{\partial z}\left(\mu\frac{\partial v}{\partial z}\right) - \frac{\partial p}{\partial y}$$
$$-\left(\frac{K(1-\varepsilon)^2}{\varepsilon^3 + b}\right)v + \rho g[\beta_T(T-T_r) - \beta_C(C-C_r)]$$
$$-\frac{\partial}{\partial z}(\rho vw_{scan})$$

(A.25)

$$\frac{\partial}{\partial t}(\rho w) + \frac{\partial}{\partial x}(\rho wu) + \frac{\partial}{\partial z}(\rho wv) + \frac{\partial}{\partial z}(\rho ww) = \frac{\partial}{\partial x}\left(\mu\frac{\partial w}{\partial x}\right) + \frac{\partial}{\partial y}\left(\mu\frac{\partial w}{\partial y}\right) + \frac{\partial}{\partial z}\left(\mu\frac{\partial w}{\partial z}\right)$$
$$-\frac{\partial p}{\partial z} - \left(\frac{K(1-\varepsilon)^2}{\varepsilon^3 + b}\right)w - \frac{\partial}{\partial z}(\rho ww_{scan})$$

(A.26)

Energy:

$$\frac{\partial}{\partial t}(\rho cT) + \frac{\partial}{\partial x}(\rho ucT) + \frac{\partial}{\partial z}(\rho vcT) + \frac{\partial}{\partial z}(\rho wcT) = \frac{\partial}{\partial x}\left(k\frac{\partial T}{\partial x}\right) + \frac{\partial}{\partial y}\left(k\frac{\partial T}{\partial y}\right) + \frac{\partial}{\partial z}\left(k\frac{\partial T}{\partial z}\right)$$
$$-\frac{\partial}{\partial t}(\rho\Delta H) - \frac{\partial}{\partial z}(\rho cTw_{scan}) - \frac{\partial}{\partial z}(\rho w_{scan}\Delta H)$$

(A.27)

Mass fraction:

$$\frac{\partial C}{\partial t} + \frac{\partial}{\partial x}(uC) + \frac{\partial}{\partial z}(vC) + \frac{\partial}{\partial z}(wC) = \frac{\partial}{\partial x}\left(D\frac{\partial C}{\partial x}\right) + \frac{\partial}{\partial y}\left(D\frac{\partial C}{\partial y}\right) + \frac{\partial}{\partial z}\left(D\frac{\partial C}{\partial z}\right) - \frac{\partial}{\partial z}(Cw_{scan})$$

(A.28)

References

1   J.C. Ion, H.R. Shercliff and M.F. Ashby, "Diagrams for laser materials processing", *Acta Metallurgica et Materialia,* 40 (1992), pp. 1539-1551.

2   W. Duley, *Laser Welding,* John Wiley and Sons Inc., New York (1999).

3   W.M. Steen, *Laser Material Processing,* Springer-Verlag, NewYork (1991).

4   S.A. David and J.M. Vitek, "Correlation between solidification parameters and weld microstructures", *International Materials Reviews,* 34 (1989) pp. 213-245.

5   T.A. Palmer and T. Debroy, "Modelling of nitrogen dissolution during the GTA welding of iron and steels", *Mathematical Modelling of Weld Phenomena 5,* Ed. H. Cerjak, Institute of Materials, London (2001) pp.95-122.

6   Z. Sun, J.C. Ion, "Laser welding of dissimilar metal combinations", *Journal of Materials Science,* 30 (1995) pp. 4205-4214.

7   R.E. Slusher, "Laser Technology", *Reviews of Modern Physics,* 71 (1999) pp.S471-S479.

8   J. Mazumder, "Laser welding: state of the art review", *Journal of Metals,* July (1982) pp.16-24.

9   B.L. Mordike, "Lasers in materials processing", *Progress in Materials Science,* 42 (1997), pp. 357-372.

10 J. Mazumder, A. Schifferer, J. Choi, "Direct Materials Deposition: Designed Macro and Microstructure," *Materials Research Innovations*, 3 (1999), pp. 118-131.

11 A.M. Prokhorov, V.I. Konov, I. Ursu and I.N. Mihailescu, *Laser Heating of Metals,* The Adam Hilger series on Optics and Optoelectronics, Ed. E.R. Pike and W.T. Welford, Adam Hilger, New York (1990).

12 T.J. Wieting and J.L. DeRosa, "Effects of surface condition on the infrared absorptivity of 304 stainless steel", *Journal of Applied Physics,* 50 (1979) pp. 1071-1078.

13 W.E. Maher and R.B. Hall, "Experimental thermal coupling of laser beams", *Journal of Applied Physics,* 49 (1978) pp. 2254-2261.

14 S. Marcus, J.E. Lowder and D.L. Mooney, "Large spot thermal coupling of CO_2 laser radiation to metallic surfaces", *Journal of Applied Physics,* 47 (1976) pp. 2966-2968.

15 Francis P. Gagliano, Robert M. Lumley and Laurence S. Watkins, "Lasers in Industry", *Proceedings of IEEE,* 57 (1969) pp. 114-147.

16 Ø. Grong, *Metallurgical Modelling of welding*, Institute of Materials, 2nd ed., London, (1997).

17 H.E. Cline and T.R. Anthony, "Heat treating and melting material with a scanning laser or electron beam", *Journal of Applied Physics*, 48 (1977) pp. 3895-3900.

18 J. Mazumder and W.M. Steen, "Heat transfer model for cw laser material processing", *Journal of Applied Physics,* 51 (1980) pp. 941-947.

19 J.A. Sekhar, S. Kou and R. Mehrabian, "Heat flow model for surface melting and solidification of an alloy", *Metallurgical Transactions A,* 14A (1983) pp. 1169-1177.

20 T. Debroy and S.A. David, "Physical processes in fusion welding", *Reviews in Modern Physics,* 67 (1995) pp.85-112.

21 G.M. Oreper and J. Szekely, "Heat and fluid flow phenomena in weld pools", *Journal of Fluid Mechanics,* 147 (1984) pp. 53-79.

22 C. Chan, J. Mazumder, M.M. Chen, "A two dimensional transient model for convection in laser melted pool", *Metallurgical Transactions A,* 15A (1984) pp.2175-2184.

23 Biswajit Basu and J. Srinivasan, "Numerical study of steady state laser melting problem", *International Journal of Heat and Mass Transfer,* 31 (1988) pp. 2331-2338.

24 Biswajit Basu and A.W. Date, "Numerical study of steady state and transient laser melting problems – I. Charateristics of flow field and heat transfer", *International Journal of Heat and Mass Transfer,* 33 (1990) pp. 1149-1163.

25 Biswajit Basu and A.W. Date, "Numerical study of steady state and transient laser melting problems – II. Effect of the process parameters", *International Journal of Heat and Mass Transfer,* 33 (1990) pp. 1165-1175.

26 C. L. Chan, J. Mazumder, M.M. Chen, "Effect of surface tension gradient driven convection in a laser melt pool: Three dimensional perturbation model", *Journal of Applied Physics,* 64 (1988) pp. 6166-6174.

27 C. L. Chan, J. Mazumder, M.M. Chen, "Three dimensional axisymmetric model for convection in laser-melted pools", *Materials Science and Technology,* 3 (1987) pp. 306-310.

28 T. Zacharia, A. H. Eraslan, and D. K. Aidun, 'Modelling of Autogenous Welding', *Welding Journal*, 67 (1988) pp. 53s - 62s.

29   T. Zacharia, S.A. David, J.M. Vitek and T. Debroy, "Weld pool development during GTA and laser beam welding of type 304 stainless steel, Part I – theoritical analysis", *Welding Research Supplement,* December (1989) pp. 499s-509s.

30   T. Zacharia, S.A. David, J.M. Vitek and T. Debroy, "Weld pool development during GTA and laser beam welding of type 304 stainless steel, Part I – experimental correlation", *Welding Research Supplement,* December (1989) pp. 510s-519s.

31   S. Kou and Y.H. Wang, "Weld pool convection and its effect", *Welding Research Supplement,* March (1986) pp. 64s-70s.

32   Natarajan Ramanan and Seppo A. Korpela, "Fluid dynamics of a stationary weld pool", *Metallurgical Transactions A,* 21A (1990) pp. 45-57.

33   A.J. Russo, R.L. Akau and J.L. Jellison, "Thermocapillary flow in pulsed laser beam weld pools", *Welding Research Supplement,* January (1990) pp. 23s-28s.

34   Pradip Dutta, Yogendra Joshi and Rama Jenaswamy, "Thermal modelling of gas tungsten arc welding process with nonaxisymmetric boundary conditions", *Numerical Heat Transfer,* 27 (1995) pp. 499-518.

35   Y. Joshi, P. Dutta, P.E. Schupp, D. Espinosa, "Nonaxisymmetric convection in stationary gas tungsten arc weld pools" *Transactions of the ASME,* 119 (1997) pp. 164-172.

36   A. Paul and T. Debroy, "Free surface flow and heat transfer in conduction mode laser welding", *Metallurgical Transactions B,* 19B (1988) pp. 851-858.

37   Randall L. Zehr, "Thermocapillary convection in laser melted pools during materials processing", *Ph.D. Thesis,* University of Illinois at Urbana-Champaign (1991).

38   J. Mazumder, "Overview of melt dynamics in laser processing", *Optical Engineering,* 30 (1991) pp. 1208-1219.

39   A. Robert and T. Debroy, "Geometry of laser spot welds from dimensionless numbers", *Metallurgical and Materials Transactions B,* 32B (2001) pp.941-947.

40   E.A. Metzbower, "Keyhole formation", *Metallurgical Transactions B,* 24B (1993) pp. 875-880.

41   John Dowden, Nazmi Postacioglu, Michael Davis and Phiroze Kapadia, "A keyhole model in penetration welding with a laser", *Journal of Physics D: Applied Physics,* 20 (1987) pp. 36-44.

42   J. Kroos, U. Gratzke and G. Simon, "Towards a self-consistent model of the keyhole in penetration laser beam welding", *Journal of Physics D: Applied Physics,* 26 (1993) pp. 474-480.

43   J. Kroos, U. Gratzke, M. Vicanek and G. Simon, "Dynamic behaviour of the keyhole in laser welding", *Journal of Physics D: Applied Physics,* 26 (1993) pp. 481-486.

44   Vladimir V. Semak, William David Bragg, Brian Damkroger and Steven Kempka, "Transient model for the keyhole during laser welding", *Journal of Physics D: Applied Physics,* 32 (1999) L61-L64.

45   John Dowden and Phiroze Kapadia, "A mathematical investigation of the penetration depth in keyhole welding with continuous CO_2 lasers", *Journal of Physics D: Applied Physics,* 28 (1995) pp. 2252-2261.

46   J. Trappe, J. Kroos, C. Tix and G. Simon, "On the shape and location of the keyhole in penetration lase welding", *Journal of Physics D: Applied Physics,* 27 (1994) pp. 2152-2154.

47   Pablo Solana and Guillermo Negro, "A study of the effect of multiple reflections on the shape of the keyhole in the laser processing of materials", *Journal of Physics D: Applied Physics,* 30 (1997) pp. 3216-3222.

48   Srikanth Sankaranarayanan and Aravind Kar, "Nonlinear effects of laser-plasma interaction on melt-surface temperature", *Journal of Physics D: Applied Physics,* 32 (1999) pp. 777-784.

49   M. Beck, P. Berger and H. Hügel, "The effect of plasma formation on beam focusing in deep penetratin welding with CO_2 lasers", *Journal of Physics D: Applied Physics,* 28 (1995) pp.2430-2442.

50   Akira Matsunawa, Jong-Do Kim, Naoki Seto, Masami Mizutani and Seiji Katayama, "Dynamics of keyhole and molten pool in laser welding", *Journal of Laser Applications,* 10 (1998) pp. 247-254.

51   Shigeki Fujinaga, Hiroo Takenaka, Toru Naikiyo, Seiji Katayama and Akira Matsunawa, "Direct observation of keyhole behaviour during pulse modulated high-power Nd:YAG laser irradiation", *Journal of Physics D: Applied Physics,* 33 (2000) pp. 492-497.

52   J.M. Jouvard, K. Girard and O. Perret, "Keyhole formation and power deposition in Nd:YAG laser spot welding", *Journal of Physics D: Applied Physics,.* 34 (2001) pp. 2894-2901.

53   H. Ki, P.S. Mohanty and J. Mazumder, "Modelling of high-density laser-material interaction using fast level set method", *Journal of Physics D: Applied Physics,* 34 (2001) pp. 364-372.

54   T. Chande and J. Mazumder, "Mass transport in laser surface alloying: Iron-nickel system", *Applied Physics Letters,* 41 (1982) pp. 42-43.

55   A. Kar and J. Mazumder, "One-dimensional finite medium diffusion model for extended solid solution in laser cladding of Hf on nickel", *Acta Metallurgica,* 36 (1988) pp. 701-712.

56   X. He, B.L. Mordike, N. Pirch and E.W. Kreutz, "Laser surface alloying of metallic materials", *Lasers in Engineering,* 4 (1995) pp. 291-316.

57   P. Mohanraj, S. Sarkar, S. Chakraborty, G. Phanikumar, P. Dutta and K. Chattopadhyay, "Modelling of transport phenomena in laser surface alloying with distributed species mass source", *International Journal of Heat and Fluid Flow,* in press (2002).

58   A. Paul and T. Debroy, "Free surface flow and heat transfer in conduction mode laser welding", *Metallurgical Transactions B,* 19B (1988) pp. 851-858.

59   F.K. Chung and P.S. Wei, "Mass, momentum and energy transport in a molten pool when welding dissimilar metals", *Journal of Heat Transfer – Transactions of the ASME,* 121 (1999) pp. 451-461.

60   S.V. Patankar, *Numerical Heat Transfer and Fluid Flow,* Hemisphere Publications, New York (1980), 2nd ed.

61   P.S. Wei and F.K. Chung, "Unsteady Marangoni flow in a molten pool when welding dissimilar metals", *Metallurgical and Materials Transactions B,* 31B (2000) pp. 1387-1403.

62   G. Phanikumar, R. Pardeshi, K. Chattopadhyay, P. Dutta and J. Mazumder, "Dissimilar metal welding of copper nickel couple by continuous wave CO_2 laser", *Trends in Welding Research,* Proceedings of 5th International Conference, Ed., J.M. Vitek, S.A. David, J.A. Johnson, H.B. Smartt, T. Debroy, ASM International, USA (1998) pp. 461-466.

63   J. Seretsky and E.R. Ryba, "Laser welding of dissimilar metals: Titanium to Nickel", *Welding Research Supplement,* July (1976) pp. 208s-211s.

64   G. Metzger and R. Lison, "Electron beam welding of dissimilar metals", *Welding Research Supplement,* August (1976) pp. 230s-240s.

65   C. Pan, R. Wang, J. Gui and Y. Shi, "Direct TEm observation of microstructures of the austenitic/carbon steels welded joint", *Journal of Materials Science,* 25 (1990) pp.3281-3285.

66   B. Majumdar, R. Galun, A. Weisheit and B.L. Mordike, "Formation of a crack-free joint between Ti alloy and Al alloy by using a high-power CO_2 laser", *Journal of Materials Science,* 32 (1997) pp.6191-6200.

67   S. Katayama, R. Usui and A. Matsunawa, "YAG laser welding of steel to aluminium", *Trends in Welding Research,* Proceedings of 5th International Conference, Ed., J.M. Vitek, S.A. David, J.A. Johnson, H.B. Smartt, T. Debroy, ASM International, USA (1998) pp. 467-472.

68   P.S. Wei, Y.K. Kuo and J.S. Ku, "Fusion zone shapes in electron-beam welding of dissimilar metals", *Journal of Heat Transfer – Transactions of the ASME,* 122 (2000) pp. 626-631.

69   T.W. Nelson, J.C. Lippold and M.J. Mills, "A fundamental investigation of the evolution of boundaries and interfaces along the fusion boundary in dissimilar metal welds", *Trends in Welding Research,* Proceedings of 5th International Conference, Ed., J.M. Vitek, S.A. David, J.A. Johnson, H.B. Smartt, T. Debroy, ASM International, USA (1998) pp. 221-226.

70   T.W. Nelson, J.C. Lippold and M.J. Mills, "Investigation of boundaries and structures in dissimilar metal welds", *Science and Technology of Welding and Joining,* 3 (1998) pp. 249-255.

71   W.F. Savage and A.H. Aronson, "Preferred orientation in the fusion zone", *Welding Research Supplement,* February (1966) pp. 85s-89s.

72   J. Clarke, D.C.Weckman and H.W. Kerr, "The columnar to equiaxed grain transition in gas tungsten arc welds", *Trends in Welding Research,* Proceedings of 5th International Conference, Ed., J.M. Vitek, S.A. David, J.A. Johnson, H.B. Smartt, T. Debroy, ASM International, USA (1998) pp. 72-76.

73   M. Rappaz, Ch-A. Gandin, J-L. Deboilles, Ph. Thevoz, "Prediction of solidification microstructures in various solidification processes", *Metallurgical and Materials Transactions A,* 27A (1996) pp. 695-705.

74   Kazutoshi Ichikawa, Atsushi Nogami, Toshihiko Koseki and Yuka Fukuda, "Modelling of solidification and grain growth in steel welds", *Mathematical Modelling of Weld Phenomena 5,* Ed. H. Cerjak, Institute of Materials, London (2001) pp.189-209.

75   M.C. Flemings, *Solidification Processing,* McGraw Hill, New York (1974).

76   R. Trivedi and W. Kurz, "Solidification microstructures: A conceptual approach", *Acta Metallurgica et Materialia,* 42 (1994) pp. 15-23.

77   W.F. Savage, E.F. Nippes and J.S. Erickson, "Solidification mechanisms in fusion welds", *Welding Research Supplement,* August (1976) pp. 213s-221s.

78   O. Grong, D.K. Matlock, "Microstructural development in mild and low-alloy steel weld metals", *International Metals Reviews,* 31 (1986), pp. 27-48.

79   G. Cam and M. Kocak, "Progress in joining of advanced materials", *International Materials Reviews,* 43 (1998), pp. 1-44.

80   T. Zacharia, S.A. David, J.M. Vitek and T. Debroy, "Heat transfer during Nd:YA pulsed laser welding and its effect on solidification structure of austenitic stainless steels", *Metallurgical Transactions A,* 20A (1989) pp. 957-967.

81   A.F.A. Hoadley, M. Picasso and M. Rappaz, "Modelling of solidification phenomena in processes involving a moving heat source", *Mathematical Modelling of Weld Phenomena,* Ed., H. Cerjak and K. Easterling, Institute of Materials, London (1993) pp. 60-71

82 W. Kurz and R. Trivedi, "Modern solidification theory applied to welding", *Trends in Welding Research,* Proceedings of the 4th international conference, Gatlinburg, Tennessee, USA (1995) pp. 115-120.

83 A.F. Norman, R. Ducharme, A. Mackwood, P. Kapadia and P.B. Prangnell, "Application of thermal modelling to laser beam welding of aluminium alloys", *Science and Technology of Welding and Joining,* 3 (1998) pp. 260-266.

84 W. Guo and A. Kar, "prediction of microstructures in laser welding of stainless steel AISI 304", *Journal of Laser Applications,* 11 (1999) pp. 185-189.

85 M. Zimmermann, M. Carrard, and W. Kurz, "Rapid solidification of Al-Cu eutectic alloy by laser remelting", *Acta Metallurgica,* 37 (1989) pp. 3305-3313.

86 M. Gremaud, M. Carrard and W. Kurz, "The microstructure of rapidly solidified Al-Fe alloys subjected to laser surface treatment", *Acta Metallurgica et Materialia,* 38 (1990) pp. 2587-2599.

87 P. Gilgien, A. Zryd and W. Kurz, "Microstructure selection maps for Al-Fe alloys", *Acta Metallurgica et Materialia,* 43 (1995) pp. 3477-3487.

88 Eric A. Brandes, Smithells Handbook, Buttersworth , London.

89 Y. Nakagawa, "Liquid immiscibility in copper-iron and copper-cobalt systems in the supercooled state", *Acta Materialia,* 6 (1958) pp. 704-711.

90 Bhaskar Majumdar, "Thermodynamics and microstructural development in immiscible systems processed through different routes", *Ph.D. Thesis, Indian Institute of Science,* (1995).

91 A. Munitz, "Liquid separation effects in Fe-Cu alloys solidified under different cooling rates", *Metallurgical Transactions B,* 18 B (1987) pp. 565-575.

92 S. Kumar, G. Phanikumar, P. Dutta and K. Chattopadhyay, "Microstuctural development of dissimilar weldments: case of MIG welding of Cu with Fe filler", *Journal of Materials Science,* (2002) in press.

93 Private communication, S. Manjini, Indian Institute of Science, Bangalore (1996).

94 P.S. Mohanty and J. Mazumder, "Solidification behaviour and microstructure evolution during laser beam-material interaction", *Metallurgical and Materials Transactions B,* 29B (1998) pp.1269-1279.

95 M. Gremaud, M. Carrard and W. Kurz, "Banding phenomena in Al-Fe alloys subjected to laser surface treatment", *Acta Metallurgica et Materialia,* 39 (1991) pp. 1431-1443.

96 G. Pascoe and J. Mackowiak, "The application of simple models to the direct calculation of possible phase boundaries in binary equilibrium phase diagrams from simple free-energy/concentration functions", *Journal of the Institute of Metals*, 1970, vol. 98, pp. 253-256.

97   M. B. Carver, "Numerical Computation of Phase Separation in Two Fluid Flow", *Journal of Fluid Engineering,* 106 (1984) pp.147-153.

98   M. Ishii, and K. Mishima, "Two-fluid Model and Hydrodynamic Constitutive Relations", *Nuclear Engineering and Design*, 82 (1984), pp.107-126.

99   A. D. Brent, V. R. Voller, and K. J. Reid, "The Enthalpy Porosity Technique for Modelling Convection-Diffusion Phase Change: Application to the Melting of a Pure Metal", *Numerical Heat Transfer*, 13 (1988) pp.297-318.

100 P. Sahoo, T. Debroy and M.J. McNallan, "Surface tension of binary metal – surfac e active solute systems under conditions relevant to welding metallurgy", *Metallurgical Transactions B,* 19B (1988) pp. 483-491.

101 B. Gallois and C.H.P. Lupis, "Effect of oxygen on the surface tension of liquid copper", *Metallurgical Transactions B,* 12B (1981) pp. 549-557.

102 A.C.D. Chaklader, A.M. Armstrong and S.K. Misra, "Interface reactions between metals and ceramics: IV, wetting of sapphire by liquid copper-oxygen alloys", *Journal of American Ceramic Society,* November (1968) pp. 630-633.

103 C.F. Baes Jr and H.H. Kellogg, "Effect of dissolved sulphur on the surface tension of liquid copper", *Transactions of AIME - Journal of Metals,* May (1953) pp. 643-648.

104 W.M. Armstrong, A.C.D. Chaklader and J.F. Clarke, "Interface reactions between metals and ceramics: I, saphire-nickel alloys", *Journal of American Ceramic Society,* March (1962) pp. 115-118.

105 T. Zacharia, S.A. David, J.M. Vitek and T. Debroy, "Modelling of interfacial phenomena in welding", *Metallurgical Transactions B,* 21B (1990) pp. 600-603.

106 Y.H. Xiao and G. den Ouden, "Measurement of surface tension of liquid metals and alloys under arc welding conditions", *Materials Science and Technology,* 13 (1997) pp. 791-794.

107 G. Phanikumar, P. Dutta and K. Chattopadhyay, "Supercomputing applications in materials enginering", *Current Science,* April 10 (2002) pp. 847-849.

108 K. Lepper, M. James, J. Chashechkina and D.A. Rigney, "Sliding behaviour of selected aluminium alloys", *Wear,* 203-204 (1997) pp.46-56.

109 B. Prinz, A. Romero and L. Ratke, "Casting process for hypermonotectic alloys under terrestrial conditions", *Journal of Materials Science,* 30 (1995) pp. 4715-4719.

110 W.K. Thieringer and L. Ratke, "The coarsening of liquid Al-Pb-dispersions", *Acta Metallurgica,* 35 (1987) pp. 1237-1244.

111 D. Uffelmann, W. Bender, L. Ratke and B. Feuerbacher, "Ostwald ripening in lorentz-force stabilised Cu-Pb dispersions at low volume fractions. I-experimental observations", *Acta Metallurgica et Materialia,* 43 (1995) pp.173-180.

112 D. Uffelmann, L. Ratke, and B. Fuererbacher, "Lorentz force stabilization of solid-liquid and liquid-liquid dispersions", *Immiscible liquid metals and organics,* Ed., L. Ratke, DGM Informationsgesselshaft mbH (1993) Oberursel, Germany, pp. 251-258.

113 A.J. McAlister, "The Aluminium Bismuth system", *Bulletin of Alloy Phase Diagrams,* 5 (1984) pp.247-250

114 L. Granasy and L. Ratke, "Homogeneous nucleation within the liquid miscibility gap of Zn-Pb alloys", *Scripta Metallurgica et Materialia,* 28 (1993), pp.1329-1334.

115 A.J. McAlister, "The Al-Bi (Aluminum-Bismuth) system", *Bulletin of Alloy Phase Diagrams,* 5 (1984) pp.247-250.

116 Private Communication, L. Ratke, DLR, Cologne, Germany.

117 C.V. Thompson and F. Spaepen, "Homogeneous crystal nucleation in binary metallic melts", *Acta Metallurgica,* 31 (1983), pp.2021-2027.

118 Fritz Falk, "Interface tension in partially miscible alloys", *Immiscible liquid metals and organics,* Ed. L. Ratke, DGM Informationsgesselshaft mbH (1993) Oberursel, Germany, pp.93-100.

119 B. Derby and J. Favier, "A criterion for the determination of monotectic structure", *Acta Metallurgica,* 31 (1983), pp. 1123-1130.

120 L. Ratke, S. Diefenbach, "Liquid Immiscible alloys", *Materials Science and Engineering,* R15 (1995) pp.263-347.

121 C. Zener, "Theory of growth of spherical precipitates from solid solution", *Journal of Applied Physics,* 20 (1949), pp.950-953.

122 I.M. Lifshitz and V.V. Slyzov, "The kinetics of precipitation from supersaturated solid solutions" *J. Phys. Chem. Solids,* 19 (1961) pp.35.

123 C. Wagner, "Theorie der Alterung von Niederschlägen durch umlösen (Ostwarld-Reifnung)", *Z. Electrochem,* 65 (1961), pp. 581.

124 L. Ratke, "Simultaneous coarsening of dispersion by growth and coagulation", *Journal of Colloids and Interface Science,* 119 (1987), pp. 391-397.

125 P.Mohanraj, S.Sarkar, S.Chakraborty, G.Phanikumar, P.Dutta, and K.Chattopadhyay., "Modelling of Transport Phenomenon in Laser Surface Alloying with Distributed Melting of Alloying Element", *International Journal of Heat and Fluid Flow*, (2002, in press).

126 R.L. Drake, "A general mathematical survey of the coagulation equation" in *Topics in Aerosol Research,* (G.M. Hidy and J.R. Brock, Eds.), 2 (1972) pp.203, Pergamon, Oxford, 1972.